

LIGHTNING PROPAGATION AND GROUND ATTACHMENT PROCESSES FROM
MULTIPLE-STATION ELECTRIC FIELD AND X-RAY MEASUREMENTS

By

JOSEPH SEAN HOWARD

A DISSERTATION PRESENTED TO THE GRADUATE SCHOOL
OF THE UNIVERSITY OF FLORIDA IN PARTIAL FULFILLMENT
OF THE REQUIREMENTS FOR THE DEGREE OF
DOCTOR OF PHILOSOPHY

UNIVERSITY OF FLORIDA

2009

© 2009 Joseph Sean Howard

To my beautiful, loving, and very understanding wife, Amber

ACKNOWLEDGMENTS

I would first like to express my sincerest gratitude and appreciation for my committee chair and Ph.D. advisor, Dr. Martin Uman. He has always extended the highest degree of kindness and friendship. This work would simply not have been possible without his support and guidance, and I will certainly never forget him. I would also like to thank my co-chair, Dr. Vladimir Rakov, for his gracious support and thoughtful comments throughout the years. Of course, there are many people to whom I am indebted for their long hours and enduring effort out at the research facility. These individuals include Jason Jerauld, Chris Biagi, Dustin Hill, Michael Stapleton, Robert Olsen III, Dr. Doug Jordan, Ziad Saleh, and George Schnetzer. I would like to extend a special thanks to Jason Jerauld for taking me under his wing and being a pillar of support through my graduate studies and to Chris Biagi for being an excellent friend and co-worker during our time together. I would also like to thank Dr. Joseph Dwyer and Dr. Hamid Rassoul, our collaborators from the Florida Institute of Technology. I especially want to thank my wife, Amber, for her tremendous support and sacrifice through these difficult years. This work was funded in part by the DARPA (HR0011-08-1-0088), the NSF (ATM 0420820, ATM 0607885, ATM 0003994, ATM 0346164, and ATM 0133773), and the FAA (99-G-043). Additionally, I received financial support for 4 years from a UF Alumni Fellowship.

TABLE OF CONTENTS

	<u>page</u>
ACKNOWLEDGMENTS	4
LIST OF TABLES	8
LIST OF FIGURES	10
ABSTRACT.....	15
CHAPTER	
1 INTRODUCTION AND LITERATURE REVIEW	17
1.1 Introduction	17
1.2 The Global Electric Circuit, Thunderclouds, and Lightning.....	21
1.3 Downward Negative Lightning.....	25
1.4 Rocket-Triggered Lightning	38
1.5 Additional Observations of Downward-Negative-Leader/Upward-Return-Stroke Sequences.....	41
1.5.1 Return-Stroke Waveforms	41
1.5.2 X-Ray Observations.....	46
1.6 Determining Lightning Locations Via Time-of-Arrival	50
1.7 The International Center for Lightning Research and Testing at Camp Blanding, Florida	60
1.8 History of the Multiple Station Experiment.....	61
2 EXPERIMENT DESCRIPTION	73
2.1 Experiment Overview	73
2.2 Control System.....	77
2.2.1 PIC Controllers	77
2.2.2 Control Computer	80
2.3 Fiber-Optic Links.....	81
2.4 Digital Storage Oscilloscopes	84
2.5 Measurement Implementation.....	91
2.5.1 Electric Field and Electric Field Time-Derivative Measurements.....	91
2.5.2 Magnetic Field Measurements	99
2.5.3 X-Ray Measurements.....	103
2.5.4 Optical Measurements.....	106
2.5.5 Channel-Base Current Measurements.....	108
2.6 Trigger and GPS Time-Stamping Systems	111
2.7 Video and Camera Systems	115
2.8 Measurement Locations and Time Delays.....	119
3 DATA	164

3.1	Data Summary and Organization	164
3.2	Data Calibration and Processing	166
4	LOCATING LIGHTNING EVENTS WITH THE MSE/TERA TOA NETWORK	174
4.1	Methodology	176
4.2	Implementation	179
4.2.1	Time Synchronization	180
4.2.2	Waveform Correlation and Visualization	182
4.2.3	Arrival Time Selection	184
4.2.4	Source Determination	186
4.2.5	Documentation	187
4.3	Accuracy of the TOA System	188
5	LOCATION OF LIGHTNING LEADER X-RAY AND ELECTRIC FIELD CHANGE SOURCES	191
5.1	Data and Analysis	192
5.2	Summary and Conclusions	195
6	RF AND X-RAY SOURCE LOCATIONS DURING THE LIGHTNING ATTACHMENT PROCESS	202
6.1	Introduction	202
6.2	Data and Analysis	203
6.2.1	MSE0604	204
6.2.2	MSE0703	211
6.2.3	MSE0704	213
6.2.4	UF0707	216
6.3	Discussion	224
6.3.1	Electric Field and Field-Derivative Comparison	224
6.3.2	Leader Phase	228
6.3.3	Post-Leader Phase	229
6.3.3.1	Leader burst	229
6.3.3.2	Slow-front pulses and the fast transition	231
6.4	Summary	232
7	EXAMINATION OF ELECTRIC FIELD DERIVATIVE WAVEFORMS ASSOCIATED WITH STEPPED LEADERS AT CLOSE RANGES	255
7.1	Presentation of Leader-Step Waveforms	257
7.2	Parameters for dE/dt Pulses of Stepped-Leaders	260
7.3	Modeling of Stepped-Leader Pulses	263
7.3.1	Calculation of Lightning Electric and Magnetic Fields	263
7.3.2	Modeling Results	267
7.4	Conclusion	272

8	SUMMARY OF RESULTS AND RECOMMENDATIONS FOR FUTURE RESEARCH	308
8.1	Summary of Results	308
8.2	Improvements to the MSE/TERA System	316
8.3	Recommendations for Future Research	318
	LIST OF REFERENCES	319
	BIOGRAPHICAL SKETCH	334

LIST OF TABLES

<u>Table</u>	<u>page</u>
2-1 List of the MSE/TERA measurements and their acquisition settings for the 2005 configuration.	128
2-2 List of MSE/TERA measurements and acquisition settings for the 2006 configuration.	129
2-3 List of MSE/TERA measurements and acquisition settings for the 2007 configuration.	130
2-4 Summary of MSE fiber-optic links used between 2005 and 2007.	138
2-5 Summary of the DSOs used in the MSE/TERA network between 2005 and 2007.	138
2-6 Configurations for the channel-base current measurements.	154
2-7 Orientation of the MSE/TERA video cameras.	159
2-8 Summary of the 2005 ICLRT survey with a WAAS-enabled Garmin eTrex Venture hand-held GPS receiver.	161
2-9 Summary of the 2006 site survey performed with an electronic transverse and surveyor level.	162
2-10 Locations of the four stations added in 2007.	163
2-11 Measured time delays for the TOA measurements.	163
3-1 List of natural cloud-to-ground flashes recorded by the MSE/TERA network.	170
3-2 List of rocket-triggered flashes recorded by the MSE/TERA network.	170
3-3 Summary of DSO allocation and settings for 2005 MSE/TERA configuration.	171
3-4 Summary of DSO allocation and settings for 2006 MSE/TERA configuration.	171
3-5 Summary of DSO allocation and settings for 2007 MSE/TERA configuration.	171
3-6 Summary of data obtained by the MSE/TERA network for natural lightning flashes	172
3-7 Summary of data obtained by the MSE/TERA network for rocket-triggered flashes.	173
5-1 Summary of the source pair location results for MSE0604.	200
5-2 Summary of the source pair location results for UF0707.	200

6-1	Summary of TOA location results for the dE/dt pulses shown in Figure 6-1 for the first stoke of MSE0604.	235
6-2	Summary of TOA location results for the dE/dt pulses shown in Figure 6-7 for the first stoke of MSE0703.	242
6-3	Summary of TOA location results for the dE/dt pulses shown in Figure 6-9 for the first stoke of MSE0704.	245
6-4	Summary of TOA location results for the dE/dt pulses shown in Figure 6-11 for the first stoke of UF0707.	248

LIST OF FIGURES

<u>Figure</u>		<u>page</u>
1-1	Classifications of cloud-to-ground lightning based on the movement and charge of the initial leader.....	66
1-2	Sequence of events in a downward negative cloud-to-ground lightning flash from the time the initial stepped leader exits the cloud base.....	67
1-3	Sequence of events in a classical-triggered lightning.....	68
1-4	Satellite image illustrating the major structural landmarks of the ICLRT.....	69
1-5	The tower rocket launcher.....	70
1-6	The mobile rocket launcher in its armed position.....	71
1-7	The Launch Control trailer.....	72
2-1	Sketch of the MSE/TERA network as it existed in 2007.....	126
2-2	Diagram illustrating the operation of the MSE network.....	127
2-3	The 2001 PIC controller.....	131
2-4	Diagram of the typical 2001 PIC controller installation.....	132
2-5	Installation of the 2001 PIC controller in an actual measurement.....	132
2-6	Housing for an RF PIC mounted with its solar cell.....	133
2-7	The 2006 PIC controller.....	133
2-8	Diagram of the typical 2006 PIC controller installation.....	134
2-9	Optical fan-out board used by the control computer to control the 2006 version PIC controllers.....	135
2-10	The MSE/TERA network control system located in the Launch Control trailer.....	135
2-11	The electric field mill that is continually monitored by the control computer.....	136
2-12	Flowchart illustrating the MSE/TERA network control system algorithm.....	137
2-13	Digital storage oscilloscopes along the west wall in Launch Control.....	139
2-14	Flat-plate antenna used in E-field and dE/dt measurements.....	140

2-15	Installation of the flat-plate antenna.	141
2-16	Frequency-domain equivalent circuit for the flat-plate antenna.	141
2-17	Diagram for the dE/dt measurement configuration.	142
2-19	Magnetic field coaxial-loop antenna.....	143
2-20	Single-ended output coaxial-loop antenna.....	144
2-21	Diagram for the magnetic field measurement configuration.	145
2-22	Diagram of the TERA box measurement.....	146
2-23	TERA box with two NaI/PMT detectors.	147
2-24	TERA box with a plastic scintillator detector.....	148
2-25	Schematic of the optical sensor circuit.	149
2-26	Diagram of the optical measurement configuration.....	149
2-27	Optical measurement assembly on top of a 2.5 m tall military canister located at the south west corner of the ICLRT site.	150
2-28	Inside of the channel-base current measurement box on the tower launcher.	151
2-29	Inside of the electronics boxes for the 2007 channel-base current measurements on the tower launcher.....	152
2-30	Diagram of the channel-base current measurements.	153
2-31	Time-domain equivalent circuit for the channel-base current measurements.	154
2-32	The optical AND trigger, buffer circuit, and OR buffer form the basis of the trigger system.	155
2-33	The GPS antenna used with the time-stamping system is mounted to the roof at the south end of Launch Control.....	155
2-34	Diagram of the 2005 trigger configuration at the ICLRT.....	156
2-35	Diagram of the 2006 trigger configuration at the ICLRT.....	157
2-36	Diagram of 2007 trigger configuration at the ICLRT.....	158
2-37	Components of the MSE/TERA video system.	159
2-38	Frame of video from the MSE/TERA video system.....	160

5-1	X-ray waveforms involved in the location of one event in MSE0604.	198
5-2	dE/dt waveforms corresponding to the X-ray pulses shown in Figure 5-1.....	198
5-3	Approximate locations for the downward leaders of MSE0604 and UF0707 shown relative to the eight TOA stations (triangles).....	199
5-4	Station 1 waveforms (using atmospheric electricity sign convention) for one event during MSE0604 at a distance of ~250 m which illustrate the typical delay of the X-ray emission from the electric field change peak.....	201
6-1	dE/dt waveforms from the three stations closest to the first stroke of MSE0604.....	234
6-2	Zoomed view of the waveforms shown in Figure 6-1.	236
6-3	Visual representation of the first stroke in MSE0604.....	237
6-4	Illustration of points used in determining the downward velocity of the MSE0604 stepped leader.....	238
6-5	Determination of the downward leader velocity for each of the four strokes presented.	239
6-6	Two synchronized pairs of co-located X-ray and dE/dt measurements from MSE0604.	240
6-7	dE/dt waveform nearest the first stroke of MSE0703.....	241
6-8	Visual representation of the first stroke in MSE0703.....	243
6-9	Two closest dE/dt waveforms for the first stroke of MSE-0704.....	244
6-10	Visual representation for the first stroke of MSE0704.	246
6-11	Two dE/dt waveforms for the first stroke in rocket-triggered flash UF0707.	247
6-12	Visual representation for the first stroke in the rocket-triggered flash UF-0707.....	249
6-13	Comparison of the Station 7 dE/dt waveform and the channel-base current for rocket-triggered flash UF0707.....	250
6-14	Single video frame imaging the first return stroke in flash UF0707.	251
6-15	Comparison of MSE0704 return-stroke waveforms measured at Station 5.	252
6-16	Comparison of MSE0604 return-stroke waveforms measured at Stations 1 and 8.	253
6-17	Comparison of UF0707 return-stroke waveforms measured at Stations 4, 7, and 9.	254

7-1	Leader step from MSE0604 exhibiting the characteristic pulse shape.	275
7-2	Diagram illustrating the spatial relationship between the leader step and the antenna. ..	276
7-3	Leader step from MSE0703 exhibiting the characteristic pulse shape.	277
7-4	Leader step from MSE0604 where the closest station is missing the initial peak.	278
7-5	Leader step from MSE0604 where the two closest stations are missing the initial peak.	279
7-6	Leader step from MSE0604 which exhibits negative dip prior to the step.	280
7-7	Another MSE0604 leader step with a negative dip.	281
7-8	First example of a leader step with secondary pulses.	282
7-9	Second example of a leader step with secondary pulses.	283
7-10	Third example of a leader step with secondary pulses.	284
7-11	Fourth example of a leader step with secondary pulses.	285
7-12	Fifth example of a leader step with secondary pulses.	286
7-13	Sixth example of a leader step with secondary pulses.	287
7-14	Seventh example of a leader step with secondary pulses.	288
7-15	Eighth example of a leader step with secondary pulses.	289
7-16	Histogram of peak dE/dt range-normalized to 100 km.	290
7-17	Illustration of the half-peak and 10-90% rise time parameters that are measured.	291
7-18	Plot of half-peak width for dE/dt leader pulses versus distance.	292
7-19	Plot of 10-90% rise time for dE/dt leader pulses versus distance.	293
7-20	Plot of half-peak width for dE/dt leader pulses versus peak dE/dt , range-normalized to 100 km.	294
7-21	Histogram of half-peak width of dE/dt leader pulses.	295
7-22	Histogram of 10-90% rise time for dE/dt leader pulses.	296
7-23	Illustration of geometry involved in calculating electric and magnetic fields on ground at horizontal distance r from a straight and vertical antenna of length $H = H_T - H_B$ over a perfectly conducting ground plane.	297

7-24	Step 1 modeling results using the Heidler model.	298
7-25	Current and current derivative waveform used in the Step 1 model results shown in Figure 7-24.	299
7-26	Step 2 modeling results using the Heidler model.	300
7-27	Current and current derivative waveform used in the Step 2 model results shown in Figure 7-26.	301
7-28	Step 2 modeling results using the Jerauld model.	302
7-29	Current and current derivative waveform used in the Step 2 model results shown in Figure 7-28.	303
7-30	Step 3 modeling results using the Heidler model.	304
7-31	Current and current derivative waveform used in the Step 3 model results shown in Figure 7-30.	305
7-32	Step 3 modeling results using the Jerauld model.	306
7-33	Current and current derivative waveform used in the Step 3 model results shown in Figure 7-32.	307

Abstract of Dissertation Presented to the Graduate School
of the University of Florida in Partial Fulfillment of the
Requirements for the Degree of Doctor of Philosophy

LIGHTNING PROPAGATION AND GROUND ATTACHMENT PROCESSES FROM
MULTIPLE-STATION ELECTRIC FIELD AND X-RAY MEASUREMENTS

By

Joseph Sean Howard

December 2009

Chair: Martin A. Uman

Co-chair: Vladimir A. Rakov

Major: Electrical and Computer Engineering

The Multiple Station Experiment/Thunderstorm Energetic Radiation Array (MSE/TERA) network operating at the International Center for Lightning Research and Testing in Camp Blanding, FL has been used to examine the close RF electric and magnetic field and X-ray environment of cloud-to-ground lightning over a period from 2005 to 2007. Data were obtained for 18 natural and 9 rocket-triggered flashes that are thought to have terminated within or very near the network. The experimental system consisted of electric field sensors (bandwidth of 0.2 Hz to 3 MHz), magnetic field sensors (10 Hz to 3 MHz), dE/dt sensors (DC to 25 MHz), and X-ray sensors (primary type had rise and fall times of 0.17 μ s and 0.9 μ s, respectively) spread around an area of about 0.5 km², with the exact number of sensors varying from year to year. For rocket-triggered flashes, the channel-base-current was also measured (DC to 8 MHz). A subset of these measurements, consisting of eight dE/dt sensors and eight X-ray sensors, provided the network with time-of-arrival (TOA) location capabilities. This TOA network, which is the focal point of the present analyses, was used to investigate the spatial and temporal relationship between leader X-ray sources and electric-field-change sources as well as the role of post-leader processes in the production of X rays. The dE/dt portion of the TOA system was also

used to track and identify low-altitude processes occurring during the leader phase, attachment process, and return stroke with a higher degree of accuracy than previously possible with similar systems. A comparison of the collected waveforms, combined with these source locations, is used to obtain new insights into some of the more perplexing aspects of lightning, such as the step-formation process, leader propagation near ground, and the attachment process.

CHAPTER 1 INTRODUCTION AND LITERATURE REVIEW

1.1 Introduction

Experiments performed at the International Center for Lightning Research and Testing (ICLRT) located in Camp Blanding, Florida have investigated a variety of topics involving atmospheric electricity, lightning physics, and lightning protection during the 16 year existence of the facility. Many of the important scientific contributions gained through this research have resulted directly from the acquisition of close (within a few hundred meters of the lightning channel) electric and magnetic field and field-derivative waveforms. In the case of rocket-triggered lightning (Section 1.4), these waveforms have typically been accompanied by simultaneous current and/or current-derivative waveforms measured at the base of the lightning channel. The use of such measurements with both rocket-triggered [*Rakov et al.*, 1998, 2001; *Uman et al.*, 2000, 2002; *Crawford et al.*, 2001; *Miki et al.*, 2002; *Schoene et al.*, 2003a] and natural [*Jerauld et al.*, 2008] lightning has been critical in filling a long-standing void in the lightning literature regarding the close lightning electromagnetic environment. Further, analyses of these data have produced useful information about the properties, physics, and theories of lightning, such as estimates of leader parameters (charge density, current, electric potential, and propagation speed) and the return-stroke propagation speed [*Jerauld et al.*, 2004; *Kodali et al.*, 2005; *Jerauld* 2007]; insights into the mechanisms of dart-stepped (and by inference stepped) leaders [*Rakov et al.*, 1998]; validation and comparison of return-stroke models [*Schoene et al.*, 2003b]; and insights into the ground attachment process of natural first strokes [*Jerauld et al.*, 2007; *Jerauld* 2007].

Following a report by *Moore et al.* [2001] of high-energy radiation accompanying negative stepped leaders in New Mexico, NaI scintillation detectors were used at the ICLRT in

conjunction with the existing field, field-derivative, and current measurements to show that energetic radiation, specifically X rays, is also produced by negative dart and dart-stepped leaders associated with rocket-triggered lightning [Dwyer *et al.*, 2003]. Later measurements by Dwyer *et al.* [2004] showed that the energetic radiation is composed of X rays with energies extending up to about 250 keV and that the emissions occurred in short, $< 1 \mu\text{s}$, burst. In addition, Dwyer *et al.* [2005] showed that X rays are produced in coincidence with leader step formation in natural first strokes, and that the X-ray emissions of stepped leaders are similar to those of dart leaders. These discoveries have already had a significant impact on the views of lightning electrical breakdown in air, and future observation may provide important insights into the processes of leader step formation and propagation. A significant aspect of the experiment discussed in this dissertation was to continue these observations.

Although the aforementioned studies have utilized a variety of experimental setups, the data, results, and capabilities are indicative of the largest and longest running experiment used at the ICLRT to obtain close electric and magnetic field and field derivatives waveforms: the Multiple Station Experiment (MSE). Historically, the MSE has been comprised of these basic measurements distributed about eight or ten locations, referred to as stations [Crawford, 1998; Jerauld, 2007; Jerauld *et al.*, 2008]. During the period of investigation discussed in this dissertation, the MSE network was gradually expanded to 24 stations and was equipped with an array of X-ray sensors (NaI scintillation detectors) and a time-of-arrival (TOA) location system.

The goal of the work presented in this dissertation has been to expand the general knowledge about cloud-to-ground lightning, particularly processes associated with downward-negative-leader/upward-return-stroke sequences, by making new observations of the close electromagnetic environment of lightning. Specifically, a new TOA system, comprised of eight

wideband electric field derivative (dE/dt) antennas and eight NaI scintillation detectors, was used to investigate the spatial and temporal relationships between the X-ray and electric field change sources associated with downward negative leaders in both natural and rocket-triggered lightning. This same set of measurements was also used to examine the role of both the attachment process and the return stroke in X-ray production. The dE/dt portion of the TOA system was used to obtain high-accuracy locations for pulses occurring at the end of the leader phase, during the attachment process, and at the start of the return stroke for several strokes involving downward negative leaders, a task that challenged previous and current TOA systems. These data provide important insights into the step formation process in lightning leaders, leader propagation near the ground, and the attachment process. Additionally, data collected by the author in collaboration with researchers at the Florida Institute of Technology have been used to investigate characteristics of the X-ray emissions and the causative energetic electrons [e.g., *Saleh et al.*, 2009]; details of the experiment and collected data sets are provided.

During the experimental period, between 2005 and 2007, data were acquired for 18 natural flashes and 9 rocket-triggered flashes that terminated within or very near the network. All of these flashes lowered negative charge to ground, i.e., all of the component strokes involved downward negative leaders. Although the analyses presented in this dissertation are limited to those flashes conducive to study with TOA techniques, all flashes are documented, as the data may be reexamined and used for other purposes during future studies.

The journal papers provided in the following list have been published or accepted as a result of the work presented in this dissertation.

- Howard, J., M. A. Uman, J. R. Dwyer, D. Hill, C. Biagi, Z. Saleh, J. Jerauld, and H. K. Rassoul (2008), Co-location of lightning leader x-ray and electric field change sources, *Geophys. Res. Lett.*, 35, L13817, doi:10.1029/2008GL034134.

- Howard, J., M. A. Uman, C. Biagi, D. Hill, J. Jerauld, V. A. Rakov, J. Dwyer, Z. Saleh, and H. Rassoul (2009), RF and x-ray source locations during the lightning attachment process, *J. Geophys. Res.*, doi.10.1029/2009JD012055, in press. (accepted 20 October 2009)
- Saleh Z., J. Dwyer, J. Howard, M. Uman, M. Bakhtiari, D. Concha, M. Stapleton, D. Hill, C. Biagi, H. Rassoul (2009), Properties of the X-ray emission from rocket-triggered lightning as measured by the Thunderstorm Energetic Radiation Array (TERA), *J. Geophys. Res.*, 114, D17210, doi:10.1029/2008JD011618.

Additional journal papers are also planned for publication from the dissertation material.

Specific new contributions to the literature that are discussed elsewhere in this dissertation are listed below.

- A TOA location system that can track low-altitude lightning sources with an altitude error on the order of only 10 m was developed.
- The first 3D locations were obtained for both X-ray and dE/dt pulses associated with individual leader steps, providing the first proof of their co-location (within 50 m).
- X-ray emissions were observed to occur 0.1 to 1.3 μs after the origin of the leader step electric field changes.
- X-ray observations combined with the TOA locations for multiple pulses within individual leader steps seem to indicate that lightning leader steps involve a space stem process similar to leader steps in long air gap discharges observed in the laboratory.
- dE/dt pulses from three post-leader processes are identified and tracked: (1) the “leader burst,” a group of pulses in the dE/dt waveforms radiated within about 1 μs and occurring just prior to the slow front in the corresponding return stroke electric field waveform; (2) dE/dt pulses occurring during the slow front; and (3) the fast transition or dominant dE/dt pulse that is usually associated with the rapid transition to peak in the return stroke electric field waveform.
- The leader burst exhibited rapid and significant downward movement, not typically observed with the preceding leader steps (the leader burst may also cover significant horizontal distances or involve simultaneous progression of the downward and upward connecting leaders), and it corresponded to a hump or step that occurred just prior to the slow front in the electric field waveform.
- It is hypothesized that the slow-front and fast-transition pulses are the result of a similar process which involves multiple connections between the upward and downward leader branches, based on video images and the similar pulse characteristics and locations observed for these two types of pulses.

- Each of the post-leader processes was shown to be associated with X-ray emissions, the first evidence that post-leader processes also produce X-rays.
- The half-peak width of the dE/dt leader-step waveforms obtained at these close ranges are shorter than reported in previous literature, indicating that the associated electric field pulses may have a faster rise time than previously thought.
- The dE/dt waveforms, TOA locations, and the transmission-line model are used to infer the leader-step current waveform and its derivative. Characteristics of these waveforms are reported.

1.2 The Global Electric Circuit, Thunderclouds, and Lightning

Before discussing specific aspects of the lightning process, it is helpful to discuss the role of lightning and thunderstorms in the classical view of atmospheric electricity as well as review some of the basic sources, classifications, and terminology of lightning. *Uman* [1987] defines lightning as a transient, high-current electric discharge whose path length is measured in kilometers. This is a general definition which encompasses many types of lightning discharges. Further, there exists a variety of cloud structures which are capable of producing lightning, such as thunderstorms, snowstorms, sand storms, volcanoes, and nuclear explosions. Since the thundercloud (or a lightning-producing cumulonimbus) is the primary charge source for lightning on Earth, this cloud type has garnered the most attention in studies pertaining to lightning and atmospheric electricity.

Thunderstorms (typically a system of thunderclouds) and their frequent production of lightning are generally believed to play a key role in the “global electrical circuit.” Various measurements have established that the Earth’s surface is negatively charged and the air is positively charged, resulting in a downward-directed electric field of about 100 V m^{-1} near the Earth’s surface during fair-weather (absence of thunderstorms) conditions. The electrical conductivity of the atmosphere increases with height, and it increases rapidly above 60 km due to the presence of free electrons [*Roble and Tzur*, 1986; *Reid*, 1986]. The electrosphere, a region of

the atmosphere near 60 km, is usually considered an equipotential region for quasi-static conditions, and it has a positive potential of about 300 kV relative to the Earth's surface. This Earth-atmosphere system can be crudely modeled as a lossy spherical capacitor [*Uman*, 1974], with the Earth's surface and electrosphere comprising the inner and outer conductors, respectively, and the atmosphere representing a weakly conducting dielectric. According to this model, the Earth's surface holds a net negative charge of approximate 5×10^5 C, with an equal positive charge distributed throughout the atmosphere [*Rakov and Uman*, 2003]. Most of the net positive charge is contained within 1 km of the Earth's surface with little charge actually residing on the electrosphere "shell." The weakly conducting atmosphere permits a fair-weather leakage current on the order of 1 kA (or current density of approximately 2×10^{-12} A m⁻²) between the inner and outer conductors. This leakage current would neutralize all the charge on Earth in about 10 minutes if there were no mechanism to replenish the charge. Since the capacitor is observed to remain charged, some mechanism must resupply the charge. *Wilson* [1920] suggested that the global circuit charge is maintained by the action of thunderstorms, with negative charge being lowered to ground primarily by lightning and corona discharges while positive charge presumably leaks from the cloud tops into the electrosphere. This idealization of charge distribution and movement is the so-called "classical" view of atmospheric electricity.

Although the mechanisms of cloud electrification are complex and beyond the scope of the discussion here, they basically involve the electrification of individual hydrometeors (atmospheric water in any form) and a process which separates the charged hydrometeors by their polarity, such as the convection mechanism [e.g., *Moore et al.*, 1989] or by gravity such as in the graupel-ice mechanism [e.g., *Jayaratne et al.*, 1983; *Baker and Dash* 1989, 1994]. The distribution of the charged particles within the cloud is equally complex and changes continually

as the cloud evolves; however, remote [e.g., *Krehbiel*, 1986] and *in situ* measurements [e.g., *Byrne et al.*, 1983] have allowed a simple model for the gross cloud charge structure of the cumulonimbus to be formulated. The charge structure is normally idealized as a vertical tripole, with a net positive charge at the top, a net negative charge in the middle, and another positive charge at the bottom. The magnitude and altitude of these charge centers vary depending on the global region, primarily the altitude at which freezing of water occurs. In Florida thunderclouds the top and middle charge centers are best represented with equal quantities of charge, on the order of 40 C, located at altitudes of 12 km and 7 km, respectively. The lowest charge center, which may be absent in some cases, is typically located at 2 km and is an order of magnitude smaller than the higher charge centers. Recent *in situ* measurements [e.g., *Marshall and Rust*, 1991; *Rust and Marshall*, 1996], however, indicate that the charge structure of a thundercloud is usually more complicated than the simple tripolar model, with additional charge regions frequently existing in the lower part of the cloud.

Lightning discharges associated with thunderstorms are broadly classified into two categories: cloud discharges (do not interact with ground) and cloud-to-ground discharges (interact with ground). The term cloud discharges encompasses three types of lightning: (i) intracloud discharges, those occurring within the confines of a thundercloud; (ii) intercloud discharges, those occurring between thunderclouds; and (iii) air discharges, those occurring between a thundercloud and clear air. Collectively, cloud discharges are estimated to account for nearly three-quarters of all global lightning [*Rakov and Uman*, 2003] and are the primary lightning threat to aircraft. It is generally believed that the majority of cloud discharges are of the intracloud type; however, there is currently no reliable data to confirm this, as the electric field records are strikingly similar for these different types of discharges.

Cloud-to-ground (CG) discharges are the most studied and best-understood type of lightning because of their practical interest (e.g., causing injury and death, disrupting power and communication systems, and igniting fires) and because they are relatively easy to study compared to cloud discharges. *Berger* [1978] classified CG discharges into four categories based on the direction of motion, upward and downward, and the sign of charge, positive or negative, of the leader that initiates the discharge, a leader being defined as a self-propagating electrical discharge that creates a channel with electrical conductivity of the order 10^4 S m^{-1} (compared to $10^{-14} \text{ S m}^{-1}$ for air at sea level, 10^{-2} S m^{-1} for typical earth, and 4 S m^{-1} for salt water). An illustration of this categorization is shown in Figure 1-1. Category 1, known as downward negative lightning, is initiated by a downward-moving negatively charged leader and ultimately lowers negative charge to ground. This category accounts for roughly 90% of CG lightning worldwide. Category 3 is also initiated by a downward-moving leader, but the leader is positively charged, and hence lowers positive charge to ground. Downward positive lightning accounts for most of the remaining 10% of CG lightning. Both types of upward discharges (Categories 2 and 4) are rare and are thought to occur only from mountain tops or tall grounded objects, such as towers. Finally, it is worth mentioning that others [e.g., *Rakov and Uman*, 2003] define the four categories of CG lightning based on the direction of the initial leader and the polarity of charge effectively lowered to ground, which would result in opposite-polarity labels for Categories 2 and 4.

Lightning, or the lightning discharge, in its entirety, whether it strikes ground or not, is usually termed a “lightning flash” or just a “flash.” Lightning flashes often appear to the human eye to flicker because the flashes are frequently composed of multiple discharge events known as strokes. The terms “stroke” or “component stroke” are only applied to components of CG

flashes. Each stroke consists of a downward leader and an upward return stroke and may involve a relatively low level “continuing current” that immediately follows the return stroke [Rakov and Uman, 2003]. The continuing current phase may also include transient processes, known as M-components, occurring along the lightning channel that result in surges in the continuing current and channel luminosity. As discussed in the next section, strokes are differentiated by the type of leader that initiates them. First strokes are initiated by stepped leaders that propagate through virgin air while subsequent strokes are initiated by dart or dart-stepped leaders that follow previously formed channels. Upward-initiated CG discharges lack a “first return stroke” of the type always observed in downward-initiated lightning; rather, it is replaced by an upward-moving leader that bridges the gap between cloud and ground and establishes an “initial continuous current” (not to be confused with the “continuing current” that may follow return strokes) that typically lasts for some hundreds of milliseconds. The initial stage of upward CG discharges, consisting of the upward leader and initial continuous current, is, however, often followed, after a no-current interval, by one or more downward-leader/upward-return-stroke sequences similar to the subsequent strokes observed in downward CG lightning. Because rocket-triggered lightning is similar in its phenomenology to upward lightning initiated from tall objects, rocket-triggered lightning can be used to study upward CG lightning as well as subsequent strokes in downward CG lightning. Since all of the data collected during this study resulted from downward negative lightning or rocket-triggered lightning, the remainder of the discussion will focus on these two types of CG discharges. Further, the data analyses will focus on processes associated with downward-negative-leader/upward-return-stroke sequences.

1.3 Downward Negative Lightning

The initial leader in negative cloud-to-ground lightning, referred to as the stepped leader, is initiated within the cloud via a process called preliminary or initial breakdown. There is no

consensus on the mechanism of this process, which has a duration from a few milliseconds to some tens of milliseconds and may precede the initiation of the stepped leader by some hundreds of milliseconds. *Clarence and Malan* [1957] suggested that initial breakdown is a vertical discharge bridging the main negative and lower positive charge centers; however, more recent studies [*Krehbiel et al.*, 1979; *Proctor et al.*, 1988; *Rhodes and Krehbiel*, 1989] suggest that initial breakdown involves the formation of multiple channels, some with considerable horizontal extent, in seemingly random directions from the cloud charge source, one of which evolves into the stepped leader.

The transition from initial breakdown to the formation of the stepped leader is thought to be associated with a train of relatively large microsecond-scale electric field pulses that have been observed by many investigators [e.g., *Kitagawa and Brook*, 1960; *Weidman and Krider*, 1979; *Beasley et al.*, 1982; *Rakov et al.*, 1996; *Nag and Rakov*, 2009]. The percentage of flashes producing detectable preliminary breakdown pulse trains varies from less than 20% to 100% [*Clarence and Malan*, 1957; *Gomes et al.*, 1998; *Nag and Rakov*, 2008]. The pulse train has an entire duration of the order of 1 ms [e.g., *Rakov et al.*, 1996; *Nag and Rakov*, 2009] and typically precedes the first return stroke by a few tens of milliseconds. The individual preliminary breakdown pulses in the train are bipolar, with the initial polarity being the same as that of the return-stroke pulse [e.g., *Weidman and Krider*, 1979]; have an overall pulse duration and interpulse interval in the range of 20–40 μs and 70–130 μs , respectively [*Rakov et al.*, 1996]; and may be comparable to or larger in amplitude than the return-stroke pulse [e.g., *Gomes et al.*, 1998]. Apparently, the characteristics of the initial breakdown pulses associated with CG lightning are different than those of cloud discharges [*Kitagawa and Brook*, 1960] as well as those associated with attempted, but failed, cloud-to-ground leaders [*Nag and Rakov*, 2009].

Exactly how the initial breakdown in the cloud is produced remains one of the more puzzling questions about lightning because the observational evidence consistently yields peak thunderstorm electric fields that are an order of magnitude weaker than the dielectric strength of air [Marshall *et al.*, 1995, 2005]. Proposed mechanisms for this initial breakdown, which focus on local intensification of the thunderstorm electric field, have included hydrometeor-initiated positive streamer systems [Loeb, 1966; Phelps, 1974], cosmic ray-initiated runaway breakdown [Gurevich *et al.*, 1992, 1997], and serial combinations of these processes [Peterson *et al.*, 2008]. Regardless of the actual initiation mechanism, a negatively-charged stepped leader is eventually formed in the cloud. The leader is referred to as “stepped” because it moves in a halting, discontinuous manner as it propagates through virgin air. The stepped leader eventually leaves the cloud and descends towards ground, often exhibiting many branches. The sequence of events in a downward negative cloud-to-ground lightning flash, from the time the stepped leader exits the cloud, is illustrated in Figure 1-2.

A variety of techniques have been used by researchers to study stepped leaders as they descend towards ground. Because stepped leaders are visible once they exit the cloud base, optical measurements are one of the most obvious and useful methods for studying their propagation characteristic. Streak cameras, so named because film is literally “streaked” across the open aperture on the order of 50 m s^{-1} , have been used for many years to obtain time-resolved images of lightning processes that occur outside of the cloud. In regard to stepped leaders, streak camera images [e.g., Schonland, 1938; Schonland *et al.*, 1938a, b; Schonland, 1956; Berger and Vogelsanger, 1966; Orville and Idone, 1982] have played a critical role in quantifying various characteristics of stepped-leader propagation, such as propagation speed, step length, and interstep interval. These same characteristics have also been studied with opto-electronic

imaging systems [Chen *et al.*, 1999; Lu *et al.*, 2008], such as the Automatic Lightning Discharge Progressing Feature Observation System (ALPS) [Yokoyama *et al.*, 1990]. These systems image lightning processes by simultaneously recording the optical waveforms produced by the sensors of a photo-diode array. One additional benefit of opto-electronic imaging systems is that the physical properties (e.g., relative light intensity, rise time, half-peak width, etc.) of the light pulses associated with leader steps can also be determined. In other studies, VHF electric field measurements have been used to image and analyze stepped leader properties [e.g., Proctor *et al.*, 1988; Shao *et al.*, 1995]. Since the stepped leader is initially unobservable from ground, electric field measurements have also played a key role in determining the overall duration of the stepped leader [Rakov and Uman, 1990]. Because the results from these aforementioned studies include variations in global location, equipment, and sample size, it is not particularly useful to focus on the individual results of each study. Instead, typical values, based on a comprehensive collection of data, provided by Rakov and Uman [2003] for the propagation characteristics of stepped leaders are simply presented here. A typical propagation speed for a stepped leader, averaged over several kilometers of channel, is $2 \times 10^5 \text{ m s}^{-1}$, with some evidence that the leader speed increases as it approaches ground [e.g., Nagai *et al.*, 1982]. The typical step length is of the order of 50 m, and the interval between steps is 20–50 μs . The mean optical step duration is 1 μs , and the mean overall leader duration is about 35 ms.

Researchers have also investigated various electrical characteristics of the stepped leader, such as total charge, charge per unit length, average leader current, and step currents. These studies have relied heavily on channel-base current measurements (assuming that the impulse charge lowered by the return stroke is approximately equal to the total charge of the leader) [Berger *et al.*, 1975], single or multiple-station electric field measurements [Brook *et al.*, 1962;

Krehbiel et al., 1979; *Krehbiel*, 1981; *Thomson*, 1985; *Proctor et al.*, 1988; *Proctor*, 1997], and remote magnetic field measurements [*Williams and Brook*, 1963]. Again, taking typical values from *Rakov and Uman* [2003], the stepped leader has step currents in excess of 1 kA, an average leader current between 100 and 200 A, and a total charge of approximately 5 C. Referring back to the previously given values for the typical stepped-leader propagation speed ($2 \times 10^5 \text{ m s}^{-1}$) and duration (35 ms), a typical channel length of 7 km can be derived. Dividing the total leader charge (5 C) by this channel length results in a charge per unit channel length of $0.7 \times 10^{-3} \text{ C m}^{-1}$, a value that is generally consistent with experimental observations [e.g., *Thomson*, 1985; *Proctor*, 1997]. Based on these observations, *Rakov and Uman* [2003] suggest that the stepped-leader channel is likely to consist of a thin core (probably less than 1 cm in diameter) that carries a longitudinal current, surrounded by a radially formed corona sheath whose radius is typically several meters.

Despite a fairly decent knowledge of the electrical and propagation characteristics of the stepped leader, the step-formation mechanism remains largely unknown, as it is not resolved in ordinary high-speed photographic records. However, some inferences may be made about negative stepped leaders in lightning based on observations of negative stepped leaders in long laboratory sparks, the latter being much better studied via the use of electronic image-converter cameras and concurrent measurements of current at one electrode of the air gap [e.g., *Gorin et al.*, 1976]. In a negative laboratory leader, a streamer zone, which is composed of both negative and positive streamers, exists in front of the downward moving leader tip. The positive streamers develop upwards, back towards the leader tip, and the negative streamers develop into the gap, away from the negative leader tip. Both types of streamers appear to start from a visible plasma formation, known as a space stem, which moves downward in the gap ahead of the leader

tip. When the space stem is sufficiently heated, it gives rise to a new segment of isolated leader channel which extends both in the upward and downward directions. The upward-extending portion of this bidirectional plasma formation is positively charged, and the downward-extending part is negatively charged. When the upward-moving positive end connects with the downward-moving negative tip of the primary leader channel, the new step is formed, and the high potential of the primary leader channel is suddenly transferred to the new leader segment. This connection generates a current pulse that propagates upward from the new step, briefly illuminating the entire channel, and causes a burst of negative streamers to be produced from the bottom of the newly added segment. Another step then begins with the formation of a new space stem ahead of the newly added channel segment.

Initial leaders in both downward negative and upward negative CG lightning exhibit stepping, suggesting that the stepping mechanism is primarily determined by the processes in the leader tip and in the leader rather than by the charge source. Hence, the step-formation mechanism in negative laboratory leaders may provide insight into the step-formation mechanism in negative lightning leaders, although lab sparks have properties that are determined by the voltage and current source. Indeed, some observations of stepped leaders in downward negative lightning have indicated a similarity with the stepping process described above for negative leaders in long laboratory sparks, particularly the final stages involving the burst of streamers (impulsive corona) and the illumination of both the step itself and the channel behind it. For instance, *Schonland et al.* [1935] reported on one downward negative stepped leader in which a faint luminosity was observed below the bottom of a few bright steps observed with streak photography. *Berger* [1967a], also using streak photography, reported two instances of a brush-like corona appearing ahead of and essentially simultaneous with leader steps in upward

negative lightning. *Chen et al.* [1999], using the ALPS system, observed luminosity waves associated with individual steps in two negative stepped leaders that propagated in the direction opposite to that of the leader advancement. *Wang et al.*[1999a], who observed similar luminosity waves for a downward dart-stepped leader in negative triggered lightning, reported that the luminosity decreases to about 10% of the original value within the first 50 m. Recently, *Biagi et al.* [2009] showed the space stem in one high-speed camera frame and referred to a similar observation in another, the first visual evidence of a space stem occurring in the step formation of a lightning leader. The close electric field derivative measurements obtained in this study often detect a multi-pulse structure associated with individual leader steps in downward negative lightning. As we shall see in Section 6.3.2, examining the vertical distribution of these pulses via TOA techniques appears to support a step-formation process similar to that observed in long laboratory sparks, including the existence of the bidirectional leader associated with a space stem.

Some tens of milliseconds (typically 35 ms) after the negative stepped leader is initiated in the cloud, the leader approaches within a few hundred meters of the ground. The high potential of the stepped-leader tip relative to ground, which is estimated to be some tens of megavolts [*Bazelyan et al.*, 1978] and probably is a significant fraction of the cloud potential, induces a strong electric field at ground. When the electric field near ground exceeds the dielectric breakdown value, one or more upward positive leaders (UPLs) are initiated from nearby objects protruding from ground or from the ground itself, signifying a transition from the leader phase to attachment phase. One of the UPLs, known as the upward connecting leader, will ultimately connect with the downward negative leader, resulting in a potentially multi-branched connection

and the launch of current waves, both upward and downward, that are the return stroke [e.g., *Jerauld et al.*, 2007].

Direct evidence for the characteristics of UPLs is considerably less available than for downward stepped leaders. In fact, for many years the existence of UPLs was only inferred from still photographs [e.g., *Golde*, 1967; *Orville*, 1968; *Hagenguth*, 1947] based on splits or loops in the lightning channel, the presence of upward and downward branching, unconnected upward discharges, and abrupt changes in the channel shape near the ground. The presence of UPLs was also inferred from some streak-camera photographs in which the stepped leader appeared to end some tens of meters above the ground [*Golde*, 1947; *Wagner*, 1967; *Orville and Idone*, 1982]; however, no UPLs were actually imaged, presumably due to their low luminosity. More recent studies, particularly those using the ALPS system, have actually imaged upward connecting leaders and have estimated their length and propagation speed. Additionally, *Biagi et al.* [2009] presented high-speed video images that unambiguously identified an upward connecting leader for eight consecutive strokes in a rocket-triggered lightning flash, although no speed could be estimated for them. Unfortunately, the nature of UPL propagation is yet to be determined. Because channel-base current waveforms purported to be associated with upward positive connecting leaders in altitude-triggered lightning (see Section 1.4) have often exhibited pulses [*Laroche et al.*, 1991; *Lalande et al.*, 1998], it was traditionally believed that UPLs involved stepping. However, *Biagi et al.*, [2009], using high-speed video along with time-synchronized electric field and channel-base current measurements, recently argued that these current pulses are likely the result of induced effects or displacement currents from downward leader steps. Long spark experiments have also indicated that positive leaders may appear to propagate continuously or intermittently, depending on the rate of voltage rise across the gap. Moreover,

the stepping mechanism in positive leaders is considerably different than that involved in negative leaders [Gorin *et al.*, 1976]. Based on the collection of available data, a upward connecting leader initiated in response to a downward-negative stepped leader is estimated to have a propagation speed of about 10^5 m s^{-1} , an average current of about 100 A, and a typical length of some tens of meters, although it may reach a few hundred meters in length if initiated from a tall structure.

According to Rakov and Uman [2003], the process by which the extending plasma channels of the upward and downward leaders make contact is called the break-through phase inside the so-called “common streamer zone,” formed when the streamer zones ahead of each leader tip come into contact. The break-through phase is one of the most poorly documented and least understood lightning processes. In fact, Biagi *et al.* [2009] only recently provided the first known image in which the streamer zones of the two leaders can be seen to overlap. Moreover, the physical processes occurring inside the common streamer zone remain largely unknown. The TOA analysis performed in this dissertation for dE/dt pulses observed after the leader phase (see Chapter 6) provides insight into this process.

When the two leaders meet inside the streamer zone to form a single channel, a large potential discontinuity exists at the junction point because the stepped-leader channel is at some tens of megavolts relative to the upward-leader channel which is essentially at ground potential. This large potential discontinuity causes two return-stroke waves to be launched from the junction point (typically located a few tens to some tens of meters above ground), with one propagating towards the cloud and the other towards the ground. The downward-moving wave quickly reaches ground, resulting in an upward-moving reflected wave which may catch up with the upward-moving return-stroke wave due to the reflected wave’s moving through a return-

stroke-conditioned channel as opposed to the leader-conditioned channel for the upward moving return-stroke wave [Rakov 1998]. When the waves bouncing between the ends of the growing return-stroke channel decay, a single upward-moving wave is formed. Because the bidirectional return-stroke wave is very short lived, the return-stroke is often characterized as simply upward moving. The return stroke neutralizes (or lowers to ground) most or all of the charge deposited by the stepped leader. Hence, the overall process by which any stroke (or component stroke) in a CG flash lowers charge to ground is accurately described as a leader-return-stroke sequence. The term “first stroke” specifically indicates a stroke which was initiated by a stepped leader.

The return stroke has been the most studied lightning process. This is not surprising considering that the return stroke is the most visible lightning process, produces a large, easily identified electromagnetic signature, and is thought to cause the majority of lightning damage. Similar to the stepped leader, streak-camera records have played an important role in determining the propagation characteristics of the return stroke [e.g., *Schonland et al.*, 1935; *Schonland*, 1956; *Boyle and Orville*, 1976; *Idone and Orville*, 1982; *Mach and Rust*, 1989]. Based on such studies, the return stroke speed, averaged over the lower few hundred meters of channel, is thought to be of the order of 10^8 m s^{-1} , although some of these studies individually reported return-stroke speeds that varied by nearly an order of magnitude. Some studies [e.g., *Schonland et al.*, 1935; *Idone and Orville*, 1982] also showed that the speed of the return-stroke wave decreases with height by as much as 25–50% over the length of the visible channel, which may be responsible for some of the discrepancy between various studies. Other researchers [e.g., *Lundholm* 1957; *Wagner*, 1963] have suggested that the return-stroke speed should increase with increasing current amplitude, but this assertion, which implies a nonlinear relationship between

wave speed and wave amplitude, is not supported by experimental observations [*Mach and Rust*, 1989; *Willet et al.*, 1989].

Current waveforms have also been an important form of observation for characterizing the return-stroke process. Due to the unpredictability in location of natural lightning, first return-stroke currents are typically measured from the ground path of elevated structures, which have an increased probability of getting struck by lightning. The most extensive collection of return-stroke currents from downward negative flashes was compiled by Karl Berger and co-workers, who measured currents with resistive shunts on top of two 70 m towers on the summit of Mount San Salvatore in Lugano, Switzerland [*Berger*, 1955a, b, 1962, 1967a, b, 1972, 1980; *Berger and Vogelsanger*, 1965, 1969; *Berger and Garbagnati*, 1984; *Berger et al.*, 1975]. To date, the summary of return-stroke currents, including 101 first-strokes, provided by *Berger et al.*, [1975] is still considered an authoritative work on the subject. According to *Berger et al.* [1975], first-stroke currents (threshold of 2 kA peak) have a 10–90% rise time of about 5.5 μs , half-peak width of about 75 μs , and overall duration of some hundreds of microseconds. The median peak current of a first-return stroke is about 30 kA, and the 95 percent and 5 percent values, that is, values which are exceeded with probabilities of 0.95 and 0.05, respectively, are 14 and 80 kA. The median value of the so-called impulse charge lowered to ground by negative first return-strokes (arbitrarily selected to exclude charge associated with the continuing current) was 4.5 C, approximating the charge on the stepped-leader channel, certainly within an order of magnitude. The characteristic shape of return-stroke current waveforms is briefly discussed in Section 1.5.1, along with electric and magnetic field and electric and magnetic field-derivative return-stroke waveforms.

Following the first return stroke and any continuing current, one or more negative-subsequent-leader/return-stroke sequences may occur after a no-current interval that lasts from a few to some hundreds of milliseconds (typically some tens of milliseconds). According to *Rakov and Huffines* [2003], approximately 80% of downward negative flashes contain more than one stroke, with the typical number of strokes per flash being 3 to 5. The term “subsequent” refers to any stroke after the first, and the two terms (first and subsequent) serve to clearly distinguish the two types of return strokes.

The “dart” leaders which usually initiate subsequent return strokes exhibit characteristics quite different from stepped leaders due to the first return stroke’s preconditioning of the channel, i.e., leaving a warm, low density air path for the dart leader to follow. Dart leaders appear to move continuously, without stepping, and propagate much faster than stepped leaders - the typical dart leader speed being about 10^7 m s⁻¹ [*Schonland et al.*, 1935; *McEachron*, 1939; *Hubert and Mouget*, 1981; *Idone et al.*, 1984; *Jordan et al.*, 1992; *Mach and Rust*, 1997]. *Rakov and Uman* [1990] found the geometric mean of the dart-leader duration to be 1.8 ms, which is much shorter than the typical stepped-leader duration of 35 ms. The total charge lowered by the dart leader is on the order of 1 C [*Brook et al.*, 1962], basically one-fifth that carried by the stepped leader, but the average current of the dart leader is greater, approximately 0.5 kA, due to its shorter duration. The mean value for peak currents in dart leaders was estimated by *Idone and Orville* [1985] to be between 1.6 kA and 1.8 kA. Occasionally, a dart leader will deviate from the previously formed channel or simply encounter a previously formed channel that has suffered more decay than usual, and from that point on the leader will continue in a manner more like that of a stepped leader, usually, however, with shorter steps and inter-step time. These

hybrid leaders are termed dart-stepped leaders, and they typically exhibit characteristics that are intermediate between stepped and dart leaders.

Upward positive connecting leaders associated with subsequent strokes are thought to have lengths on the order of 10 m or less [Rakov and Uman, 2003]. Orville and Idone [1982] and Idone et al. [1984] both inferred upward connecting leaders of roughly 20–30 m in length for a few events, but Orville and Idone [1982] also reported that they did not observe any evidence of upward connecting leaders with 21 other subsequent strokes. Wang et al. [1999b], using the ALPS optical system, inferred the existence of two upward connecting leaders in rocket-triggered lightning, whose strokes are similar to natural subsequent strokes, having lengths of 7–11 m and 4–7 m. Biagi et al. [2009] presented high-speed video frames that showed upward connecting leaders ranging between 10 and 20 m in length for eight sequential strokes in a rocket-triggered lightning, three of which were initiated by dart-stepped leaders.

According to Berger et al. [1975], the median peak current for a natural negative subsequent return stroke is 12 kA, and the 95 percent and 5 percent values, that is, values which are exceeded with probabilities of 0.95 and 0.05, respectively, are 4.6 and 30 kA. Since the total charge lowered by a dart leader is about one-fifth of that lowered by a stepped leader, it is not surprising that subsequent return strokes lower a similar ratio of charge to ground compared to first return strokes. The current 10–90% rise time and duration of subsequent strokes are also typically an order of magnitude shorter than for first strokes. The propagation velocity of subsequent return strokes, however, is similar to first return strokes, being on the order of 10^8 m s^{-1} [Boyle and Orville, 1976; Hubert and Mouget, 1981; Idone and Orville, 1982; Idone et al., 1984; Willet et al., 1988, 1989; Mach and Rust, 1989; Olsen et al., 2004]. The peak optical intensity (assumed to be positively correlated with current) and the optical rise time have been

observed to decrease and increase, respectively, with height [*Jordan and Uman, 1983; Jordan et al., 1995, 1997*].

1.4 Rocket-Triggered Lightning

The rocket-and-wire technique is a method of artificially triggering a cloud-to-ground lightning flash from a natural thunderstorm. Simply stated, this technique initiates lightning by using an ascending rocket to rapidly raise a thin conducting wire (known as the triggering or trailing wire) into the air beneath a thundercloud. Depending on the grounding conditions of the trailing wire, two types of triggered lightning can result. In “classical” triggered lightning, the trailing wire is conducting along its entire length and grounded. In “altitude” triggered lightning, the bottom of the conducting trailing wire is electrically isolated by a non-conducting gap (sometimes made from insulating Kevlar cable). The non-conducting gap typically has a length of some hundreds of meters. A triggered flash is composed of an initial stage (IS) and typically one or more downward-leader-upward-return-stroke sequences. The strokes that follow the IS predominately lower negative cloud charge to ground and are thought to be similar, if not identical, to subsequent strokes in downward negative lightning. The stepped-leader/return-stroke sequence observed in downward negative lightning can be replicated by altitude triggering. Since very few cases exist where positive charge was lowered to ground by triggered lightning and none occurred during this study, the typical polarity, negative, is assumed for the remainder of this discussion.

The differentiating factor between classical and altitude-triggered lightning is what occurs during their initial stages (IS). In a classical-triggered lightning, the IS consists of an upward positive leader followed by the initial continuous current (ICC), a process similar to what is observed in upward positive lightning from tall towers. In a typical altitude-triggered lightning, the IS consists of a bidirectional leader (positive upward and negative downward) extending

from the electrically isolated trailing wire, with the downward-extending part imitating a natural stepped leader. The downward-extending portion eventually initiates an upward positive leader from ground or a grounded object and produces an “initial-stage” return stroke (also known as a “mini” return stroke) when these two leaders meet, bridging the non-conducting gap. This return stroke, however, is not quite the same as natural first and subsequent strokes or the strokes that follow the IS in rocket-triggered lightning. The result of the initial-stage return stroke, when the return stroke reaches the channel top, is an intensified upward positive leader (previously the upward-propagating part of the bidirectional leader) which continues towards the cloud before finally being followed by an initial continuous current. Since altitude-triggered flashes are considerably more difficult to initiate, the classical-triggering technique was used exclusively in this study. It should be mentioned that unintentional altitude triggering can sometimes occur as the result of an accidental breakage of the trailing wire during classical triggering. However, no such incidents occurred during this study, so there is no need to discuss altitude triggering henceforth.

The rockets used with this technique are usually about 1 m in length and are constructed from either fiberglass or plastic. The trailing wire we use is Kevlar-reinforced copper of diameter about 0.2 mm, with the spool mounted on the rocket. The rocket is launched when adequate thunderstorm conditions exist locally. Although these conditions may vary by region, the following three conditions are thought to be necessary for successful triggering at the ICLRT.

- A static field measured at ground near the launcher having a magnitude of about -5 kV m^{-1} or greater (using atmospheric electricity sign convention, negative charge overhead).
- A thundercloud directly overhead and not just the edge of the storm. An additional field reading, measured some hundreds of meters away, is usually used to confirm an extensive charge layer overhead.

- Lightning activity within a few kilometers and preferably occurring in intervals of approximately one minute. This usually occurs at the end of a storm, after the major lightning activity where flashes occur every few seconds.

The initial rocket speed is about 200 m s^{-1} , and when the rocket reaches about 300 m (or possibly less), an upward positive leader (UPL) is initiated from the tip of the wire. This leader propagates upward with an average speed of about 10^5 m s^{-1} . As the upward leader increases in length, the current produces I^2R heating which cause the destruction of the triggering wire. The destruction of the wire, which effectively disconnects the UPL from ground, and the subsequent reestablishment of current is associated with a unique current signature known as the initial current variation (ICV) [Wang *et al.*, 1999c; Rakov *et al.*, 2003; Olsen *et al.*, 2006]. The ICV is characterized by a gradual rise in current, due to the upward leader; a relatively rapid decrease in current, due to the destruction of the wire; a brief period of current interruption or lower current value; and a rapid increase in current, due to the formation of a plasma channel that reconnects the UPL with ground. The total ICV duration is reported not to exceed 10 ms [Wang *et al.*, 1999c]. Once the UPL has been reconnected to ground, it continues upward to bridge the gap between the ground and cloud and eventually establishes the ICC. The transition from the UPL to the ICC has not been precisely identified from current measurements, but the UPL is estimated to last 30–40 ms based on the average leader speed and height of the negative charge center in the cloud. The entire duration of the IS, including both the UPL and ICC, is reported to have geometric-mean duration of 279 ms by Wang *et al.* [1999c]. Following the ICC, there is a no-current interval that last some tens of milliseconds before the first negatively-charged dart leader, if one occurs, traverses the gap between cloud and ground, propagating at an average speed of about 10^7 m s^{-1} . When the dart-leader reaches ground, it connects with ground or an upward connecting leader and initiates an upward return stroke that propagates towards the cloud at a speed of about 10^8 m s^{-1} . After an interval of some tens to hundreds of milliseconds, more

strokes may follow. The primary stages in a classical-triggered lightning flash are illustrated in Figure 1-3. The success rate at the ICLRT for classical-triggered lightning has typically averaged about 50%, two rockets launched for each lightning trigger.

1.5 Additional Observations of Downward-Negative-Leader/Upward-Return-Stroke Sequences

1.5.1 Return-Stroke Waveforms

The process of leader attachment to ground or to a grounded object remains one of the most poorly understood and least documented processes in cloud-to-ground lightning. This process is important to understanding lightning physics and is also fundamental to methods of lightning protection; however, the microsecond or sub-microsecond scale of the processes involved combined with the low-luminosity of UPLs has made direct observation very difficult. An important form of observation has been the return-stroke waveforms obtained with current, electric and magnetic field, and electric and magnetic field-derivative measurements.

A number of researchers have reported measured characteristics for negative lightning first-return-stroke electric fields and/or field derivatives. Most of these measurements were performed at distances of some tens of kilometers from the lightning channel and generally over seawater, with the desired result that the radiation field component of the overall electric field is dominant and is not much affected by propagation [e.g., *Weidman and Krider, 1978; Cooray and Lundquist, 1982; Murray et al., 2005*]. *Lin et al.* [1979] measured and characterized negative first-stroke electric and magnetic fields at distances ranging from 1 to 200 km over land, and *Master et al.* [1984] reported some first-stroke electric fields ranging from 1 to 20 km. *Jerauld et al.* [2008] presented first-stroke electric and magnetic fields and field derivatives for 18 first return strokes each observed simultaneously at multiple distances ranging from less than 100 m to about 1 km. In most of these studies, involving the entire range of reported distances, the

first-stroke electric and magnetic field waveforms are shown to exhibit a slow-front-fast-transition sequence. When the field propagation is over tens of kilometers of seawater, as observed by *Weidman and Krider* [1978], the distant first-stroke electric field is typically characterized by a gradual rise (slow front) to 0.4–0.5 of the peak value in several microseconds (2–8 μs), followed by a fast transition ($\sim 0.2 \mu\text{s}$ or less) to peak. In addition to distant first-stroke electric and magnetic fields, slow fronts and fast transitions have also been observed in first-stroke currents measured from towers [*Berger et al.*, 1975; *Eriksson*, 1978; *Visacro et al.*, 2004], close first-stroke electric and magnetic field and field-derivative measurements [*Jerauld et al.*, 2008], and in distant electric fields for subsequent strokes that were initiated by dart and dart-stepped leaders [*Weidman and Krider*, 1978]. For each waveform type, the qualitative description for the slow front and fast transition is similar; however, the slow-front amplitude to peak value ratio and the time duration for each phase varies. According to *Weidman and Krider* [1978], distant electric field measurements of dart-leader-initiated strokes had smaller slow-front amplitude to total field peak ratios (~ 0.2) and shorter slow-front durations (0.6–0.9 μs) than distant first-stroke electric fields. The distant electric field measurements of dart-stepped-leader-initiated strokes had similar slow-front amplitude to total field peak ratios as first-strokes and slow-durations ($\sim 4 \mu\text{s}$) between that of first and dart-leader-initiated strokes. The amplitude and duration of the fast-transition in distant electric fields for both dart-leader and dart-stepped-leader initiated strokes were similar to first-strokes.

The similarity in features among the current, electric and magnetic field, and electric and magnetic field-derivative waveforms certainly suggests that the waveforms are closely related and probably result from a common process. The relationship between the current and field (and field-derivative) measurements has been illustrated to a degree by so-called “engineering”

return-stroke models, such as the transmission-line (TL) model [e.g., *Uman and McLain, 1969*], which provide a means of calculating electric and magnetic fields from a spatial and temporal channel current distribution (or charge density). One very popular model is the single-wave TL model, which expresses remote fields in terms of an assumed current waveform (usually obtained from a channel-base-current measurement) that originates from ground and propagates up a straight and vertical channel without distortion or attenuation at a constant return-stroke speed. This simple model has performed reasonably well in reproducing both close [e.g., *Schoene et al., 2003b*] and distant [e.g., *Willett et al., 1988*] fields for the first few microseconds of strokes in rocket-triggered lightning. Interestingly, it is how such models fail to fit the data that often provide new insights into the attachment and return-stroke processes. One particularly convenient result of the single-wave TL model is that it predicts distant radiation fields, assumed to have propagated over a perfectly conducting ground, have the same shape as the channel-base current, with the amplitudes differing only by a scaling factor. However, it has been observed that distant electric and magnetic field waveforms often exhibit a much sharper peak than the current waveform. Hence, it has been postulated that estimating the peak current (assumed to be due to the return-stroke) from distant electric fields slightly overestimates the peak current that would be measured at the channel base [*Uman et al., 1973; Weidman et al., 1986; Willett et al., 1988, 1989*]. This postulate evoked the hypothesis that the return stroke actually consists of two current waves that propagate upward and downward from the junction point of the upward and downward leaders, as discussed earlier. The reasoning behind this hypothesis being that both current waves would contribute to the electric field for a short time (sub-microsecond) but only one would be measured at ground.

A more perplexing aspect of the return-stroke waveform has been the origin of the slow front. *Berger and Vogelsanger* [1969], who noted a tendency for slower current wave fronts to be associated with longer upward leaders in natural positive lightning, suggested that the upward connecting leader may be responsible for the slow front frequently observed in tower-based current measurements of first strokes. On its face, this assumption seems very reasonable since first-strokes typically produce longer UPLs than subsequent strokes, and the slow front is more pronounced (longer duration and larger amplitude) in first strokes. Because a close relationship is expected between the current and field return-stroke waveforms, the slow-fronts observed in field waveforms have often been attributed to an upward connecting discharge as well. However, *Weidman and Krider* [1978] were unable to accurately reproduce the observed slow fronts in the electric fields by modeling a single upward-connecting discharge with both velocity and current rising exponentially to peak (based on observations of exponential increases in upward “streamer” velocity in long laboratory sparks [*Wagner, 1960*]). Although their calculated fields were similar in shape and duration to the measured fields, the calculated field amplitudes were far too small when using reasonable upward-leader lengths and currents. Hence, they concluded that a single upward-propagating leader discharge cannot radiate the observed slow-front field.

Jerauld et al. [2007] recently reported an unusual triggered lightning stroke which produced current, electric field, and magnetic field waveforms, the latter two measured at 15 m and 30 m, with a slow front and fast transition similar to that typically observed in natural-negative first-stroke currents and their distant electric fields. Based on modeling results, which used the channel-base current as input, and comparisons with natural-negative first-stroke waveforms, *Jerauld et al.* [2007] argued that the physics behind the initial several-microsecond-

duration slow front involves a pair of microsecond-duration current waves, each having a peak value up to some tens of kiloamperes, propagating in opposite directions from the junction point of the descending stepped leader and the upward connecting leader, as the two leaders approach each other. The fast transition was also viewed as a pair of current waves, resulting from the final connection of the leaders, which also propagate away from the junction point in opposite directions. This model is also plausible for subsequent strokes, with the observable differences between the slow fronts of first and subsequent strokes being related to the charge and speed of the leaders. Considering the typical peak current for first strokes initiated by stepped leaders and subsequent strokes initiated by dart leaders (about 30 and 12 kA, respectively) and the ratios of the corresponding slow-front amplitude to total field peak (about 0.4 and 0.2 μs), the ratio of the first stroke to subsequent stroke front currents can be inferred to be about 5, which happens to be approximately the same ratio as the total charge on stepped and dart leaders. The slow fronts of dart-leader-initiated strokes are thought to be of shorter duration because of the lower charge density and faster propagation of the dart leader produce a shorter UPL for the downward return stroke wave.

Finally, it should be mentioned that pulses sometimes appear superimposed on the slow front of the field-derivative records. *Jerauld et al.* [2007] reported that these “slow-front pulses” produce a radiation field that is similar in shape but smaller in amplitude than the radiation field of the fast transition. Likewise, the slow-front pulses seen in *Murray et al.* [2005] are similar in appearance but usually smaller than the fast transition. Both *Murray et al.* [2005] and *Jerauld et al.* [2007] also observed a burst of pulses (termed a “leader burst” by *Murray et al.* [2005]) directly before the start of the slow-front rise. The pulses of the leader burst do not resemble the slow-front pulses or the pulses associated with preceding leader steps. *Murray et al.* [2005] had

no explanation for either the slow-front pulses or the leader burst, other than suggest that the electromagnetic environment near the attachment point is probably more complex than what would be produced by a single current pulse propagating up a single channel. *Jerauld et al.* [2007] also offered no explanation for the leader burst, but they did speculate that the slow-front pulses may be the result of smaller connections in the attachment regions, based on multiple channel sections observed in the attachment region and multiple pulses in the current record. In this dissertation, three-dimensional locations are provided for slow-front pulses and leader bursts. These locations provide the first characterization of the leader burst process and appear to support the hypothesis made by *Jerauld et al.* [2007] regarding the slow-front pulses.

1.5.2 X-Ray Observations

Wilson [1925] first suggested that strong electric fields in thunderclouds might accelerate free electrons to relativistic energies thereby generating penetrating radiation as the electrons interacted with air molecules. These so-called “runaway” electrons are generated when the force exerted on the electrons by the thunderstorm electric field exceeds the effective frictional force, predominately due to the ionization energy losses, experienced by the electrons moving through the air. Although many attempts to determine if energetic radiation is produced in and around thunderclouds were made following *Wilson’s* prediction [e.g., *Schonland and Viljoen*, 1933; *Halliday*, 1934; *Hill*, 1963; *Susczynsky et al.*, 1996], it took many decades for credible observations to be produced. *Parks et al.* [1981] and later *McCarthy and Parks* [1985] observed X-ray enhancements in thunderclouds for several seconds prior to lightning. Since the X rays ceased when a lightning occurred, these emissions were interpreted as resulting from energetic electrons produced by the large-scale electric field inside the thundercloud instead of from lightning. *Eack et al.* [1996, 2000] also reported X-ray enhancement lasting up to 20 sec from inside and above the thunderclouds using balloon-borne measurements. Later, *Fishman et al.*

[1994] reported on approximately 50 intense terrestrial gamma-ray flashes (TGFs) that had been observed over a four year period using the Burst and Transient Source Experiment (BATSE) data from the Compton Gamma Ray Observatory (CGRO). TGFs were initially inferred to be associated with high-altitude discharges, such as red sprites [Nemiroff *et al.*, 1997], based on their correlation with thunderclouds and lightning [Inan *et al.*, 1996]. However, examination of theoretical calculations for the TGF spectra compared with new measurements from the RHESSI spacecraft have indicated that the thundercloud is a more likely source [Smith *et al.*, 2005; Dwyer and Smith, 2005; Carlson *et al.*, 2007]. The production of energetic radiation from inside the thundercloud is not so surprising considering that the peak electric fields observed inside of thunderclouds [Marshall *et al.* 1995, 2005] are slightly larger than the estimated value necessary for runaway breakdown [Gurevich and Zybin, 2001; Symbalisty *et al.*, 1998; Dwyer, 2003].

Until recently, the evidence was certainly less convincing for emissions of energetic radiation from lightning, and the general consensus was that thunderstorms produce such emissions but lightning probably does not. This view began to change, however, when Moore *et al.* [2001] reported the detection of energetic radiation emissions immediately preceding the first return stroke in downward negative lightning, and Dwyer *et al.* [2003] reported similar results for dart leaders in rocket-triggered lightning. Dwyer *et al.* [2004] reported that these emissions were composed of multiple, brief bursts of X-rays in the 30–250 keV range, with each burst typically lasting less than 1 μ s. Further, they showed that the source of the X-ray bursts travelled from cloud towards the ground, supporting the view that the leader front is the source of the X rays. Dwyer *et al.* [2005] compared X-ray and electric field waveforms that were simultaneously obtained during the stepped-leader phase of downward negative CG lightning. The conclusion of this analysis was that the production of X rays is associated with the formation of leader steps.

The characteristics of the stepped-leader X-ray emissions were also determined to be similar to emissions from dart leaders. The role of the attachment process and return stroke in the production of X rays was not precisely determined by these studies.

The aforementioned discoveries have had a profound impact on the views of lightning electrical breakdown in air, in that lightning can no longer be considered a conventional low-energy (eV) discharge, but often involves an electron distribution function that includes a significant high-energy (keV to MeV) component. Further, the similarity of characteristics for X-ray emissions from both dart leaders, which generally appear to move continuously and without stepping, and stepped leaders indicates that all leaders may involve stepping to some degree as well as share a common mechanism of propagation, although years of optical measurements have revealed significant differences in their propagation characteristics [e.g., *Schonland*, 1938, 1956; *Schonland et al.*, 1938a,b; *Orville and Idone*, 1982; *Jordan et al.*, 1992; *Mach and Rust*, 1997]. Consequently, it may be possible to unify the different types of negative leaders observed in nature.

At this time, the only viable models for explaining the lightning-leader X-ray emissions involve runaway electrons, as thermal emission is basically excluded since the maximum lightning-channel temperature, which actually occurs during the return stroke, is only about 30,000 K. However, it is unclear how the lightning leader produces these energetic electrons. In recent years, the relativistic runaway electron avalanche (RREA) model has gained great popularity, becoming the standard runaway breakdown model for atmospheric processes [*Gurevich et al.*, 1992; *Gurevich and Zybin*, 2001], such as the X-ray emissions produced inside thunderclouds. However, *Dwyer* [2004] found that the observed energy spectrum and flux of the leader X-ray emissions were inconsistent with the RREA model. Further, the RREA model

requires a high electric field (minimum of approximately 300 kV m^{-1} at STP conditions) over considerable distances (10's to 100's of meters, depending on the field strength), and it is not clear how such an extensive field would be generated at the leader front [see *Miki et al.*, 2002]. According to *Dwyer* [2004], there is presently only one alternative to the RREA model: the so-called cold runaway electron model, which describes the production of runaway electrons out of the bulk free-electron population [*Gurevich*, 1961]. Under the cold runaway model, the average energy of the runaway electrons can have any value [*Babich*, 2003]; hence, this model can account for the observed energy spectrum. However, this model does require high electric field values (approximately an order of magnitude greater than the breakdown field) that are not expected to exist at the leader front [*Bazelyan and Raizer*, 2000]. Nevertheless, such values have not been ruled out observationally.

Continued observation of these leader-produced X rays is important for characterizing the X-ray emissions, determining the production mechanism of the runaway electrons, and better understanding leader propagation. The Thunderstorm Energetic Radiation Array (TERA) was added to the Multiple Station Experiment (MSE) at the ICLRT for this specific purpose. In theory, the combination of field, field-derivative, and X-ray measurements gathered during this experiment should facilitate a thorough investigation into various aspects of these X-ray emissions. In this dissertation, the spatial and temporal relationship between leader X-ray and electric field change sources is investigated, as well as the role of post-leader processes in X-ray production. Data from this experiment were also provided to collaborating researchers at the Florida Institute of Technology (FIT) so that other aspects such as the luminosity and characteristic energy of the source runaway electrons, directionality and attenuation of the X-ray

emissions, and the possible radiation dosage near the source could be investigated [e.g., Saleh *et al.*, 2009].

1.6 Determining Lightning Locations Via Time-of-Arrival

Generally speaking, time-of-arrival (TOA) analysis is a method for deducing the location (as well as the time of occurrence, if desired) of a point source that emits a disturbance which propagates at a known and constant velocity. In the case of lightning, various processes emit a broad spectrum of electromagnetic radiation that can be detected and used for such an analysis. A single time-of-arrival sensor, located at the i_{th} station, provides the time (t_i) at which some portion of the lightning electromagnetic field is measured by that sensing antenna. In a general Cartesian-coordinate system, this time is dependent on the excitation time of the source (t), antenna location (x_i, y_i, z_i), source location (x, y, z), propagation speed (v) of the electromagnetic field, and any propagation delay (d_i) associated with the measurement, as expressed by Equations 1-1 and 1-2.

$$t_i = t + \frac{R_i}{v} + d_i \quad (1-1)$$

$$R_i = \sqrt{(x - x_i)^2 + (y - y_i)^2 + (z - z_i)^2} \quad (1-2)$$

All of the subscripted terms (except R_i) and the propagation speed are observable; hence, there are four unknowns (x, y, z, t) associated with any single TOA observation. Since a single measurement does not provide any useful information about the source location, the TOA technique requires a collection of observations from multiple sensors. Over the years, a variety of data analysis techniques and hardware have been used in the retrieval of lightning locations from ground-based radio-frequency TOA measurements. As will be briefly discussed here, TOA analyses have varied by the type (VLF, LF, VHF, and wideband) and number of antennas used,

the size of the antenna baselines, whether a two-dimensional or three-dimensional fix of the source was desired, and the mathematical means for retrieving the source location.

Whether a two-dimensional or three-dimensional source was desired, early TOA analyses primarily utilized time-differences-of-arrival (TDOA) between pairs of stations to determine lightning source locations, i.e., arrival times of the form given in Equation 1-1 were differenced in pairs. Note that this technique eliminates the time of occurrence (t) as a variable in the equations, and the resulting expressions depend only on the TDOA rather than the individual arrival times themselves. The time difference for each pair of stations defines, in general, a hyperboloid of revolution about the baseline between the two stations, hence, evoking the term “hyperbolic system.” One branch of the hyperboloid can be excluded based on the order in which the antennas are excited, and the other branch represents the locus of all possible source points capable of producing the measured time difference. A three-dimensional source location (x, y, z) can be determined from the intersection of three or more such hyperboloids obtained from four or more stations. Once a solution is determined, the time of occurrence (t) can be obtained by inserting the source location back into one of the original equations (Equation 1-1). Of course, not all lightning analyses require a source location as rigorous as a three-dimensional solution. In many situations only a two-dimensional (x, y) solution, representing an “average” flash location or simply the position of a storm region, is required. In such cases the altitude component of R_i , or the $(z - z_i)$ term, can be eliminated, reducing the problem to an intersection of hyperbolas. For the two-dimensional problem, the use of three antennas produces a system of two equations with two unknowns, i.e., two intersecting hyperbola branches, which can be solved graphically or via numerical methods. Unfortunately, two hyperbolas may intersect at two locations, failing to uniquely identify the source location. In such instances, another

observation, such as another antenna or video records, is necessary to remove the ambiguity in the source location.

The utility of hyperbolic systems was apparently first illustrated by *Lewis et al.* [1960], who used a pair of receiving stations located in New England to determine the direction to lightning discharges in western Europe. This network actually consisted of four stations arrayed in a triangular formation around a central station, such that at least one baseline was nearly perpendicular to any desirable direction of interest. The system utilized spherical geometry to account for propagation over the Earth's surface in finding the locus of points for a constant measured arrival-time difference between receivers. The stations of this system were separated by over 100 km and operated at VLF and LF frequencies (4–45 kHz). Since these sensors were located more or less due west of Europe, the system was relatively insensitive to the east-west position of the source but was quite sensitive to its north-south position. Hence, the system could basically provide the direction to lightning events which was then be used to estimate their north-south position. The resultant “positions” obtained for 150 sferics (radiation events produced by lightning) compared favorably to the locations determined by the magnetic direction-finding (DF) network operated by the British Meteorological Office (BMO), with an average absolute deviation of 31 nautical miles.

The TOA system described by *Lewis et al.* [1960] became the forerunner for other long-baseline TOA systems that actually provided two-dimensional source locations for lightning discharges, as opposed to simple direction finding. *Lee* [1986] described a seven-station TOA network that ultimately replaced the BMO's narrowband magnetic DF network. The flash location accuracy for this system was estimated to be between 2 and 20 km. The sensors were separated by 250–3300 km and operated in the 2 to 18 kHz frequency range. A commercial

system known as the Lightning Positioning and Tracking System (LPATS) was also developed in the 1980s. The LPATS, operating at LF and VLF frequencies, used four or more stations separated by 200 to 400 km to determine locations via measured time differences in arrival times. LPATS networks, including a US national network, have been described by various researchers [e.g., *Lyons et al.*, 1989; *Rakov*, 1990; *Casper and Bent*, 1992; *Holle and Lopez*, 1993]. The location accuracy of LPATS, as with all TOA systems, is directly related to the time synchronization between the various sensors, and the timing accuracy has greatly improved since the system's inception due to the recent availability of GPS timing. According to *Rakov and Uman* [2003], recent versions of LPATS provide location accuracy better than 1 km.

Although the system described by *Lewis et al.* [1960] was characterized by a very large baseline (> 100 km), its operation also inspired the use of very-short-baseline (tens to hundreds of meters) TOA systems. The premise of these systems is that a hyperboloid defined by a time difference between two stations degenerates, in the limit, to a plane when the range to the lightning source is significantly larger than the baseline between the stations. This approximation allows the azimuth angle of arrival to be estimated with a simple analytical expression, avoiding the more complex hyperbolic formulations. Further, the short baseline precludes the problem of proper pulse identification usually associated with long-baseline TOA systems. Of course, very-short-baseline systems are not without their concerns and drawbacks. For instance, a two-sensor station involves a 180° ambiguity in the arrival (azimuth) angle, and the unknown elevation of the source introduces error in the azimuth angle determination. *Oetzel and Pierce* [1969], who first suggested that two short-baseline stations could be used for line-of-sight location of lightning VHF sources, also suggested that three closely spaced sensors (two ninety-degree baselines) could be used to determine the azimuth angle (without ambiguity) as

well as the elevation angle to the source. Hence, it should be possible to use two such stations to determine three-dimensional locations. *Cianos et al.* [1972] and *Murty and MacClement* [1973] both tested the direction finding technique suggested by Oetzel and Pierce by using a pair of VHF antennas separated on the order of 100 m. Later, *MacClement and Murty* [1978] tested the direction finding capability for both the elevation and azimuth angles to the source by adding a third sensor. *Taylor* [1978] attempted to find three-dimensional lightning locations by using two four-sensor stations, each station consisting of a pair of horizontally spaced sensors (for the azimuth angle) and a pair of vertically spaced sensors (for the elevation angle). The baseline of each pair was 13.74 m. Although some examples of data recorded simultaneously at the two stations were presented, there was significant difficulty in identifying the same events at each station, due to a lack of adequate techniques for synchronization. Three-dimensional locations were provided in some subsequent studies that involved an upgraded version of Taylor's system [*Ray et al.*, 1987; *Rust and MacGorman*, 1988], but locations were only obtained for about 20 to 30 percent of the signals detected at one site.

The more challenging task of determining the three-dimensional location (x, y, z) of a lightning source from the natural hyperbolic formulations in the time domain was pioneered by *Proctor* [1971, 1981, 1983] and *Proctor et al.* [1988] in South Africa. As previously mentioned, the solution to this problem can be considered as the intersection of three or more hyperboloids obtained from four or more stations. Proctor and co-workers utilized five VHF stations arrayed in a cross-shaped formation, with the two nearly-perpendicular baselines having lengths of about 30 km (E-W) and 40 km (N-S). This system operated at 250 MHz [*Proctor*, 1971], 253 MHz [*Proctor*, 1981], or 355 MHz [*Proctor*, 1983; *Proctor et al.*, 1988] with a 5 MHz bandwidth (the central station had a bandwidth of 10 MHz). The analog signal from each of the outlying

stations was telemetered back to the central station where the signal could be recorded. A trigger of the network would initiate a 250 ms acquisition of each measurement. These records were manually examined to determine the arrival times for events. Unfortunately, this approach was very tedious and could be extremely time consuming, taking as long as 6 months per 250 ms record. Using the set of arrival times for each event, *Proctor* [1971] presented a nonlinear numerical solution that involved iterative improvements of an initial source location estimate. Four stations were used in determining the solution, with the fifth station being used to confirm the adequacy of the four-station solution. From the timing errors (Δt), which were estimated to be about 70 ns rms, the uncertainty in determining the horizontal coordinates (x, y) for sources located within the boundaries of the network was predicted to be about $c\Delta t \cong 20$ m. The uncertainty in determining the height (z) of sources was on the order of 100 m but could exceed 1 km for sources near or beyond the boundaries of the network or for low-altitude sources within the network. Although the hyperbolic approach presented by *Proctor* [1971] is conceptually useful for understanding the solution, the formulations are complex and analytically intractable for all but a few ideal network configurations, such as the arrangement used by *Proctor* [1971].

Using Proctor's approach, Lennon and co-workers implemented a seven-station network (56–75 MHz receivers) for monitoring lightning over and around Kennedy Space Center (KSC), Florida [*Lennon, 1975; Poehler and Lennon, 1979; Lennon and Poehler, 1982*]. This network, known as the Lightning Detection and Ranging (LDAR) system, was comprised of an approximately circular array of six measurements, about 16 km in diameter, concentric with a central seventh station. For processing purposes, the network was conceptually visualized as two interlaced Y-shaped arrays, one upright and the other upside down, each consisting of three outlying stations and the central station. When the signal at the central station exceeded a

specified level, data segments of approximately 100 μ s were recorded for each station. These signals were telemetered to the central station, the time of arrival for the largest peak in this time window was determined for each station, and a solution was determined for each of the Y-shaped networks. Unless the two independent solutions were consistent, within pre-established limits, the source solution was discarded. This network typically located ten to thirty radiation events per lightning flash. Using geometric dilution of precision (GDOP) formulations and assuming a timing error of 20 ns, *Poehler*[1977] estimated 7–11 m rms uncertainties in plan locations (x, y) over the network and an order of magnitude larger (72–100 m) errors in the vertical for sources at 8 km altitude.

An improved, second-generation version of the LDAR system, operating at 66 MHz with a 6 MHz bandwidth, was developed by Lennon and coworkers in the early 1990s [*Maier et al.*, 1995]. The new version significantly improved detection efficiency and was able to process up to a maximum of ten thousand points per second. The improved efficiency was due, in large part, to a change in the solution algorithm. Instead of discarding an event when the two independent solutions are inconsistent, a “voting” procedure involving 18 additional four-station solutions is performed. If sufficient consistency is apparent, a final solution based on all 20 of the possible four-station solutions, each appropriately weighted, is obtained. Even with the improved algorithm, *Starr et al.* [1998] estimated that LDAR discards about 60 percent of all detected events because it cannot find a self-consistent solution. Nevertheless, *Bocippio et al.* [2001] estimated that the LDAR flash detection efficiency (at least one location from a flash) remains above 90 percent out to 94 to 113 km from the network centroid, the detection efficiency dropping off rapidly beyond that range.

Another TOA system was also developed at the KSC by *Thomson et al.* [1994]. This system consisted of five wideband dE/dt antennas, with four of the stations distributed at a radius of approximately 10 km from the central station. The signals from the outer stations were telemetered to the central station where all signals were recorded. The central (master) station had a bandwidth of 800 Hz to 2 MHz while the 4 outer (slave) stations had a bandwidth of 800 Hz to 4 MHz. Relative timing between the stations was nominally adjusted to within 400 ns by using television synch signals and later improved to better than 50 ns during the analysis phase. Using a method known as the “weighted hyperbola” technique, *Thomson et al.* [1994] extended Proctor’s mathematical approach by independently using all five possible combinations of four-station data to find weighted mean values for x , y , z and t .

Despite the relative success of the aforementioned systems that provide three-dimensional solutions, none permit a clear interpretation of the retrieval errors associated with the TOA problem. This fact motivated *Koshak and Solakiewicz* [1996] to examine an analytic solution which clarified the specific effects of measurement errors, network geometry, source position, and measurement differencing schemes on the solution. A detailed development of this method was presented by *Koshak and Christian* [1994], with a similar development being provided by *Hager and Wang* [1995]. This approach differs from the hyperbolic approach in that Equation 1-1 is first solved for R_i and then squared prior to being differenced with other stations. This approach results in a system of equations that is linear in the unknowns and can be solved with standard linear inversion techniques [*Twomey*, 1977]. In the linear formalism, the source location and time-of-occurrence are viewed geometrically as an intersection of hyperplanes in the four-dimensional Minkowski space (x, y, z, t) . Of course, this method does not eliminate the time of occurrence (t) as a variable, so at least five stations are necessary to provide a minimally

determined system. If all of the stations are exactly planar, however, it is possible to determine a three-dimensional solution using only four stations, as the altitude is eliminated as a variable from the system of equations. The source altitude is later recovered from one of the original equations. Unfortunately, the inability to accurately determine the source altitude is a significant shortcoming associated with this approach, and it results from the lack of vertical separation between the sensors.

Currently, lightning mapping arrays (LMA), like the ones operating at New Mexico Tech [Thomas *et al.*, 2004] and the Marshall Space Flight Center [Koshak *et al.*, 2004], are among the most popular TOA systems in the research setting. These networks are typically comprised of 10 to 15 VHF sensors and cover areas tens of kilometers in diameter. The LMA is fashioned after the LDAR system in that it is automated to search for the peak radiation event over a short time window (typically 80 μ s), determine arrival times for each station, and calculate the source location and time of occurrence. A fundamental difference between the LMA and the LDAR system, however, is that independent GPS timing allows the TOA values to be determined at each LMA station. Hence, the data rate between each station and the central site is greatly reduced because there is no need to transmit the analog signal - only arrival times. Even though the LMA is a research-grade product, it also possesses the impressive ability to provide real-time processing. Of course, this versatility places demanding requirements on the solution algorithm. Since the hyperplane approach is very straightforward and computationally inexpensive, it is an enticing option; however, the poor altitude determination associated with this approach precludes it from being the primary solution algorithm. Nevertheless, LMA algorithms typically utilize the rapid hyperplane approach to obtain an initial solution estimate. This estimate is usually improved with a simple altitude constraint prior to being used as the starting point for an iterative

nonlinear least squares algorithm. The location errors associated with the LMA are typically estimated from either the covariance matrix produced by the nonlinear least squares algorithm, simple geometric models using approximate timing errors, Monte Carlo simulations, or experimental testing. The New Mexico Tech LMA has been shown to have timing errors of approximately 40 ns rms for deterministic transmitter pulses and about 50 ns rms for lightning signals. For sources between about 6 and 12 km altitude over the network, the location accuracies were found to be about 6 to 12 m rms in the horizontal position and about 20 to 30 m rms in the vertical.

Since the groundbreaking work of D. E. Proctor and co-workers in South Africa, there has been tremendous progress in the hardware, solution algorithms, data visualization, and overall accuracy of TOA systems. These systems have provided the ability to map the spatial progression of lightning flashes, and they have useful applications in weather monitoring, analyzing storm structure, and locating the initiation and ground strike points of flashes. Despite some remarkable capabilities, some of the properties generally shared by these TOA networks inherently prevent them from accurately analyzing low-altitude lightning processes. First, the size of TOA networks is generally some tens of kilometers in diameter in order to monitor the greatest area possible and detect the maximum number of lightning strikes. Based on the error analysis presented by *Thomas et al.* [2004], the altitude uncertainty is highly dependent on the ratio of the horizontal distance between the source and the closest station to the height of the source. Unfortunately for large networks, the altitude uncertainty can be several hundred meters or even some kilometers for sources within a kilometer of ground. Second, these systems are usually automated in order to provide real-time processing, so they only analyze one event per some specified time interval (typically 80 μ s). Hence, in the final millisecond prior to the return

stroke, in which a leader may travel several hundred meters, these systems could only provide a maximum of about 12 locations for that interval.

A new type of TOA system, which is specifically designed to locate low-altitude processes, is presented in this dissertation. This TOA system is composed of eight wideband dE/dt antennas and eight X-ray detectors, which are a subset of the MSE/TERA network at the ICLRT. Times-of-arrival are manually selected, and a nonlinear least squares algorithm is utilized to determine source locations. Some of the goals for this system included producing the first high-resolution TOA images of lightning leaders within several hundred meters of ground, determining the spatial and temporal relationships between X-ray and electric field change sources associated with lightning leaders, and examining the role of the attachment phase and return stroke in X ray production. The hardware for this network is discussed in Chapter 2 and the details of its operation are provided in Chapter 4.

1.7 The International Center for Lightning Research and Testing at Camp Blanding, Florida

The lightning-triggering facility at Camp Blanding, Florida was founded by the Electric Power Research Institute (EPRI) and their contractor, Power Technologies, Inc. (PTI), in 1993. In 1994, the University of Florida (UF) Lightning Research Group assumed responsibility for the facility and in 1995 renamed the site the International Center for Lightning Research and Testing (ICLRT). Since 2005, the facility has been jointly operated by UF and the Florida Institute of Technology (FIT). During its existence, nearly 50 researchers (not employed by UF) from 13 countries have visited the ICLRT to conduct experiments related to atmospheric electricity, lightning physics, and lightning protection. A synopsis of the triggered-lightning experiments typically performed at the ICLRT was provided by *Rakov et al.* [2005], who reviewed the principal results obtained from 1993 to 2002.

Figure 1-4 shows a Microsoft Virtual Earth satellite image illustrating the position of the major structural facilities at the ICLRT site. The ICLRT is located at approximately 29.94° N, 82.03° W and occupies about 1 km² on the Camp Blanding National Guard Base, located in north central Florida. The site location was chosen in part because of the restricted airspace provided by the military and necessary to rocket-triggered lightning operations. Historically, lightning has been triggered from three platforms at the ICLRT: (1) an underground launcher located in the northwestern portion of the site, which is surrounded by a 70 × 70 m² ground plane (buried metal screen); (2) a launcher atop an 11 m wooden tower located near the center of the site (Figure 1-5); (3) and a mobile launcher (Figure 1-6), fixed to the arm of a bucket truck, which can be moved around the site. Only the latter two launchers have been used since 2005. All of the launchers are equipped with resistive shunts for measuring the lightning channel-base current.

The metal “Launch Control” trailer pictured in Figure 1-7 is located approximately 50 m north of the launch tower and is the center for triggering operations. This building houses the launcher controls and provides electromagnetic shielding for video and data acquisition equipment. The trailer is located underneath a system of grounded catenary wires and is surrounded by a buried metal counterpoise, both of which provide lightning protection for the trailer. During triggering operations, the Launch Control trailer is powered by a diesel generator so that the equipment inside is not affected by a surge or failure in the power grid, both common occurrences in the presence of nearby lightning.

1.8 History of the Multiple Station Experiment

The Multiple Station Experiment (MSE) is composed of a network of sensors at the ICLRT that acquires close (within several hundred meters) electric and magnetic field and field-derivative waveforms. The MSE is the longest-running ICLRT experiment and has operated continuously since 2002. Although this network has seen many changes throughout the years, its

operation through 2007 can be generalized into three eras: 1997 to 1999, 2002 to 2004, and 2005 to 2007.

The original MSE system (1997–1999) was operated primarily by UF Masters and Ph.D. student David Crawford and consisted of ten stations (numbered 1–10), with the vertical electric field (E) measured at each station and two components (north-south and east-west) of the azimuth magnetic induction (B) measured at two stations (a total of 4 B-field measurements) [Crawford *et al.*, 2001; Jerauld *et al.*, 2003]. These measurements were transmitted from the sensors to the Launch Control trailer (see Section 1.7) via Nicolet Isobe 3000 fiber-optic links having a nominal bandwidth of DC-15 MHz. The fiber optic transmitters, along with other electronics at these remote sensors, were powered by 12 V lead-acid batteries that required constant monitoring and replacing. In Launch Control, the waveforms were digitized and stored with 12-bit vertical resolution at 10 MHz by a Nicolet Multipro digitizer. The digitizer acquired a continuous record of 51.2 ms (40 ms pretrigger) for each event, typically acquiring only one stroke per flash. This system was triggered from the combined output of the two crossed-loop magnetic field sensors, configured so that only lightning near or within the network would typically trigger the system.

Primary responsibility for the second era (2002–2004) of the MSE belonged to Dr. Jason Jerauld, then a Ph.D. student. During this era, many significant changes to the structure and operation of the network were implemented [Jerauld, 2007]. The total station count was reduced from ten to eight by removing two of the original E-field measurements, although the station numbering was kept constant for the remaining stations. Two new electric field derivative (dE/dt) measurements were added to the network and two of the remaining E-field measurements were converted to dE/dt measurements, making a total of six E-field and four dE/dt

measurements. Both of the crossed-loop B-field sensors were reduced to a single-loop configuration, and four new single-loop magnetic field derivative (dB/dt) measurements were installed. Both types of field-derivative measurements provided higher bandwidth than their directly-measured field counterparts, allowing them to detect fast pulses that are generally unresolved in the field measurements. However, factors such as limited dynamic range of the digitizer (e.g., limited amplitude resolution inherently and due to digitizer noise), amplitude offset introduced by the fiber optic links, and possibly unexplained grounding effects (resulting in field enhancement) did not allow the time-integrated field derivatives to completely substitute for the directly-measured fields [*Jerauld, 2007; Jerauld et al., 2008*]. Therefore, the updated MSE regime benefited from a combination of field and field-derivative measurements that worked in complementary fashion.

The network was reconfigured to trigger from the simultaneous output of two optical sensors that viewed the network at low altitude from opposite corners of the site. This technique was found more reliable than the magnetic sensors for restricting the data acquisition to flashes within or very near the network. The trigger output was fed into a computer timing card which provided a GPS timestamp for each trigger, allowing the MSE data to be correlated with other systems such as the National Lightning Detection Network (NLDN) [*Jerauld et al., 2005*]. A video system was also deployed to help determine the location and channel geometry for strokes that triggered the network. This system consisted of four camera sites whose video signals were transmitted to Launch Control and recorded.

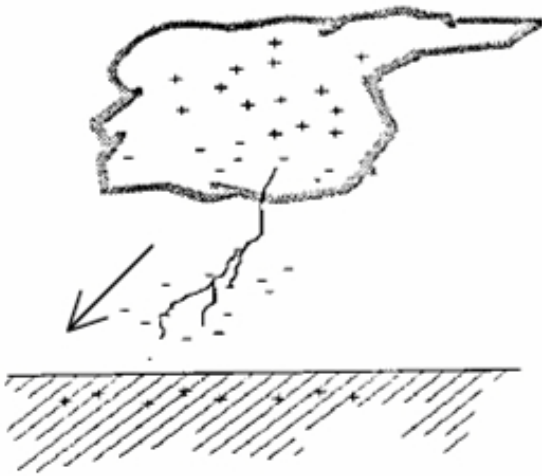
In addition to the new measurements, the network functionality was greatly improved by the implementation of a control system (see Section 2.2). Among other benefits, this system provided remote capability for powering measurements off and on, measuring battery voltages,

and setting various attenuation values. These tasks could be performed from a central computer (located in Launch Control) and greatly reduced the pre-storm tasks and the overall need for day-to-day maintenance. Further, the central computer could monitor local thunderstorm conditions by measuring the quasi-static electric field at ground (via an electric field mill) and automatically arm and disarm the network when appropriate.

Improvements were also made in terms of data transmission and storage. Many of the Nicolet Isobe 3000 fiber-optic links were replaced with Opticomm MMV-120C (see Section 2.3) fiber-optic links that had a nominal bandwidth of DC-30 MHz. The directly-measured fields and optical signals were digitized as continuous records, with 12-bit amplitude resolution, up to 1.6 s at 10 MHz on a Yokogawa DL716 (see Section 2.4) digital storage oscilloscope (DSO). The field-derivative measurements were digitized by LeCroy brand (two models) DSOs (see Section 2.4) with 8-bit amplitude resolution, sampled at rates up to 200 MHz. Unlike the Yokogawa DSO, the LeCroy digitizers did not store waveforms as continuous records but as “segments,” so that a 5 ms window was acquired with each stroke that triggered the digitizer.

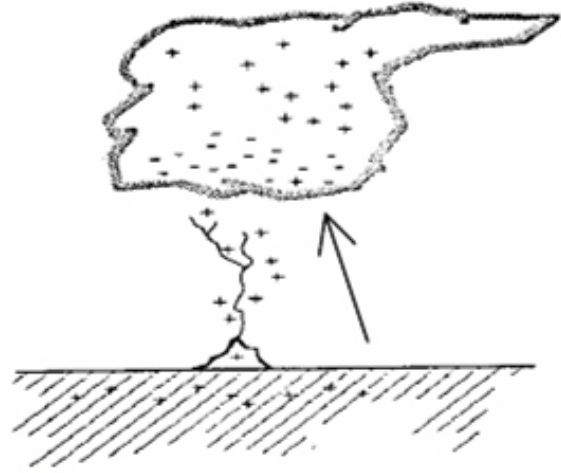
The author, who began work with the MSE in 2004 under the tutelage of Dr. Jerauld (who was then a Ph.D. student) and assumed primary responsibility for the MSE in 2005, supervised the third era (2005–2007) of the MSE. This third era built upon the previous setup and involved considerable expansion of the network and the introduction of new capabilities. In particular, an eight-station time-of-arrival network was implemented as well as an array of NaI scintillation detectors to examine the production of X-rays from nearby cloud-to-ground lightning. This setup is discussed at length in Chapter 2 and was used to acquire the data presented in this dissertation. Since 2007, the MSE has continued to operate although further changes have been implemented. The current system includes faster plastic scintillators, a more advanced video

system, and electric field sensors that are more responsive to positive cloud-to-ground lightning at distances to 20 km. The experimental work with which the author was involved is being continued by Ph.D. students Chris Biagi and Dustin Hill. Both Biagi and Hill began their work at the ICLRT in 2006 under the supervision of the author.



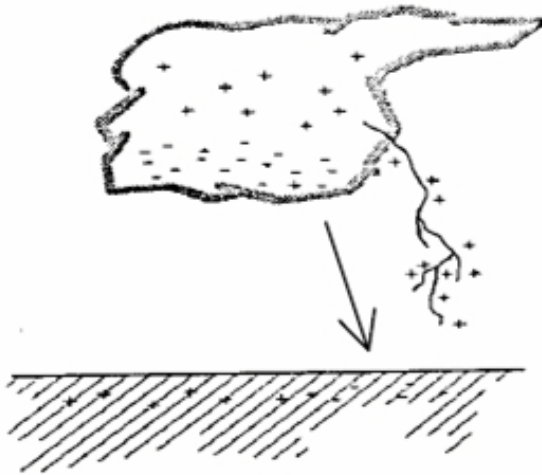
1

Downward Negative



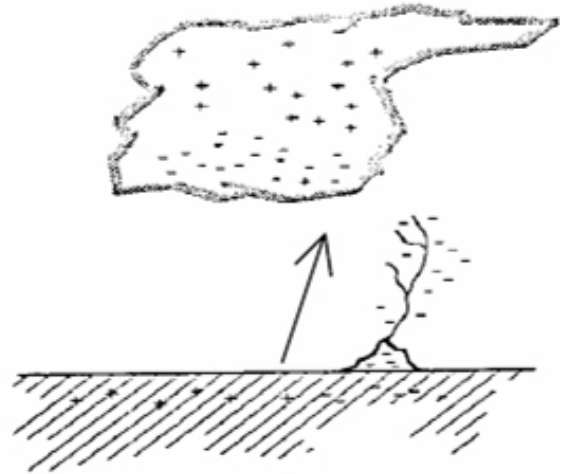
2

Upward Positive



3

Downward Positive



4

Upward Negative

Figure 1-1. Classifications of cloud-to-ground lightning based on the movement and charge of the initial leader. Adapted from *Uman* [1987].

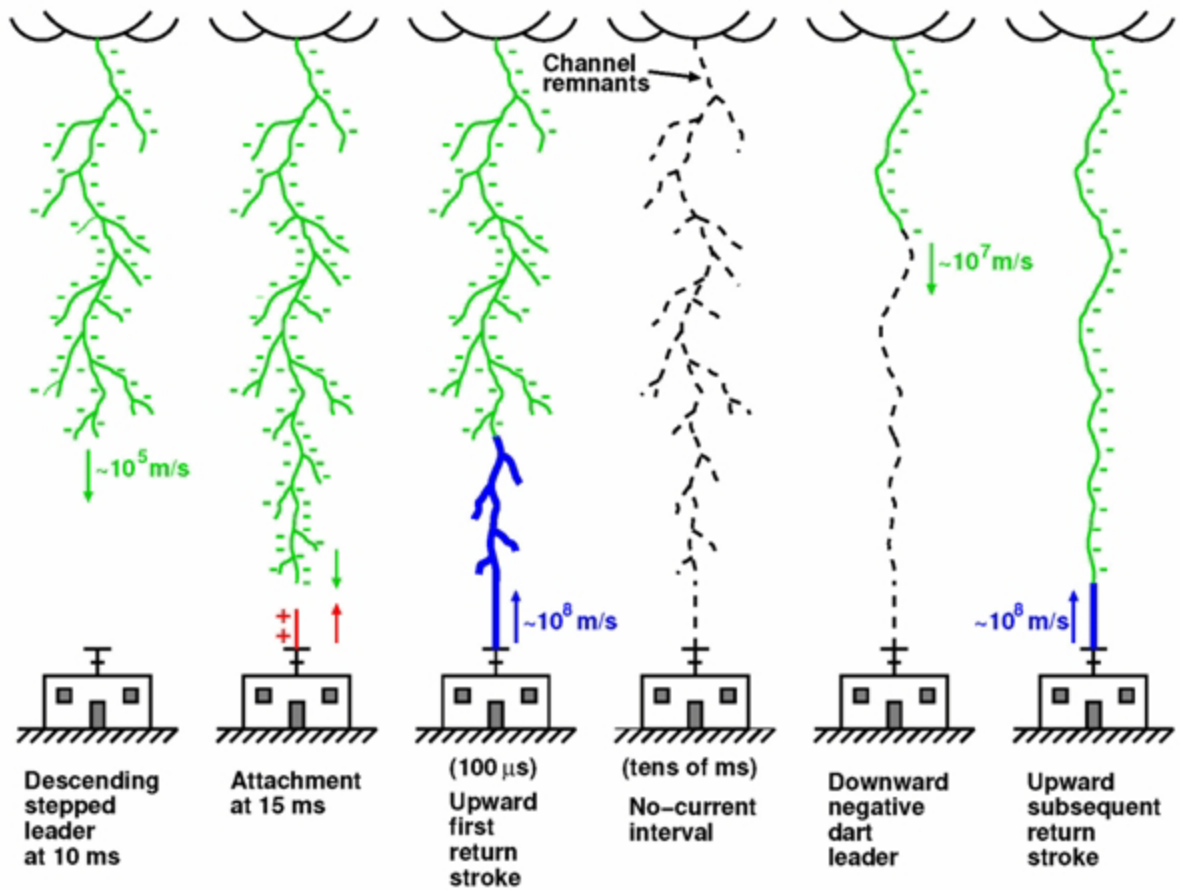


Figure 1-2. Sequence of events in a downward negative cloud-to-ground lightning flash from the time the initial stepped leader exits the cloud base. Adapted from *Jerauld* [2007].

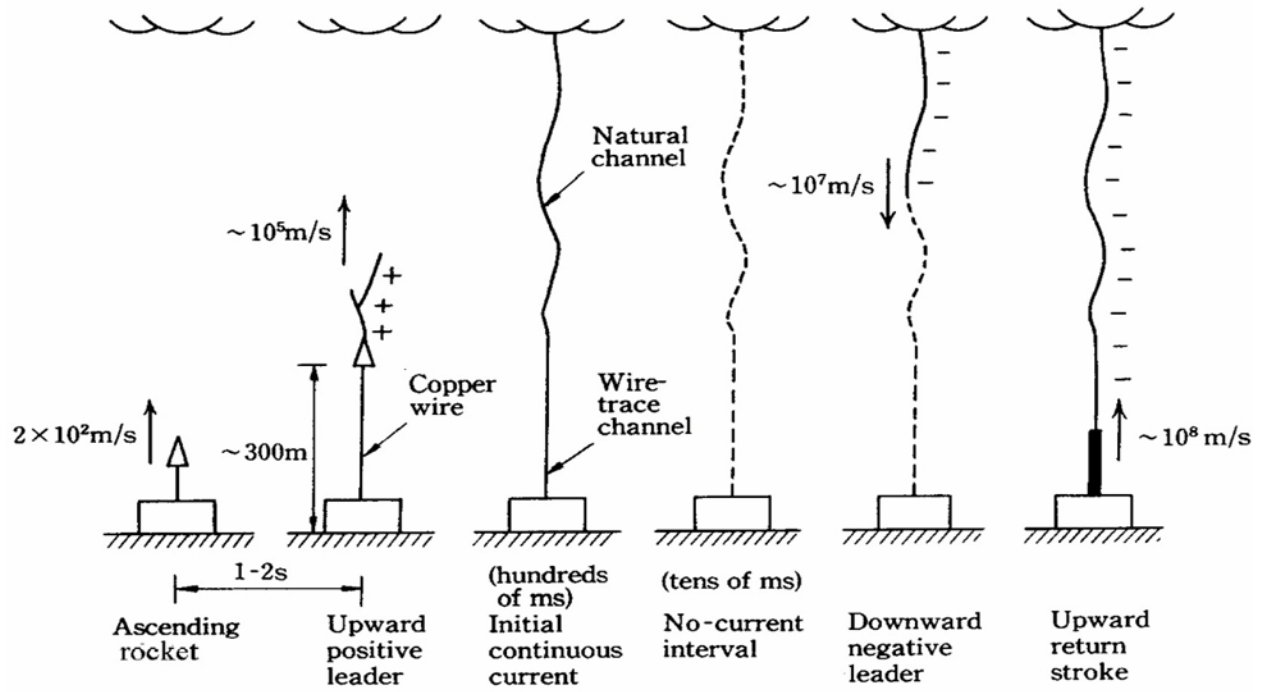


Figure 1-3. Sequence of events in a classical-triggered lightning. Adapted from *Rakov et al.* [1998].



Figure 1-4. Satellite image illustrating the major structural landmarks of the ICLRT.

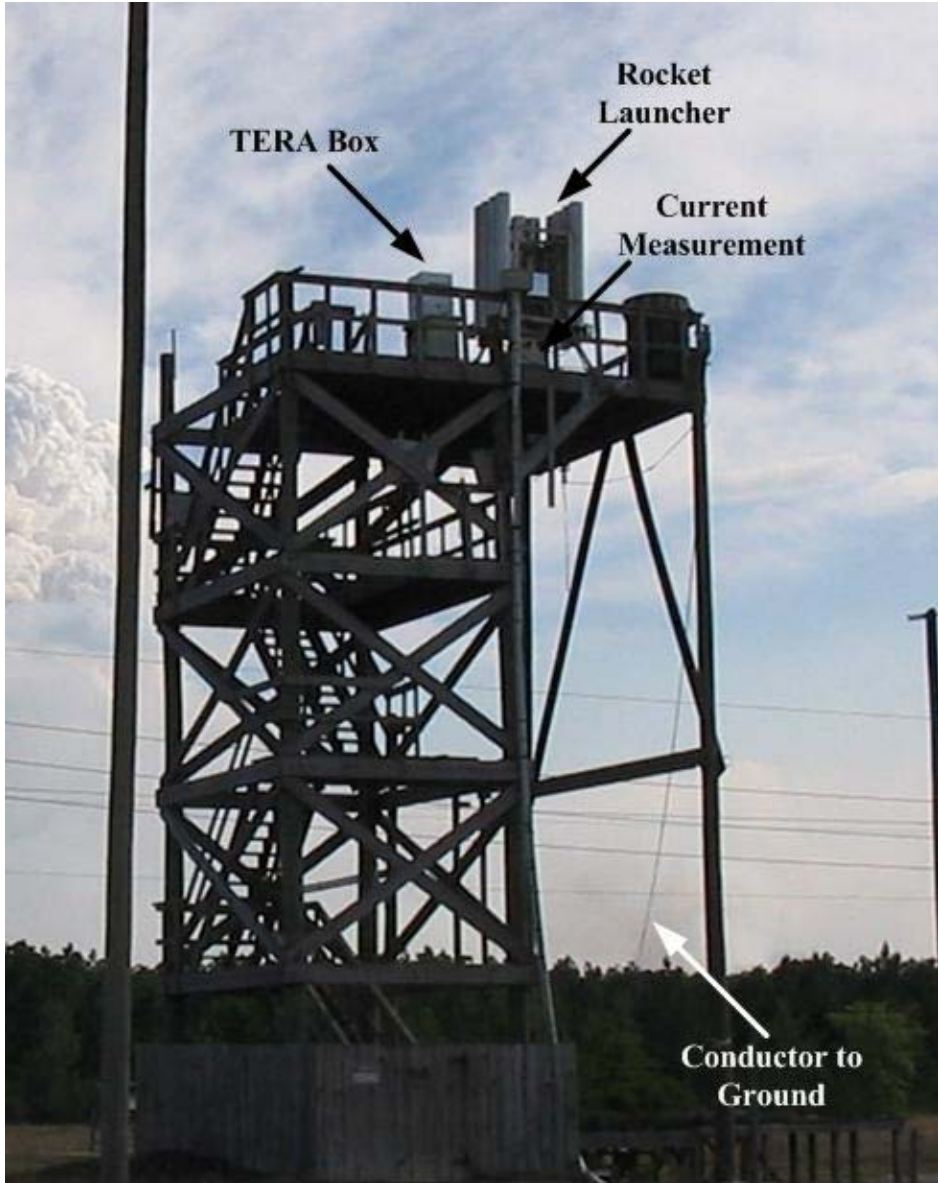


Figure 1-5. The tower rocket launcher.

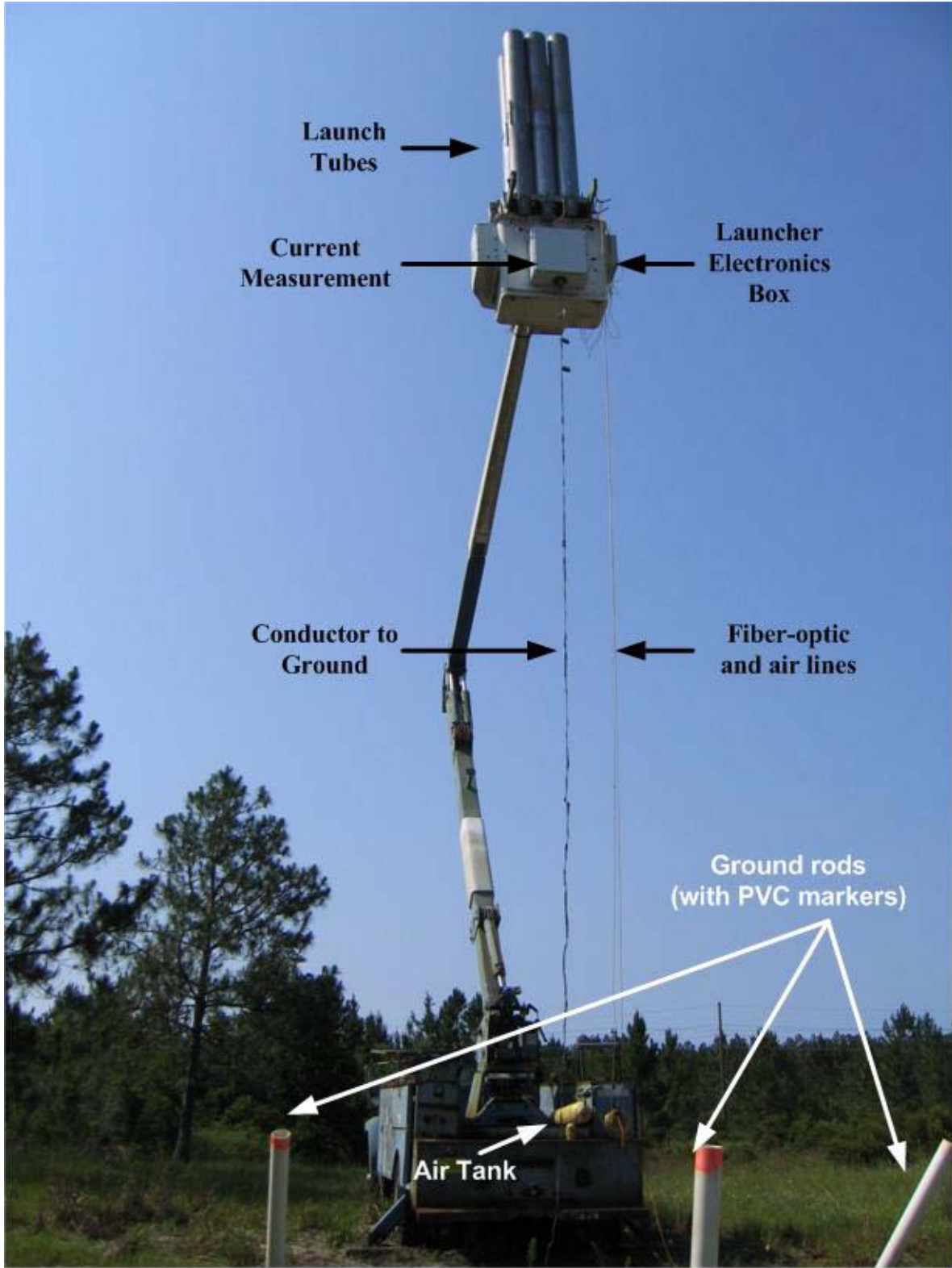


Figure 1-6. The mobile rocket launcher in its armed position.



Figure 1-7. The Launch Control trailer.

CHAPTER 2 EXPERIMENT DESCRIPTION

2.1 Experiment Overview

A brief history of the Multiple Station Experiment (MSE) was provided in Section 1.8. The third era (2005–2007) of the MSE, the details of which are the subject of this chapter, was used to obtain the data presented and discussed in this dissertation. The third era also marked the largest expansion of the network to date. The deployment of a 24-station array of NaI scintillation detectors was a major component of this expansion. The other major development involved the co-location of eight of these NaI scintillation detectors with eight dE/dt sensors to form a time-of-arrival (TOA) network. These changes were also accompanied by significant upgrades in the control system for the experiment. Unlike the two previous eras, operation of the network extended beyond the typical summer storm season (primarily May - August) and was sustained year round. In addition, the size and operation of the network changed significantly with each year of the third era; hence, it is necessary to present multiple configurations for certain aspects of the network. Because the International Center for Lightning Research and Testing (ICLRT) workforce is largely comprised of students, the majority of the network modifications are necessarily implemented at the start of each summer semester, after academic-year classes end, in preparation for the upcoming storm season. Therefore, the network is typically configured at the beginning of a storm season and then maintained in that form until the beginning of the next storm season. The three primary setups used during the third era of the MSE are referred to hereafter as the 2005, 2006, and 2007 configurations. This section briefly discusses the significant changes introduced with each of these configurations. The remainder of this chapter provides details about the equipment and operation of the network.

In 2005, an array of NaI scintillation detectors, designed to observe energetic radiation emissions (composed mostly of X-ray bursts [Dwyer *et al.*, 2004, 2005]) produced during nearby lightning leader propagation, was added to the MSE field and field-derivative measurements. This group of sensors, known as the Thunderstorm Energetic Radiation Array (TERA), was designed by researchers at the Florida Institute of Technology. In the first year of this expansion, ten TERA boxes (see Section 2.5.3), each containing two sensors, were deployed at the ICLRT. Each sensor was comprised of a NaI scintillator mounted on a photomultiplier tube (PMT). To help determine the energy spectrum of the X-ray emissions, one sensor in each box, identified as the SPMT, was covered with a lead shield while the other remained unshielded, known as the UPMT. Seven of these TERA boxes were placed at pre-existing MSE stations, one was placed on the tower launcher, and the final two were placed at the optical sensor locations. The UPMT sensors from four of these TERA boxes along with the co-located dE/dt antennas at those stations formed the basis of a preliminary TOA network that was used to determine the feasibility of a larger TOA system. These four stations provided an exactly determined system of equations which could be solved for source locations; however, location accuracy could not be estimated due to lack of redundancy. Other changes to the MSE included the discontinuation of the dB/dt measurements and the transition of all MSE measurements, except for the channel-base current measurement at the Tower, to Opticomm fiber-optic links. Additionally, the four-camera video system was temporarily disabled due to significant remodeling done in Launch Control; the video system did not resume until 2006. Since 2005, the collection of field, field-derivative, and X-ray sensors at the ICLRT has been known as the MSE/TERA network.

In 2006, the expansion of the network continued. Ten more TERA boxes were deployed; seven of them contained only a UPMT detector, and three of them contained both SPMT and

UPMT detectors. The station numbering for the MSE/TERA network was changed so that each TERA box (numbered 1–20) corresponded to a specific station. Hence, locations such as the two optical measurements (SWO and NEO), the Tower, and new TERA box locations were now considered stations in the MSE/TERA network. This change in the nomenclature did not alter the numbering for any of the previous MSE stations, but the ten original TERA boxes were shuffled around to agree with the new notation. The TOA network was also completed in 2006, with the addition of four new dE/dt antennas. The TOA network was composed of eight stations, including eight dE/dt antennas and eight UPMT detectors. The large number of measurements added to the network also required a change in the network control system. The primary component of this change was a new generation of PIC controllers, the devices which facilitate control of the measurements via the control computer in Launch Control. These new PIC controllers provided a transition from wireless control links to more reliable direct glass-fiber connections between stations and the control computer. Additionally, these PIC controllers could support up to two measurements as well as relay control commands to additional PIC controllers, generally reducing the amount of hardware necessary to operate each station. More information about the control system and the PIC controllers can be found in Section 2.2.

The setup of the MSE/TERA network in 2007 was very similar to the setup in 2006, except for the addition of three new stations (Stations 21, 23, and 24). Station 22 was also created at that time, but the TERA box (containing a UPMT and SPMT) and other equipment at that location were used in an ancillary project performed for Uppsala University, Sweden. Station 22 was incorporated into the MSE/TERA at the end of 2007. Each of the three new stations was equipped with a dE/dt antenna and a TERA box, although none of them was added to the TOA network. All three of these TERA boxes contained a UPMT detector. One of them also

contained a SPMT detector, and the other two also contained a new plastic scintillator/PMT (PPMT) detector, which has a faster response time but lower sensitivity than the NaI scintillators. The two PPMT detectors were recorded on a LeCroy DSO along with the dE/dt measurements from those same stations in order to correlate X-ray bursts and dE/dt pulses with better time resolution than had previously been achieved with the NaI detectors. The other dE/dt antenna, co-located with the TERA box containing two NaI detectors, was designed with a larger surface area and did not utilize any attenuation from the PIC controller, so it was more sensitive to dE/dt activity than any other antenna in the network. Following the modifications in 2007, the MSE/TERA network consisted of 24 stations and over 60 measurements. The layout of the MSE/TERA network at the end of 2007 is shown in Figure 2-1. The diagram given in Figure 2-2 illustrates the operation of the MSE system and summarizes the relationship between network components.

During the third era of the MSE, the digitizer settings remained fairly constant for the MSE measurements. The electric and magnetic field, optical, and TERA measurements were sampled continuously for 2 s (1 s pretrigger) at 10 MHz, with 12-bit amplitude resolution, on Yokogawa DL750 DSOs. The dE/dt and TERA measurements in the TOA network were sampled by LeCroy model DSOs at 250 MHz in segmented memory mode. Each segment was 2 ms with 1 ms of pretrigger. The plastic scintillator/PMT detectors and other dE/dt measurements were also digitized on a LeCroy DSO with similar settings to the TOA measurements. The channel-base current of the rocket-triggered lightning was recorded on both LeCroy and Yokogawa DSOs. Tables 2-1, 2-2, and 2-3 provide a list of the MSE/TERA measurements and their typical acquisition settings during the 2005, 2006, and 2007 configurations, respectively.

2.2 Control System

The primary components of the control system are the central control computer and a device known as a PIC controller. The most vital component of the MSE/TERA network is the control computer because it monitors and controls virtually every aspect of the network. The central component for each measurement at the ICLRT is the PIC controller (so named because the original version contained a PIC brand 16F873-2007SP microcontroller), which provides important functionality and facilitates communication between the measurement and the control computer. This section discusses the operation of the different versions of PIC controllers as well as the control computer.

2.2.1 PIC Controllers

Because the electronics at each measurement are battery powered, it is critical to minimize power consumption. Power management, along with other important functionality, is achieved with the PIC controller. By 2006, three versions of PIC controllers were in use at the ICLRT. Despite some differences in their physical construction, the number of channels supported, and the type of communication link used, the basic operation of the PIC controller is the same for each version. Each PIC controller is powered by a 12 V battery, and power to the measurement electronics (e.g. fiber-optic transmitter, amplifier, PMT tube) is supplied via connectors from the PIC controller. The measurement waveform is passed through the PIC controller by a pair of BNC connectors. Each PIC controller channel (one or two depending on the PIC controller version) is assigned a hexadecimal address, which enables the PIC controller to interpret specific commands sent by the control computer. These commands can configure the PIC controller to switch power on or off to the measurement electronics, attenuate the measurement signal, and supply a calibration signal for the fiber-optic link. Signal attenuation can be achieved in any combination of -3, -6, -10, -14, and -20 dB, with each value being used once at most. To utilize

these nominal attenuation values, the output of the PIC controller must be terminated in 50Ω . The calibration signals available from the PIC controller are a 100 Hz square wave with amplitudes of either $0.1 V_{pp}$ or $1 V_{pp}$ into 50Ω .

The original version of PIC controllers, pictured in Figure 2-3, was designed during the 2001 season by project engineers Michael Stapleton and Keith Rambo, providing the aforementioned functionality to individual measurements. Figure 2-4 provides a diagram of a typical PIC controller (2001 version) installation, and Figure 2-5 shows a photograph of this configuration in an actual measurement. As shown in Figures 2-4 and 2-5, the measurement electronics are housed in a metal enclosure in order to minimize the electromagnetic coupling due to lightning. The output of the sensor (e.g., a flat plate antenna or loop antenna) is fed into the metal enclosure via a BNC bulkhead feed-through connector and is connected to the input of the PIC controller. The output of the PIC controller is connected to the input of the fiber-optic transmitter through a 50Ω terminator. PIC controller receives commands and transmits responses via a pair of 1 mm diameter plastic fibers that are connected to a 900 MHz RF transceiver, known as an RF PIC, located outside of the metal enclosure (pictured in figure 2-6), again in order to minimize electromagnetic coupling to the measurement electronics due to lightning. The RF PIC is powered by its own 12 V battery which is continually charged by a 10 W solar cell fitted with a voltage regulator. The control computer is also connected to a 900 MHz transceiver (see Figures 2-2 and 2-10), allowing the computer to control measurements via the 900 MHz link. For stations containing more than a single measurement, the link between the RF PIC and PIC controller necessarily includes a fiber fan-out board, which allows the RF PIC to interface with up to 8 PIC controllers. As will be discussed shortly, the original PIC

controllers can also operate in a “slave” mode, interacting with the control computer through the plastic fiber ports of a newer version PIC controller.

Several concerns arose when the two channel TERA boxes were first introduced in 2005: (1) the TERA boxes contained two measurements, but the original PIC controllers supported only one channel; (2) limited space made it very difficult to place two PIC controllers in a TERA box; and (3) there were not enough RF PICs, fiber fan-out boards, or original PIC controllers available to complete future network expansions planned for the future. It was clear that a new type of PIC controller would be necessary. The new PIC controller, referred to as the 2005 PIC controller, was specifically designed for placement inside the TERA boxes and the ability to pass two measurement signals. Additionally, the new PIC controller was designed to communicate with the control computer via plastic fibers, like the original PIC controller, or through a single glass fiber that was readily available from the fiber bundles already deployed at each station for data waveform transmission. The glass-fiber communication links were intended to interface with the control computer through a 24-port optical fan-out board located in Launch Control (Figure 2-2). Each port of the optical fan-out board provided bi-directional communication, allowing 24 new PIC controllers to be supported. The intended benefit of the glass-fiber link was to simplify the installation of the new PIC controller, bypassing the need for an RF PIC or a fiber fan-out board. Unfortunately, several design issues with both the optical fan-out board and the PIC controller prevented the ideal operation of the new PIC controllers. The primary disappointment was that the glass-fiber link did not operate properly, so the 2005 PIC controller could only be controlled via the plastic fibers. Additionally, the ability to individually power the measurement electronics for each channel did not function as expected. However, the remaining

functionality of the 2005 PIC controller did operate properly, and these PIC controllers were occasionally used in a single measurement configuration, similar to the original PIC controllers.

After the problems encountered with the 2005 PIC controllers were analyzed and corrected, another PIC controller version was designed by Michael Stapleton and Ph.D. student Robert Olsen III in 2006. The 2006 PIC controller was nearly identical in appearance to the 2005 PIC controller, but operated with the initially desired functionality. The new PIC controller design also provided a “slave” mode feature in which additional PIC controllers (2001 version) could communicate with the control computer through the plastic fiber ports of the 2006 PIC controller. Therefore, stations with a 2006 PIC controller did not require an RF PIC, and stations with a TERA box and only one additional measurement did not require a fiber fan-out board. For reasons that are still being investigated, the 2005 and 2006 PIC controllers cannot operate in the slave mode. A photograph of a 2006 PIC controller is shown in Figure 2-7 and a diagram of its typical installation is given in Figure 2-8. In addition to the corrections made to the PIC controller design, the 24-port optical fan-out board was also redesigned and installed in an equipment rack at the north end of the Launch Control trailer, as pictured in Figure 2-9.

2.2.2 Control Computer

The control computer, pictured in Figure 2-10, is responsible for controlling the PIC controllers and oscilloscopes, reading and displaying the output of an electric field mill, automatically arming and disarming the MSE/TERA network based on the field mill output, enabling and disabling video acquisition, triggering the still 35 mm cameras when a rocket is fired, and controlling the mobile launcher (the tower launcher has its own control unit). These functions are accomplished with custom LabView applications that were written by Ph.D. student Robert Olsen III. The primary LabView application, used to arm and disarm the MSE/TERA network, utilizes a list of active PIC controller and DSO addresses along with a

predefined set of configuration settings to automatically control the network based on the present thunderstorm conditions. The output of an electric field mill (Figure 2-11), which measures the quasi-static electric field at ground level and can be used as an indicator of thunderstorm conditions, is continually monitored by the control computer using a National Instruments data acquisition card. When the field mill reading exceeds a threshold value (typically ± 2 kV/m), the control computer broadcast the desired configuration settings over the 900 MHz RF links and the glass-fiber connections, activating the measurements in the field. Additionally, the digitizers and digital video recorders located in Launch Control are configured by the control computer through a GPIB or Ethernet interface. Arming the network is a multi-step process by which measurements are powered up, calibration signals (generated by the PIC controllers and transmitted over the fiber-optic links) are recorded on the digitizers, each PIC controller is set to the proper voltage attenuation setting, video acquisition is initiated, and the digitizers are armed. Once this process is complete, the network is ready to acquire data. If the field mill reading falls below the threshold value for ten or more minutes, the network is disarmed using a procedure which is basically the inverse of the arming procedure. This automated system minimizes the power consumption by each measurement and allows the network to acquire data when no personnel are on site. A flowchart representation of the control computer arming algorithm is presented in Figure 2-12.

2.3 Fiber-Optic Links

Fiber optic links, which are immune to electromagnetic interference from nearby lightning, were used to transmit the analog data from each sensor in the field to the Launch Control trailer, where the signals were digitized and stored. As noted in Section 1.8, beginning in 2002, an effort was made to gradually phase-out the Nicolet Isobe 3000 fiber-optic (FO) links, which were used in the original MSE network, and replace them with Opticom MMV-120C FO links,

which were smaller in size, performed more reliably, provided greater bandwidth, and required only a single fiber for data transmission. Since 2005, all the MSE/TERA measurements have utilized the Opticomm FO link, with the sole exception of the 2005 base-current measurement at the Tower, which used an Isobe FO link. The transition to Opticomm links was completed in 2006. This section provides details for both the Opticomm and Isobe FO links, with Table 2-4 providing a summary of the typical characteristics for each type of link.

Opticomm MMV-120C. The Opticomm MMV-120C fiber-optic links utilize frequency modulation (FM) with a carrier frequency of 70 MHz and operate at an optical wavelength of 1310 nm. Because the Opticomm links were originally intended as video fiber-optic links, the manufacturer agreed to alter the design so they could be used in the MSE/TERA network. First, the input and output resistances of 75 Ω (standard value for video equipment) were changed to 68 k Ω and 50 Ω , terminated respectively. A large input resistance is desired because it can be lowered to any required value by simply adding a smaller resistance in-line terminator in parallel. The value of 68 k Ω was selected because it was the highest value the manufacturer could achieve without sacrificing the performance of the link. The output resistance was chosen because the MSE/TERA network is almost exclusively a 50 Ω system (e.g., BNC cables and oscilloscope input resistances). Second, the low-frequency cutoff was modified from 5 Hz (-3 dB) to DC by the manufacturer. The nominal input range is ± 1 V for the transmitter. When the receiver is terminated in 50 Ω , the nominal output range is also ± 1 V and typically saturates at ± 1.2 V. The manufacturer lists the signal-to-noise ratio as about 67 dB; however, this value was acquired using the short-haul RS-250C standard in which the signal is low-pass filtered with a cut-off frequency of about 5 MHz. In practical applications the signal-to-noise ratio over the

entire bandwidth is several dB lower than the value obtained under the short-haul RS-250C standard.

Optical Cable Corporation (OCC) BX series water resistant armored cables were used with the Opticomm links. Each armored cable consisted of two armored outer jackets surrounding either four (BX-04 series) or six (BX-06 series) sub-cables. Each sub-cable was Kevlar reinforced and contained a 62.5/125 μm (core/cladding) graded index multi-mode fiber-optic cable that was terminated with a ST connector. The nominal index of refraction for the fibers was 1.483. The color-coded sub-cables were twisted around a strength member running through the center of the cable.

Nicolet Isobe 3000. The Nicolet Isobe 3000 fiber-optic links utilize a combination of amplitude modulation (AM) and pulse-width modulation (PWM). The FO transmitter has an input resistance of 1 M Ω and has selectable input ranges of ± 0.1 V, ± 1 V and ± 10 V. Additionally, the gain and offset of the link can be manually adjusted at the receiver end. The output range of the receiver is fixed at ± 1 V regardless of the selected input range. Therefore, the Isobe FO link effectively attenuates the signal by -20 dB (0.1 V/V) when the transmitter is set to the ± 10 V range and amplifies the signal by 20 dB (10 V/V) when the transmitter is set to the ± 0.1 V range.

The Isobe links used 200 μm multi-mode Kevlar reinforced duplex fiber-optic cables with SMA connectors. The nominal index of refraction for the fibers was 1.429. These fibers, manufactured by the OFS Fitel Corporation, were arranged in six-fiber armored cables. The individual sub-cables were color coded and twisted around a strength member. Since each Isobe link required two fibers, each cable could supply a maximum of only three links.

2.4 Digital Storage Oscilloscopes

Digital storage oscilloscopes (DSOs), primarily used as digitizers, were employed to record all of the MSE/TERA measurements. Each digitizer was given a unique identifier, which also corresponded to the device's GPIB or Ethernet address, allowing the control computer to automatically configure the instrument when the network was armed and disarmed. Due to the varying nature of the measurements and the continual improvements in technology, several types of digitizers were employed at the ICLRT. The two brands of digitizers utilized by the MSE/TERA network were LeCroy and Yokogawa, with two different models per brand being used. Table 2-5 summarizes the characteristics for each DSO model used in the MSE/TERA network between 2005 and 2007. In general, the Yokogawas have better amplitude resolution and longer time records, but the LeCroys have greater bandwidth and higher sampling rates. Another important difference is that the Yokogawas could only be triggered once per flash, while the LeCroys acquired data in segmented memory mode. In the segmented mode, the total acquisition memory was equally divided among a designated number of segments which required individual triggers. Segmented memory mode was particularly useful for acquiring data from individual return strokes without wasting memory on the relatively long and usually uninteresting inter-stroke intervals. In summary, the LeCroys and Yokogawas worked in complementary fashion, with the LeCroys recording fast records (>10 MHz) of relatively short duration (several hundred microseconds to several milliseconds) and the Yokogawas recording slower records over the duration of the flash.

The digitizers were located along the north and west walls at the north end of the Launch Control trailer, near the FO receivers. Figure 2-13 shows three 19-inch racks along the west wall that housed ten of the MSE/TERA scopes. The LeCroys were mounted directly into the racks, while the Yokogawas were placed on metal shelves that were mounted to the racks. Each

digitizer received power through an uninterruptible power supply (UPS) which was used for battery backup and surge protection, particularly when the Launch Control trailer was switched from the power grid to the diesel generator and vice versa. Signals were transmitted via lengths of coaxial cable from the FO receivers directly to the front of the LeCroy oscilloscopes. The Yokogawas, however, have their channel inputs on the right side of the digitizer. Therefore, a BNC feed-through panel was mounted directly above each Yokogawa scope. These panels had 32 connectors arranged in 16 columns with 2 connectors each. Both connectors in each column were connected via 2 ft RG-223 coaxial jumpers to a BNC T-connector attached to a single channel input. This configuration provided front-side access with 2 connectors per Yokogawa channel. The top connector in each column was generally reserved for the incoming signal, and the bottom connector was used for feeding the signal to another scope channel or for terminating into the proper impedance. The following paragraphs provide specific details on the operation of each type of DSO.

Yokogawa DL716. The Yokogawa DL716 is a 16 channel DSO with 12-bit amplitude resolution, a maximum bandwidth of 4 MHz (-3 dB), and a maximum sampling rate of 10 MHz. The maximum record length is 16 megasamples per channel when all 16 channels are used simultaneously. At the maximum sample rate (10 MHz), the maximum record length corresponds to a time interval of 1.6 s. Because each sample is recorded with 12-bit resolution, two bytes (16 bits or one word) are required to store each sample (four bits are thrown away). Therefore, digitizing a 1.6 s record on all 16 channels sampled at 10 MHz requires 256 megawords or 512 megabytes. The record length of the DL716 makes it ideal for obtaining continuous full-flash records of lightning data. Unfortunately, one major disadvantage of the DL716 is that it takes up to 15 minutes to write data from memory to the hard disk when all the

channels are used at their maximum record length. During this interval, no new data can be recorded. Although this DSO model has been used to record many types of signals throughout the years, its use in the MSE between 2005 and 2007 was restricted to the channel-base current measurement (see Tables 2.1 and 2.3).

The voltage sensitivity for each DL716 channel can be set from 5 mV per division to 20 V per division with a maximum peak-to-peak input range of 250 V. The input resistance of each channel is 1 M Ω with a shunt capacitance of 30 pF. The input signal is either AC or DC coupled and is low-pass filtered with a -3 dB cutoff of 500 Hz, 5 kHz, 50 kHz, 500 kHz, or 4 MHz. The DL716 can be triggered by any of these 16 channels or by an external TTL level trigger input. Additionally, complex triggering schemes can be generated by OR triggering any combination of the 16 channels with the trigger level and slope of each channel capable of being set individually. One caveat of the Yokogawa scopes is that the trigger coupling cannot be isolated from the signal coupling used on a channel; therefore, it is impossible to record a channel using DC coupling and trigger from the same channel using AC coupling.

Configuration of the DL716 is performed over an IEEE 488.2 (GPIB) bus by issuing a series of commands or loading a set of predefined settings from the hard disk of the DSO. Nearly every setting can be manipulated over GPIB, allowing the digitizer to be remotely configured and armed by the control PC, as previously discussed in Section 2.2.2.

When the digitizer is triggered, the waveforms of all active channels are stored on the internal hard disk (9.2 GB) or an external SCSI hard disk that can be added for additional storage space. The data are recorded to a single binary file (having an extension “.WVF”) that is paired with an ASCII header file (having an extension “.HDR”). The file names, which are set by the LabView control program via the GPIB interface, are typically of the form

“DMMDDXXX.HDR” and “DMMDDXXX.WVF,” where MM is the month, DD is the day, and XXX is a number from 000 to 999, the latter number increasing with each additional data file saved on a given day. The calibration files obtained before and after each arming of the network are also stored to the hard disk with the form “CMMDDXXX.HDR” and “CMMDDXXX.WVF.” Any of the files can be retrieved at a later time via a 10Base-T Ethernet connection using the File Transfer Protocol (FTP).

Yokogawa DL750. The Yokogawa DL750, like the DL716, is a 16 channel DSO with 12-bit amplitude resolution and a maximum sampling rate of 10 MHz. The operation of the DL750 is nearly identical to the DL716, with the exception of a few features discussed next. The selection of the low-pass bandwidth filters is the same as the DL716 except that the maximum bandwidth is 3 MHz instead of 4 MHz. The maximum record length was extended from 16 megasamples to 25 megasamples per channel although, for unknown reasons, only 20 megasamples are obtained when all 16 channels are used at the maximum sample rate (10 MHz). Hence, the maximum record length obtained with the maximum sample rate corresponds to a time interval of 2 s, not 2.5 s. One significant improvement in the DL750, however, is that the write-to-hard-disk time is reduced to approximately 5 minutes. The nomenclature used for the stored waveforms was also altered, although this fact does not represent a significant change in the design of the DL750 from the DL716. The data waveforms have the form “DXXXX.HDR” and “DXXXX.WVF”, and the calibration files have the form “CXXXX.HDR” and “CXXXX.WVF,” where XXXX is a number that starts at 0000 and incrementally increases with each additional file stored on the same day.

Finally, we mention a significant and somewhat unfortunate difference between the DL750 and DL716 models. Both Yokogawa models display an amplitude range of 10 divisions. The

DL716 and both of the LeCroy DSO models divide their visible (displayed) amplitude range into a number of values which is determined by the bit depth of the scope. For some reason, the DL750 divides its amplitude range into 20 divisions while displaying 10 of them. Since the voltage sensitivity is selected by adjusting the volts per division setting, the total amplitude range is twice that expected from the vertical display. Because differences in the DL716 and DL750 header files were minor and both scopes used the same equation for the bit value to voltage conversion, the software programs used to parse the binary files accurately reproduce known input waveforms, such as the calibration signals. Hence, this unexpected difference in the scope models went undetected until after the 2007 experiment concluded and in-depth analysis began. Two adverse effects resulting from the amplitude range being double what is expected are (1) the amplitude resolution is half as accurate (twice as much difference between quantization levels) as expected and (2) the amplitude range of the measurement may not be set by the oscilloscope, but possibly by another component that may not operate linearly near saturation. For measurements recorded on the DL750, the vertical range is limited by the fiber-optic link at approximately ± 1.2 V. Fortunately, most of the measurements never reach the FO saturation voltage, which is partially why this effect was not detected earlier, but for future operations it is important to be aware of this possibility. The X-ray sensors appear to be the only measurements regularly affected in data that has already been collected.

LeCroy LT344 Waverunner. The Lecroy LT344 is a four channel DSO with 8-bit amplitude resolution, a maximum sample rate of 500 MHz, and a maximum bandwidth of 500 MHz. The LT344 has a maximum record length of one megabyte per channel when all four channels are used. Since one byte (8 bits) is used to store each sample point, the total record length is one megasample per channel and corresponds to a time interval of 2 ms when using the

maximum sampling rate of 500 MHz. As previously mentioned, however, the LT344 is not typically used to acquire a continuous record but is used in segmented memory mode. In segmented memory mode, the total acquisition memory is equally divided among multiple segments, with each segment requiring an individual trigger. If, for example, four segments are desired, the acquisition memory is divided into four segments of 250 kilosamples per channel, with the time interval of each segment being dependent on the selected sampling rate. As noted earlier, segmentation of the memory is particularly useful for obtaining short waveforms at the time of individual return strokes while disregarding the relatively long inter-stroke intervals. Then, the triggering event (i.e., the return stroke) can be set to occur at a specific point in the record by using the pre-trigger option. For example, a pre-trigger setting of 50% means that the first half of each segment consist of data obtained before the trigger point in that segment. The pre-trigger setting applies to all segments; it cannot be set individually.

The input resistance of each LT344 channel can be set to either 50 Ω or 1 M Ω . The voltage sensitivity can be set from 2 mV per division to 10 V per division with a maximum RMS input voltage of 5 V and 280 V when the input resistance is 50 Ω and 1 M Ω , respectively. Each channel can be AC or DC coupled and individually configured with an internal low-pass filter of 25 MHz, 200 MHz, or 500 MHz (-3 dB). The LT344 can be triggered from any of these four channels, an external trigger input, or a complex triggering scheme involving multiple channels. Unlike the Yokogawa oscilloscopes, the trigger coupling can be set independently of the coupling used to measure the channel input. Further, the external trigger is not TTL; hence, options such as the input resistance, coupling, trigger level, and slope are selectable for the external trigger.

Similarly to the Yokogawa oscilloscopes, the LT344 is remotely configured and armed by the control computer. Unlike the Yokogawa DSOs, the LT344 can be remotely controlled with either a GPIB or Ethernet connection. The control computer has always utilized the Ethernet link for controlling the LeCroy oscilloscopes remotely.

The LT344 is equipped with a PCMCIA Type III slot, which is used to add hard disk storage. A 128 MB compact flash card was used in the LT344, providing enough storage for 32 events in which the entire record length (1 MB per channel) is obtained for all four channels. When the digitizer is triggered, a binary file, containing all segments, is generated for each active channel. Unlike the Yokogawa files, the header information is stored in the same file as the waveform data. The file names for the lightning data files are of the form “ACX.YYY,” where X is the channel number (1–4) and YYY is a number that increases from 000 with each additional file saved on the same day. The calibration files are of the form “SCX.YYY.” Unlike the Yokogawa DSOs, the LT344 does not support FTP and requires the use of a proprietary protocol for file transfer; therefore waveforms are retrieved from the DSO using a 10Base-T Ethernet connection and the LeCroy *Scope Explorer* software.

LeCroy LT374 Waverunner2. The LeCroy LT374 is the successor of the LT344 DSO model. The operation of the LT374 is essentially identical to the LT344 except for a few small differences, which we note next. The maximum sampling rate was increased to 2 GHz, and the maximum acquisition memory was increased to four megabytes per channel. The maximum bandwidth (500 MHz) of the LT374 is identical to the LT344, but the 25 MHz low-pass filter previously available on the LT344 was replaced on the LT374 with a 20 MHz setting.

2.5 Measurement Implementation

2.5.1 Electric Field and Electric Field Time-Derivative Measurements

The electric field and electric field time-derivative (dE/dt) sensors used at the ICLRT are aluminum flat-plate antennas that are placed essentially flush with the Earth, as shown in Figure 2-14. The antenna consists of an electrically isolated circular plate mounted flush with the top face of a hollow aluminum housing. The circular plate is supported from the bottom face of the housing by six nylon standoffs and is isolated from the remainder of the top face by an annular air gap that is 6 mm wide. The circular plate on all but one of the MSE/TERA flat-plate antennas has a diameter of about 0.444 m and a corresponding area of 0.155 m². The circular plate of the large dE/dt antenna that was added to the network in 2007 has a diameter of 1.215 m and a corresponding area of 1.159 m². The voltage appearing between the circular plate and the housing is output by a female BNC connector mounted to the side of the housing. The outer conductor of the BNC connector makes physical contact with the antenna housing and the center conductor is linked to the circular plate via the center conductor of a short length of RG-223 coaxial cable. The housing of the antenna, which serves as the electrical ground for the sensor, is connected to a 3-m ground rod by a short length of 12 AWG wire.

The electronics for each E-field and dE/dt measurement were placed in a metal enclosure (known as a Hoffman box) which was buried underground near the antenna. Each hole was about a half meter deep and the Hoffman box was placed on an angled shelf so as to drain any water acquired in the hole away from the box. The Hoffman box was placed underground so that it would be protected from the external environment (temperature, humidity, rain) and the area near the antenna would be as flat as possible. In addition, a piece of reflective insulation was placed over the hole to shield the equipment from the heat of the sun and limit the rainwater that could enter the hole. A length of coaxial cable with male BNC connectors connected the antenna

to a female BNC bulkhead feed-through connector mounted to the Hoffman box. This cable was enclosed in metal shield braid which was secured to the male BNC connectors at each end by wire clamps. Therefore, the shield braid and Hoffman box were electrically connected to the grounded housing of the antenna.

Because the conductivity of the soil at the ICLRT is typically only about $2.5 \times 10^{-4} \text{ S m}^{-1}$ [Rakov *et al.*, 1998], a relatively low value, these antennas are potentially susceptible to some enhancement in the local electric field. That is, true ground is not at the surface. In order to minimize this effect, wire mesh was extended from each side of the antenna housing to simulate a larger ground plane around the antenna. During the 2005 and 2006 seasons, the length of the mesh was approximately one meter on the side with the hole for the electronics and approximately a third of a meter on the remaining sides. The size of this simulated ground plane was altered in 2007 because some disagreement had been observed between the amplitudes of the integrated dE/dt and the measured E-field waveforms obtained at the same location, as noted by *Jerauld* [2007] and *Jerauld et al.* [2008]. At Stations 4, 5, and 9, which contain both an E-field and dE/dt antenna, a large single ground plane that was made of field fence and extended at least 5 m beyond each side of both antennas was deployed. Further, the ground rods of both measurements, which had previously been electrically isolated from each other, were connected to the single ground plane. The ground planes of the other E-field and dE/dt measurements were extended to approximately 1.5 m on each side using hardware cloth. Figures 2-14 and 2-15 illustrate the implementation of the flat plate antennas. We will not further discuss the effects of extending these ground planes here, as the difference between the integrated dE/dt and measured E-field waveforms is still being investigated. The primary sources suspected for this difference are grounding effects and field enhancement, likely related.

It is important to note that the E-field and dE/dt sensors described here are intended to measure only the vertical component (perpendicular to ground) of the vectors \vec{E} and $d\vec{E}/dt$, respectively. This is because, for a perfectly conducting surface (approximated by the antenna and surrounding ground plane), boundary conditions state that the horizontal component (tangential to the ground) of the E-field is zero. Therefore, the terms “E-field measurement” and “dE/dt measurement” only refer to the vertical component of the electric field and electric field derivative, respectively, measured at ground level.

In order to understand how the same sensor is used to measure two different physical quantities, it is necessary to consider the Thevenin or Norton equivalent circuit for the flat-plate antenna. This analysis begins by considering the boundary of a perfectly conducting ($\sigma = \infty$) surface. The boundary condition for the normal component of \vec{E} at the surface of a perfect conductor specifies

$$\vec{D} \cdot \hat{n} = \epsilon \vec{E} \cdot \hat{n} = \rho_s \quad (2-1)$$

The quantity \vec{D} is the electric displacement vector at the surface and is expressed in $C m^{-2}$, \hat{n} is the unit vector normal to the surface, ϵ is the permittivity of the dielectric medium, \vec{E} is the electric field vector and is expressed in $V m^{-1}$, and ρ_s is the surface charge density also expressed in $C m^{-2}$. The equality shown in Equation 2-1 requires that the medium above the plate is linear, isotropic, homogeneous, and non-conducting. Assuming that the normal unit vector corresponds to the \hat{z} component in the Cartesian coordinate system and the permittivity of air is essentially that of free space ($8.85 \times 10^{-12} F m^{-1}$), Equation 2-1 can be rewritten as

$$\epsilon_0 E_z = \rho_s \quad (2-2)$$

The quantity E_z is simply the magnitude for the vertical component of the electric field vector, \vec{E} , and ϵ_0 is the permittivity of free space. If E_z is uniform over the plate, then the

surface charge density must also be uniform, and the total charge on the plate can be found by simply multiplying ρ_s by the area of the plate.

$$Q_{plate} = \epsilon_0 A_{plate} E_z \quad (2-3)$$

For a circular plate, E_z is considered uniform if the diameter of the plate is less than about a sixteenth of a wavelength. If the highest frequency component measured from E_z is 25 MHz (the highest bandwidth of any digitizer in the MSE/TERA network), then the smallest wavelength will necessarily be 12 m. One sixteenth of a wavelength is 0.75 m, which is larger than the 0.444 m diameter of the plates used in the MSE. However, the diameter of the large dE/dt antenna added in 2007 is larger than 0.75 m, so Equation 2-3 and the analysis discussed hereafter does not strictly hold for this antenna. Consequently, the purpose of the large antenna was simply to detect weak radiation events, such as upward-positive-leader pulses in the initial stage of rocket-triggered lightning, and not estimate physical quantities.

Taking the time derivative of Equation 2-3, one can obtain the time domain Norton equivalent short circuit current, $i(t)$, of the flat-plate antenna.

$$i(t) = \frac{d}{dt} Q_{plate}(t) = \frac{d}{dt} [\epsilon_0 A_{plate} E_z(t)] = \epsilon_0 A_{plate} \frac{d}{dt} E_z(t) \quad (2-4)$$

Hence, the flat-plate antenna in the presence of a uniform time-varying electric field can be viewed as a current source whose magnitude is proportional to the time derivative of the normal component of the electric field. This Norton equivalent current source provides the basis for the equivalent circuit; however, the analysis of the equivalent circuit is typically performed in the frequency domain. The relationship between a general time-domain signal, $x(t)$, and its corresponding frequency domain signal, $X(\omega)$, is specified by the well-known Fourier transform. Because differentiation with respect to time corresponds to multiplication by the complex

number $j\omega$ in the frequency domain, the expression for the magnitude of the equivalent current source in the frequency domain becomes

$$I(\omega) = \varepsilon_0 A_{plate} j\omega E_z(\omega) \quad (2-5)$$

The quantities $I(\omega)$ and $E_z(\omega)$ designate that the current and normal component of the electric field, respectively, are now functions of angular frequency ω and not time. Equation 2-5 defines the current source in the general frequency-domain equivalent circuit shown in Figure 2-16. The circuit in Figure 2-16 shows that the current source is in parallel with the source impedance, Z_S , of the antenna and the load impedance, Z_L , of any external components connected to the antenna. In general, the source and load impedances can be resistive, capacitive, inductive, or any combination of the three.

If the output of the antenna is taken as the voltage across the load impedance, then the output voltage of the antenna in the frequency domain is defined as

$$V_{out}(\omega) = I(\omega)Z_{total} = I(\omega)(Z_S || Z_L) = \varepsilon_0 A_{plate} j\omega E_z(\omega) \left(\frac{Z_S Z_L}{Z_S + Z_L} \right) \quad (2-6)$$

The frequency-independent gain of the antenna is given by the quantity $\varepsilon_0 A_{plate}$. If the quantity $Z_S Z_L / (Z_S + Z_L)$ is real and equal to unity, then the output is simply $j\omega E_z(\omega)$ (or dE/dt) scaled by the frequency-independent gain $\varepsilon_0 A_{plate}$. Conversely, if the quantity $Z_S Z_L / (Z_S + Z_L)$ is imaginary and equal to $1/(j\omega)$, then the output is simply $E_z(\omega)$ (E-field) scaled by the frequency independent gain $\varepsilon_0 A_{plate}$. Therefore, the output of the antenna depends on the source and load impedances.

Jerauld [2003] used a generalized load impedance, consisting of a capacitor and resistor in parallel, to analyze the operation of both the E-field and dE/dt antennas. This analysis begins by specifying the source impedance of the antenna. Typically, the source impedance is dominated by the capacitance between the circular plate and the antenna housing, with any

resistive or inductive components contributed by the length of wire connecting the plate to the BNC connector being neglected. Therefore, the source impedance, Z_S , is assumed to be purely capacitive and is determined by the capacitance of the antenna itself, C_{ant} . The capacitance measured for the MSE/TERA flat-plate antennas is typically about 80 pF.

$$Z_S = \frac{1}{j\omega C_{ant}} \quad (2-7)$$

As stated previously, the load impedance for either an E-field or dE/dt antenna can be represented by a resistor and capacitor in parallel; any inductive components are ignored. The capacitor, C_{int} is typically known as an integrating capacitance and the resistor, R , is known as the load impedance. Hence, the load impedance is represented as

$$Z_L = \frac{1}{j\omega C_{int}} || R = \frac{\frac{R}{j\omega C_{int}}}{R + \frac{1}{j\omega C_{int}}} = \frac{R}{1 + j\omega R C_{int}} \quad (2-8)$$

Since all components of the source and load impedances are in parallel with the current source, the capacitive terms can be combined into a single term, C , having a corresponding impedance of $1/j\omega(C_{ant} + C_{int})$. Hence, the total impedance, Z_{total} , is expressed as

$$Z_{total} = \frac{R}{1 + j\omega R (C_{ant} + C_{int})} = \frac{R}{1 + j\omega R C} \quad (2-9)$$

Substituting Equation 2-9 into Equation 2-6 yields

$$V_{out}(\omega) = I(\omega)Z_{total} = \varepsilon_0 A_{plate} j\omega E_z(\omega) \left(\frac{R}{1 + j\omega R (C_{ant} + C_{int})} \right) \quad (2-10)$$

The interpretation of the response of the antenna in the frequency domain depends on whether the antenna is to be viewed as an E-field or dE/dt sensor. In the case of a dE/dt sensor, no integrating capacitor is used ($C_{int} = 0$). This configuration has been shown to correspond to a single-pole low-pass filter with a pass-band gain equal to $\varepsilon_0 A_{plate} R$ and a cutoff frequency, ω_0 , given by Equation 2-11 [e.g., *Jerauld*, 2003]. Therefore, if the dE/dt waveform has no

significant frequency content above ω_0 , the output voltage of the dE/dt sensor is expressed in the time domain by Equation 2-12.

$$\omega_0 = \frac{1}{RC_{ant}} \quad (2-11)$$

$$V_{out-dE}(t) = \varepsilon_0 A_{plate} R \frac{d}{dt} E_z(t) \quad (2-12)$$

For the dE/dt sensors used in the MSE/TERA network, the resistor, R , has value of 50 Ω . Hence, the cutoff frequency, ω_0 , in the frequency domain is approximately $2.5 \times 10^8 \text{ s}^{-1}$. The corresponding frequency is

$$f_0 = \frac{\omega_0}{2\pi} = \frac{2.5 \times 10^8}{2\pi} \approx 40 \text{ MHz} \quad (2-13)$$

Since the maximum bandwidth allowed by any of the digitizers in the MSE/TERA network is 25 MHz, Equation 2-12 accurately describes the non-attenuated output of the dE/dt sensors. In practice, however, the PIC controller and the fiber optic link of each sensor also affect the measured output voltage. Therefore, a more complete expression for the output voltage of the dE/dt sensor is given in Equation 2-14. A diagram of the dE/dt measurement setup is shown in Figure 2-17.

$$V_{out-dE}(t) = \varepsilon_0 A_{plate} R G_{PIC} G_{link} \frac{d}{dt} E_z(t) \quad (2-14)$$

The quantity G_{link} , which is typically near unity, is calculated from the calibration signals obtained before and after each storm. The PIC controller attenuation is set to -6 dB for the dE/dt measurement, giving G_{PIC} a value of 0.5. Using these values with the values previously given for the permittivity of free space, resistor, and area of the plate results in a calibration factor of approximately $29.2 \text{ kV m}^{-1} \mu\text{s}^{-1}/\text{V}$, meaning that a single volt recorded on the digitizer corresponds to a dE/dt value of $29.2 \text{ kV m}^{-1} \mu\text{s}^{-1}$ measured at the antenna.

As previously stated, Equation 2-10 also describes the output voltage for the E-field sensor. For the E-field configuration, the integrating capacitance is selected so that it dominates the antenna capacitance. In addition, the load resistance, R , is typically very large, so that the output of the antenna approaches that of an ideal flat-plate electric-field antenna. This configuration has been shown to correspond to a single-pole high-pass filter with a pass-band gain equal to $\epsilon_0 A_{plate} / C$ and a cutoff frequency, ω_0 , given by equation 2-15 [e.g., *Jerauld*, 2003]. For frequencies much greater than the cutoff frequency the output voltage of the E-field sensor is expressed in the time domain by Equation 2-16.

$$\omega_0 = \frac{1}{RC} \quad (2-15)$$

$$V_{out-E}(t) = \frac{\epsilon_0 A_{plate}}{C} E_z(t) \quad (2-16)$$

It is important to emphasize that ω_0 denotes the low-frequency roll-off in the case of the E-field sensor. For the MSE/TERA E-field sensors, the integrating capacitance typically has a value of 0.2 μF , and the load resistance, which corresponds to the input impedance of a high-impedance amplifier, is about 5 $\text{M}\Omega$. Hence, the E-field sensors provide an adequate approximation of the electric field waveform down to the frequency, f_0 .

$$f_0 = \frac{\omega_0}{2\pi} = \frac{1\text{s}^{-1}}{2\pi} \approx 0.2 \text{ Hz} \quad (2-17)$$

The implications of this frequency constraint are perhaps more apparent when viewed in terms of the decay time constant. This time constant is the inverse of ω_0 and is typically denoted by τ .

$$\tau = RC = \frac{1}{\omega_0} = 1 \text{ s} \quad (2-18)$$

The decay time constant has a simple physical interpretation when the electric field is a step-function [see *Jerauld*, 2003]. At time $t = \tau$, the output of the antenna is a factor of $1/e$ less

than it was at time $t = 0$. Therefore, the output of the antenna is only valid for periods of time that are relatively short compared to τ . This behavior is expected since the electric field flat-plate antenna is a high-pass filter in the frequency domain.

As with the dE/dt sensors, the output of the electric field sensors is usually modified by other components such as the PIC controller, high-impedance amplifier, and fiber-optic link. Therefore, a more complete expression for the output voltage of an electric field sensor is given in Equation 2-19. A diagram of the E-field measurement setup is shown in Figure 2-18.

$$V_{out-E}(t) = \frac{\epsilon_0 A_{plate}}{C} G_{PIC} G_{amp} G_{link} E_z(t) \quad (2-19)$$

Since the high-impedance amplifier is used to amplify the electric field signal by a factor of two ($G_{amp} = 2$), there is no need for the attenuation settings of the PIC controller ($G_{PIC} = 1$). As previously mentioned, the value of G_{link} is typically near unity and is obtained from the pre-storm and post-storm calibration waveforms. Using typical values provided above for the quantities in Equation 2-19 we obtain a nominal calibration factor of about $73 \text{ kV m}^{-1}/\text{V}$ for the electric field sensors.

2.5.2 Magnetic Field Measurements

The magnetic field antennas used in the MSE/TERA network are single-ended coaxial loop antennas having an area of 0.533 m^2 . The coaxial cable is placed inside of PVC pipe to maintain a rigid shape and protect the cable from the sun and rain. The inner conductor of the cable is the actual wire comprising the loop antenna. The outer conductor, which is soldered together at the bottom of the antenna and broken at the top, prevents current from being induced on the inner conductor by an external electric field. Each end of the antenna loop is terminated in the characteristic impedance of the cable (50Ω), with one of the terminating resistors corresponding to the input resistance of an active integrator. The output end of the loop is fed to

a female BNC feed-through connector mounted to the side of a Hoffman box located on the ground next to the antenna. Inside the box, the other end of the feed-through connector is connected, via a short length of 50 Ω coaxial cable, to the input of the active integrator that provides the 50 Ω termination resistance for the output end of the antenna. In order to eliminate ground loops, all electronic components were isolated from each other and the metal box by pieces of plastic and Styrofoam.

As shown in Tables 2-1, 2-2, and 2-3, the magnetic field antennas were located at Stations 4 and 9. Although the magnetic field sensors were originally constructed as orthogonal crossed-loop pairs (Figure 2-19), equipment availability, such as fiber-optic links and DSO channels, restricted the operation of the sensors to a single-loop configuration. The remainder of this section provides the primary results of the detailed analysis for a single-ended output coaxial-loop magnetic field antenna [e.g., *Jerauld, 2003*].

The loop antennas used in the MSE/TERA network measure the component of the magnetic field vector, \vec{B} , which is normal to the plane of the antenna loop. The vector \vec{B} is known as the magnetic induction or magnetic flux density. In a linear, homogenous, and isotropic medium, such as air, the magnetic induction, \vec{B} (units of Wb m⁻¹ or T), is related to the magnetic field intensity, \vec{H} (units of A m⁻¹), by the permeability of the medium, μ , as expressed in Equation 2-20. The value of μ for air is very close to that of free space, $\mu_0 = 4\pi \times 10^{-7} \approx 1.257 \times 10^{-6}$ H m⁻¹. Since \vec{B} and \vec{H} differ by only a constant, the term “magnetic field” is often used to refer to either \vec{B} or \vec{H}

$$\vec{B} = \mu\vec{H} \tag{2-20}$$

Figure 2-20 shows a diagram (A) and equivalent circuit (B) for a single-ended output loop antenna. As shown in Figure 2-20, each end of the cable is terminated in its characteristic

impedance, which is 50Ω . Because the antenna is single ended, the output voltage is measured across only one end of the cable. The 50Ω termination resistance at the output end of the cable takes the form of the input resistance of an active integrator. From Faraday's Law, a time-varying magnetic field, \vec{B} , with a component normal to the plane, B_{norm} , of a loop with area, A_{loop} , will induce a voltage, V_{loop} .

$$V_{loop}(t) = -A_{loop} \frac{d}{dt} B_{norm}(t) \quad (2-21)$$

As shown in Figure 2-20, $V_{loop}(t)$ corresponds to the electromotive source in the frequency-domain equivalent circuit. The source impedance is typically considered to be the resistance of the loop, R_{loop} , in series with the inductance of the loop, L_{loop} . Because the gain and bandwidth of the antenna are dependent on the total resistance of the loop antenna, it may be desirable to add an external resistance in-line with the inner conductor. Typically, this external resistance is inserted at the point where the outer conductor was broken, as shown in Figure 2-20. The output voltage, V_{out} , is measured across one of the 50Ω resistors. Frequency-domain techniques reveal that this loop antenna is a first-order low-pass filter with an upper cutoff frequency, ω_0 , which is expressed as

$$\omega_0 = \frac{R_{loop} + 100}{L_{loop}} \quad (2-22)$$

Since no external resistance was added to the loop of the MSE/TERA network antennas, R_{loop} is simply the inherent resistance of the inner conductor, which is virtually zero. L_{loop} was measured to be approximately $4 \mu\text{H}$. Therefore, the upper cutoff frequency of the loop antenna is $\omega_0 = 2.5 \times 10^7 \text{ s}^{-1}$ or $f_0 = 4 \text{ MHz}$. If no significant frequency content exists above the cutoff frequency, then the time-domain output voltage can be expressed as

$$V_{out}(t) = -\frac{A_{loop}}{2} \frac{100}{R_{loop} + 100} \frac{d}{dt} B_{norm}(t) \quad (2-23)$$

From Equation 2-23, the output voltage of the loop antenna is seen to be proportional to the derivative of the magnetic field and not the magnetic field itself. Hence, an active integrator is used to integrate the output of the loop antenna and generate a voltage, V_{out-B} , that is proportional to B_{norm} . The active integrator, which was designed by consulting engineer George Schnetzer, has a bandwidth of about 10 Hz to 5 MHz and introduces an integration constant, k_{int} , of approximately $2.5 \times 10^5 \text{ s}^{-1}$. Additionally, the output resistance of the active integrator and the in-line terminator at the input of the FO link, which are both 50Ω , result in a voltage division by a factor of two. The upper frequency limit of the active integrator, being greater than that of the loop antenna, does not affect the bandwidth of the magnetic field measurement. Actually, it is the anti-aliasing filter of the DSO, and not the loop antenna, that limits the upper frequency of the magnetic field measurement to 3 MHz. On the other hand, the non-ideal response of the active integrator, which can be viewed in the time domain as introducing a decay time constant, does limit the low-frequency response of the measurement. Interestingly, the active integrator necessarily has a non-ideal response; otherwise, even the smallest DC offset would cause the output the integrator to saturate. The decay time constant of the active integrator to the derivative of an input step function was measured to be approximately 15 ms and corresponds to a lower frequency limit, $f_0 \approx 10 \text{ Hz}$. Assuming that the frequency content of the magnetic field lies within the bandwidth of the measurement and accounting for the integrator, PIC controller, and FO link, the time-domain expression for the output voltage of the magnetic field measurement becomes

$$V_{out-B}(t) = -k_{int} \frac{A_{loop}}{4} \frac{100}{R_{loop} + 100} G_{PIC} G_{link} B_{norm}(t) \quad (2-24)$$

For the magnetic field measurements, the PIC controller sets an attenuation of -6 dB, so the quantity G_{PIC} has a value of 0.5. Using a nominal value of unity for G_{link} and the previously

mentioned values for the remaining quantities of Equation 2-24 results in a nominal calibration factor of $-60 \mu\text{T}/\text{V}$ for the magnetic field measurement. It is worth noting that the negative sign of the nominal calibration factor is somewhat arbitrary and results from the negative sign present in Faraday's Law. The polarity of the recorded waveform, however, is determined by the orientation of the lightning channel relative to the loop antenna. In other words, the same lightning channel located on opposite sides of the loop will result in waveforms of identical amplitude but opposite polarity. Finally, a diagram of the magnetic field setup is provided in Figure 2-21.

2.5.3 X-Ray Measurements

The MSE/TERA X-ray measurements are deployed in stand-alone metal enclosures known as TERA boxes. The design of the TERA measurements is illustrated in Figure 2-22. Each box is constructed something like a shoe box and consists of a bottom housing, which supports the X-ray sensors and the measurement electronics, and a lid that fits over the bottom housing with a 15 cm vertical overlap. The housing and the lid are both constructed of 0.32 cm (1/8") thick aluminum and are each welded on eight seams. The lid rests atop the bottom housing and is secured with a spring loaded drawer latch on each side of the box. A gasket is placed along the top rim of the bottom housing and mates with a lip inside of the lid to prevent the entry of light into the box. In addition, the inside of the box is painted black to absorb any light that may enter through the gasket. The TERA box is intended to provide a light-free environment for the scintillator and protect the measurement electronics from electromagnetic interference (EMI), while also allowing X rays with energies down to about 30 keV to enter from all directions.

The MSE/TERA network utilized two types of X-rays sensors between 2005 and 2007. The primary X-ray sensor used in the network was a 7.6 cm \times 7.6 cm cylindrical NaI(Tl)/Photomultiplier tube (PMT) detector manufactured by Saint Gobain (3M3 series). The

detector is a hermetically-sealed package consisting of a NaI scintillator that is optically coupled to a PMT. The scintillator is mounted in an aluminum container, and a mu-metal magnetic light shield is fitted over the PMT. The NaI/PMT detector is mounted on an Ortec photomultiplier tube base (model 296), which contains internal HV supplies and divider chains, allowing the sensitivity of the sensor to be adjusted. The entire unit (NaI/PMT detector and tube base) is then wrapped in black electrical tape and aluminum tape to ensure the device is light tight. The sensor is checked for light leaks with a bright strobe light before placing the detector inside the TERA box. The second type of X-ray sensor consists of a 36 cm × 25 cm × 1 cm plastic scintillator with a 5.08 cm diameter PMT attached to a light guide at the end of the scintillator. The unit is made light tight by wrapping it in black plastic. As noted earlier, the plastic scintillator has much less sensitivity to X rays (i.e., it has a larger calibration factor) but has a faster response time than the NaI scintillators.

Each TERA box is powered by a single 12 V battery and utilizes a 2006 PIC controller which is capable of supporting two measurements. The measurement electronics are mounted to an aluminum housing, known as the Field Replaceable Unit (FRU), inside the TERA box. The FRU can be removed from the box, and individual components, such as the PIC controller or FO transmitters, can be readily removed and exchanged. The anode output of each sensor is connected to the PIC controller and then to its corresponding FO transmitter via coaxial cables, as was shown in Figure 2-8. Unfortunately, the anode output of the PMT bases cannot supply enough current to drive a 50 Ω load; therefore, the output of the PIC controller is terminated with the high impedance of the FO transmitter, and the attenuation settings of the PIC controller cannot be used with these measurements. A short fiber-optic jumper connects the output of the

FO transmitter to a female ST connector mounted on the side of the TERA box, from which the signal is transmitted to Launch Control.

Although the TERA boxes are constructed to support two X-ray sensors, some of the boxes contain only one sensor due to equipment availability. Nevertheless, every TERA box contains one NaI/PMT detector in which the scintillator is unobscured by any additional attenuator. In this case, the X-ray sensor simply rests in a 0.32 cm thick lead tube which extends only from the base of the scintillator to below the PMT and tube base. This measurement is identified as the unshielded or unattenuated sensor (UPMT). In the boxes containing an additional NaI/PMT detector, the lead tube holding the second sensor is extended to 4.5 cm above the top of the scintillator and is covered with a cap of the same thickness. This measurement is identified as the shielded sensor (SPMT). A TERA box containing two NaI/PMT detectors is shown in Figure 2-23. The shielded measurement, which is essentially “blind” to X rays below 300 keV, is used in conjunction with the unshielded measurement to help determine the energy spectrum of the X-ray emissions. In 2007 two boxes were deployed in which the second sensor utilized a plastic scintillator (PPMT). Because the plastic scintillator detectors were much larger than the NaI detectors, the lids on these two TERA boxes were nearly twice as tall as the others. A TERA box with a plastic scintillator is illustrated in Figure 2-24. These sensors were deployed in order to get improved temporal resolution between the X rays and dE/dt radiation and potentially identify structure in the individual X-ray emissions. Tables 2-1 through 2-3 identify which type of X-ray sensors were deployed at each station during the different configurations of the third era.

As previously mentioned, the various x-ray measurements are responsive to different energy spectra, and the sensitivity of individual sensors can be changed by adjusting the HV

supply and the divider chains. Since the output voltage depends on the electronic settings and the attenuation effects of the aluminum housing and possibly a lead tube, an analytical expression is not useful for obtaining a calibration factor. Instead, each sensor is empirically calibrated using a radioactive source, typically Cs-137, which emits a known energy (662 keV) photon. The output voltage obtained in response to the known source is used to obtain the calibration factor for the sensor. During 2005 and 2006, the UPMT and SPMT sensors both had average calibration factors of about 3.5 MeV/ V. In 2007 the average calibration factors for the UPMT and SPMT sensors were about 5.3 MeV/ V and 11.5 MeV/ V, respectively. The PPMT sensors, being less sensitive than the NaI/PMT detectors, could not detect the radioactive source; hence an actual calibration factor was not be obtained for the PPMT sensors. The fact that the PPMT sensors could not be calibrated was not a critical hindrance, as their primary purpose was to provide enhanced temporal resolution of the X-ray emissions. Tables 2-1 through 2-3 indicate the typical amplitude ranges observed by the different sensors during different configurations of the MSE/TERA network. The same tables also contain the measured response times for the NaI and plastic detectors.

2.5.4 Optical Measurements

The two optical measurements of the MSE/TERA network are located at the northeast and southwest corners of the site and are designated the “Northeast Optical” (NEO) and “Southwest Optical” (SWO) measurements, respectively. Both sensors are placed on elevated structures and are angled to view towards the center of the site. These measurements are responsive to bright lightning processes, particularly to return strokes, at low altitudes and play the critical role of producing a trigger signal for the data acquisition (see Section 2.6). These sensors are not absolutely calibrated to any physical quantity, but even the uncalibrated but linear waveforms

possess intrinsic scientific value. Therefore, the full waveforms are recorded on a Yokogawa DL750 before being converted into a logic-level pulse by the trigger system.

The circuit for the optical sensor, shown in Figure 2-25, is a reversed biased EG&G C30807E N-type silicon PIN photodiode in series with a 1 k Ω resistor. The series combination of the photodiode and resistor is in parallel with a 45 V battery and a capacitor that protects the sensitive photodiode from voltage spikes. The photodiode has an active area of 1 mm, a dark current of 1 nA, a response time of 3 ns, and is sensitive to wavelengths between 400 and 1100 nm. Any light incident on the lens of the photodiode will generate electron-hole pairs in the depletion region of the device, resulting in a current through the circuit. This current produces the optical signal in the form of a voltage across the 1 k Ω resistor. The output of the optical circuit is fed into an amplifier with an input impedance of 1 M Ω and a gain of ten before it is passed to the PIC controller. Because some of the observed light signals were relatively small (particularly for subsequent strokes), no attenuation was applied by the PIC controller, and the 50 Ω terminator was removed from the input of the FO transmitter in order to increase the gain by another factor of two. A diagram of the optical measurement is shown in Figure 2-26.

The optical circuit was mounted against the inside of a Hoffman box with a hole drilled in the box just large enough for the lens of the photodiode to project through. A piece of 10 cm (4 inch) diameter PVP pipe, approximately 7.5 cm in length, was mounted on the outside of the Hoffman box centered on the photodiode. The inside of the PVC pipe and the circular portion of the Hoffman box surrounding the photodiode were painted black. The open end of the pipe was sealed with a circular piece of glass and fitted with a cover milled from copper-coated fiberglass, the material typically used for milling circuit boards. The cover was painted black and mounted to the glass with water-tight silicon. A 4 mm window, which was cut with a milling machine,

ran horizontally across the cover. This window provided elevation and azimuth views of approximately 65 m and 1.2 km, respectively, at a distance of 1 km. A photograph of the optical measurement assembly is shown in Figure 2-27.

2.5.5 Channel-Base Current Measurements

As previously mentioned, all of the rocket-launching platforms at the ICLRT are equipped with a measurement of the lightning channel-base current. During the 2005 season, rocket-triggering operations were performed from the tower launcher and mobile launcher (position indicated in Figure 1-4). No rocket launches were performed during the 2006 season, and all triggering operations were performed from the tower in 2007. Directly below each of these launchers is a 0.61 m \times 0.61 m (2 ft \times 2 ft) Hoffman box that is electrically connected to the launcher. The current sensor itself, a non-inductive resistor (also known as a shunt), is bolted to the bottom of Hoffman box as shown in Figure 2-28. The BNC output of the shunt faces upward inside the box, while the lug of the shunt outside the box is connected via a length of copper-tinned shield braid to the strike point. Hence, the current path is through the launcher to the Hoffman box; from the shunt housing, which is in contact with the box, to the lug; and from the lug to the strike point.

The output voltage produced at the BNC terminal is the voltage appearing between the shunt housing and the lug, and it is directly proportional to the current through the shunt, as expected from Ohm's Law. As seen in Figure 2-28, a BNC T connector (either T or F configuration) is placed directly on the shunt output and splits the output into two parallel branches. Each of these branches consists of a short length of coaxial cable and a 50 Ω series resistor that is connected to a BNC bulkhead feed-through connector mounted to one of the aluminum electronics boxes inside of the Hoffman box. These boxes contain the electronics for two measurements of the channel-base current on different amplitude scales. The primary

distinction between the two measurement setups is the PIC controller attenuation settings. The purpose of using two measurements is to achieve greater dynamic range than that attainable with a single measurement, allowing the current to be measured from a few tens of amperes to tens of kiloamperes. The measurement using less attenuation is referred to as the “low current” measurement and is designed to sense currents from some tens of amperes to several kiloamperes, typically associated with long duration currents (tens to hundreds of milliseconds) of the initial stage of classical-rocket triggered lightning, as well as continuing currents following return strokes. The measurement using greater attenuation is referred to as the “high current” measurement and is used to sense currents up to some tens of kiloamperes, typically associated with lightning return strokes.

The electronics boxes themselves are mounted to a Plexiglas backing with nylon bolts and the entire structure is held in place with four metal mounting bolts from the back of the Hoffman box. The Plexiglas serves to electrically isolate the electronics boxes from the Hoffman box, so that the only electrical connection between the electronics boxes and the shunt (and hence the Hoffman box it is mounted on) are the shields of the short coaxial cables. It is very important that the electronics boxes not make contact with the Hoffman box at any other point because when large currents are flowing on the outer box (during a trigger) the potential of different points on the inner box may not be uniform (due to the effective resistance and inductance of the box material caused by the skin effect) and hence a ground loop may result, causing a current to flow in the shields of the coaxial cables, which would distort the waveforms.

Inside the electronics boxes, the BNC bulkhead feed-through connector is connected to the PIC controller input with a short length of coaxial cable. The output of the PIC controller is connected to the input of the FO transmitter via a coaxial cable with a 50 Ω in-line terminator

placed at the end. The output signal is finally transmitted to Launch Control over a glass fiber-optic cable. In 2005 the electronics boxes at the tower and mobile launchers both contained original PIC controllers (2001 version) that were controlled by the control computer via plastic fiber links from an RF PIC near the launcher. In 2007 only one of the boxes contained an original PIC controller, and it operated in slave mode to a 2006 PIC controller located in the other electronics box. It is noted that although the 2006 PIC controller supports two channels, it cannot be used to control both current measurements. The problem is that both channels of the PIC controller share a common ground plane, and both channels connect to the output of a single sensor. Hence, the shields of the coaxial cables going from the shunt to the PIC controller form a closed loop and become susceptible to induced currents. Figure 2-29 shows the inside of the electronics boxes for the 2007 current measurement setup.

The diagram in Figure 2-30 illustrates the general setup of the channel-base current measurement. The time-domain equivalent circuit for this configuration is shown in Figure 2-31. The quantities $I_s(t)$ and R_s constitute the current source in the equivalent circuit and represent the current flowing through the shunt and the resistance of the shunt, respectively. The shunt is in parallel with two resistive branches, with each branch comprised of a $50\ \Omega$ resistor in series with a $50\ \Omega$ in-line attenuator in series with another $50\ \Omega$ resistor. The coaxial cables have no effect on the equivalent circuit since they are terminated in their characteristic impedance. The $50\ \Omega$ in-line attenuators are the equivalent circuit of the PIC controller and their only effect is to attenuate the input signal by the factor of G_{PIC} . If the circuit is broken, the impedance looking into either end of the attenuator will be $50\ \Omega$ (hence the term “ $50\ \Omega$ attenuator”); therefore, the total resistance of each branch is $100\ \Omega$.

The voltage across the shunt and across each branch, $V_s(t)$, is determined by both the resistance of the shunt and the load.

$$V_s(t) = (R_s \parallel 100 \Omega \parallel 100 \Omega) I_s(t) \quad (2-25)$$

Since the resistance of the shunt is on the order of milliohms, the expression for $V_s(t)$ simplifies to

$$V_s(t) \approx R_s I_s(t) \quad (2-26)$$

Taking into account the attenuation of the PIC controller, the voltage division between the two 50Ω resistors, and the affects of the fiber-optic link, the output voltage for the current measurement can be expressed as

$$V_{out-I}(t) = \frac{1}{2} R_s G_{PIC} G_{link} I_s(t) \quad (2-27)$$

Equation 2-27 is valid for the frequencies in the passband region determined by either the shunt or the digital oscilloscope (see Tables 2-1 through 2-3). Assuming a nominal gain of unity for the fiber-optic link, the nominal calibration factor for the current measurement is given by

$$\left(\frac{I_s(t)}{V_{out-I}(t)} \right)_{nom} = \frac{2}{R_s G_{PIC}} \quad (2-28)$$

A summary of the channel-base current measurements during the third era of the MSE/TERA network is given in Table 2-6.

2.6 Trigger and GPS Time-Stamping Systems

A significant concern for the MSE/TERA network as well as other experiments at the ICLRT is the ability to provide a reliable trigger signal to all of the devices that record the lightning data. Although each digital oscilloscope is capable of triggering directly from one or more waveform channels, the measurements on a particular DSO do not always provide a reliable indicator of nearby lightning. Hence, it is often necessary to distribute those few measurements which can indicate a nearby lightning strike to the multiple digitizers, typically as

an external input to the digitizers. As was discussed in Section 2-4, the threshold and coupling are selectable for the external trigger input on the LeCroy digitizers, but the Yokogawa digitizers have only a TTL-level external trigger input. Therefore, the trigger system must account for these different specifications. Further, it is also desirable to produce an accurate time stamp with each trigger so that data can be properly documented and potentially correlated with other systems, such as the NLDN. This section describes the equipment used to implement the trigger and time-stamping systems.

Two sources have traditionally provided the trigger signal at the ICLRT. The first source is derived from the optical sensors placed at the northeast and southwest corners of the site. A circuit located in Launch Control (see Figure 2-32) is used to “AND” the two optical signals, meaning that both optical measurements must simultaneously exceed a trigger threshold (≈ 100 mV) for the circuit to output a logic-level (≈ 5 V into high impedance) pulse having a duration of about 20 μ s. This triggering method is responsive to all lightning within or near the network, but it is particularly useful for natural lightning. The second trigger source is used only with rocket-triggered lightning and is derived directly from the channel-base current. This triggering method requires the high current measurement (recorded on a LeCroy DSO) to exceed some threshold (typically between 5 and 7 kA) and the digitizer on which the current is recorded to produce a trigger signal from its rear output. The trigger pulse generated by the digitizer has a peak voltage into high impedance of about 5 V and last as long as the remainder of the memory segment, which is approximately 0.5 ms for a LeCroy oscilloscope set to 1 ms segments and 50% pretrigger.

Even with reliable sources providing the trigger signal, there is still a task in distributing the trigger to other devices. In theory the signal from each trigger source can be daisy-chained to

multiple devices; however, this approach can be logistically confusing and inflexible and also results in the digitizers triggering at different times due to non-uniform trigger delays. In addition, neither of the two trigger sources is capable of driving a 50 Ω load, yet almost every coaxial cable at the ICLRT is terminated in 50 Ω , the characteristic impedance of the cables, in order to eliminate reflections and minimize the effects of noise pickup. To address these issues, a pair of trigger buffers was constructed to distribute the signals from the trigger sources. The basis for each buffer circuit is the Texas Instruments 74SN25244 high-current TTL buffer, providing 8 TTL-level (≈ 2 V) outputs, each capable of driving a 50 Ω load, from a single input. Hence, eight devices, each terminated in 50 Ω , can be triggered from a single trigger source supplied to each buffer circuit. As long as proper termination guidelines are observed, additional devices can be triggered by daisy-chaining multiple devices from a single buffer output; however, differences in trigger times need to be accounted for in any time critical analysis.

The two buffer circuits were placed in a common metal enclosure (see Figure 2-32) and labeled “Channel 1” and “Channel 2,” with the two inputs located on the rear and the pair of eight BNC outputs located on the front. Historically, Channel 1 has been used to distribute the channel-base current trigger and Channel 2 has been used to distribute the optical trigger, although other configurations are certainly possible. For instance, it is possible to create a 16-channel buffer by connecting the two inputs to a single source. For the LeCroy digitizers triggered from the buffer, the external trigger input is set to +1 V threshold, positive edge, DC-coupled, and 50 Ω termination. For the Yokogawa digitizers, the buffer output was simply connected to the external trigger input with an in-line 50 Ω terminator placed at the end of the cable.

To provide additional flexibility to the trigger system, another circuit was constructed that is essentially identical to the buffer circuit, except that an OR gate precedes the buffer input; hence, this device, which is known as the “OR buffer,” has two inputs. If the two inputs correspond to the current and optical trigger sources, this circuit provides a buffered trigger output for both natural and triggered lightning. Like the other buffer circuits, the OR buffer (see Figure 2-32) has eight outputs that are each capable of driving a 50 Ω load.

A direct extension of the trigger system is the GPS time-stamping system, which accurately documents the time for each data acquisition. Because the time stamp is needed for both natural and triggered lightning, the trigger for the time-stamping system is always provided by the OR buffer. One output from the OR buffer is fed into a Datum (now called Symmetricom) bc627AT timing card housed in the PC that displays the NLDN data. The timing card is synchronized to GPS time with a special antenna mounted to the roof on the south end of Launch Control (Figure 2-33). When a trigger is detected, the timing card, which is designed to account for internal latency, latches the time stamp internally. A software program written in C++ then accesses the card, retrieves the time, and writes the time to a text file. Although the software is adjustable, the program typically waits a few seconds for subsequent trigger events. If additional triggers occur during this time interval, all subsequent times are written to the same text file as the original trigger. One limitation incurred by the software, however, is a minimum re-arming time of a few milliseconds, though this is shorter than the typical lightning inter-stroke interval. The accuracy for each time stamp is estimated to be approximately 1 microsecond.

Like the rest of the MSE/TERA network, the trigger and time-stamping systems are usually reconfigured at the start of each storm season. In 2005 nearly all the MSE/TERA digitizers were triggered from the optical source buffer circuit (Channel 2). Two of the

MSE/TERA digitizers were triggered directly from the channel-base current measurement, and one of those digitizers provided the trigger source for the current buffer circuit (Channel 1). Although several digitizers were triggered from the current-source buffer circuit, none of them belonged to the MSE/TERA network. In 2006 there was no attempt to produce rocket-triggered lightning; hence, all devices at the ICLRT were triggered by the optical source. In 2007 the trigger system was reconfigured so that every device, except the digitizers that were triggered directly from the channel-base current measurement, could be triggered from both trigger sources. Diagrams for the 2005, 2006, and 2007 trigger configurations are shown in Figures 2-34, 2-35, and 2-36, respectively.

2.7 Video and Camera Systems

Another important task performed at the ICLRT is the acquisition of video and photographic records for onsite lightning events. This task is approached differently for natural and triggered lightning. For rocket-triggered lightning, the time and location of the lightning flash are known; hence, obtaining optical records for these flashes is relatively easy. Typically, the launcher platform is viewed from multiple positions with both Sony DCR-TRV900 Mini-DV camcorders and Nikon 35 mm SLR still cameras. When a storm approaches, staff members turn on the camcorders and begin recording. If storm conditions last longer than the tape length (90 minutes), the tapes are either rewound or replaced (depending on whether a flash was previously recorded) before recording is resumed. If a flash is recorded, the video is transferred from a DV tape deck to a PC using Adobe Premiere software and an IEEE-1394 (commercially known as Firewire) interface. The 35 mm SLR cameras are each equipped with a zoom lens, focused to infinity, loaded with 100-speed film, and fitted with one or more 72 mm 4X neutral density (ND) filters. All of the still cameras are set to bulb mode (meaning that the shutter stays open as long as the contact is closed), and the contact closure of each camera is connected to a device known

as a “camera PIC.” Like the original PIC controller (see Section 2.2.1), the camera PIC interfaces with the control computer via an RF PIC. When a rocket is fired, the control computer sends a command to each camera PIC and the camera contact is closed for six seconds, resulting in a six-second exposure. The exposure time and camera settings are such that the initial stage and all of the return strokes can be imaged without over-exposing the film.

Unfortunately, obtaining optical images for natural lightning is not quite as straightforward. Although cameras can certainly be placed to provide adequate coverage of the network, the unpredictable occurrence of natural lightning poses problems for the types of cameras used at the ICLRT to image triggered lightning. For example, setting a prolonged exposure time for the still cameras may overexpose the film or result in multiple flashes being imaged in the same picture, and the stand-alone digital video cameras are limited by both battery run-time and tape length. Further, these devices are not particularly amenable to automation and neither possesses pretrigger capability. Hence, a different approach, which utilizes continuous video feeds and a centralized, programmable recording device, is used to record natural lightning.

The video system used to record natural lightning at the ICLRT, referred to hereafter as the MSE/TERA video system, was initially constructed in 2001. It was comprised of four Cohu 1300 Series CCD cameras that were placed in each of the Instrument Station (IS) buildings seen in Figure 2-1. The placement of the cameras in these buildings allowed the 12 V camera batteries to be continually charged while also providing fairly adequate coverage of the site. The video signal from each camera was transmitted back to Launch Control over 62.5/125 μm fiber by an Opticomm MMV-110 fiber-optic video link. In Launch Control the four video signals were combined into a single frame (providing a convenient view of the entire ICLRT site at a

glance) by quad-view security monitor, time stamped, and ultimately recorded by a Sony SR2000 TIVO digital video recorder (DVR). The DVR was equipped with two 80 GB hard disk, providing approximately 36 hours of record time, and was set to continuous loop recording. When an event was recorded, the device could be stopped, and the video could be extracted. Unfortunately, this method of recording proved impractical during the offseason, when the site was largely unattended; so the DVR was equipped with an after-market network controller in 2004, allowing the control computer to automate the operation of the DVR and limit recording to periods in which the network was armed.

Due to major reconstruction in Launch Control as well as a later attempt to upgrade the DVR, the MSE/TERA video system was not operational for all of the 2005 and part of the 2006 storm seasons. The intended replacement for the TIVO DVR was an E-400-DVR purchased from PolarisUSA. The specifications for this device indicated that the DVR could be externally triggered to acquire short segments of video with several seconds of pretrigger, which would greatly reduce the size of the video files and also eliminate the need to search large files for a specific event. Further, the new DVR could record up to four video signals as well as generate the quad display; hence, this device should have eliminated the need for the large security monitor and improved the recording resolution while eliminating the need for any additional recording devices. Unfortunately, the pretrigger capability of DVR did not perform as expected, and the extraction of video files from the DVR proved very difficult. Ultimately, the E-400-DVR did eliminate the need for the large security monitor, but the video was not recorded on this new DVR. The output of the E-400-DVR was fed into a time-stamp unit, which was manually set and typically within several seconds of GPS time, before being sent to the input of the TIVO DVR for recording. As was done in 2004, the operation of the TIVO DVR was automated by the

control computer. Figure 2-37 shows the components of the MSE/TERA video system after it was reestablished in 2006. The orientation of each camera is given in Table 2-7 and is also illustrated in Figure 2-1 by the arrows emanating from the IS buildings. The angles provided in Table 2-7 represent the bearing, where due north corresponds to 0° and due east corresponds to 90°, from each camera to a PVC marker that was placed fairly central to the 90° view angle of the camera. Finally, an image of a lightning obtained by the video system is shown in Figure 2-38. It should be noted that the four video signals in the recorded video are not generator locked (gen-locked), meaning that the horizontal and vertical timing of the individual video signals are not synchronized to a single reference signal. Although an attempt was made in 2002 to gen-lock the cameras, it was unclear if it actually worked and was hence discontinued. The primary effect from this lack of synchronization is that a single event captured by all four cameras might not show up in all four quadrants of a single frame.

The DVR digitizes the video at 30 frames per second with 720×480 resolution using MPEG-2 compression. The video is interlaced, meaning that each frame is composed of two fields, with the odd field containing the odd-numbered horizontal lines of the frame and the even field containing the even lines. The fields have half the vertical resolution of a frame (360 lines versus 720) and are recorded/displayed at 60 fields per second, yielding an effective frame rate of 30 frames per second. Video is extracted from the DVR either by directly copying the MPEG files over an Ethernet connection or by connecting the analog output of the DVR to a JVC Mini DV recorder/player and re-digitizing the video over a Firewire interface. Although the first method, which does not include an analog stage, is theoretically superior to the latter, there is little difference in the two methods due to the relatively poor quality of the recorded video and the high quality of the JVC unit. Further, the DVR was not designed for direct file transfer, and

this task was only accomplished through 3rd party software which was often unreliable. Once extracted, the video can be manipulated with a variety of software packages. For instance, the video frames can be separated into even and odd fields, yielding higher temporal resolution at the expense of vertical resolution.

In general, the MSE/TERA video system can provide information such as the strike location, channel geometry, and stroke multiplicity for a lightning flash. However, the usefulness of the video is often limited by the reduced resolution, relatively poor temporal resolution (compared to the time scale of lightning processes), effects of rain, and the lack of synchronization between the different cameras. As a result, some flashes appear only as a bright blob or sometimes as a point of light near the ground, and there is sometimes ambiguity between the strokes of a flash due to lack of synchronization. The effects of these limitations are often compounded when multiple channel termination points are present, which occasionally occurs with natural lightning. Nevertheless, the video provides a rough estimate of the strike location, which can be compared with locations determined by other methods, as well as an indication to whether a flash had multiple strike points. Interstroke intervals observed in the field records can usually be correlated with luminous events in the video record, at least up to the video field resolution of 16.7 ms.

2.8 Measurement Locations and Time Delays

The locations of measurement sensors and the time delays associated with signal transmission from the sensor to the DSO have long played a critical role in the analyses of lightning data obtained with the MSE network. The locations have been used to calculate the distance of sensors from the lightning strike point, allowing waveforms to be characterized by range, and the time delays have been used to align features in different waveforms. More importantly, these quantities are critical for TOA analysis, as the arrival time (the time an event

is recorded for each station) depends on both the propagation time from the source to the sensor and the transit time from the sensor to the digitizer located in Launch Control. Indeed, an effort to minimize the errors in the TOA solutions provided the motivation to obtain more accurate measurements for these quantities than had previously been obtained. The locations and time delays, as well as the methods used to obtain them, are discussed in this section.

Locations for the MSE stations have been surveyed several times since 1999 with Global Positioning System (GPS) receivers. Initially, this was done with a differential GPS (DGPS) receiver which, in addition to the satellite navigation signals, received correction signals from a ground-based reference station, providing accuracy within several meters. The Wide Area Augmentation System (WAAS) was later developed as an alternative to DGPS, differing from DGPS in that ground-based stations relay corrections to an enabled receiver through special WAAS satellites in orbit. The WAAS system theoretically provides location accuracy to better than 3 m 95% of the time. A WAAS-enabled Garmin eTrex Venture GPS receiver was used to perform additional surveys of the MSE stations and other site landmarks in 2004 and 2005. Of course, both the DGPS and WAAS receivers determine locations in terms of latitude and longitude which are expressed in decimal degrees or degrees-minutes-seconds format, neither format being particularly convenient for linear measurements. Fortunately, the U.S. National Geodetic Survey (NGS) developed the State Plane Coordinate System (SPCS), in which GPS coordinates are represented in a Cartesian coordinate system. Once the coordinates are converted, distances can be easily calculated using simple Euclidean geometry. The SPCS divides each state into as many as five zones, with zone boundaries typically following county lines and no zone occupying more than a single state. Each zone is then projected onto a planar surface, with the projection method being dependent on the geometry of each zone. Multiple

zones are used in order to minimize the distortions necessarily involved with projecting an ellipsoid surface (the Earth is an oblate spheroid) onto a planar surface. Each zone has an independent set of coordinates, with the origin typically located southwest of the zone such that all points within the zone have positive coordinates. X distances run east-west and are typically called “eastings” because distances are measured east of the origin. Y distances run north-south and are referred to as “northings” because distances are measured north of the origin. The maximum linear error of the SPCS is specified to be 1 in 10,000, meaning a 10,000 meter line measured in state plane coordinates may be in error by as much as 1 meter. Unfortunately, the accuracy of the SPCS is only as good as the device (e.g., GPS receiver) that provides the original coordinates (the latitude and longitude that are converted into SPCS).

Latitude and longitude coordinates obtained for a station, site landmark, or even a lightning stroke (provided by systems such as the NLDN) can be converted to SPCs via the utility on the website <http://www.ngs.noaa.gov/TOOLS/spc.html> provided by the NGS. This utility can generate SPCs based on two different geodetic reference systems; the coordinates obtained during the ICLRT surveys have always been converted to SPCs based on the North American Datum of 1983 (NAD 83). Unfortunately, the position of the ICLRT, in the northwest region of the “Florida East” zone, resulted in SPC values that were very large relative to the size of the site. More manageable coordinate values, denoted here as the “Camp Blanding Coordinates” (CBC), were obtained by adjusting the coordinates to correspond with an origin located approximately at the southeast corner of the Office Trailer (Figure 2-1). The Camp Blanding coordinates are obtained by subtracting 100003.674 m and 622156.976 m from the east (X) and north (Y) SPC values, respectively. A summary of the 2005 survey in CBC is provided in Table 2-8. Note that only one location was measured at each station in the 2005 survey. At that time,

each numbered station contained at least a one flat-plate antenna; hence, the GPS receiver was placed at the center of the circular plate at each station. If a station contained more than one flat-plate antenna, the E-field measurement was used.

In 2006 a survey of the site was conducted by certified Surveyor and Mapper for the State of Florida, David Thomas. The primary intent of this survey was to accurately determine the relative positioning (plan-view coordinates as well as altitude) between the sensors of the TOA network; additionally, positions were also determined for several site landmarks and all the other MSE/TERA measurements operating at that time. An Electronic Total Station Transverse (TOPCONGTS-4B) was used to turn an angle and distance to each measurement, and a surveyor level (WILDNA2) was used to determine the relative elevation between measurements. Over short distances, such as the dimensions of the ICLRT, this equipment can determine a position in any coordinate direction to within 1 cm. However, this accuracy is unnecessary due to the fact that some sensors, such as the flat-plate antennas, have relatively large dimensions compared to this resolution. Further, the X-ray detectors were not measured individually; rather, a single measurement was made to the top center of each TERA box containing the detectors. A correction for the lid's height above the sensors (0.186 m) was easily included, but some uncorrected error remained in the plan-view directions. Hence, the locations determined in this survey are typically considered accurate to within 20 cm in any coordinate direction. Of course, the survey itself only provides the relative positioning of the network measurements, essentially an accurate map that can be oriented in any direction in the plane. To generate actual coordinates for the map, a point and bearing must be selected. In order to provide some correlation with GPS coordinates, the position of the Station 5 E-field measurement in the 2005 CBC was used as the reference point, and a due east bearing was determined from the access

road bordering the north edge of the site. The results from the 2006 survey (CBC values) are summarized in Table 2-9. These coordinates, which are very similar to the 2005 survey, are the values actually used in the TOA calculations to be discussed in subsequent chapters. Since the measurement locations were not altered between 2005 and 2007, the coordinates in Table 2-9 are also accurate for the same measurements in 2007 and for the measurements that existed in 2005. However, the list does not include the measurements that were added in 2007. Since these measurements were not part of the TOA network, only a single location was obtained with the WAAS-enabled receiver at each station. The locations for these stations are summarized in Table 2-10.

The signal transit time delay associated with each measurement (from the sensor to DSO) is another critical component in the analysis of lightning data. Two methods have traditionally been used to measure these delay times for the MSE/TERA measurements. Prior to 2005, the delays were always determined in an indirect and piecewise fashion. The delays could be viewed to consist of two parts: the delay of the electronics and the delay directly proportional to the fiber length. The electronic delay consists of any delay not resulting from the glass fiber, such as coaxial cables, measurement electronics, and fiber-optic electronics. The coaxial delay could be approximated from a knowledge of the cable length, and the delay from the measurement electronics could be measured in the laboratory. The delay associated with the fiber-optic electronics was usually determined from a few fiber-optic units using a specific setup. The delay times from these units were then averaged, and the resulting value was assumed to be the constant delay for that model. The glass-fiber delay was determined with an Agilent E6000C Optical Time-Domain Reflectometer (OTDR). The OTDR, which also determines the length of the fiber, actually measures the transit time for light pulse injected at one end of the fiber to be

reflected from the other end back to the light source. The delay of the fiber is one half of the round-trip delay. The overall delay of the measurement is the summation of the fiber delay and all components of the electronic delay.

In 2005, a new system was designed and built by Ph.D. student Rob Olsen III to determine directly the end-to-end delay for individual measurements. Central to this delay measuring system is a special test link which runs from Launch Control to the sensor in the field. The test link is comprised of a pair of Infineon fiber-optic transceivers connected by a 1 km length of single-mode fiber with LC connectors. In Launch Control, the output of a pulse generator is monitored by an oscilloscope before being fed into one of the FO transceivers (acting as the FO transmitter) of the test link, which injects the signal into the single-mode fiber running to the measurement in the field. At the measurement, the other FO transceiver (acting as the FO receiver) of the test link injects the signal into the measurement as close to the sensor as possible. The signal is then transmitted through the measurement's electronics and FO link back to oscilloscope input in Launch Control, where the round-trip delay is measured. The delay for just the test link, which was previously measured, is then subtracted from the round-trip delay. The difference is the transit time delay of the measurement. The obvious benefit of this system is an unambiguous method for determining the delay of each measurement to within about 2 ns.

In 2005 the delay for each measurement was obtained with this system, including multiple delays for those measurements recorded on multiple oscilloscope channels. Unfortunately, the single-mode fiber used with the delay system is unshielded and particularly fragile. Hence, it is extremely tedious to roll the fiber out to each station. Indeed, many of the delays measured in 2005 were acquired simply because the fiber was already deployed at that station and there was a potential benefit in obtaining a precise delay time. After using these delays in the data analysis,

however, it was obvious that the precision of this system was unnecessarily accurate for many of the measurements, particularly those recorded on the Yokogawa DSOs. Therefore, this system was subsequently used only with the TOA measurements, which require very accurate time delay measurements. Nevertheless, the time delays obtained in 2005 remain very accurate for many measurements in the network to this day. Typically, the time delay for each TOA measurement was determined at the start of each storm season. Of course, various factors, which were usually associated with the need to maintain and repair equipment, could cause the time delay values to change, so the spreadsheet containing the time delays was maintained as a running file in each storm day directory (see Chapter 3). Basically, any time that the time delay associated with a TOA measurement was suspected to have changed, a new measurement for the time delay was made and the spreadsheet file was updated. Because it is unrealistic to present the time delays for all the measurements to each oscilloscope channel for every storm day, it is simply noted that the time delay files exist. However, the time delays for the TOA measurements are particularly important and were used for much of the analysis in following chapters, so a list of time delays for the TOA measurements on 2 June 2006 is presented in Table 2-11 as an example.

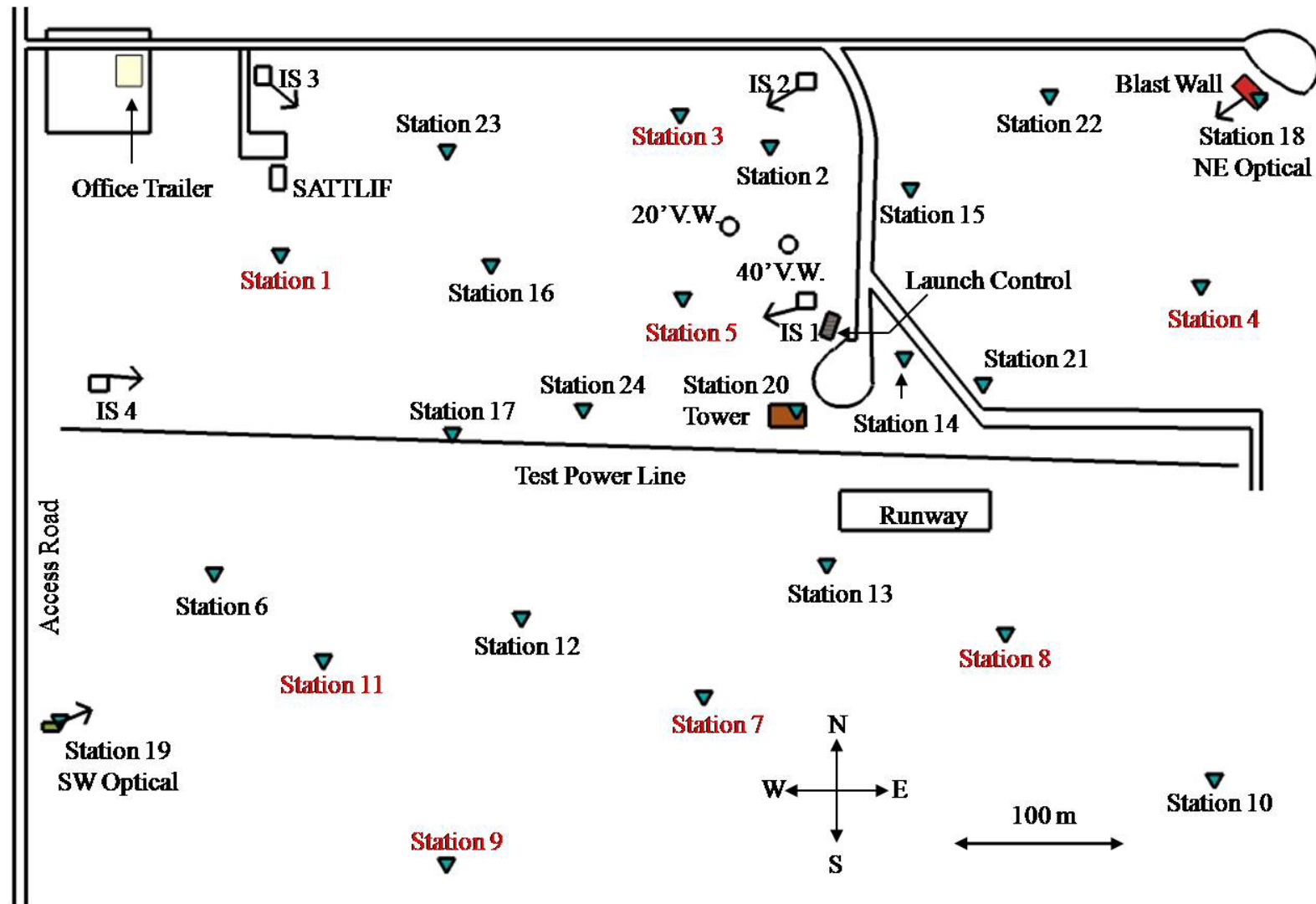


Figure 2-1. Sketch of the MSE/TERA network as it existed in 2007. The locations of the stations and site landmarks are drawn approximately to scale. The locations for the TOA sensors are identified by the red text labels.

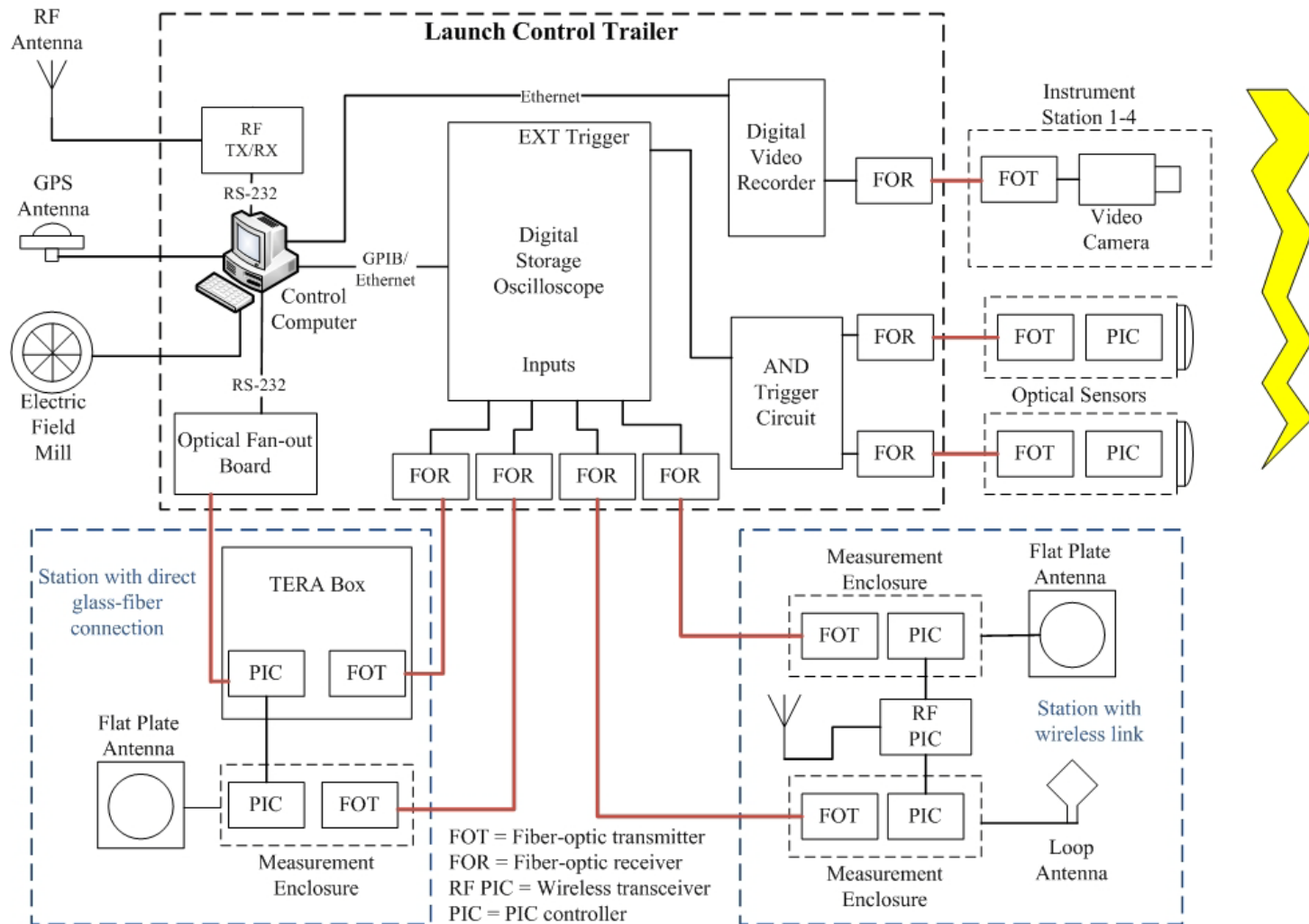


Figure 2-2. Diagram illustrating the operation of the MSE network. Prior 2006, all stations communicated with the control computer via RF PIC controllers. A simple example of such a station is illustrated in the box outlined with a blue-dotted line at the bottom right of the figure. Following the 2006 network expansion, most stations utilized a direct glass-fiber link. A simple example is illustrated in the blue-dotted box at the bottom left of the figure.

Table 2-1. List of the MSE/TERA measurements and their acquisition settings for the 2005 configuration.

Sensor	DSO model	Stations	Amplitude range	Sampling rate	Record length	Bandwidth
E-field	Yokogawa DL750	2, 4, 5, 6, 9, 10	± 85 kV m ⁻¹	10 MHz	2 s	0.2 Hz ^a -3 MHz ^b
B-field	Yokogawa DL750	4, 9	± 70 μ T	10 MHz	2 s	10 Hz ^c -3 MHz ^b
TOA dE/dt	LeCroy LT374	1, 4, 8, 9	± 30 kV m ⁻¹ μ s ⁻¹	200 MHz	10 segments, 2 ms each	DC-20 MHz ^b
	LeCroy LT344		± 10 kV m ⁻¹ μ s ⁻¹	250 MHz	2 segments, 2 ms each	DC-25 MHz ^b
TOA UMPT	LeCroy LT374	1, 4, 8, 9	4 MeV	200 MHz	10 segments, 2 ms each	See note ^d
UMPT	Yokogawa DL750	1, 2, 4, 5, 6, 8, 9, NEO, SWO, Tower	4 MeV	10 MHz	2 s	See note ^d
SMPT	Yokogawa DL750	1, 2, 4, 5, 6, 8, 9, NEO, SWO, Tower	4 MeV	10 MHz	2 s	See note ^d
Optical	Yokogawa DL750	NEO, SWO	+2 V	10 MHz	2 s	DC-1 MHz ^e
Base Current (Mobile)	LeCroy LT344	Mobile	-45 to +10 kA ^f	100 MHz	10 segments, 1 ms each	DC-25 MHz ^b
	Yokogawa DL716		± 60 kA ^f	10 MHz	1.6 s or 800 ms	DC-4 MHz ^b
Base Current (Tower)	LeCroy LT344	Tower	-45 to +10 kA ^f	100 MHz	10 segments, 1 ms each	DC-5 MHz ^g
	Yokogawa DL716		± 60 kA ^f	10 MHz	1.6 s or 800 ms	DC-4 MHz ^b

a) Limited by the decay time constant of the integrating circuit. b) Limited by the digitizer. c) Limited by the active integrator. d) Response of X-ray detectors is usually specified in terms of the rise and fall times for a single x-ray. For the NaI/PMT detectors these are approximately 0.17 μ s and 0.90 μ s, respectively. e) Limited by preamplifier. f) Sign indicates the polarity of charge lowered to ground. g) Limited by a low-pass filter placed on the output of the Isobe fiber-optic receiver.

Table 2-2. List of MSE/TERA measurements and acquisition settings for the 2006 configuration.

Sensor	DSO model	Stations	Amplitude range	Sampling rate	Record length	Bandwidth
E-field	Yokogawa DL750	2, 4, 5, 6, 9, 10	$\pm 85 \text{ kV m}^{-1}$	10 MHz	2 s	$0.2 \text{ Hz}^{\text{a}}\text{-}3 \text{ MHz}^{\text{b}}$
B-field	Yokogawa DL750	4, 9	$\pm 70 \text{ }\mu\text{T}$	10 MHz	2 s	$10 \text{ Hz}^{\text{c}}\text{-}3 \text{ MHz}^{\text{b}}$
TOA dE/dt	LeCroy LT374	1, 3, 4, 5, 7, 8, 9, 11	$\pm 30 \text{ kV m}^{-1} \text{ }\mu\text{s}^{-1}$	250 MHz	8 segments, 2 ms each	DC-20 MHz ^b
TOA UMPT	LeCroy LT344	1, 3, 4, 5, 7, 8, 9, 11	4 MeV	250 MHz	2 segments, 2 ms each	See note ^d
UMPT	Yokogawa DL750	1-20	4 MeV	10 MHz	2 s	See note ^d
SPMT	Yokogawa DL750	1-10, 18, 19, 20	4 MeV	10 MHz	2 s	See note ^d
Optical	Yokogawa DL750	18, 19	+2 V	10 MHz	2 s	DC-1 MHz ^e

a) Limited by the decay time constant of the integrating circuit. b) Limited by the digitizer. c) Limited by the active integrator. d) Response of X-ray detectors is usually specified in terms of the rise and fall times for a single x-ray. For the NaI/PMT detectors these are approximately $0.17 \text{ }\mu\text{s}$ and $0.90 \text{ }\mu\text{s}$, respectively. e) Limited by preamplifier.

Table 2-3. List of MSE/TERA measurements and acquisition settings for the 2007 configuration.

Sensor	DSO model	Stations	Amplitude range	Sampling range	Record length	Bandwidth
E-field	Yokogawa DL750	2, 4, 5, 6, 9, 10	$\pm 85 \text{ kV m}^{-1}$	10 MHz	2 s	$0.2 \text{ Hz}^{\text{a}}\text{-}3 \text{ MHz}^{\text{b}}$
B-field	Yokogawa DL750	4, 9	$\pm 70 \text{ }\mu\text{T}$	10 MHz	2 s	$10 \text{ Hz}^{\text{c}}\text{-}3 \text{ MHz}^{\text{b}}$
TOA dE/dt	LeCroy LT374	1, 3, 4, 5, 7, 8, 9, 11	$\pm 30 \text{ kV m}^{-1} \text{ }\mu\text{s}^{-1}$	250 MHz	8 segments, 2 ms each	$\text{DC-}20 \text{ MHz}^{\text{b}}$
TOA UMPT	LeCroy LT344	1, 3, 4, 5, 7, 8, 9, 11	6 MeV	250 MHz	2 segments, 2 ms each	See note ^d
UMPT	Yokogawa DL750	1-24	6 MeV	10 MHz	2 s	See note ^d
SMPT	Yokogawa DL750	1-10, 18, 19, 20, 22, 24	14 MeV	10 MHz	2 s	See note ^d
Other dE/dt	LeCroy LT344	21, 23	$\pm 30 \text{ kV m}^{-1} \text{ }\mu\text{s}^{-1}$	250 MHz	2 segments, 2 ms each	$\text{DC-}25 \text{ MHz}^{\text{b}}$
Large dE/dt	LeCroy LT344	24	$\pm 2 \text{ kV m}^{-1} \text{ }\mu\text{s}^{-1(\text{e})}$	250 MHz	2 segments, 2 ms each	$\text{DC-}25 \text{ MHz}^{\text{b}}$
Plastic PMT	LeCroy LT344	21, 23	See note ^f	250 MHz	2 segments, 2 ms each	See note ^g
Optical	Yokogawa DL750	18, 19	+2 V	10 MHz	2 s	$\text{DC-}1 \text{ MHz}^{\text{h}}$
Base Current	LeCroy LT344	Tower	$\pm 60 \text{ kA}^{\text{i}}$	100 MHz	10 segments, 1 ms each	$\text{DC-}8 \text{ MHz}^{\text{j}}$
(Tower)	Yokogawa DL716		$\pm 50 \text{ kA}^{\text{i}}$	10 MHz	800 ms	$\text{DC-}4 \text{ MHz}^{\text{b}}$

a) Limited by the decay time constant of the integrating circuit. b) Limited by the digitizer. c) Limited by the active integrator. d) Response of X-ray detectors is usually specified in terms of the rise and fall times for a single x-ray. For the NaI/PMT detectors these are approximately 0.17 μs and 0.90 μs , respectively. e) Calculated from Equation 2-14 although the assumption of a uniform time-varying electric field across the large circular plate is not strictly satisfied. f) The PPMT detectors could not be calibrated with the Cs-137 radioactive source. g) The rise and fall times for the PPMT detectors are approximately 14 ns and 24 ns, respectively. h) Limited by preamplifier. i) Sign indicates the polarity of charge lowered to ground. j) Limited by current-viewing resistor (CVR).

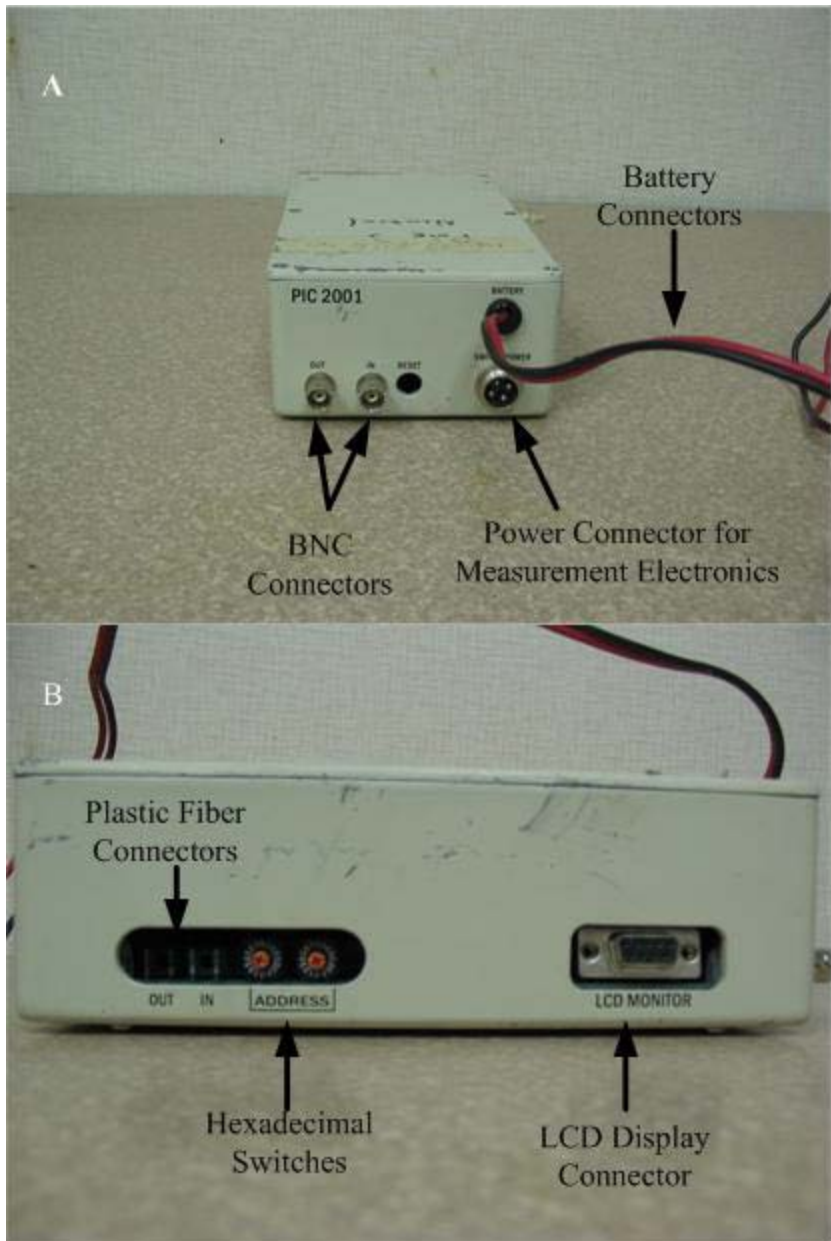


Figure 2-3. The 2001 PIC controller. A) Front view. B) Side view.

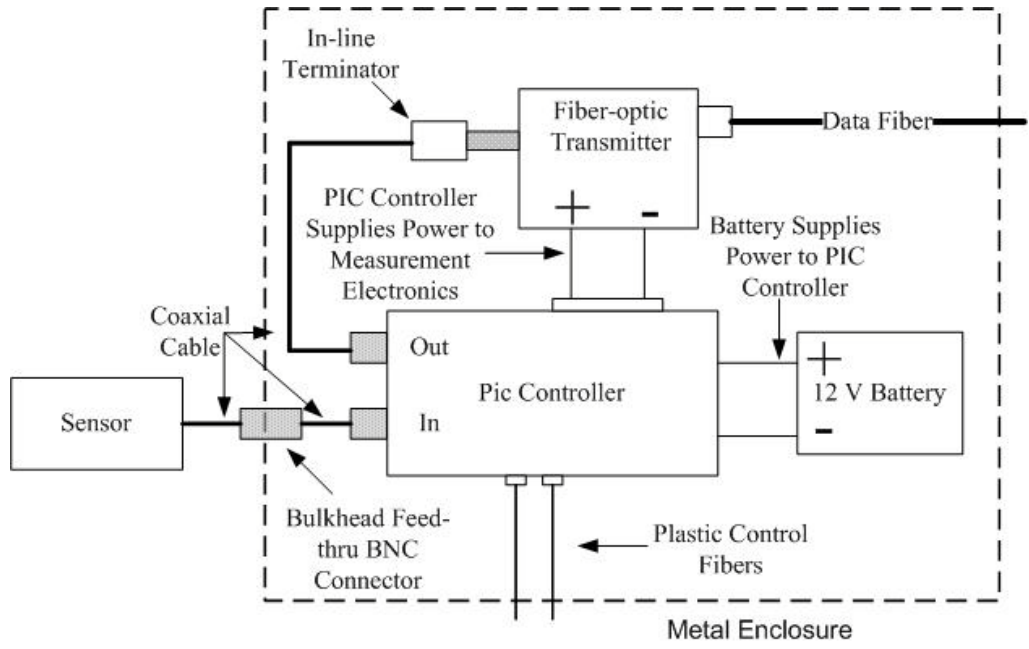


Figure 2-4. Diagram of the typical 2001 PIC controller installation.

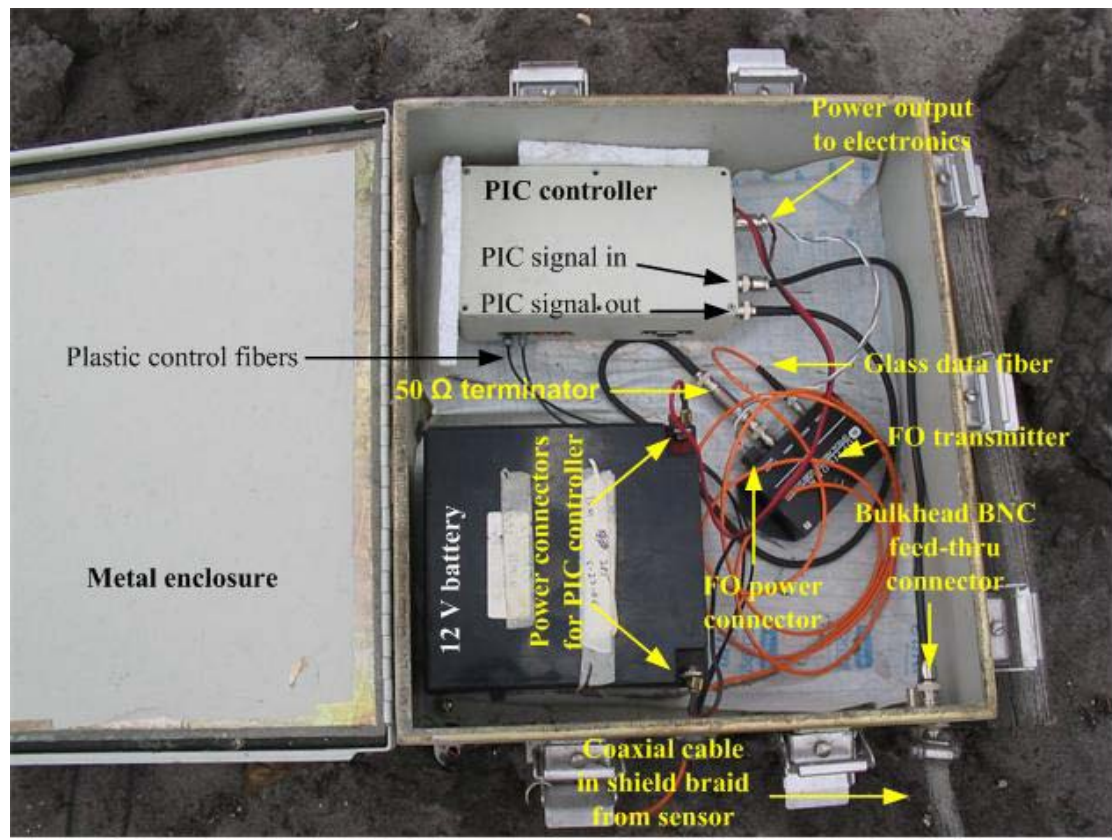


Figure 2-5. Installation of the 2001 PIC controller in an actual measurement.

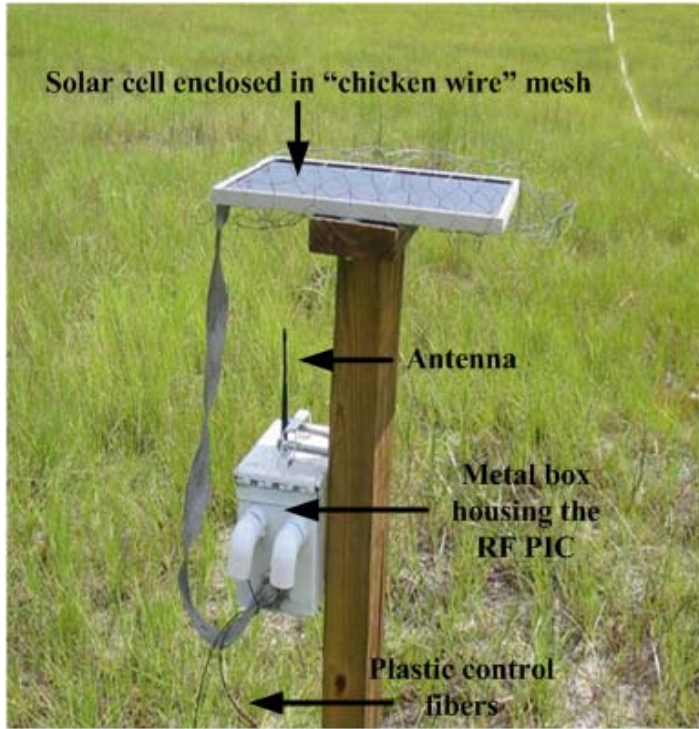


Figure 2-6. Housing for an RF PIC mounted with its solar cell.

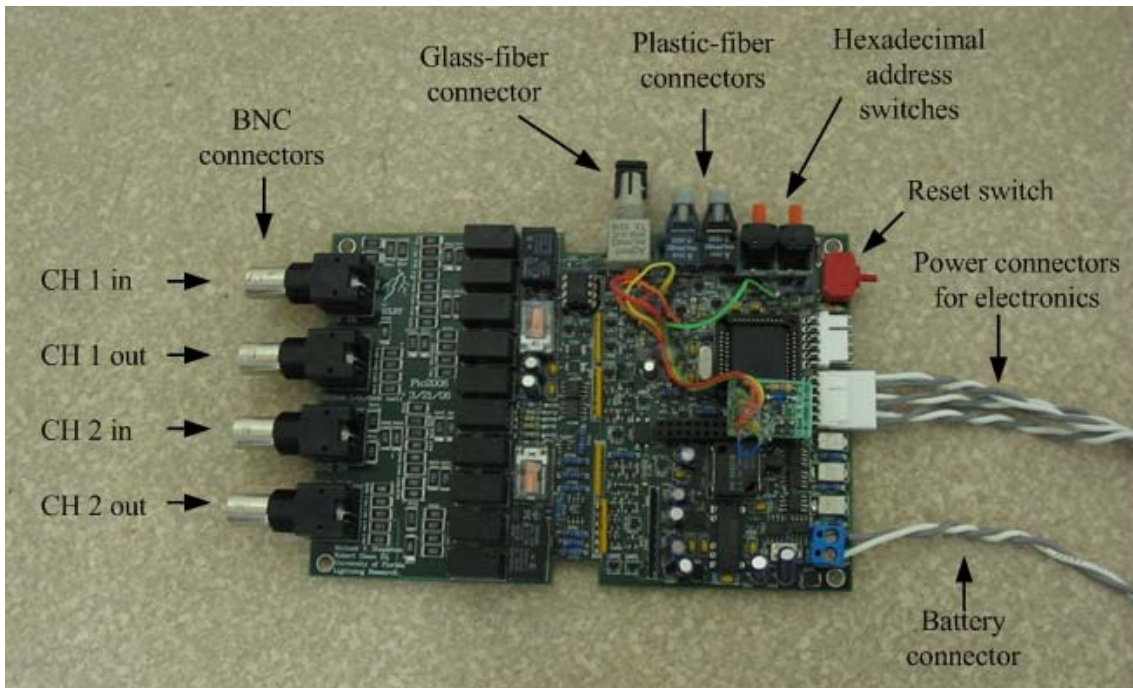


Figure 2-7. The 2006 PIC controller.

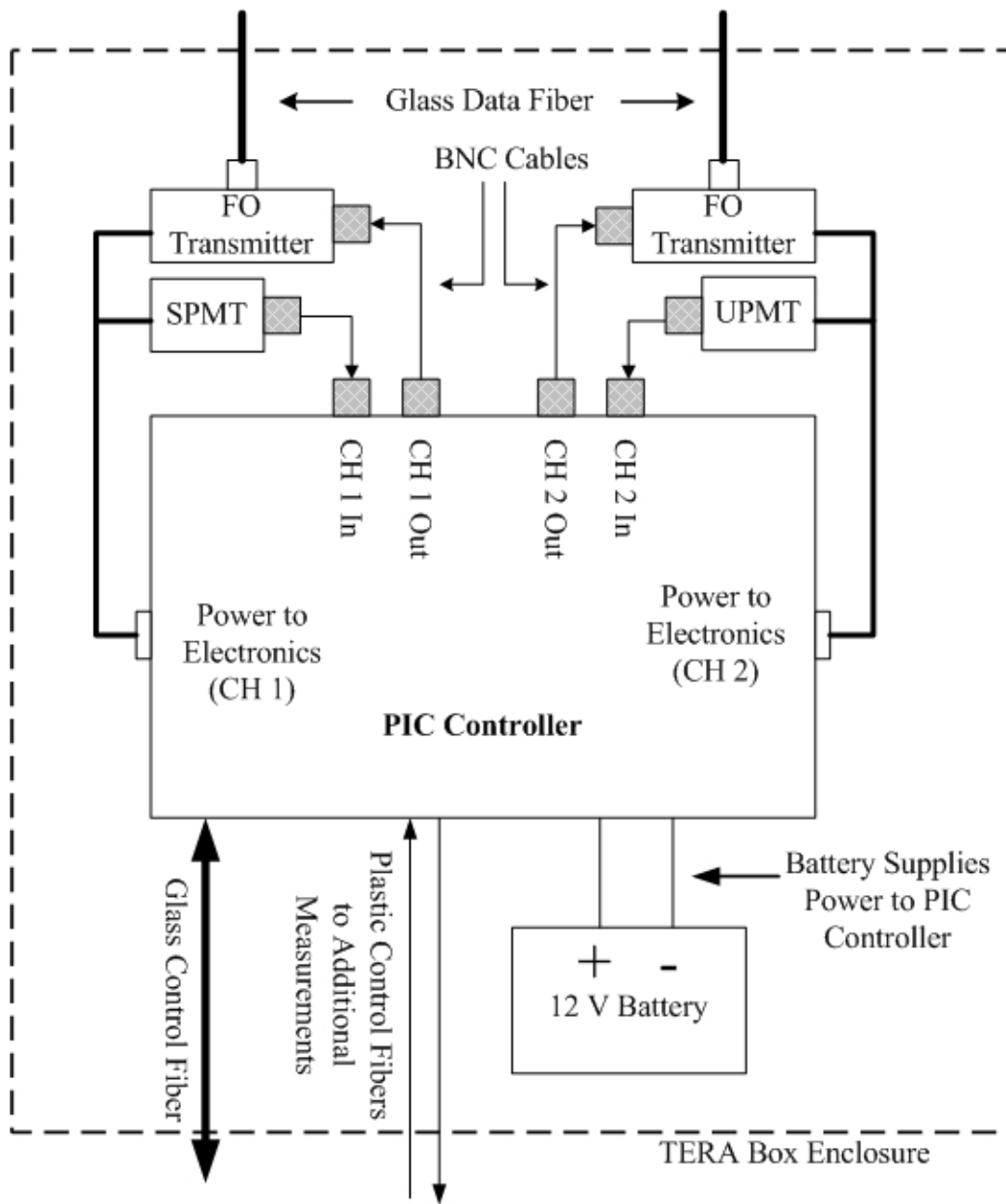


Figure 2-8. Diagram of the typical 2006 PIC controller installation.



Figure 2-9. Optical fan-out board used by the control computer to control the 2006 version PIC controllers.

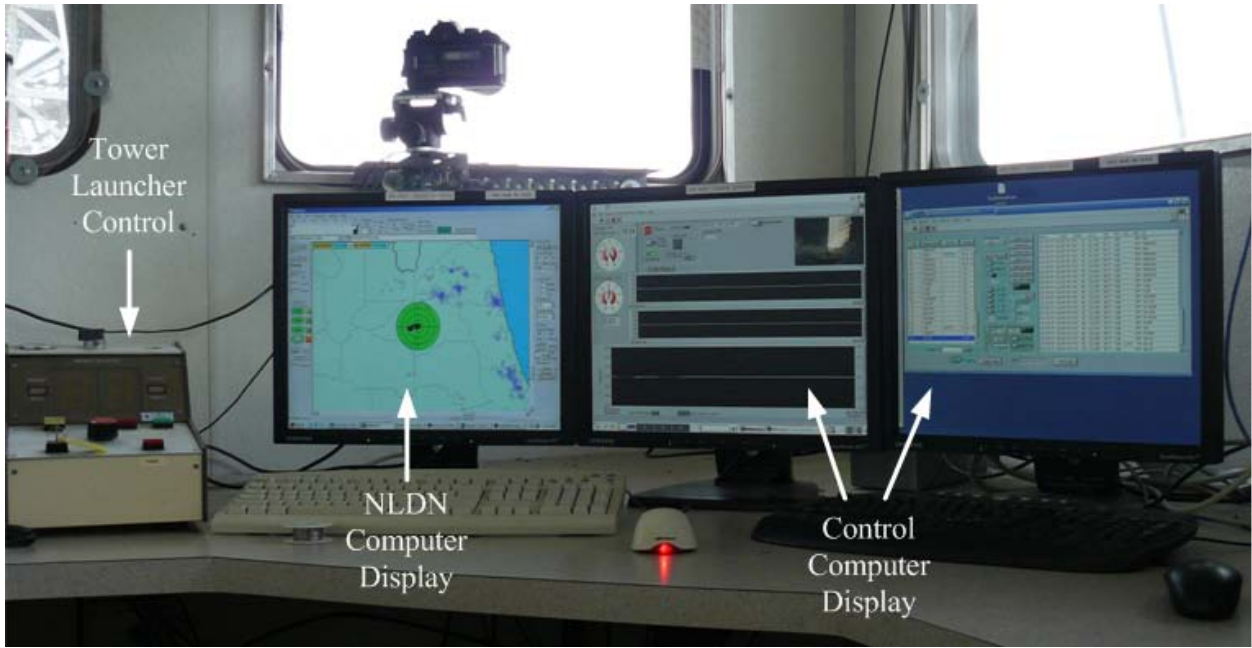


Figure 2-10. The MSE/TERA network control system located in the Launch Control trailer. The control center is also used for rocket-triggered lightning operations.



Figure 2-11. The electric field mill that is continually monitored by the control computer. The field mill is located approximately 10 m west of the Launch Control trailer.

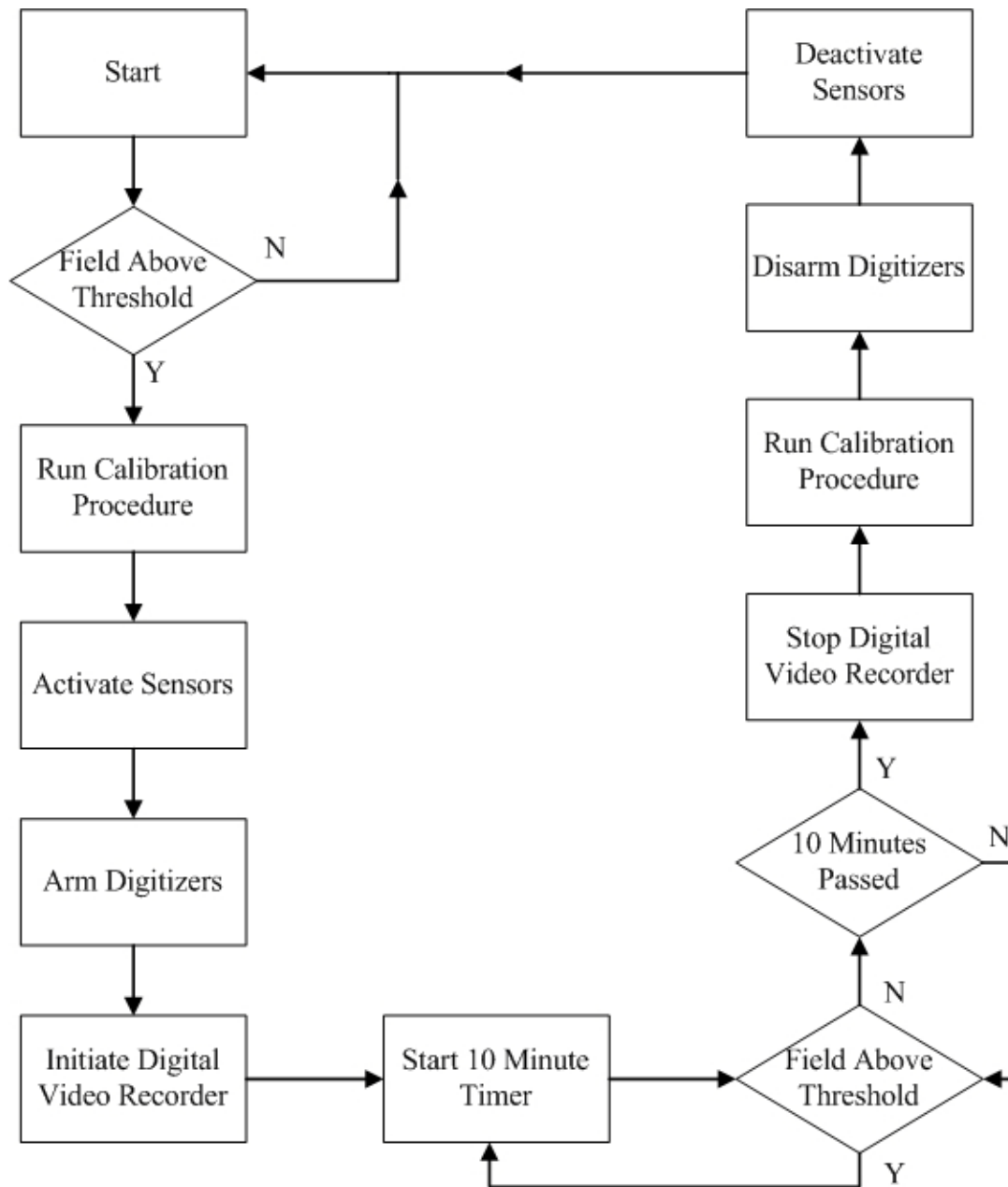


Figure 2-12. Flowchart illustrating the MSE/TERA network control system algorithm.

Table 2-4. Summary of MSE fiber-optic links used between 2005 and 2007.

Model	Fiber	Fiber connector	Signal to noise ratio (approx)	Nominal -3 dB bandwidth	Transmitter input resistance	Receiver output resistance	Input range	Output range (in 50 Ω)
Opticomm MMV-120C	62.5/125 μm	ST	59 dB	DC-30 MHz	68 k Ω	50 Ω	± 1 V	± 1 V
Nicolet Isobe 3000	2 \times 200 μm	SMA-0905	60 dB	DC-15 MHz ^a	1 M Ω	50 Ω	Selectable ^b	± 1 V

a) 5 MHz passive filters were typically placed on the output of the Isobe receivers. b) The allowable input ranges were ± 0.1 V, ± 1 V, and ± 10 V.

Table 2-5. Summary of the DSOs used in the MSE/TERA network between 2005 and 2007.

Brand	Model	Quantity	Control protocol	Amplitude resolution (bits)	Number of channels/digitizer	Maximum sample rate	Maximum bandwidth	Maximum record length	Input resistance
LeCroy	LT374L	2	Ethernet	8	4	2 GHz	500 MHz	4 MS/Ch	50 Ω or 1 M Ω
LeCroy	LT344L	6	Ethernet	8	4	500 MHz	500 MHz	1 MS/Ch	50 Ω or 1 M Ω
Yokogawa	DL750	4	GPIB	12	16	10 MHz	3 MHz	25 MS/Ch	1 M Ω
Yokogawa	DL716	1	GPIB	12	16	10 MHz	4 MHz	16 MS/Ch	1 M Ω

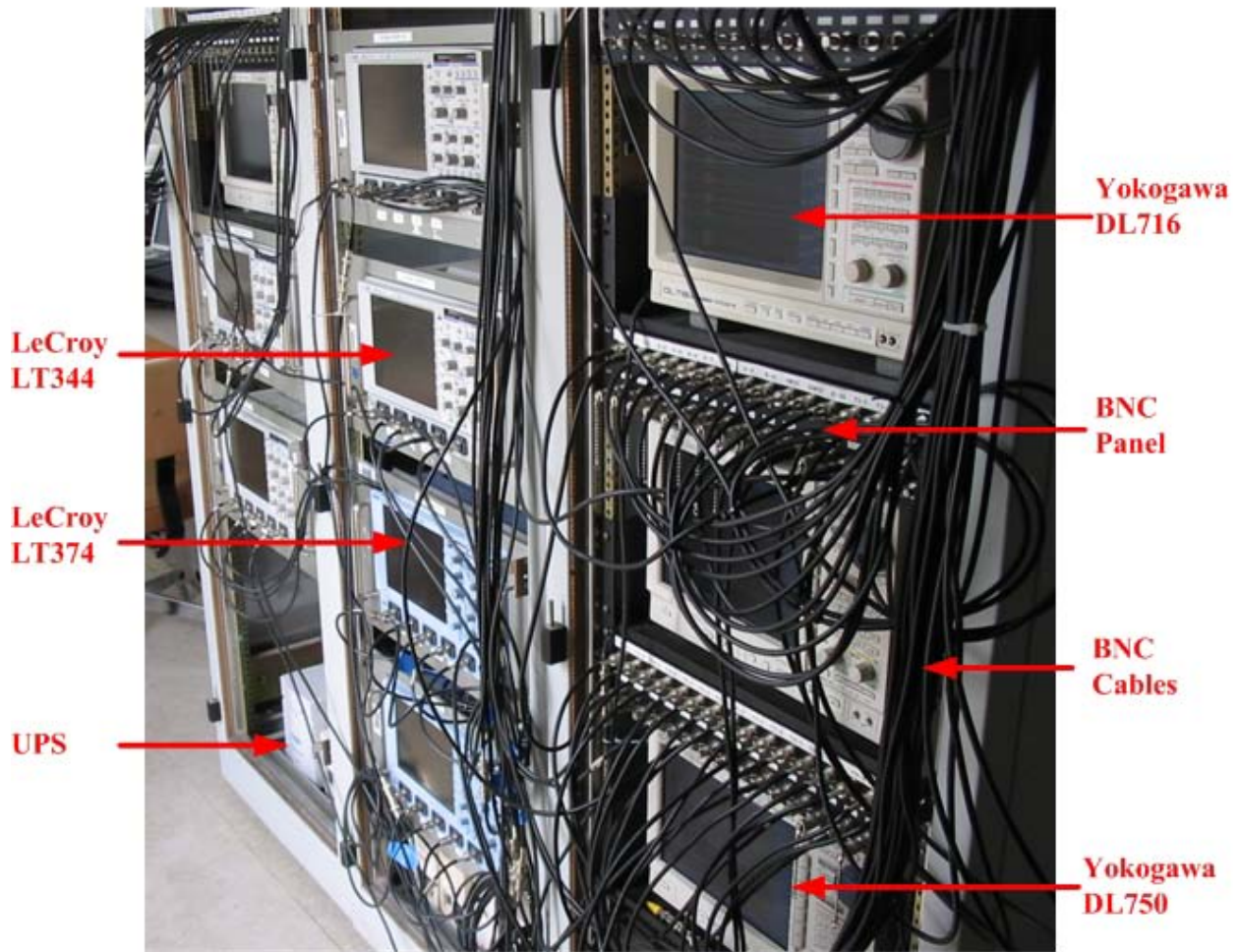


Figure 2-13. Digital storage oscilloscopes along the west wall in Launch Control. The different oscilloscope models are indicated as well as some of the auxiliary components. Note that this photograph was taken in 2006, and the arrangement of DSOs was somewhat different in 2005 and 2007.

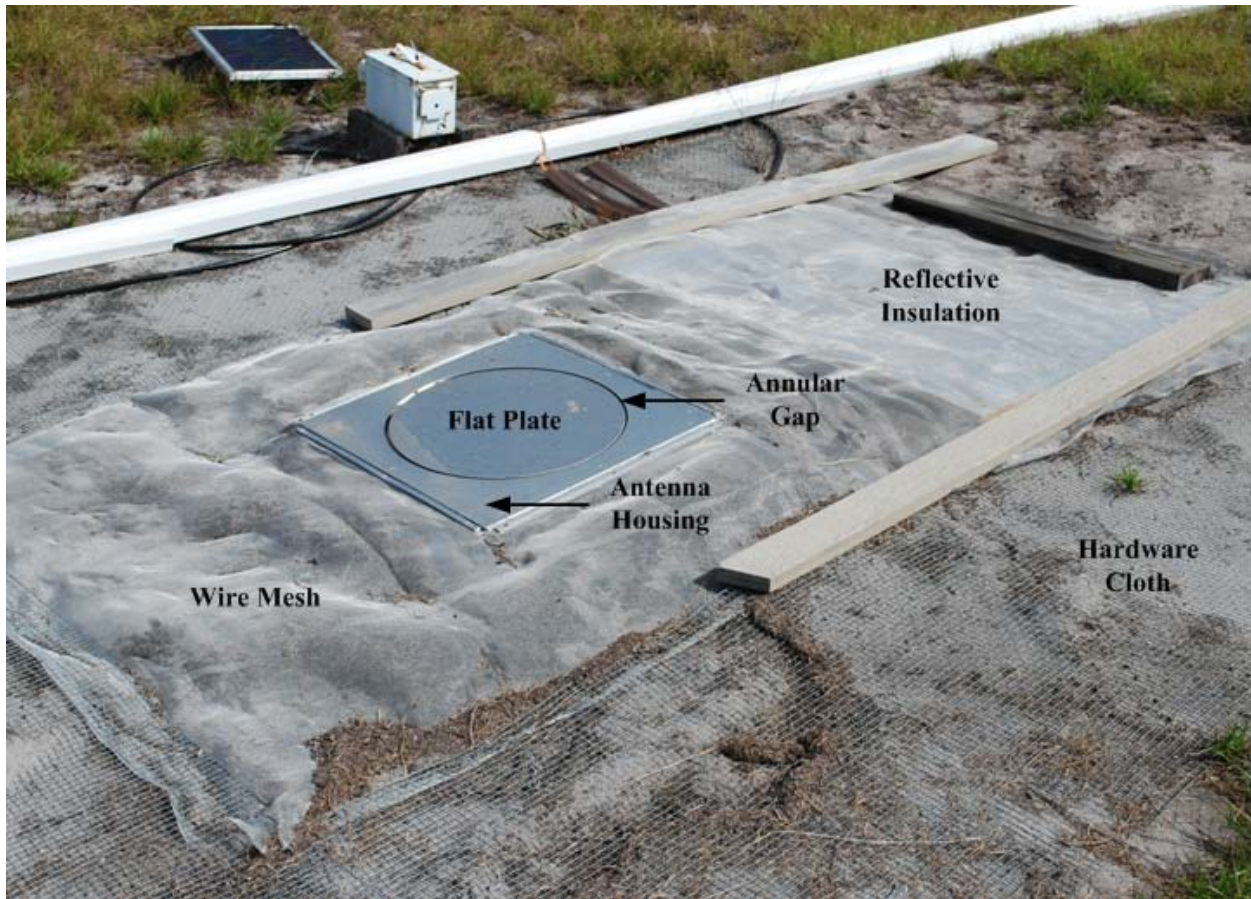


Figure 2-14. Flat-plate antenna used in E-field and dE/dt measurements. The sensing element of the antenna is the circular portion of area $\approx 0.155 \text{ m}^2$ surrounded by an annular air gap. The remainder of the structure is the antenna housing, grounded via a 3-m ground rod. A simulated ground plane, consisting of wire mesh and hardware cloth, extends from the top face of the housing and serves to reduce the effects of electric field enhancement. A piece of reflective insulation, located under the wire mesh and over the hole containing the Hoffman box, protects the measurement electronics from environmental elements.

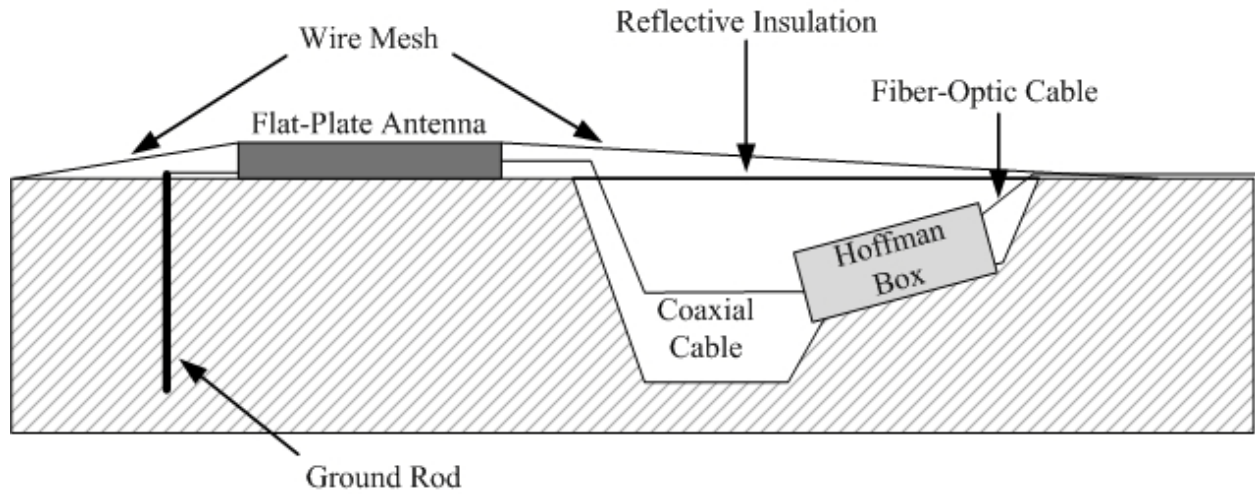


Figure 2-15. Installation of the flat-plate antenna.

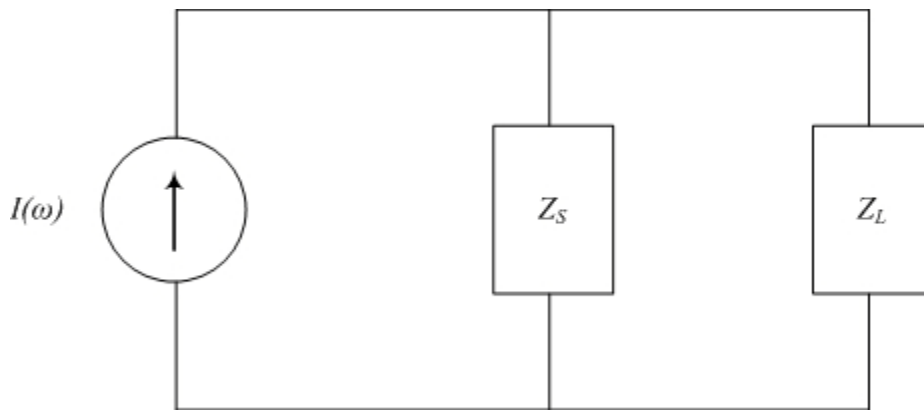


Figure 2-16. Frequency-domain equivalent circuit for the flat-plate antenna. The Norton equivalent current source feeds a general load impedance, Z_L .

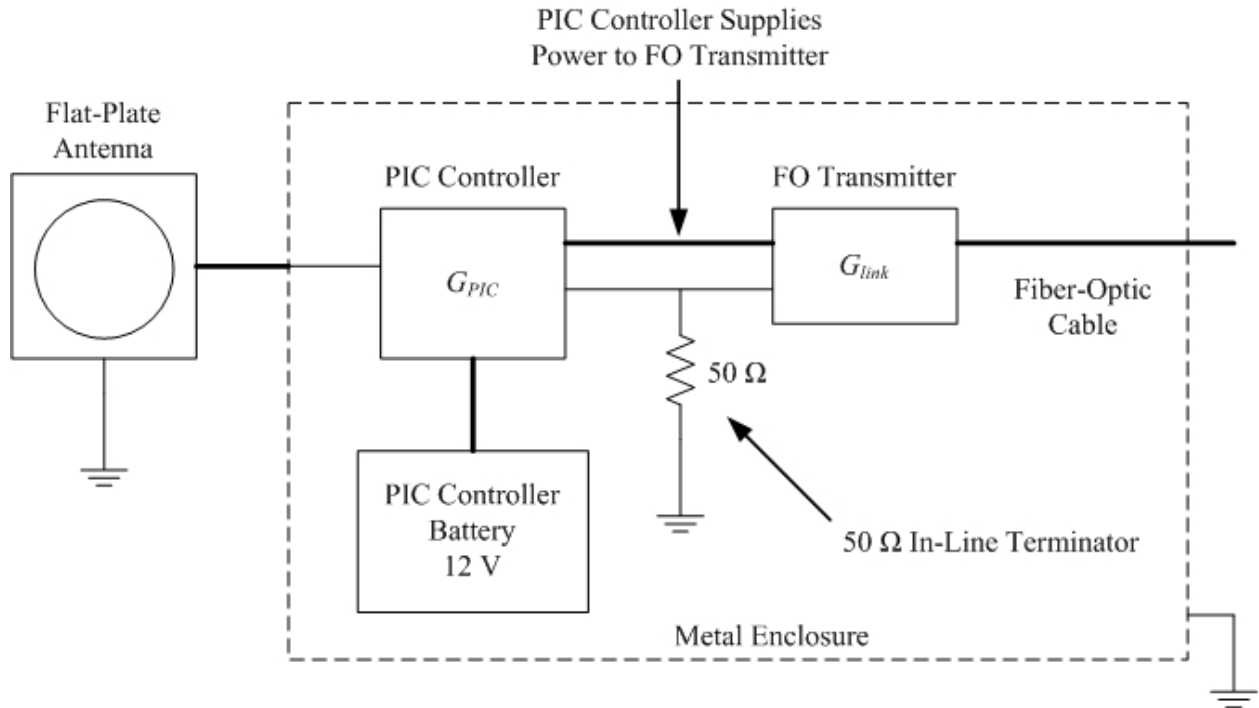


Figure 2-17. Diagram for the dE/dt measurement configuration.

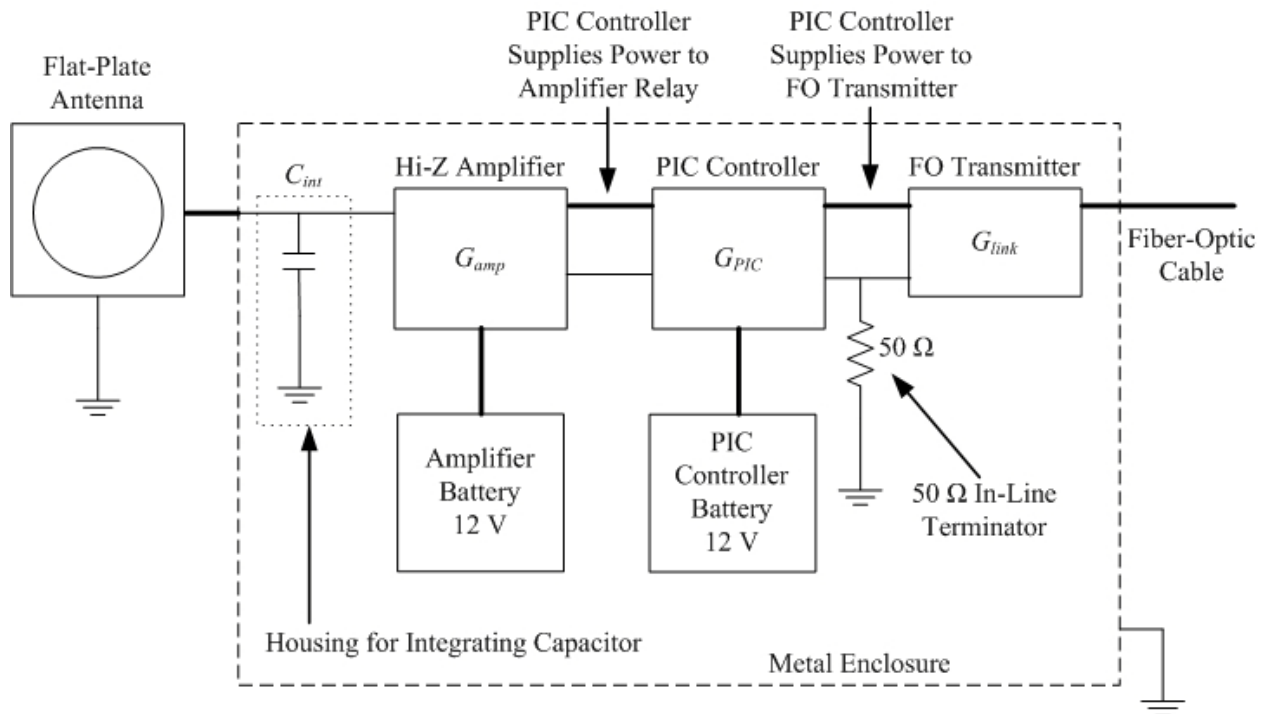


Figure 2-18. Diagram for the E-field measurement configuration.



Figure 2-19. Magnetic field coaxial-loop antenna. Only one of the perpendicular loops was used at each station. The Hoffman box near the antenna houses the measurement electronics.

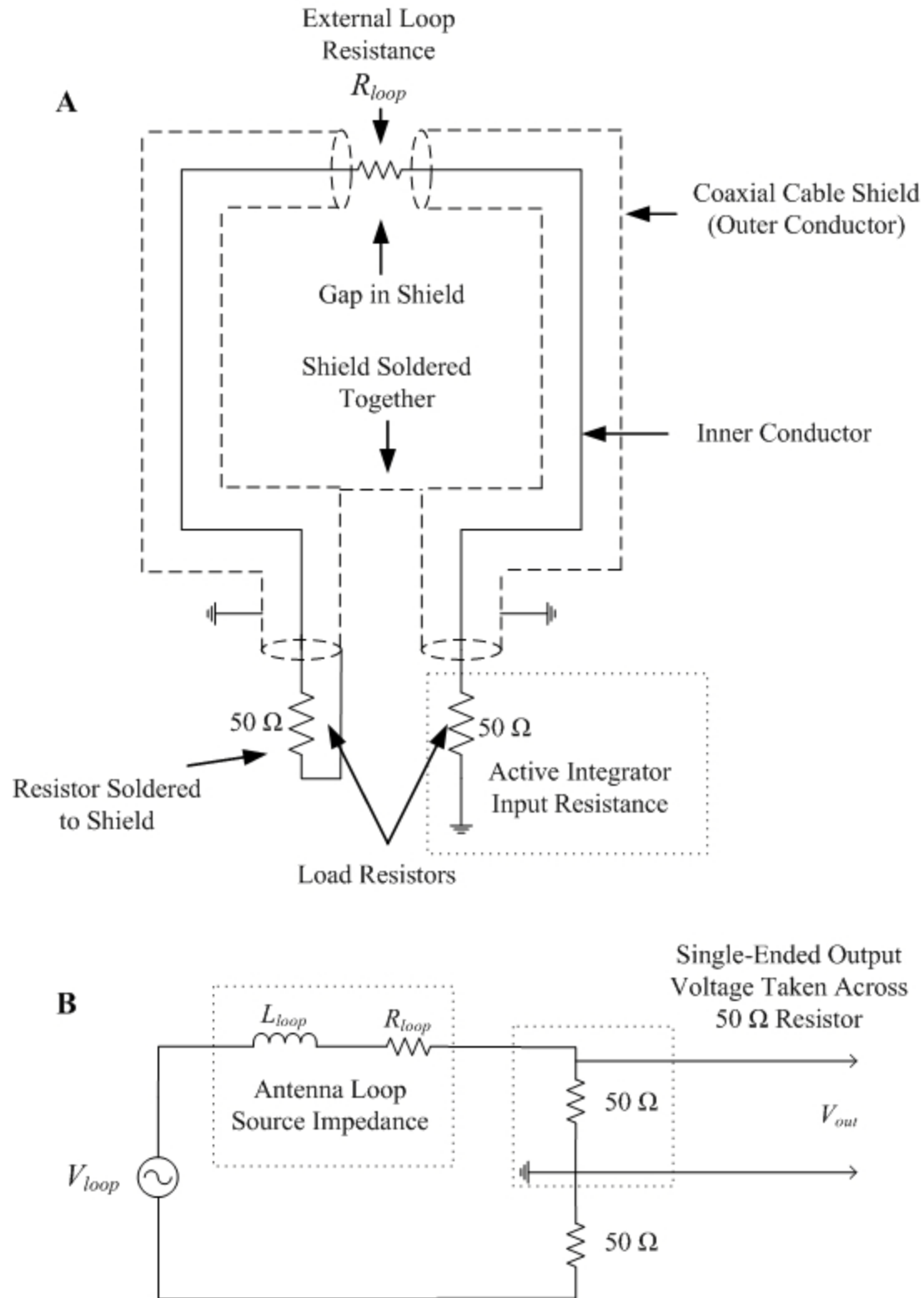


Figure 2-20. Single-ended output coaxial-loop antenna. A) Diagram. B) Equivalent circuit.

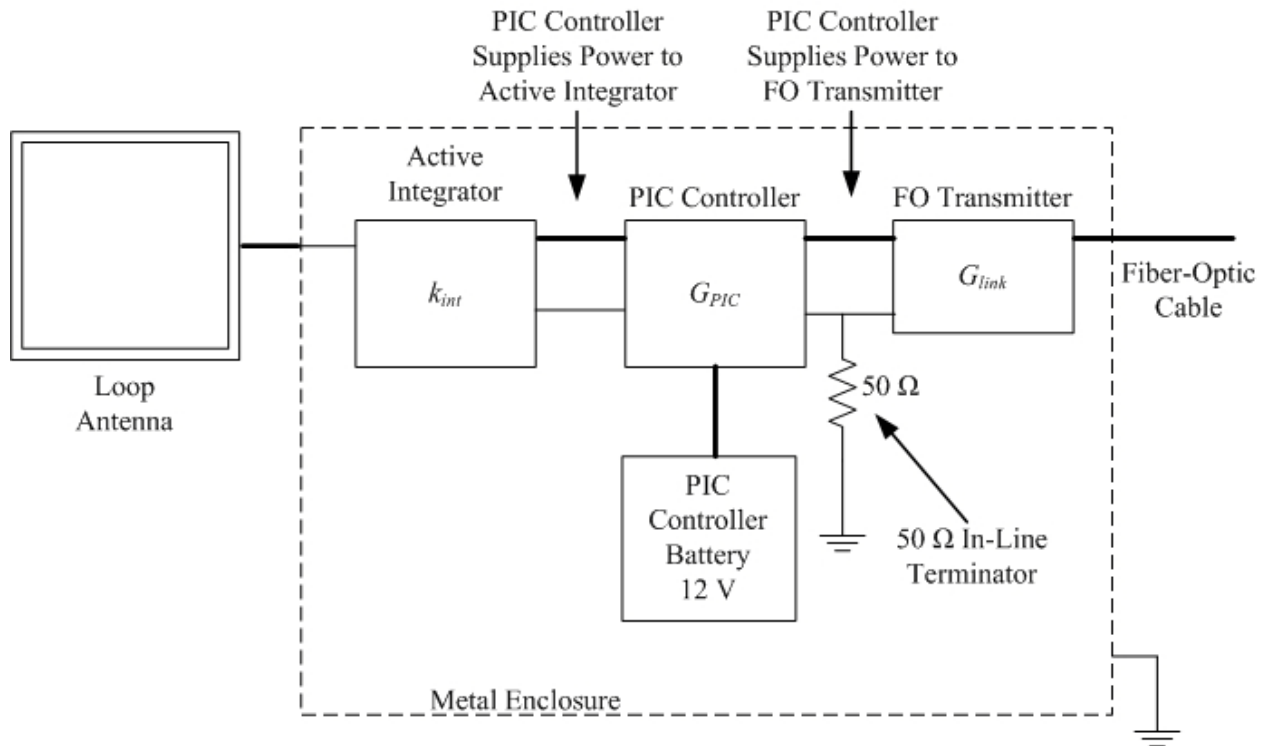


Figure 2-21. Diagram for the magnetic field measurement configuration.

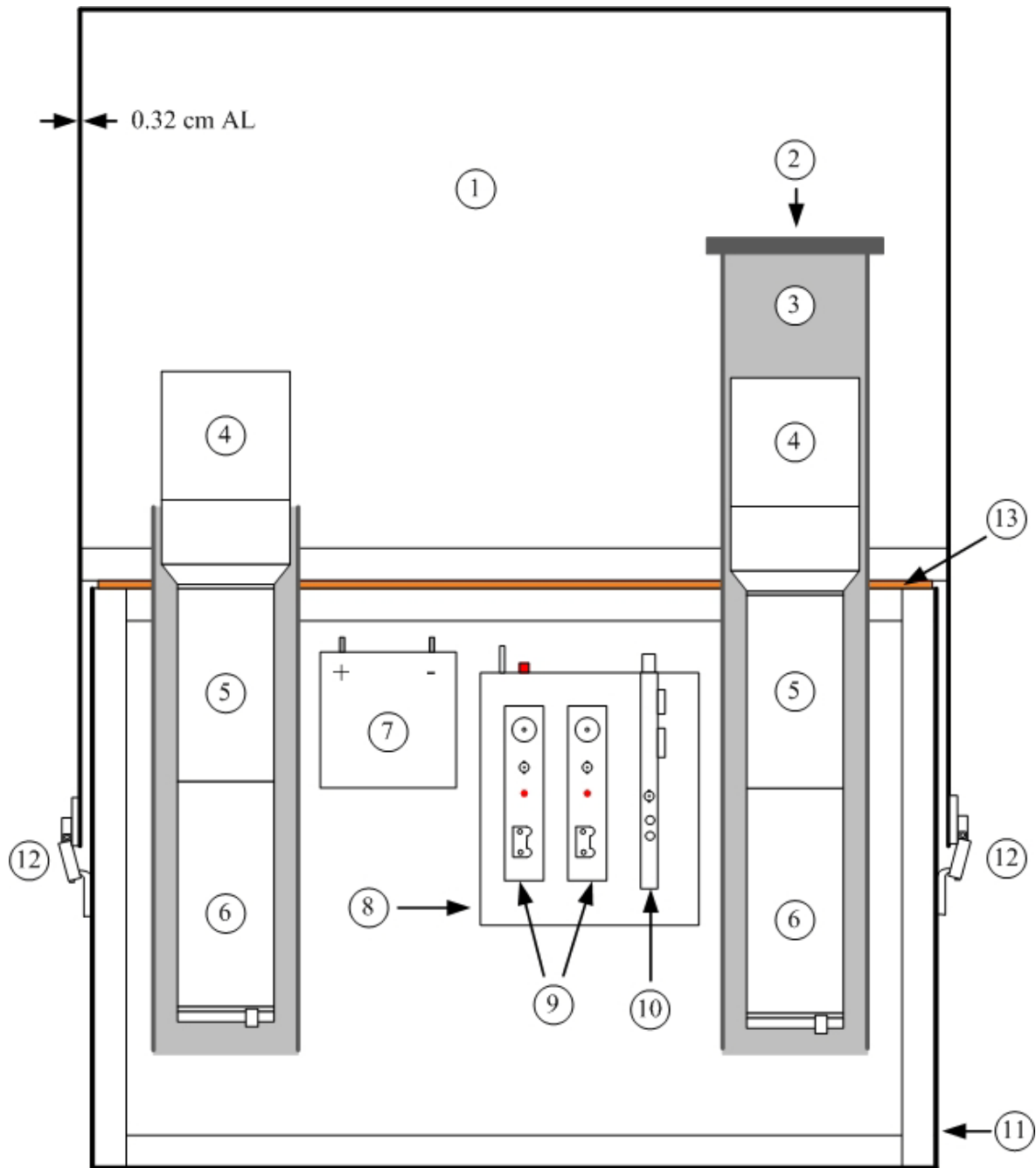
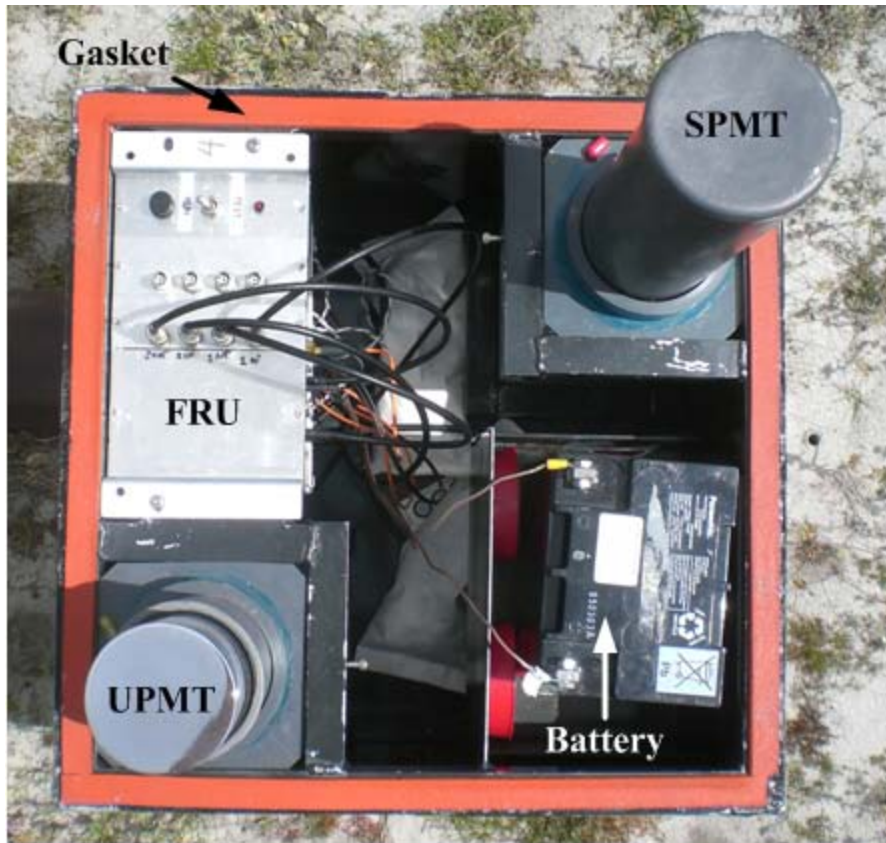
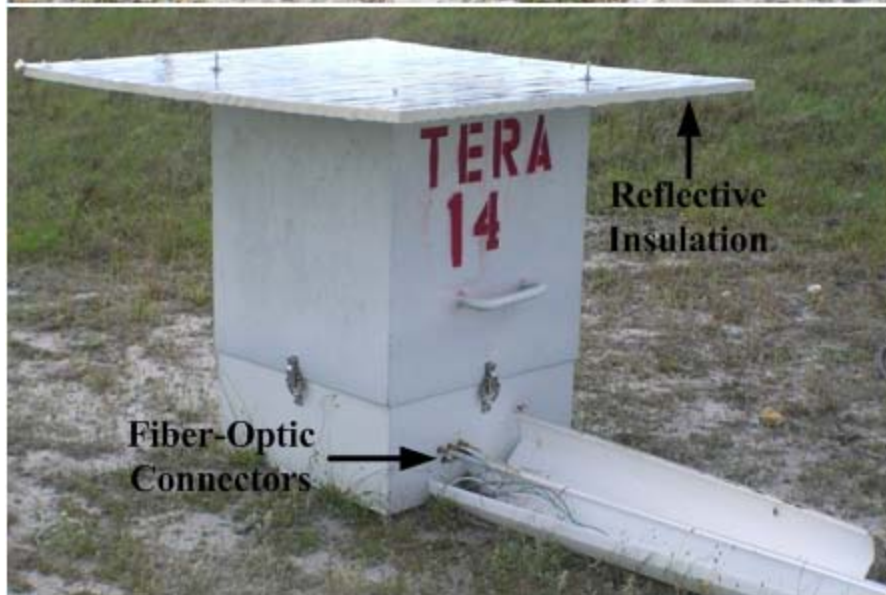


Figure 2-22. Diagram of the TERA box measurement. The components are as follows: 1) aluminum lid, 2) lead cap, 3) lead attenuator (can also be used as a collimator if the cap is removed), 4) NaI scintillator, 5) Photomultiplier Tube (PMT), 6) PMT base (HV supply and voltage divider chains), 7) 12 V battery, 8) Field Replaceable Unit (FRU), 9) FO transmitters, 10) PIC controller, 11) aluminum housing, 12) spring loaded drawer latch, 13) gasket.



A



B

Figure 2-23. TERA box with two NaI/PMT detectors. A) With the lid removed. B) With lid in place.

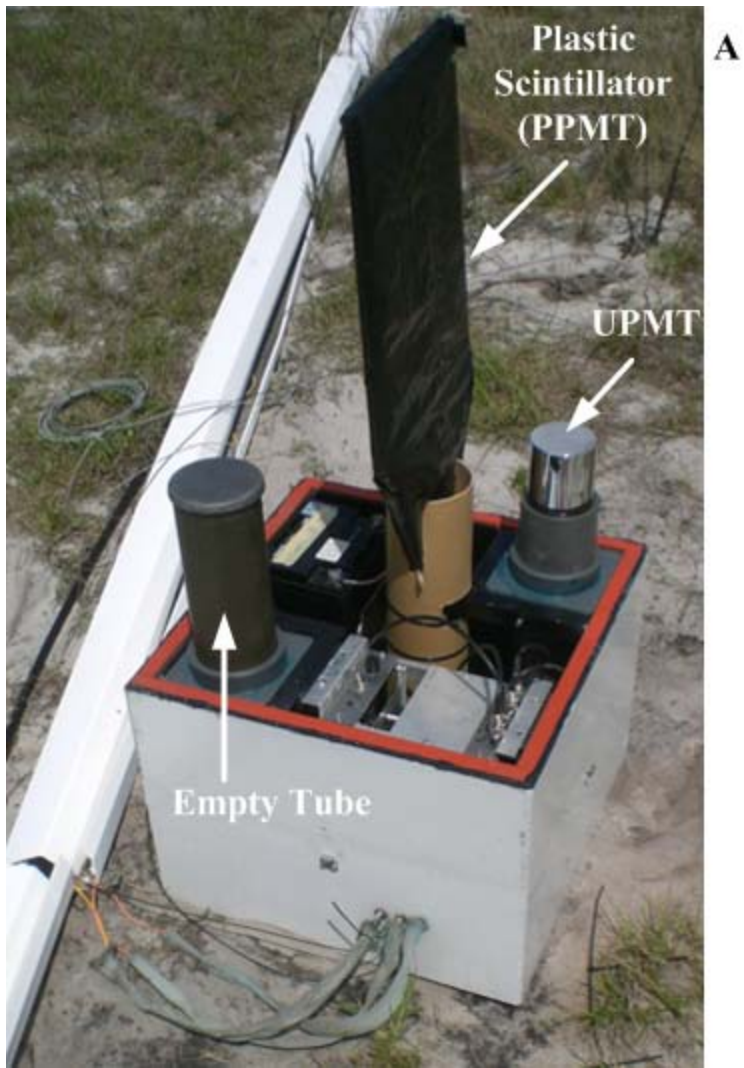


Figure 2-24. TERA box with a plastic scintillator detector. A) With lid removed. B) With the lid in place. Notice that the lead attenuator does not contain a NaI/PMT detector. As with every TERA box, the UPMT is operational.

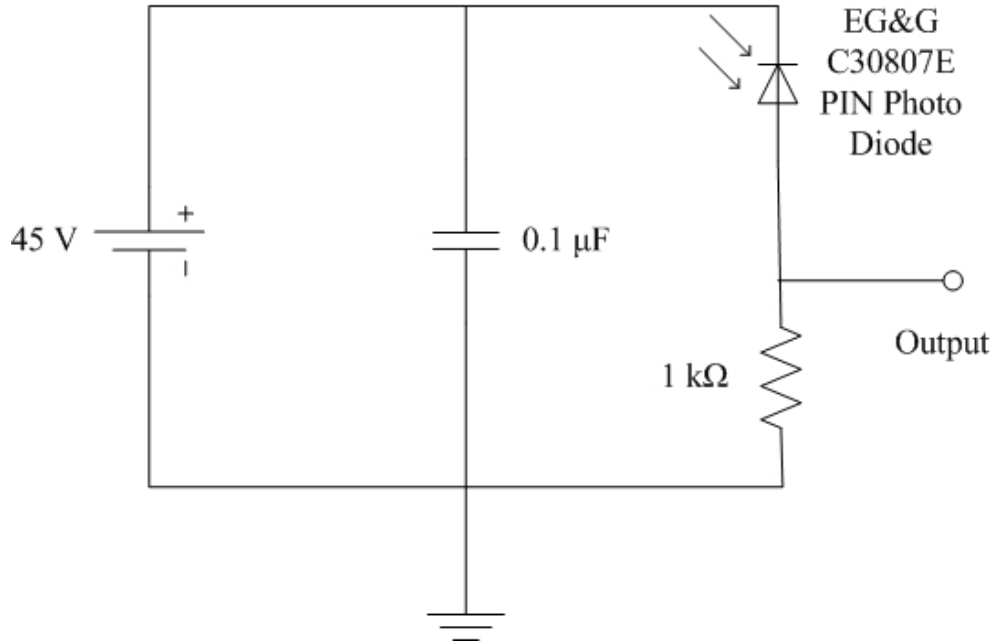


Figure 2-25. Schematic of the optical sensor circuit.

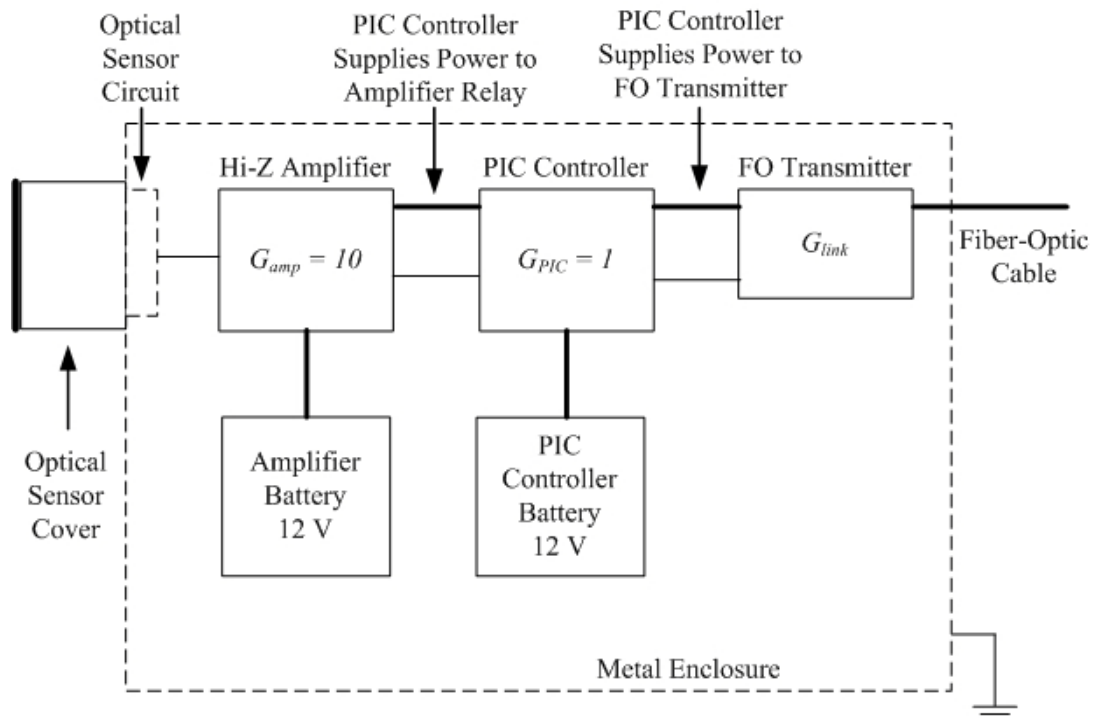


Figure 2-26. Diagram of the optical measurement configuration.

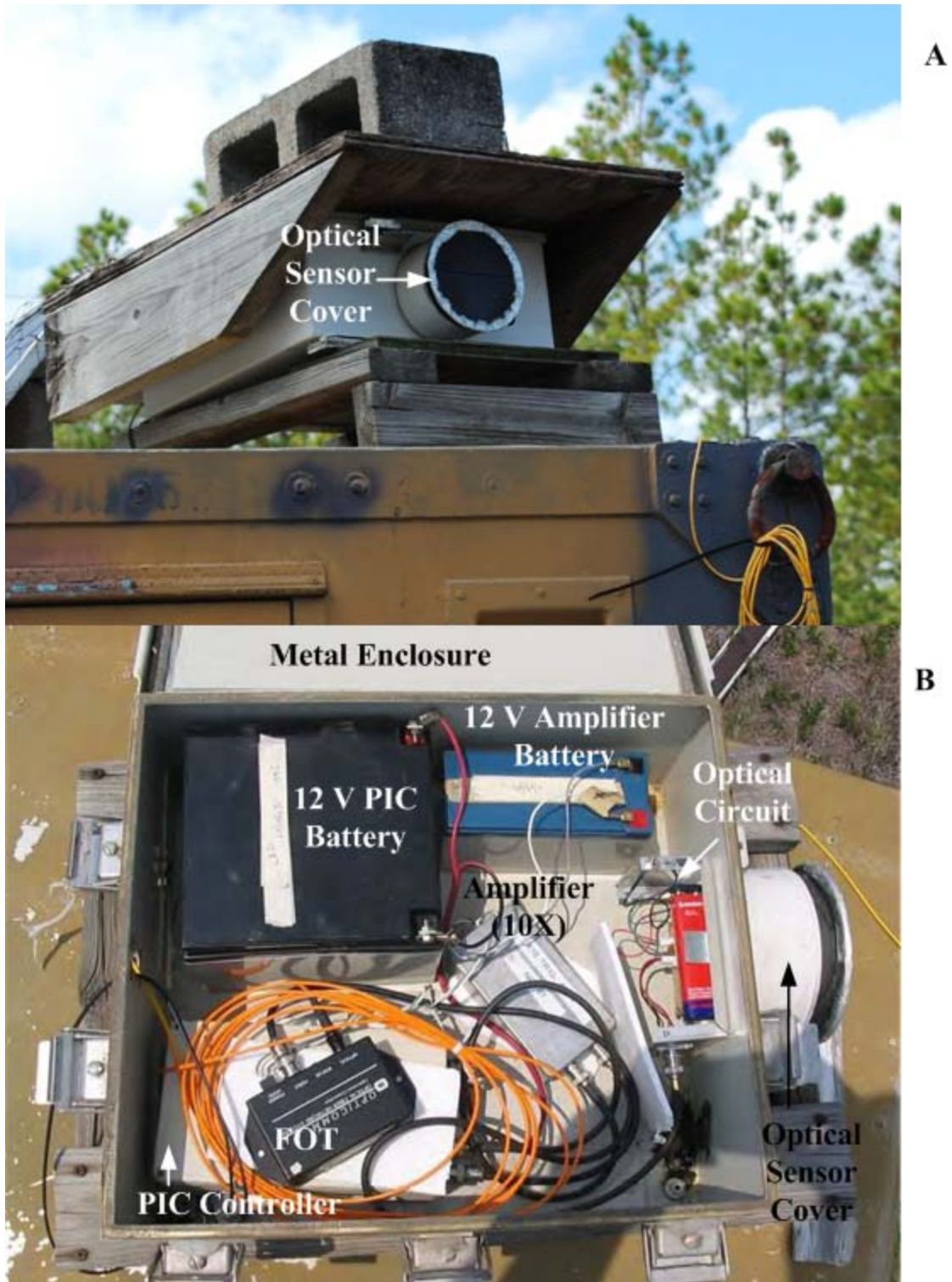


Figure 2-27. Optical measurement assembly on top of a 2.5 m tall military canister located at the south west corner of the ICLRT site. A) Closed measurement box. B) Open measurement box

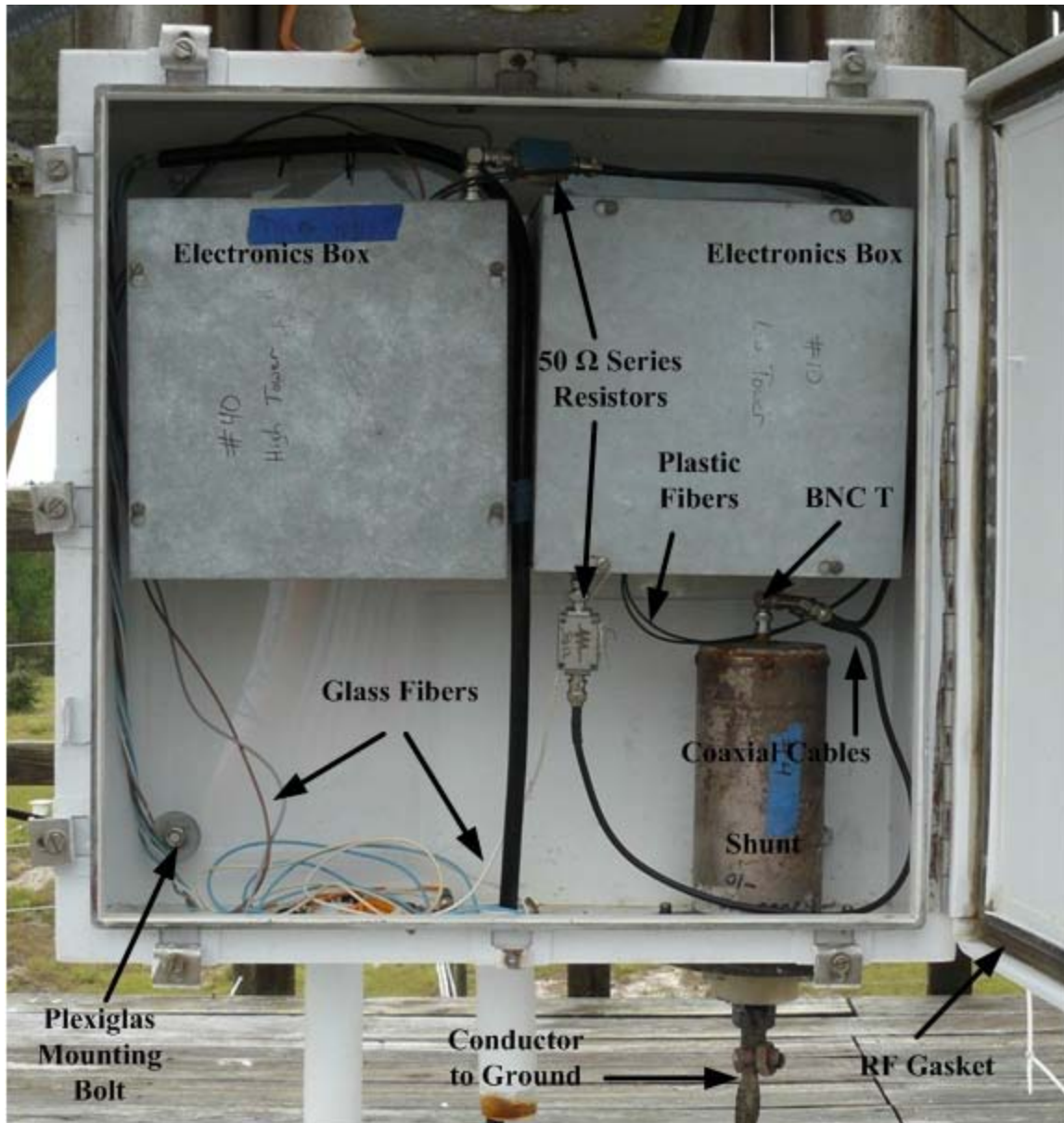


Figure 2-28. Inside of the channel-base current measurement box on the tower launcher. The shunt is mounted to the bottom of the Hoffman box with six metal bolts. The chassis of the electronics boxes are electrically from the Hoffman box and each other by a sheet of Plexiglas.

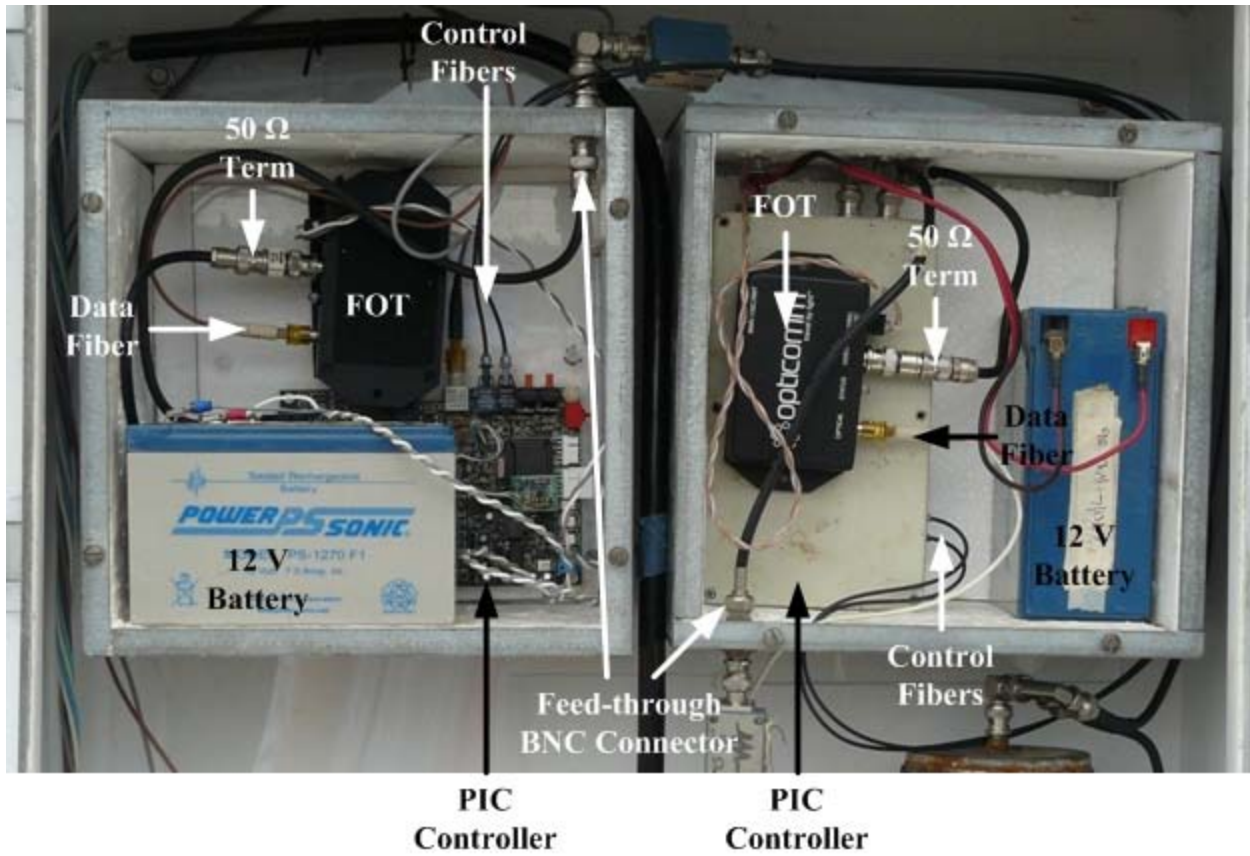


Figure 2-29. Inside of the electronics boxes for the 2007 channel-base current measurements on the tower launcher.

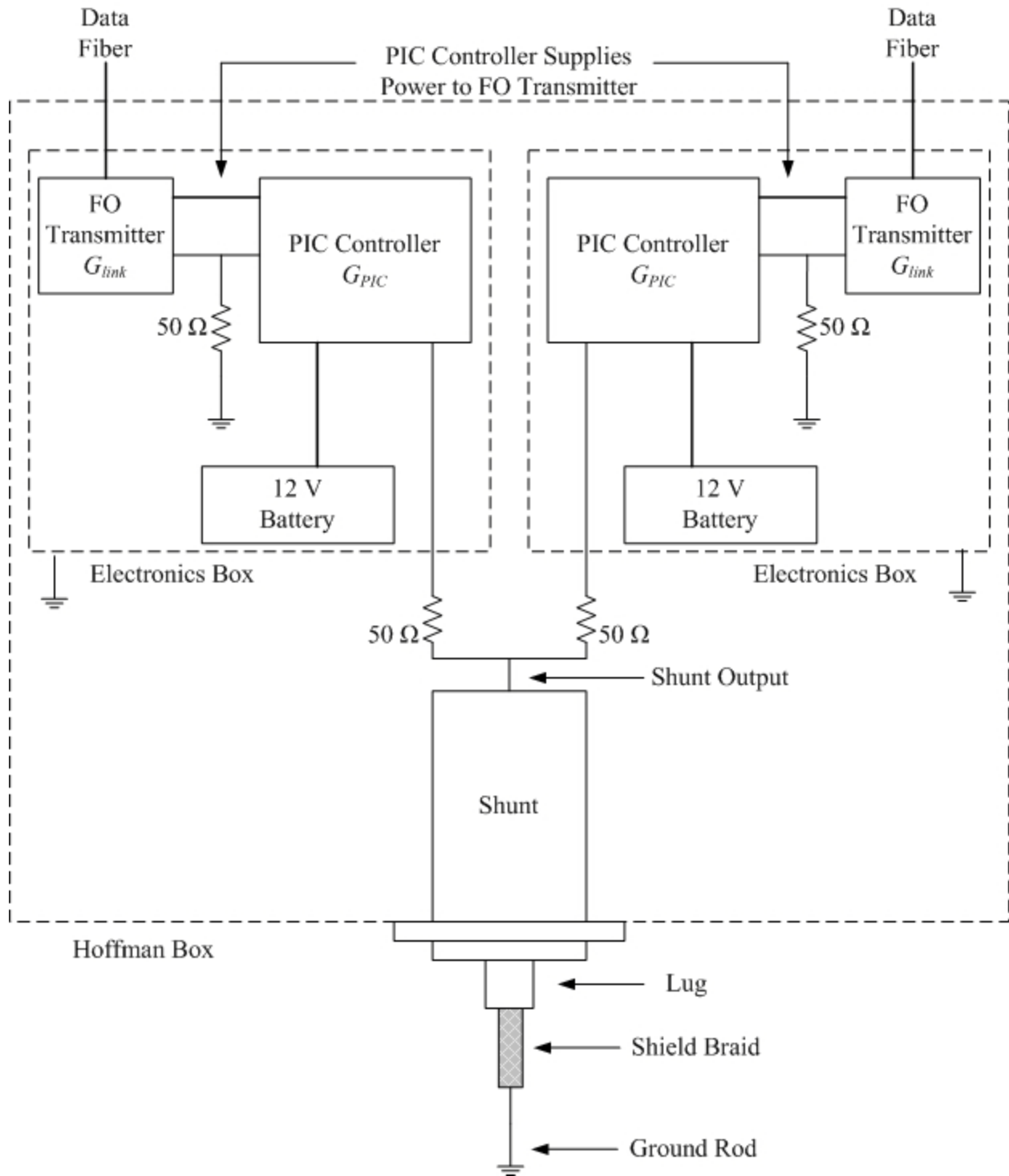


Figure 2-30. Diagram of the channel-base current measurements.

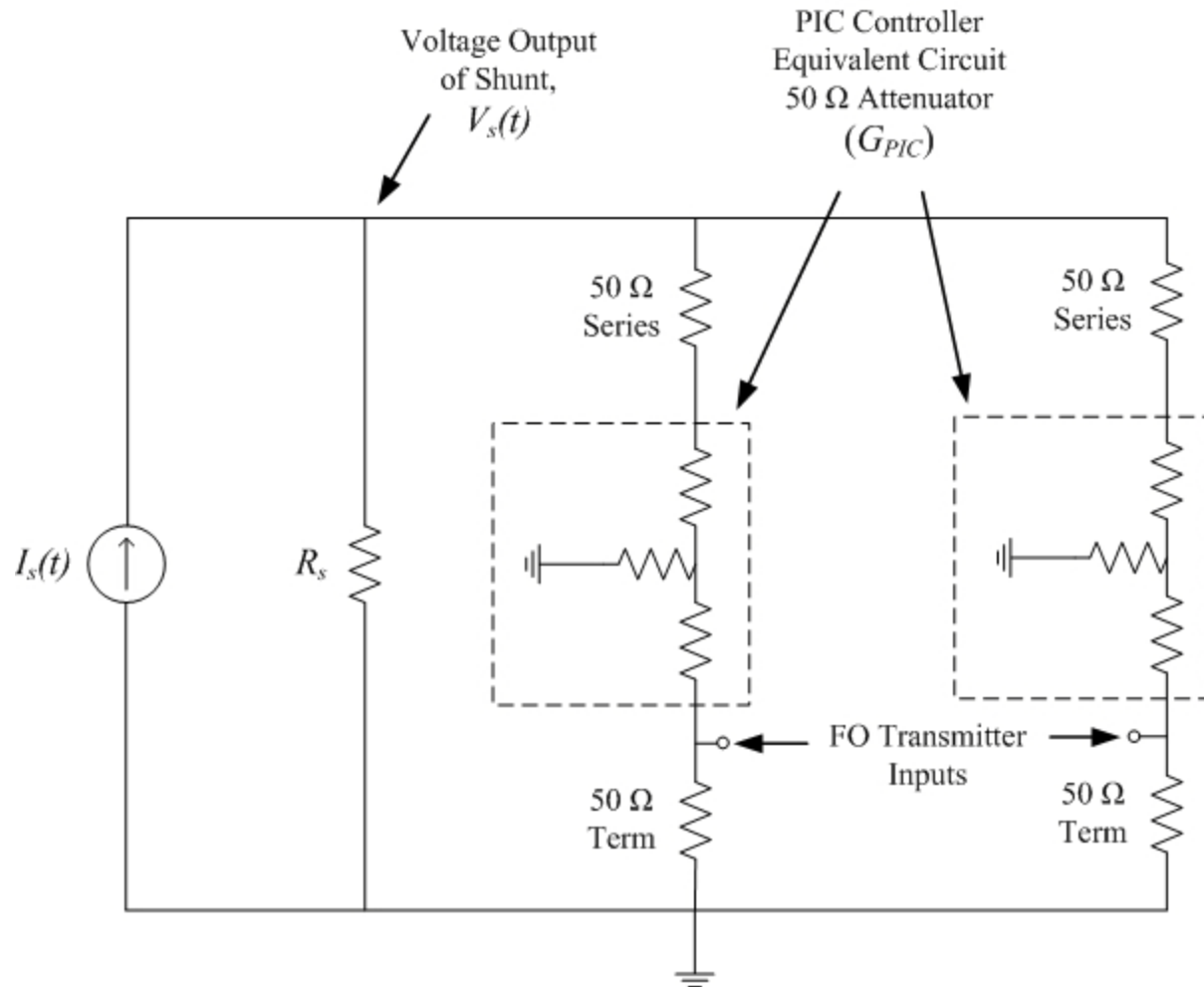


Figure 2-31. Time-domain equivalent circuit for the channel-base current measurements.

Table 2-6. Configurations for the channel-base current measurements

Location (year)	Shunt model	R_s (m Ω)	Measurement	G_{PIC}	Nominal cal factor (kA/V)
Mobile (2005)	R-2800-4	2.460 ^a	High	0.01122 (-39 dB)	-72.46
			Low	0.11220 (-19 dB)	-7.246
Tower (2005)	R-5600-8	1.231 ^a	High	0.02239 (-33 dB)	-72.57
			Low	0.22387 (-13 dB)	-7.257
Tower (2007)	R-7000-10	1.000 ^b	High	0.03162 (-30 dB)	-63.25
			Low	0.31623 (-10 dB)	-6.325

a) Measured by George Schnetzer and within a few percent of the nominal value. b) Nominal value



Figure 2-32. The optical AND trigger, buffer circuit, and OR buffer form the basis of the trigger system.



Figure 2-33. The GPS antenna used with the time-stamping system is mounted to the roof at the south end of Launch Control.

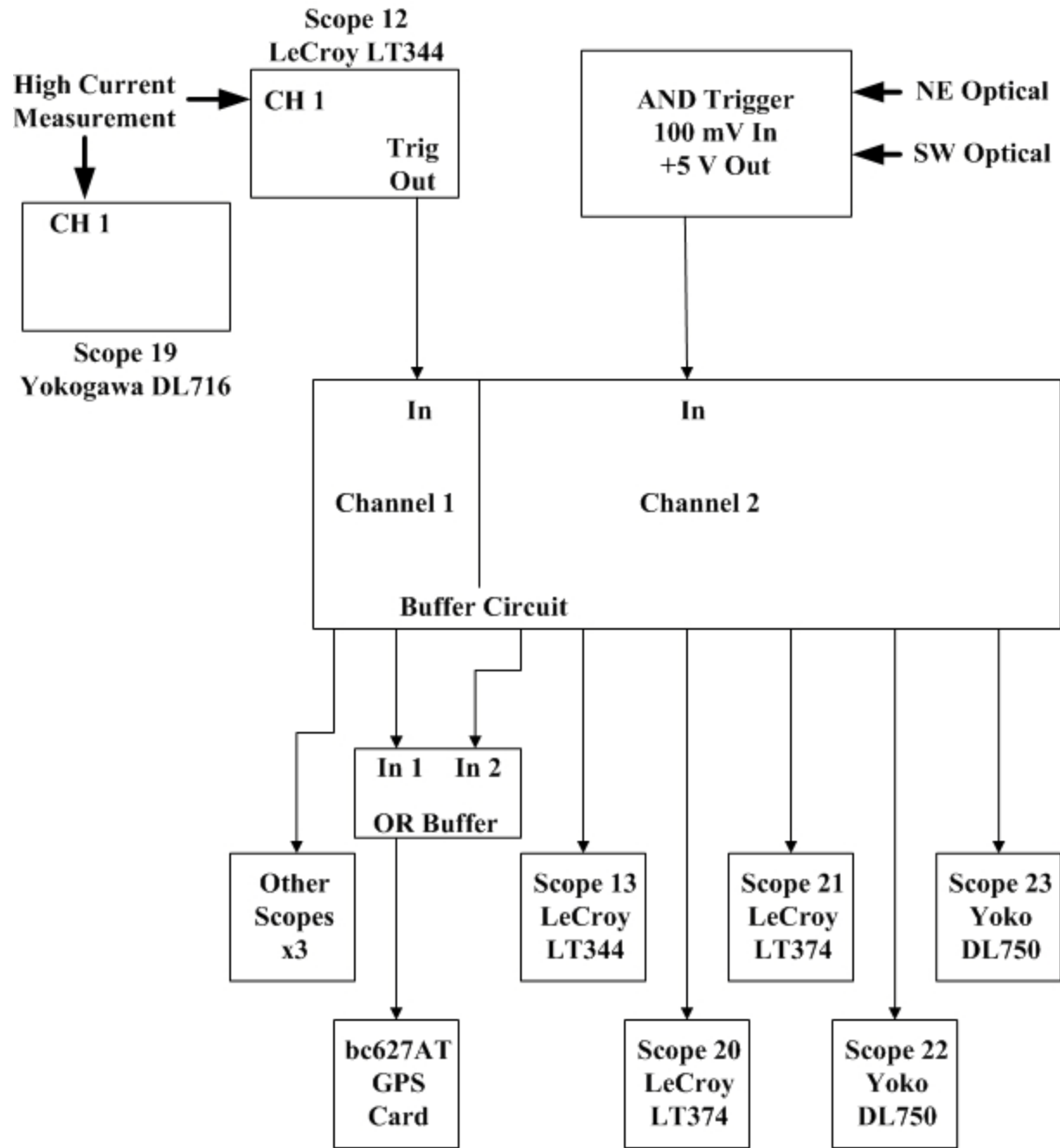


Figure 2-34. Diagram of the 2005 trigger configuration at the ICLRT.

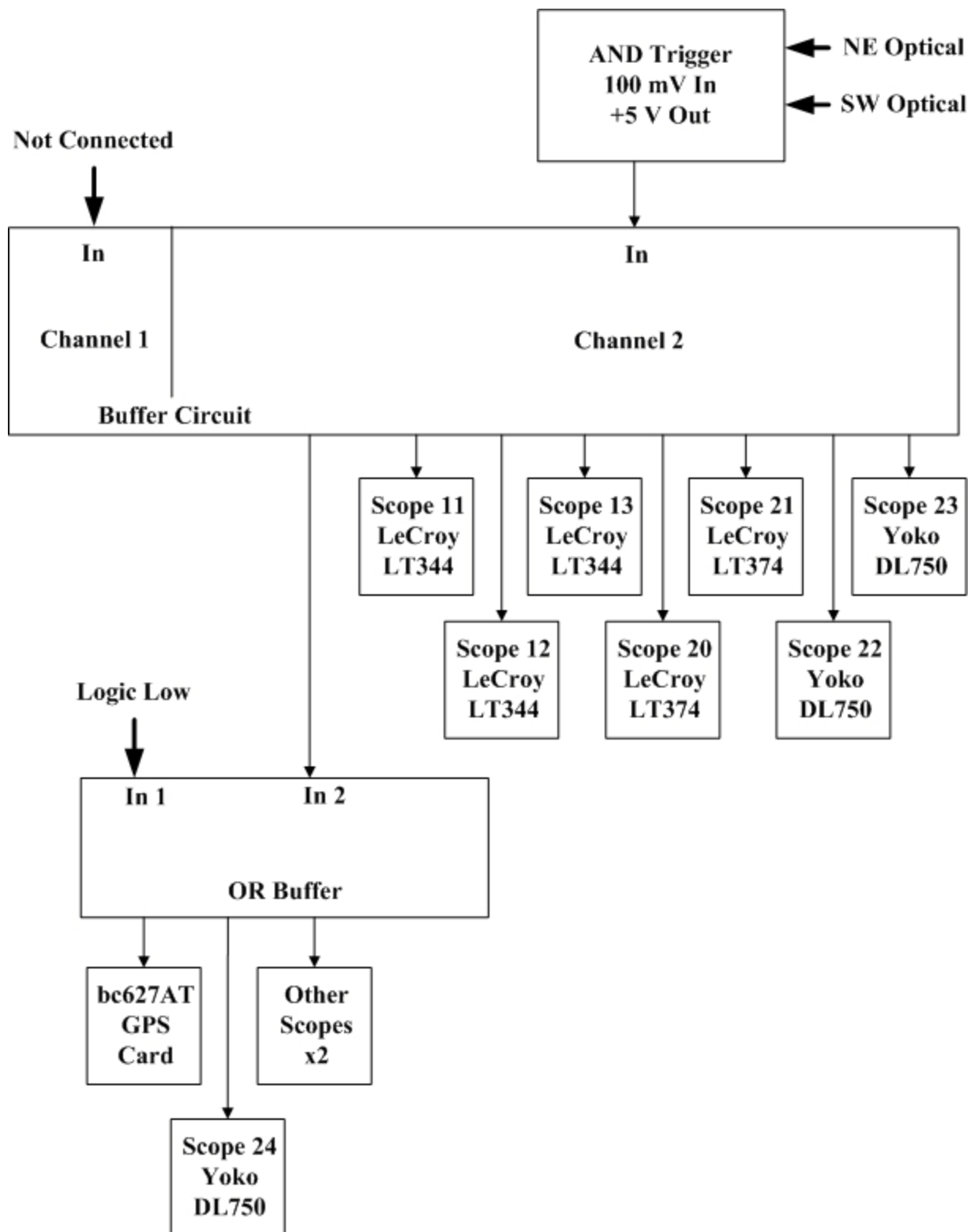


Figure 2-35. Diagram of the 2006 trigger configuration at the ICLRT.

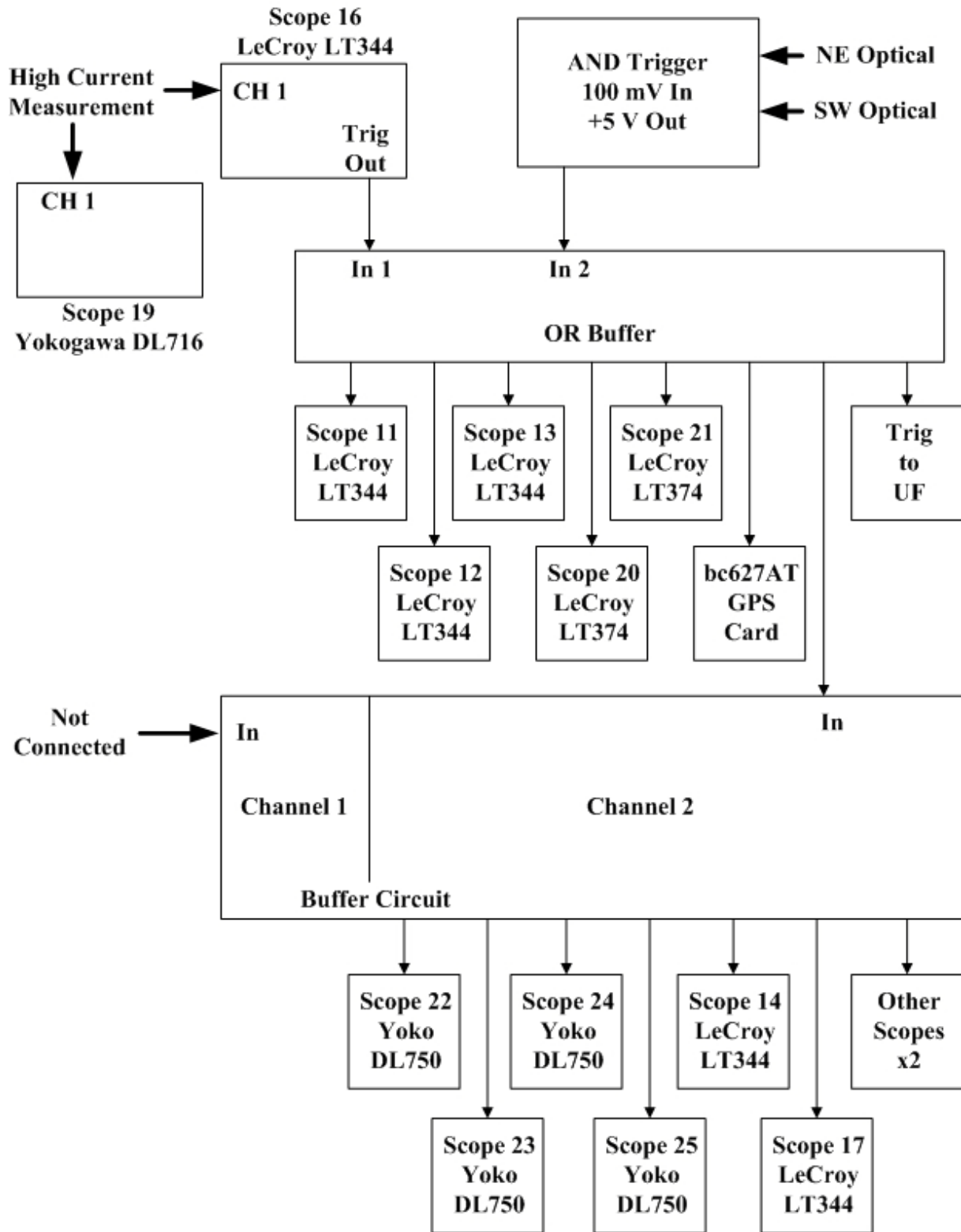


Figure 2-36. Diagram of 2007 trigger configuration at the ICLRT.



Figure 2-37. Components of the MSE/TERA video system.

Table 2-7. Orientation of the MSE/TERA video cameras. The bearing given for each camera follows the convention where due north corresponds to 0° and due east corresponds to 90°.

Camera location	Camera orientation
Instrument Station 1 (IS1)	255° (west-southwest)
Instrument Station 2 (IS2)	240° (southwest)
Instrument Station 3 (IS3)	130° (southeast)
Instrument Station 4 (IS4)	95° (east)



Figure 2-38. Frame of video from the MSE/TERA video system. Each quadrant corresponds to a different camera in MSE/TERA video system, with the labels indicating the locations of the cameras (Figure 2-1). The time stamp superimposed on the image is useful for finding the position of the flash within the video file.

Table 2-8. Summary of the 2005 ICLRT survey with a WAAS-enabled Garmin eTrex Venture hand-held GPS receiver. The Camp Blanding coordinates were obtained by subtracting 100003.674 m and 622156.976 m from the east (X) and north (Y) SPC values, respectively. All measurements are assumed to be coplanar.

Location	Latitude [°N]	Longitude [°W]	CBC east (X) [m]	CBC north (Y) [m]
Tower	29.94267	82.03184	383.885	-196.415
Mobile launcher	29.94330	82.02862	695.382	-129.367
Launch control (north end)	29.94319	82.03159	408.539	-138.987
NEO	29.94441	82.02906	654.007	-5.938
SWO	29.94099	82.03632	-50.313	-378.753
Station 1	29.94348	82.03498	81.547	-103.893
Station 2	29.94404	82.03195	374.631	-44.449
Station 4	29.94330	82.02932	627.802	-128.761
Station 5	29.94323	82.03249	321.69	-133.772
Station 6	29.94180	82.03539	40.284	-289.771
Station 8	29.94147	82.03055	507.232	-330.558
Station 9	29.94025	82.03394	178.726	-462.857
Station 10	29.94070	82.02919	637.768	-417.094
Office trailer (SE corner)	29.94441	82.03583	0	0
IS1	29.94324	82.03182	386.384	-133.245
IS2	29.94442	82.03183	386.595	-2.429
IS3	29.94433	82.03515	65.984	-9.519
IS4	29.94276	82.03603	-20.536	-181.962
Runway west	29.94219	82.03161	405.612	-249.824
Runway east	29.94221	82.03059	504.107	-248.492

Table 2-9. Summary of the 2006 site survey performed with an electronic transverse and surveyor level. All altitudes are referenced to the lowest measurement, TERA-19.

Measurement/location	CBC east (X) [m]	CBC north (Y) [m]	CBC altitude (Z) [m]
dE-1	81.3194	-107.2991	0.887
TERA-1	82.189	-117.7328	1.319
E-2	370.2983	-43.5955	2.555
TERA-2	373.6173	-33.3371	2.918
dE-3	317.2518	-24.6509	0.655
TERA-3	316.9929	-34.5767	1.554
E-4	627.5529	-127.4205	2.673
B-4	621.2462	-128.1443	3.49
dE-4	624.6943	-126.0237	2.615
TERA-4	635.69	-133.1277	3.337
E-5	321.6905	-133.7728	2.174
dE-5	318.8967	-133.101	2.201
TERA-5	323.2554	-143.5353	2.533
E-6	42.1913	-295.3425	0.207
TERA-6	44.7821	-304.3321	0.323
dE-7	331.2264	-368.2023	1.4
TERA-7	327.495	-358.7748	2.308
dE-8	509.2816	-331.0304	2.804
TERA-8	514.8105	-338.2716	2.85
E-9	178.3085	-461.8215	2.193
B-9	174.7677	-467.1145	3.046
dE-9	179.3169	-466.7787	2.11
TERA-9	169.7385	-466.4853	2.772
E-10	632.6201	-416.978	3.341
TERA-10	632.4164	-426.2675	4.009
dE-11	106.6451	-346.7788	0.054
TERA-11	114.0736	-353.3915	0.462
TERA-12	223.5446	-321.8022	1.528
TERA-13	403.8057	-290.3318	3.262
TERA-14	449.5367	-168.3533	3.664
TERA-15	453.1969	-68.5025	2.146
TERA-16	205.6084	-113.4305	1.378
TERA-17	182.8037	-213.0525	1.01
NEO (18)	657.4838	-6.4646	
TERA-18	659.0355	-15.3104	5.273
SWO (19)	-48.8973	-382.2924	
TERA-19	-46.5333	-374.4515	0.0
TERA-20 (tower)	385.9739	-199.0185	16.602
Office trailer (SE corner)	-0.5446	-6.6529	
Field mill (launch control)	392.7921	-152.2022	
Launch Control (SE corner)	405.163	-153.1962	
Launch Control(NE corner)	408.3599	-143.994	
Launch Control (SW corner)	402.8183	-152.3587	

Table 2-10. Locations of the four stations added in 2007. These positions were determined with a WAAS-enabled Garmin eTrex Venture hand-held GPS receiver. The CBC were determined in an identical manner to the values presented in Table 2-8.

Location	Latitude [°N]	Longitude [°W]	CBC east (X) [m]	CBC north (Y) [m]
Station 21	29.9428	82.03068	496.005	-183.01
Station 22	29.94434	82.03029	535.19	-12.633
Station 23	29.94402	82.03397	179.595	-44.911
Station 24	29.94265	82.03312	260.289	-197.52

Table 2-11. Measured time delays for the TOA measurements. Each time delay corresponds to the transit time from the sensor to the respective scope channel on which the signal was recorded. The times listed were obtained from the storm day directory of 2 June 2006.

Measurement	Scope (channel)	Delay time (ns)
dE-1	LeCroy 20 (1)	2577
dE-3	LeCroy 20 (2)	1174
dE-4	LeCroy 20 (3)	1508
dE-5	LeCroy 20 (4)	643
dE-7	LeCroy 21 (1)	1624
dE-8	LeCroy 21 (2)	1891
dE-9	LeCroy 21 (3)	3150
dE-11	LeCroy 21 (4)	3022
TERA-1	LeCroy 12 (1)	2565
TERA-3	LeCroy 12 (2)	1216
TERA-4	LeCroy 12 (3)	1499
TERA-5	LeCroy 12 (4)	636
TERA-7	LeCroy 13 (1)	1667
TERA-8	LeCroy 13 (2)	1881
TERA-9	LeCroy 13 (3)	3141
TERA-11	LeCroy 13 (4)	3062
TERA-1	LeCroy 11 (1)	2571
TERA-7	LeCroy 11 (2)	1673
dE-1	LeCroy 11 (3)	2583
dE-7	LeCroy 11 (4)	1630

CHAPTER 3 DATA

Operating the Multiple Station Experiment/Thunderstorm Energetic Radiation Array (MSE/TERA) network and documenting the data obtained between 2005 and 2007 has accounted for a significant portion of the author's Ph.D. research. Enough data were acquired during this period that the analyses presented in subsequent chapters of this dissertation represent only a fraction of the total data set. Most of the data that are not analyzed here were either obtained by the author on behalf of collaborative researchers or simply fell outside the scope of the author's primary interest. However, these data may prove useful for future studies, so it is important to document all of the data acquired. This chapter provides an overview of the natural and rocket-triggered lightning data recorded by the MSE/TERA network between 2005 and 2007. Included in this overview are a list of the recorded flashes, a summary of the data recorded for each flash, and some details of the oscilloscope and trigger configurations for each event. In addition, the file structure used to document the recorded data is outlined. Finally, the steps used to calibrate and process the raw data recorded by the digitizers are also discussed.

3.1 Data Summary and Organization

During the period from 2005 to 2007, data were acquired for 9 rocket-triggered flashes and 18 natural flashes that terminated within or very near the network. All of these flashes lowered negative charge to ground. Lists of the natural and rocket-triggered lightning flashes recorded by the MSE/TERA network are given in Tables 3-1 and 3-2, respectively. Each flash is given a unique identifier which indicates the type of flash and in what year it was recorded. Natural flashes are labeled with the nomenclature MSEYYFF, where MSE indicates that it was a natural flash, YY indicates the two-digit year, and FF identifies the flash number for that year. Rocket-triggered flashes are labeled with the nomenclature UFYYFF, where UF indicates a rocket-

triggered lightning, YY is the year, and FF identifies the shot attempt for that year. The flash numbers, FF, for the natural and rocket-triggered flashes are unrelated, i.e., there can be both flashes MSE0501 and UF0501. This fact is further evident in that the natural flash identifiers are consecutive in number and the rocket-triggered flashes are recorded only for successful shot attempts. The trigger times given to six decimal places in Tables 3-1 and 3-2 were obtained with the GPS time-stamping system and should have an accuracy of a few microseconds. If the time-stamping system was not triggered for a flash, the time was obtained from the oscilloscope header files and should be accurate to within a few minutes. Also included in Tables 3-1 and 3-2 are the trigger configuration used for each flash (see Section 2.6) and a comment, if necessary, about the data set. Complete data sets were not obtained for all flashes. This was primarily due to the relatively long rearming time of the Yokogawa oscilloscopes; however, other circumstances occasionally caused some oscilloscopes not to trigger.

The lightning data are sorted according to storm day (date) and oscilloscope ID. All data recorded on the same day are placed into a single directory whose name corresponds with the date, e.g., all data recorded for MSE0503 through MSE0506 (see Table 3-1) are located in the “/082805/” directory. Inside the storm day directory, data are further divided into folders that correspond to the different oscilloscopes used to record the data. Hence, data recorded by Scope 13, for example, on 28 August 2005 are located in the “/082805/Scope13/” folder. Inside each oscilloscope ID folder are the binary pre-storm and post-storm calibration files as well as all the data files obtained by that scope on that day. The nomenclature used to label these binary files was discussed in Section 2.4.

Additional files, which document the data acquisition, are also included in each storm day directory. Among these are the text files generated by the GPS time-stamping system and the

running spreadsheet that documents the measurement time delays (see Section 2.8). A spreadsheet entitled “MMDDYY_Data_List,” where MMDDYY is the storm day, provides a list correlating each measurement to its appropriate binary file for each flash. Another spreadsheet, entitled “Equipment_Table_MMDDYY,” provides an in-depth description of each measurement, including the sensor’s nominal transducer factor, attenuation setting of the PIC controller, address of the PIC controller, color of the data fiber used, associated oscilloscope channel(s), the fiber-optic link pair, and the final calibration factor (physical units/volt) that includes the gain of the fiber-optic link (see Section 3.2). Finally, a text document that recounts the general storm conditions, chronicles the flash events, describes the acquired data set, discusses known equipment problems, and provides flash details is generated for each storm day.

Deciding the best method to summarize the acquired data was a difficult task. One approach would have been a table listing all the oscilloscope file names obtained with each flash; however, such a table would have been unwieldy and not particularly informative as to the types of data acquired with each flash. Instead, a series of tables are used here to summarize the collection of data. Tables 3-3, 3-4, and 3-5 list the types of measurements (see Chapter 2) assigned to each oscilloscope during the 2005, 2006, and 2007 configurations, respectively. Tables 3-6 and 3-7 indicate the types of data acquired for each flash. The collection of these tables, combined with Tables 3-1 and 3-2, provide a quick reference of the available data and indicate which oscilloscopes were used. Persons with access to the raw data can then use the appropriate “MMDDYY_Data_List” spreadsheet to locate specific binary files.

3.2 Data Calibration and Processing

The analysis of recorded data usually requires some manipulation of the raw waveforms, typically in the form of time shifts that account for differences in time delays, amplitude shifts that account for vertical offset introduced by the fiber-optic links, and application of calibration

factors that scale the raw amplitude data recorded (in units of volts) to the proper physical units (such as kV m^{-1} for electric field). Of course, the binary data files recorded by the oscilloscopes are never altered directly. The binary files are read by programs written in an interactive computing environment, such as Matrix Laboratory (MATLAB) or Interactive Data Language (IDL), either by the author or other University of Florida Ph.D. students. These programs typically read one channel at a time and return the timing and amplitude data as separate vectors (or arrays for the LeCroy oscilloscopes, which may record multiple segments). Additional programs used to plot, compare, and analyze the data typically apply the aforementioned corrections to the waveforms.

When waveforms need to be temporally aligned, the time axes of the waveforms are shifted (simple addition or subtraction of a scalar value to the time vector) according to the values recoded in the time delay spreadsheet. For analyses that are extremely time critical, such as time-of-arrival (TOA), additional steps are taken to account for any potential differences in the oscilloscope trigger times. The amplitude and vertical offset calibration involves multiple quantities and is expressed analytically in Equation 3-1.

$$P = G_{nom} G_{FOL} (v_{scope} - v_{offset}) \quad (3-1)$$

The quantity P is the calibrated data in physical units (e.g., kV m^{-1} for electric field). The quantity v_{scope} is the actual voltage recorded on the oscilloscope, and v_{offset} is the vertical offset that is assumed to be artificial and introduced by the fiber-optic link. The value of v_{offset} is typically approximated by averaging the first thousand samples of a given waveform; however, care must be taken in the case of x-ray waveforms that no background events were detected in this 1000 sample window. G_{nom} is the nominal calibration factor that converts the waveform units from volts to physical units, and it represents any gain or attenuation from

amplifiers, active integrators, and/or PIC controllers. The nominal calibration factors were briefly discussed for each of the MSE/TERA measurements in Chapter 2. The quantity G_{FOL} is an estimate of the low-frequency gain of the fiber-optic link (FOL), and its value, which is near unity (except for the optical measurements), may differ for each storm day. Hence, the value of G_{FOL} is determined each storm day using the calibration signal generator of the PIC controller. As discussed in Section 2.2.1, the PIC controller can produce a 100 Hz square-wave with peak-to-peak amplitude of 0.1 or 1 V that is injected into the FO transmitter of the measurement and recorded in Launch Control. Typically, the calibration waveforms are obtained when the network is being armed and disarmed, with the lightning data being recorded between the two sets of calibration signals. When both pre-storm and post-storm calibration waveforms are available, the amplitudes are averaged and divided by the actual amplitude of the calibration waveform, which is known. The value of G_{FOL} is then obtained by taking the reciprocal, as expressed in Equation 3-2.

$$G_{FOL} = \frac{2(v_{cal-actual})}{v_{cal-pre} + v_{cal-post}} \quad (3-2)$$

The quantity $v_{cal-actual}$ is the actual peak-to-peak amplitude of the calibration waveform generated by the PIC controller. The quantities $v_{cal-pre}$ and $v_{cal-post}$ are the peak-to-peak amplitudes of the calibration waveforms recorded before and after the storm, respectively. In calculating the peak-to-peak amplitude of the recorded calibration signals, all points are separated into groups of values that fall above and below zero. Each group is averaged, and all points falling outside $\pm 10\%$ of the average value are discarded. The average of each group is then recalculated, yielding estimates of the positive and negative levels that are reasonably immune to waveform noise and overshoot, both of which can yield biased peak-to-peak values. It is noted, however, that overshoot is typically not a problem with the Opticomm FO links used

with the majority of MSE/TERA measurements. The values obtained by this technique for the positive and negative levels are eventually subtracted to yield the effective peak-to-peak value. If only one of the two calibration measurements is obtained, then that value is simply divided into $v_{cal-actual}$ to determine G_{FOL} . If neither calibration signal is obtained, then the nominal calibration factor is used. The final calibration factor for every measurement is documented in the “Equipment_Table_MMDDYY” spreadsheet located in each storm day directory.

Table 3-1. List of natural cloud-to-ground flashes recorded by the MSE/TERA network. All flashes lowered negative charge to ground. Flash times given with microsecond precision were obtained from the GPS time-stamping system. Flash times given with minute precision had to be obtained from the oscilloscope records and should be considered accurate within a few minutes. The trigger configuration (see Section 2.6) used for each flash is also provided.

Flash ID	Date	Time (UT)	Trigger configuration	Comment
MSE0501	07/23/2005	23:02:19.949412	2005	
MSE0502	07/29/2005	17:21:30.282984	2005	TOA data only
MSE0503	08/28/2005	19:26:10.133826	2005	
MSE0504	08/28/2005	19:28:51.397462	2005	TOA data only
MSE0505	08/28/2005	19:31:05.242503	2005	TOA data only
MSE0506	08/28/2005	19:35:25.090621	2005	
MSE0507	09/28/2005	20:23:28.474499	2005	See note ^a
MSE0601	02/03/2006	08:44:30.001257	2005	
MSE0602	04/09/2006	01:46	2005	
MSE0603	06/02/2006	22:07:50.180395	2006	No TOA data
MSE0604	06/02/2006	22:08:50.549345	2006	TOA data only
MSE0701	07/01/2007	19:41:27.878000	2006	TERA data only
MSE0702	07/01/2007	19:51:51.410175	2006	TERA data only
MSE0703	07/14/2007	16:24:50.284319	2007	
MSE0704	07/16/2007	23:26:59.992925	2007	
MSE0705	07/31/2007	20:00:24.216051	2007	
MSE0706	10/04/2007	21:08:45.021801	2007	
MSE0707	10/05/2007	18:33:22.890584	2007	

a) A significant number of measurements were not operational for this event due to environmental factors

Table 3-2. List of rocket-triggered flashes recorded by the MSE/TERA network. All flashes lowered negative charge to ground. Flash times given with microsecond precision were obtained from the GPS time-stamping system. The trigger configuration (see Section 2.6) used for each flash is also provided.

Flash ID	Date	Time	Location	Trigger configuration	Comment
UF0501	07/02/2005	23:22:46.039946	Mobile	2005	
UF0503	07/02/2005	23:37:26.980331	Mobile	2005	
UF0510	07/31/2005	20:02:41.108662	Tower	2005	Current data only
UF0512	07/31/2005	20:13:54.272410	Tower	2005	
UF0514	08/04/2005	18:44:24.486010	Tower	2005	
UF0517	08/04/2005	19:32:33.170124	Tower	2005	
UF0520	08/05/2005	21:24:30.949257	Tower	2005	
UF0521	08/05/2005	21:30:38.028912	Tower	2005	Current data only
UF0707	07/31/2007	19:35:44.855113	Tower	2007	Larger RS current

Table 3-3. Summary of DSO allocation and settings for 2005 MSE/TERA configuration

Scope ID	Model	MSE/TERA Usage	Sampling rate	Record length
12	LT344	Current	100 MHz	10 segments, 1 ms each
13	LT344	TOA dE/dt	250 MHz	2 segments, 2 ms each
19	DL716	Current	10 MHz	1.6 s or 800 ms
20	LT374	TOA dE/dt, TOA X ray	200 MHz	10 segments, 2 ms each
21	LT374	TOA dE/dt, TOA X ray	200 MHz	10 segments, 2 ms each
22	DL750	E, B, X ray, Optical	10 MHz	2s
23	DL750	X ray	10 MHz	2s

Table 3-4. Summary of DSO allocation and settings for 2006 MSE/TERA configuration

Scope ID	Model	MSE/TERA Usage	Sampling rate	Record length
11	LT344	TOA sync scope	250 MHz	2 segments, 2 ms each
12	LT344	TOA X rays	250 MHz	2 segments, 2 ms each
13	LT344	TOA X rays	250 MHz	2 segments, 2 ms each
20	LT374	TOA dE/dt	250 MHz	8 segments, 2 ms each
21	LT374	TOA dE/dt	250 MHz	8 segments, 2 ms each
22	DL750	E, B, X ray, Optical	10 MHz	2s
23	DL750	X ray	10 MHz	2s
24	DL750	X ray	10 MHz	2s

Table 3-5. Summary of DSO allocation and settings for 2007 MSE/TERA configuration

Scope ID	Model	MSE/TERA Usage	Sampling rate	Record length
11	LT344	TOA sync scope	250 MHz	2 segments, 2 ms each
12	LT344	TOA X rays	250 MHz	2 segments, 2 ms each
13	LT344	TOA X rays	250 MHz	2 segments, 2 ms each
14	LT344	Large dE/dt	250 MHz	2 segments, 2 ms each
16	LT344	Current	100 MHz	10 segments, 1 ms each
17	LT344	Other dE/dt, PPMT	250 MHz	2 segments, 2 ms each
19	DL716	Current	10 MHz	800 ms
20	LT374	TOA dE/dt	250 MHz	8 segments, 2 ms each
21	LT374	TOA dE/dt	250 MHz	8 segments, 2 ms each
22	DL750	E, B, X ray, Optical	10 MHz	2s
23	DL750	X ray	10 MHz	2s
24	DL750	X ray	10 MHz	2s
25	DL750	X ray	10 MHz	2s

Table 3-6. Summary of data obtained by the MSE/TERA network for natural lightning flashes

Flash ID	TOA dE/dt	TOA X ray	E-field	B-field	TERA	Optical	Other dE/dt	Large dE/dt	PPMT
MSE0501	Yes	Yes ^a	Yes	Yes	Yes	Yes	-	-	-
MSE0502	Yes	Yes ^a	No	No	No	No	-	-	-
MSE0503	Yes	Yes	Yes	Yes	Yes	Yes	-	-	-
MSE0504	Yes	Yes	No	No	No	No	-	-	-
MSE0505	Yes	Yes	No	No	No	No	-	-	-
MSE0506	Yes	Yes ^a	Yes	Yes	Yes	Yes	-	-	-
MSE0507	No	No	Yes	Yes	Yes	Yes	-	-	-
MSE0601	Yes ^a	Yes ^a	Yes	Yes	Yes	Yes	-	-	-
MSE0602	Yes ^a	Yes ^a	Yes	Yes	Yes	Yes	-	-	-
MSE0603	No	No	Yes	Yes	Yes	Yes	-	-	-
MSE0604	Yes	Yes	No	No	No	No	-	-	-
MSE0701	No	No	No	No	Yes	No	-	-	-
MSE0702	No	No	No	No	Yes	No	-	-	-
MSE0703	Yes	Yes	Yes	Yes	Yes	Yes	No	Yes	No
MSE0704	Yes	Yes	Yes	Yes	Yes	Yes	No	Yes	No
MSE0705	Yes	Yes	Yes	Yes	Yes	Yes	Yes	Yes	Yes
MSE0706	Yes	Yes	Yes	Yes	Yes	Yes	No	No	No
MSE0707	Yes	Yes	Yes	Yes	Yes	Yes	Yes	Yes	Yes

a) TOA analysis cannot be attempted due to malfunctioning stations or an obvious absence of signature events

Table 3-7. Summary of data obtained by the MSE/TERA network for rocket-triggered flashes. All of the flashes listed in this table produced at least a single return stroke for which the current was measured.

Flash ID	TOA dE/dt	TOA X ray	E-field	B-field	TERA	Optical	Other dE/dt	Large dE/dt	PPMT
UF0501	Yes ^a	Yes ^a	Yes	Yes	Yes	Yes	-	-	-
UF0503	Yes ^a	No	Yes	Yes	Yes	Yes	-	-	-
UF0510	No	No	No	No	No	No	-	-	-
UF0512	Yes	Yes	Yes	Yes	Yes	Yes	-	-	-
UF0514	Yes	Yes ^a	Yes	Yes	Yes	Yes	-	-	-
UF0517	Yes	Yes ^a	Yes	Yes	Yes	Yes	-	-	-
UF0520	Yes	Yes ^a	Yes	Yes	Yes	Yes	-	-	-
UF0521	No	No	No	No	No	No	-	-	-
UF0707	Yes	Yes	Yes	Yes	Yes	Yes	Yes	Yes	Yes

a) TOA analysis cannot be attempted due to malfunctioning stations or an obvious absence of signature events

CHAPTER 4 LOCATING LIGHTNING EVENTS WITH THE MSE/TERA TOA NETWORK

Knowing the location of lightning processes relative to the individual Multiple Station Experiment/Thunderstorm Energetic Radiation Array (MSE/TERA) sensors is often critical in analyzing or modeling lightning data. For some analyses the radial distance between the sensors and the ground strike point is all that is required. This information is easily obtained for rocket-triggered flashes, but it is generally more difficult to obtain for natural flashes. Although video records (when available) can provide an indication of the lightning location, the relatively low image quality and lack of synchronization between individual cameras in the MSE/TERA video system make an adequate determination difficult. In recent years, time-of-arrival (TOA) measurements have been obtained for a subset of measurements in the MSE/TERA network in order to locate lightning processes.

TOA techniques were first used with MSE measurements in 2002 in an attempt to reliably and accurately determine the two-dimensional $(x, y, 0)$ strike locations for natural flashes observed by the network. The four dE/dt measurements of the MSE, due to their relatively high bandwidth (upper-frequency limit of about 20 MHz) and high time resolution (5 ns for most flashes), were chosen to form a hyperbolic position-fixing system. The arrival time for each dE/dt measurement was selected from the peak return-stroke value. As discussed in Section 1.6, this type of system utilizes the differences in arrival times to define a set of hyperbolas, with the intersection of these hyperbolas identifying the source location. A minimum of three measurements, which provides two independent time-difference equations with two unknowns (x, y) , is required to determine a two-dimensional (2D) source location, but a fourth measurement may be required if the intersection is not unique, i.e., two distinct hyperbolas may intersect at two locations. Clearly, the four dE/dt sensors can provide an overdetermined system (three time-

difference equations with two unknowns) that can be solved for the lightning location using a non-linear optimization technique. In practice, however, the lightning location was determined by averaging the solutions from the four independent three-station combinations. This latter method was preferred because an erroneous arrival time could usually be detected through the comparison of the independent solutions. Further, it was not unusual for one arrival time to be absent either due to signal saturation or a problem with a sensor, in which case the location was determined from a single three-station combination. *Jerauld* [2007] discusses this approach, presents a graphical interpretation of the solution (i.e., plots of intersecting hyperbolas), and provides the location results for the natural flashes observed by the MSE between 2002 and 2004. The accuracy for this system, which was determined by comparing the calculated locations for rocket-triggered flashes with the known positions of the launchers, was found to be better than 10 m for lightning strikes occurring within the network boundaries.

In 2005, following sufficient success in providing 2D strike locations, an initial attempt to track various lightning processes, such as the leader and attachment phases, in three dimensions was made using the same TOA system. As discussed in Section 1.6, four sensors can provide three independent time-difference equations with three unknown spatial coordinates (x , y , z), i.e., the solution can be viewed as the intersection of three hyperboloids in space. In general, it is possible for three hyperboloids to intersect at two equivalent points in space, resulting in dual, nonunique solutions; however, typical TOA applications allow one of these solutions to be ruled out because it exists beneath the plane of the sensors (assuming the sensors are coplanar or nearly coplanar), i.e., one of the solutions is located beneath the ground. Of course, determining the source location is not limited to using only the time-difference equations. One alternative is to plug the observed arrival times into Equation 1-1 and solve the resulting system of non-linear

equations (typically via numerical methods). The hyperplane approach (discussed in Section 1.6) is another alternative, but this technique requires that the sensors be exactly coplanar when using only four sensors. The small altitude differences between the sensors cause the source altitude to be very poorly determined with the hyperplane technique. During this preliminary attempt to find 3D locations, the two former techniques were tested and produced similar, if not identical, results. Unfortunately, it was quickly evident that there were serious shortcomings in the system's ability to locate sources in three-dimensions. Most significantly, the use of four sensors did not permit any kind of estimation for the location accuracy, and there appeared to be significant errors in the altitude determinations, based on the erratic altitude values calculated for sequential leader steps. These issues were not the result of an inferior retrieval algorithm, but primarily a lack of additional independent observations. Hence, the TOA network required additional sensors to provide sufficient 3D resolution. Starting with the 2006 network configuration (see Tables 3-1, 3-2, 3-4, and 3-5), the TOA portion of the MSE/TERA network was expanded to eight stations. Further, each of these stations was also equipped with an unshielded PMT (UPMT) detector, in the first attempt to locate sources of energetic radiation associated with the lightning channel. The operation of this eight-station TOA system is the topic of discussion for the remainder of the chapter.

4.1 Methodology

Similar to other TOA systems, the objective of the MSE/TERA TOA network is to use a set of measured arrival times to solve the TOA equation (Equation 1-1) for the source location and time of occurrence. As noted in Section 1-6, the primary differences in this system compared to others is its high spatial resolution for low-altitude sources, which is permitted by the network's small physical size, and its high temporal resolution, achieved with a high sample rate and the manual examination of the waveform records. This system is also designed to locate

two types of sources – electric field change sources and X-ray sources. Note that electric field change sources are located using arrival times obtained only with the dE/dt measurements, and X-ray sources are located using arrival times obtained only with the UPMT sensors. The dE/dt and X-ray TOA measurements are not used interchangeably (i.e., electric field change sources are located using only arrival times obtained with the dE/dt antennas) although they are time-synchronized, as discussed in Section 4.2.

The solution algorithm for this network is largely patterned after the algorithms used for the LMA networks described by *Thomas et al.* [2004] and *Koshak et al.* [2004]. The key element is the nonlinear least squares Marquardt algorithm, which incorporates the best features of a gradient search with a Newton-type iteration. This algorithm minimizes the chi-square goodness of fit value given in Equation 4-1.

$$\chi^2 = \sum_{i=1}^N \frac{(t_i^{obs} - t_i^{fit})^2}{\Delta t_{rms}^2} \quad (4-1)$$

The value t_i^{obs} is the measured arrival time at the i_{th} station, t_i^{fit} is the predicted arrival time from Equation 1-1 for each trial solution, and N is the number of stations participating in the solution. The quantity Δt_{rms} is the uncertainty of the timing measurements. The uncertainty term is representative of the combined errors in determining the arrival time from the waveform, the transmission delay associated with the measurement, and the precise location of the sensor, which is equivalently represented with a timing error. In general, the uncertainty may be different for each observation; however, this term is considered constant and the same for all of the dE/dt measurements (and likewise for all of the X-ray measurements), due to their identical construction. The uncertainty is described as a root-mean-square (rms) error because it is also assumed to be Gaussian distributed. The Marquardt algorithm minimizes χ^2 in an iterative manner by linearizing the TOA equation for each station around successive trial solutions and by

solving the linearized equations to obtain the next trial solution. As discussed by *Bevington* [1969], the linearized curvature matrix used to obtain the solution can be inverted to obtain the covariance matrix describing the uncertainties of the (x, y, z, t) values, i.e., the square root of the diagonal elements in the covariance matrix corresponds to the predicted rms errors for the solution variables.

It is worth noting that the timing uncertainty Δt_{rms} may not necessarily be known a priori (an initial value of 40 ns was assumed for this dissertation); however, the resultant χ^2 values can be readily scaled to any constant rms timing error by multiplying by $(40 \text{ ns}/\Delta t_{actual})^2$. As discussed in Section 4.3, the timing uncertainty is an important metric for gauging the accuracy of any TOA system, and the ability to scale the goodness of fit values is also an important feature in determining the timing uncertainty. The goodness of fit values can also be normalized relative to the number of measurements N by determining the reduced chi-square value, $\chi_v^2 = \chi^2/v$, where $v = (N - 4)$ is the number of degrees of freedom (i.e., the number of redundant measurements) for the solution.

The maximum number of arrival time measurements available for any single event is obviously eight; however, it is more common than not for some of these measurements to be unavailable, usually due to the lack of detection at some stations or possibly a malfunctioning sensor. Moreover, the accuracy of the measured arrival times is not guaranteed beforehand, i.e., individual arrival times may be adversely affected by signal-to-noise effects, which cause weaker signals to be timed less accurately than strong signal, or spurious noise sources, although the visual comparison of the waveforms usually prevents this. In order to minimize the effect of these poorly determined arrival times, solutions are attempted and compared for all possible station combinations where $N \geq 5$, five being the minimum number of stations needed for

redundancy and error estimation. The solution producing the smallest reduced chi-square value and smallest location uncertainty (from the trace of the covariance matrix) is considered the valid result. The metric used is the product of χ_v^2 and the trace.

In truth, the use of the Marquardt algorithm is only part of the multi-stage procedure that translates physical measurements into arrival times and then ultimately into 3D source locations. A discussion of the overall procedure as well as the computer programs involved is provided in the following section.

4.2 Implementation

The TOA network is physically constructed of eight dE/dt antennas and eight UPMT sensors located at Stations 1, 3, 4, 5, 7, 8, 9, and 11 (see Figure 2-1). As documented in Tables 3-4 and 3-5, the dE/dt waveforms are recorded on two LeCroy LT374 DSOs (Scopes 20 and 21) and the UPMT signals are recorded on two LeCroy LT344 DSOs (Scopes 12 and 13). The four lower station numbers are stored on Scopes 12 and 20, while the higher station numbers are stored on Scopes 13 and 21. Additionally, one channel from each scope (Stations 1 and 7 were used) was transmitted over a 4 ft (1.22 m) length of coax to Scope 11 (LeCroy LT344) for the purposes of time synchronization, as discussed below. For any type of trigger event (see Figures 2-35 and 2-36), each of these scopes records a 1 ms segment of data (with 50% pretrigger) at 250 MS/s. One difference in the oscilloscopes, however, is that the LeCroy LT374 models are capable of recording up to 8 segments for a flash (i.e., up to 8 strokes), while the LeCroy LT344 models can only record up to 2. Once the data are obtained, the steps necessary to calculate source locations include timebase synchronization, waveform correlation and visualization, event identification, arrival time selection, source determination (Marquardt algorithm), and documentation. All of these tasks are accomplished with author-written functions based in MATLAB®.

4.2.1 Time Synchronization

Timebase synchronization is the first step, and it is the only step in which both the dE/dt and X-ray waveforms are used together. Following synchronization, the two types of waveforms are processed separately to locate their respective types of sources. Since we are interested in comparing the times of occurrence for the X-ray and electric field change sources, it is critical that all of the TOA waveforms are referenced to a common timebase. The need for timebase synchronization arises from the fact that the waveforms are stored across four different oscilloscopes. Although the system was designed to have identical trigger delays and utilizes similar scopes with similar settings, there is still the potential for differences in the oscilloscope trigger times. One potential source for this difference is that the oscilloscopes may actually trigger at different times due to slight differences in the individual trigger circuits, e.g., bandwidth or internal delays. The other source of this error is that the horizontal offset, due to the use of the pretrigger function, is not the same for each oscilloscope. In fact, consecutive triggers on the same oscilloscope with identical settings may produce different offsets, typically ± 1 sample of the desired offset. Hence, this latter type of error is usually limited to a maximum of 2 sample points, which would be 8 ns at 250 MHz. Although this error appears small, it should be accounted for if at all possible because this error is systematic and it will affect at least four of the measurements.

The key to performing the timebase synchronization is the use of Scope 11, which records one signal from each of the four TOA oscilloscopes. Since these signals are recorded on the same oscilloscope, their exact temporal relationship (at least to the resolution of the instrument) is known. All that is needed is to determine the horizontal shifts necessary to replicate the same temporal relationship between the corresponding signals on Scopes 12, 13, 20, and 21. The time synchronization is completed by applying identical time shifts to the measurements on

corresponding oscilloscopes. The program used to accomplish this task is called `scorr06.m`, where the extension “m” stands for M-file, the default binary file type for MATLAB. The program `scorr06.m` basically determines how much each signal on Scope 11 lags its corresponding signal on the TOA oscilloscopes by using an autocorrelation function. Since each signal was delayed from a TOA oscilloscope to Scope 11 by an identical length of cable and the system was designed with identical trigger settings and delays, all of the signals on Scope 11 should ideally lag their corresponding signal on the TOA oscilloscopes by the same amount. Due to the errors discussed above, the lag values will generally not be the same. To achieve synchronization, one of the signals (dE/dt at Station 7) is chosen as a reference and the timebases of the other TOA scopes are adjusted so that if the autocorrelations were performed again they would all lag by the same amount as the reference station. It is noted that the autocorrelation is not performed on the entire waveform as its computational expense would be too great (each LeCroy data segment contains 250,000 points). Instead, five overlapping 50 μ s segments (typically around the return stroke to ensure sufficient structure) are extracted from each waveform and the autocorrelation is performed on them. The results from the five calculations are compared and the mode is selected as the proper value. Initially, it was uncertain how severe the differences in trigger times would be, but preliminary results show that the difference in trigger times is almost always zero, with the maximum ever observed being two sample points (8 ns). This is an important result in the event that more than two strokes are recorded for a single flash (although none were in this study), as Scope 11 can only record two strokes. It would not be optimal, but a zero difference in the trigger times could be assumed with a high percentage of being correct and a fairly minimal effect, although no definite effects are predicted here, if the assumption was wrong.

4.2.2 Waveform Correlation and Visualization

From here on, the tasks of locating dE/dt and X-ray sources are handled separately. Although these tasks utilize the same methodology, different programs are used, as we shall note. At this point, it is clear that the waveforms need to be viewed so that events of interest can be identified. Because of the different transmission delay times and the unknown location of the source, a common event will appear at a different time on each channel. Hence, it can be very difficult to keep track of the same event across eight different channels, especially near the return stroke where there is a lot of waveform structure. For the task of identifying events and eventually selecting arrival times, it would be much more helpful if all the waveforms were shifted in time so that common events would typically appear at nearly the same time value in a plot. Although stepped leaders generally have great spatial extent, capable of producing a wide range of time differences, the range of the dE/dt antennas and the X-ray sensors is relatively limited. Moreover, the return stroke of the dE/dt waveforms can be used to unambiguously determine the strike location, a region that is known to have involved stepped leader activity producing similar time differences.

The process of correlating and plotting the waveforms for easy event identification is accomplished with two programs. The programs dEcorr06.m and dEwave06.m are used for the dE/dt waveforms, and the programs xcorr06.m and xwave06.m for the X-ray waveforms. The program dEcorr06.m selects one station as a reference (Station 7) and performs a cross correlation, using a 50 μ s segment just prior to the return stroke to get good structure and avoid signal saturation, with all of the other available dE/dt waveforms. The peak value of the correlation function is then used to determine the optimum time shift for each waveform. It is noted that this shift is actually determined as a number of samples instead of seconds because the correlation function requires the timebase interval for each waveform to be exactly the same, and

this is not precisely true of the floating-point values returned by the different oscilloscopes. The time delay determined for each waveform is returned in a structure which is then called by the dEwave06.m program. The dEwave06.m program applies the appropriate time shift to each waveform, removes any vertical offset present in the each waveform, introduces artificial levels of vertical offset to facilitate easy viewing of the waveforms (increasing offset with increasing station number), and then displays all the waveforms (color coded) in a single plot. Note that the time base of this plot has units of sample number.

The xcorr06.m and xwave06.m programs operate very similarly to their corresponding counterparts for the dE/dt waveforms, although there are some important differences. There is a particular problem with attempting to correlate X-ray waveforms from different stations due to the nondistinguishable waveshape of X-ray pulses. The resultant correlation function typically has multiple peaks, the largest of which may not correspond to the best time shift for the intended purpose. In fact, it is possible that the peak value corresponds to a shift time that is physically impossible due to the constraints of the station positions and their associated delays. This is a result of every X-ray event having the same characteristic shape. The trick is to pick the peak value of the correlation function within the range of physically possible values. To ensure the proper time is selected, xcorr06.m calls another program windel.m, which opens and reads a text file (DelayWindows.txt) containing the highest and lowest time delay value that each station can have with respect to the reference channel. These delay values were previously calculated in Mathcad[®] using the station locations (Table 2-9), transmission delays (see Table 2-11), and the knowledge that the sources providing these two delays correspond to the station locations themselves. Following the appropriate selection of a delay time for each waveform, xwave06.m calls the returned structure and generates a plot similarly to dEwave06.m.

4.2.3 Arrival Time Selection

The process of event identification involves little more than using the zoom and scroll features of the previously generated plots to identify events that have a strong correlation in time (as well as structure in the case of dE/dt), so there is no need to devote a full section to it. The important step is determining the appropriate arrival time for each station once an event has been identified. For the dE/dt waveforms this process is almost completely automated and involves the `dEindices06.m` and the `dEtimes06.m` programs. The first step in determining the arrival times is to use the plot cursor to export a point before (called “Start”) and after (called “Stop”) the dE/dt event to the workspace. A vector called “notime” should also be defined in the workspace with the entries corresponding to any station that did not detect this specific event. The vector, notime, can have its entries entered in any order, but it cannot have more than three entries. The program `dEindices06.m` uses these three variables to extract the data between the Start and Stop points for each waveform that is not identified in the vector, notime. The program then identifies the position of the peak value in each extracted segment. However, the program does not return the corresponding sample number from the plot axis; rather, it returns the position index for that sample number in the time vector of the corresponding waveform. Returning the position index instead of the sample number bypasses the need to add back the shift that was applied when generating the plot. The program ultimately returns an eight element vector “I,” with the entries corresponding to the position index for the event in each waveform. The first entry in the vector, I, corresponds to Station 1, and subsequent entries correspond to ascending station numbers in the TOA network. Any station that was identified in the vector, notime, has its corresponding position in vector, I, filled with 0. In certain cases, where a peak may be somewhat rounded (more than one sample point at the peak value) or Start and Stop points cannot be set to properly identify the same event on all channels (closely spaced events),

the position index for one or more data points can be exported manually to the workspace using the plot cursor. Once in the workspace, simple vector operations can be used to construct the appropriate vector of indices, I . The program `dEtime06.m` then calls the vector, I , and finds the corresponding time values from the appropriate oscilloscope time vectors. This program also corrects for any trigger time differences that were detected with the `scorr06.m` program. The `dEtime06.m` program returns the times in vector T , which has zeros in the same entries as vector I .

The procedure for selecting arrival times from the X-ray waveforms is much more troublesome and involves much more manual effort. The `xtime06` program is very similar to `dEtime06.m`, but there is no counterpart for the `dEindecies06.m` program because an appropriate algorithm for automatically selecting the arrival times could not be generated. Hence, the arrival times for the X-ray events are manually exported, one at a time, to the workspace, where the vector, i , is constructed using manual command entry. The entries of “ i ” are generally defined as the first data point that indicates a negative going trend, below any background noise. It was soon discovered that there are far fewer X-ray events that can be located than dE/dt events, due to lack of correlated observation at 5 or more sensors. Furthermore, it also observed that some of the X-ray events appear to be the superposition of multiple events, usually observed as an observable change of slope in the sensor response. Therefore, it was often necessary to try multiple combinations of arrival times and compare the reduced chi-square values and location uncertainties to determine which times were most appropriate. The bottom line is that selecting data points for X-ray events is much more difficult than for dE/dt . Once the points are selected, however, `xtime06.m` calls vector “ i ” and returns the vector “ t ” of appropriate arrival times, similarly to `dEtime06.m`. Note that the program `xtime06.m` is also passed a vector, nox , which is

similar to the notime vector passed to dEindicies06.m. The nox vector is really implemented as a safety precaution, due to the manual construction of vector, i. The nox vector just insures that a time is not accidentally entered for a channel that did not observe the event.

4.2.4 Source Determination

This portion of the procedure is little more than using the arrival times, obtained from the previous steps, along with some information about the TOA system in a Marquardt algorithm (see Section 4.1) to find the source solution. The program used for this step is TOAultimsol.m, and it is used for both dE/dt and X-ray sources, though not at the same time. This program requires two inputs: a vector of times, provided either by dEtimes06.m or xtines06.m, and a character variable (regardless of case) of either “t” or “d.” The purpose of the character input is to specify whether the times provided are associated with the dE/dt (“d”) or TERA measurements (“t”). The program accesses a text document (Parameter.doc) which contains the time delay and location for every dE/dt and UPMT sensor in the TOA network, and the state of the character variable determines which set of values is retrieved by the program. From the nonzero terms in the vector of times, the program also calculates every possible combination for $N \geq 5$. The program systematically inserts each of these combinations into a readily-available nonlinear least squares Marquardt algorithm. For any station combination that converges, the source location, estimated location errors (from the covariance matrix), reduced chi-square value, and metric used for comparing solutions (product of trace and reduced chi-square value) are computed and stored into an output matrix. The solution producing the lowest metric value is flagged as the optimal and used as the final solution.

It is noted, that unlike the LMAs described by *Thomas et al.* [2004] or *Koshak et al.* [2004], this network does not utilize the hyperplane approach to obtain an initial guess for the unknowns. Due to the small network size, a central point in the network at an altitude of 200 m

was simply used as the initial guess for all solutions. In Camp Blanding coordinates this point is precisely identified as (300, -200, 200), which is basically due east of the Tower launcher by about 85 m. At least one event from each flash was solved using various initial points that extended up to several hundred meters outside the network, and no significant difference in the resultant solution was observed. A reasonable initial guess for the time of occurrence is obtained by subtracting $2 \mu\text{s}$ from the mean of the observed arrival times. Finally, it should also be noted that all times are relative to the trigger time of Scope 21, since all the TOA scopes were synchronized to that oscilloscope. However, GPS timing can easily be obtained by exchanging the trigger time, $t = 0$, with the time recorded by the GPS time-stamping system.

4.2.5 Documentation

The final step of the source location process is to store the results for longevity, while possibly using a format that permits easy access and analysis. Storing the results as an M-file in MATLAB is not particularly useful because these files are somewhat difficult to edit and the workspace is a poor tool for viewing long lists of results. The program `excelultimout.m` was written so that the results returned for each event by `TOAultimsol.m` could be exported to a spreadsheet. This program simply requires a file name and a pointer (e.g., A1) to the first cell of data storage. Subsequent events can be stored in the same spreadsheet by simply changing the cell pointer. Along with the results returned by `TOAultimsol.m`, the documentation program documents that time vector that produced the results, in case there is ever a need to redo the analysis or compare it with a new technique. The location results for each flash are stored in a single spreadsheet (`Locations.xls`) which is located in the appropriate storm day directory under the folder “/Simultaneous TOA.”

4.3 Accuracy of the TOA System

Due to a variety of limiting factors, every TOA system has finite resolution. It is important to know the accuracy provided by a TOA system if its results are to be useful. Unfortunately, it is very difficult to provide a simple, singular metric to describe the accuracy of a TOA system because the uncertainty in any individual source location is dependent on factors such as the geometry of the network, the number of stations used, and even the location of the source. As previously mentioned, the Marquardt algorithm itself provides one method of estimating solution errors. The final linearization of the algorithm yields a covariance matrix describing the location uncertainties. The validity of the covariance error estimates was checked by *Koshak et al.* [2004] using a Monte Carlo simulation, showing that the uncertainties are well approximated by the linearized equations and that normally distributed timing uncertainties give normally distributed position uncertainties.

Perhaps the most encompassing description for the accuracy of a TOA network is the uncertainty of the timing measurements (Δt_{rms}) because this quantity can be used with simple geometric calculations [*Thomas et al.*, 2004] or a Monte Carlo analysis [*Koshak et al.*, 2004] to calculate the location uncertainties for specific regions monitored by the network. Unfortunately, Δt_{rms} is dependent on many factors, including the number of stations used and the nature of the source itself, and it is not particularly easy to calculate. *Thomas et al.* [2004] showed that the deterministic pulses of a sounding balloon and the pulses of lightning produced slightly different timing errors (43 ns versus 50 ns, respectively) on the same system. According to *Thomas et al.* [2004], the most accurate method for determining the timing uncertainty is to compare the distribution of reduced chi-square values (χ_v^2) obtained for the solutions with the theoretical distributions, which depends only on ν when the measurement errors are Gaussian

distributed. Recall that regardless of the initial value of timing uncertainty used in the Marquardt algorithm, the reduced chi-square values are readily scaled to any value of timing uncertainty. Unfortunately, this method of calculating the timing uncertainty requires separate distribution comparisons for sources located by different numbers of stations, i.e., many sources have to be located for each degree of freedom. Since we only record several flashes per year with perhaps tens to a hundred sources located per stroke, a sufficient number of solutions is not currently available for such an analysis.

In order to make some approximation for the timing uncertainty of our network, we attempted to use a geometric model to work backwards from some covariance error estimates to the timing uncertainty. For a source located inside the network, it can be shown from simple geometric considerations that the horizontal uncertainty is determined primarily by distant stations and is essentially independent of the source's altitude. *Thomas et al.* [2004] suggests that the plan location has a radial rms error Δd , as expressed in Equation 4-2.

$$\Delta d = \frac{v\Delta t_{rms}}{\sqrt{2}} \quad (4-2)$$

The quantity v is simply the speed of the signal propagation, the speed of light in this case. Getting somewhat ahead of ourselves, we used a collection of sources from flashes UF0707 and MSE0604 (both discussed in the following chapters) that occurred within the boundaries of the network to determine the average horizontal uncertainty from the covariance estimates. Working backwards from Equation 4-2, we estimated that the timing uncertainty was 20–30 ns. As an additional check, a Monte Carlo simulation was performed, where timing errors in this range were intentionally introduced to a known source, so that covariance estimates for known errors could be compared with the lightning data. To our surprise, the new covariance estimates were much larger than for the lightning data. Indeed, we then ran additional Monte

Carlo simulations for source locations similar to the aforementioned flashes at several altitudes and different timing errors that ranged from 4 to 30 ns. For both flashes, covariance estimates of the horizontal errors (Δx and Δy) from the lightning data were best matched using timing errors of 6–10 ns in the Monte Carlo analysis. This range of values was secondarily supported by the fact that the reduced chi square values for the lightning sources used in this analysis had to be scaled to a timing error of approximately 10 ns to produce a mean value of 1. In conclusion, we estimate that the network experiences timing errors of about 6–10 ns inside its boundaries. Using timing errors of this magnitude, a Monte Carlo analysis for multiple points within the network indicates that sources are typically located to within 2–3 m in the plan directions and within 10 m in the vertical.

CHAPTER 5 LOCATION OF LIGHTNING LEADER X-RAY AND ELECTRIC FIELD CHANGE SOURCES

As noted in section 1.5.2, stepped leaders in downward negative lightning [Moore *et al.*, 2001; Dwyer *et al.*, 2005] and negative dart leaders in rocket-triggered lightning [Dwyer *et al.*, 2003, 2004] have been shown to produce X-ray emissions as they propagate towards ground. In addition, the X-ray emissions from stepped leaders were found to be coincident with the formation of leader steps, a process observed in the corresponding electric field records [Dwyer *et al.*, 2005]. Since these observations clearly implicate leader steps as the source of X-ray production, the X-ray and electric field change sources associated with the leader steps are expected to have close temporal and spatial relationships. Unfortunately, the temporal relationship illustrated by Dwyer *et al.* [2005] was only accurate to approximately one microsecond, as the leader step locations were not precisely known and the X-ray and electric field sensors were separated by a few hundred meters. This timing uncertainty, though small, precluded a determination of whether the electric field change occurs before the X-ray emission or vice versa. No estimate for the spatial relationship between these two source types has been previously reported. This chapter addresses the issue of independently locating the sources of X-ray emissions and the corresponding leader step electric field changes via time-of-arrival (TOA) measurements, which may ultimately allow advancement on many of the issues discussed in Section 1.5.2. Because the TOA technique provides the time of occurrence for each located source, the temporal relationship between these two source types is also determined. The information presented in this chapter is in part published by the author in Howard *et al.* [2008], which provided the first quantitative description of the spatial and temporal relationship between the leader X-ray and electric field change sources.

5.1 Data and Analysis

The analysis discussed in this chapter requires accurate locations to be obtained for both the X-ray and electric field change (from dE/dt pulses) sources due to individual leader steps. Although numerous flashes were recorded using the 2005 network configuration (4 TOA stations), early results indicated that locations obtained from four stations were not sufficient for this analysis. The dE/dt waveforms resulted in poor altitude determinations, based on the erratic movement of sequential leader steps, and no estimate of error could be obtained for any coordinate determination. Since X-ray sources are generally more difficult to locate than electric field change sources, it was unreasonable to think accurate X-ray source locations could be determined using only four stations. Therefore, this analysis was restricted to data obtained with the 2006 or 2007 configurations (8 TOA stations). TOA data were obtained for seven flashes (including both natural and rocket-triggered events) using these two configurations; however, the natural flashes, MSE0706 and MSE0707, were immediately ruled out due to unique features in the waveforms and/or problems with measurements on the storm days of those respective flashes. All five remaining flashes were searched thoroughly for locatable X-ray sources (coincident detection at five or more station). Unfortunately, three of these flashes exhibited weak X-ray emissions or occurred in unfavorable locations (due to high X-ray attenuation in the atmosphere), such that none of the X-ray sources could be located. Hence, only two recorded flashes have produced locatable X-ray sources to date.

Findings are reported from one negative stepped leader, MSE0604, occurring on 2 June 2006 and one negative rocket-triggered dart-stepped leader, UF0707, occurring on 31 July 2007. The X-ray waveforms (prior to cross-correlation) involved in the solution for one event of MSE0604 are shown in Figure 5-1, with the arrival times indicated by large arrows. Each arrival time corresponds to a deflection in one of the waveforms, and all the arrival times occur within

an allowable “time window” which is physically constrained by propagation paths and measurement time delays. As seen in both the Station 3 and Station 5 waveforms, it is possible for the response from separate X-ray bursts to overlap due to the slow response of the NaI detectors. Therefore, there may be multiple possibilities for the arrival time on a particular channel, as indicated by the small arrows seen in Figure 5-1. Fortunately, cross-correlation of the waveforms, performed during the TOA analysis, typically places the correct times in the closest proximity to each other. Further, potential arrival times are generally separated in time enough that the incorrect values are seriously detrimental to the reduced chi-square value (see Section 4.1) and the location error estimates (see Section 4.3), thus allowing them to be ruled out in favor of times that provide a more accurate solution. Nevertheless, there is some trial and error in determining the best set of arrival times for each X-ray source. The slow response of the NaI detectors, the nondistinguishable pulse shape, and the relatively high X-ray attenuation in air make X-ray sources much more difficult to locate than electric field change sources. This fact is evident in the generally higher chi-square values, larger location uncertainties, and far fewer locatable sources for X rays than for electric field changes. Therefore, our method was to first identify locatable X-ray events (correlated detection on $N \geq 5$ stations), determine the best solution based on our metric, and then determine the associated leader step location from dE/dt records. The dE/dt waveforms shown in Figure 5-2 are from the leader step associated with the X-ray emission shown in Figure 5-1. The arrival times, indicated with arrows, are selected from waveform peaks occurring within a restrictive time window, as noted above.

The approximate locations of the two flashes discussed here can be seen relative to the eight TOA stations in Figure 5-3. Since the downward leader was the source of the X-ray emissions and leader-step electric field changes, the location for MSE0604, which is indicated in

Figure 5-3 by the intersection of error bars in the x and y directions ($\sigma_x = 10$ m and $\sigma_y = 25$ m), was determined by averaging dE/dt source locations from the final 10 leader steps. It is worth noting, however, that the actual strike point was to a tree located approximately 60 m northward. The dE/dt source locations for UF0707 were generally in the volume above the Tower, shown in Figure 5-3, from which the rocket initiating the lightning was launched.

For these two flashes, seven total X-ray/ dE/dt source pairs were identified, three from flash MSE0604 and four from UF0707. The local source coordinates (x, y, z), time of occurrence relative to trigger time (t), covariance estimates for the location errors ($\Delta x, \Delta y, \Delta z$), and the number of stations (N) used are given for each source from MSE0604 and UF0707 in Tables 5-1 and 5-2, respectively. Additionally, the differences in geometric distance (ΔR) and time of occurrence (Δt) between the X-ray and dE/dt sources are calculated for each pair. The tables show that each pair of X-ray/ dE/dt sources is co-located in space by less than 50 m. As expected, the sequences of 3 natural sources and 4 triggered sources move downward with increasing time. Tables 5-1 and 5-2 also show that all the differences in time of occurrence (Δt) are of the same sign. By the convention used here, this means that each located X-ray source occurred after the corresponding dE/dt source, with the amount of delay ranging from 0.1 to 1.3 μ s. Figure 5-4 illustrates the delay typically observed in the X-ray emission by showing dE/dt and integrated dE/dt (electric field) waveforms on the same timebase with the corresponding X-ray burst at the same station. The delay observed in Figure 5-4 is not exactly the delay determined from the source solutions (Δt), as the timing has not been adjusted for any possible differences arising from the propagation paths; nevertheless, including these adjustments would not alter the fact that the located X rays are emitted after the dE/dt peaks. For observations made very close to the leader tip (the measurements in Figure 5-4 are ~ 250 m from the source), the

positive dE/dt peak (radiation field) becomes small compared with the negative electrostatic field change that apparently drives the runaway electrons that produce the X rays.

For the sake of thoroughness, a comment should be made regarding the final source pair listed for UF0707 in Table 5-2. The electric field change and X-ray emission of this source pair were similar in appearance and exhibited comparable spatial and temporal relationships as other entries in Table 5-2; hence, *Howard et al.*, [2008] believed this source pair to correspond with the final step of a dart-stepped leader. Following that publication, however, a more in-depth TOA analysis of leader steps and post-leader processes from the dE/dt waveforms suggested that this source pair was more likely associated with a post-leader process, termed a “leader burst” (see Chapter 6). Because the final leader step and leader burst are sometimes difficult to distinguish, especially based on appearance, this source pair was retained in Table 5-2 for completeness. Regardless of the causative process, the spatial and temporal relationship determined for this X-ray and electric field change source pair is valid.

5.2 Summary and Conclusions

The locations provided in Tables 5-1 and 5-2 show that the sources of X rays and leader step electric field changes are co-located in space within 50 m and that the located X rays are emitted 0.1 to 1.3 μs after the origin of the leader step electric field change. These results not only confirm previous reports on the association of X-ray emissions with downward negative leaders [*Moore et al.*, 2001; *Dwyer et al.*, 2003, 2004, 2005] but also quantify a close spatial and temporal relationship between the sources of X rays and leader step electric field changes. Further, Tables 5-1 and 5-2 show these relationships to be very similar for a stepped leader and a rocket-triggered dart-stepped leader, supporting the idea of a common mechanism of X-ray production in different types of leaders. The close spatial relationship between the source types indicates that the X-ray emissions are produced locally by the leader front and that the runaway

electrons do not traverse large distances. This fact highlights another inconsistency with the RREA model and X-ray emissions from lightning leaders (see Section 1.5.2).

The delay observed in the locatable X rays and the peaks in the leader step field change indicates that the negative electrostatic field change is responsible for the X-ray emissions. Considering the physical mechanism for an individual downward leader step, in which there is probably a current pulse whose rate of change produces the radiation field, followed by the lowering of significant charge causing the electrostatic field, one might predict that the source of the X rays, runaway electrons, should be beneath the source of the electric field change. The results presented here cannot unequivocally confirm this hypothesis, but this view is not contradicted by the data presented. All but one of the seven source pairs in Tables 5-1 and 5-2 have the X-ray source lower in the z coordinate than the dE/dt source, and that lone pair has the two located 7 m apart; however, the uncertainties in the X-ray locations are relatively large. It is noteworthy that every difference in geometric distance (ΔR) for the source pairs of MSE0604 contains a large x component in the same direction which comprises a significant portion of ΔR . If this represents some systematic error in locating one of the source types, no plausible explanation was found for it.

It should be noted that some X-ray emission may occur prior to the source responsible for the peak dE/dt . As seen in Figure 5-1, X rays (denoted by small arrows) are clearly detected at Station 3 and Station 5 prior to the arrival time used in the least squares algorithm. This phenomenon, which was observed for other events, usually occurs at the stations closest to the source. This observation may indicate an X-ray source with a time varying intensity, meaning that the X-ray emission is initially weak and becomes more intense after the leader process that causes the peak values in the associated dE/dt waveforms. It may be possible to obtain a clearer

view of this early X-ray phenomenon, as well as improve the overall location accuracy for X-ray sources, by increasing the detector density and/or using scintillators with faster time response.

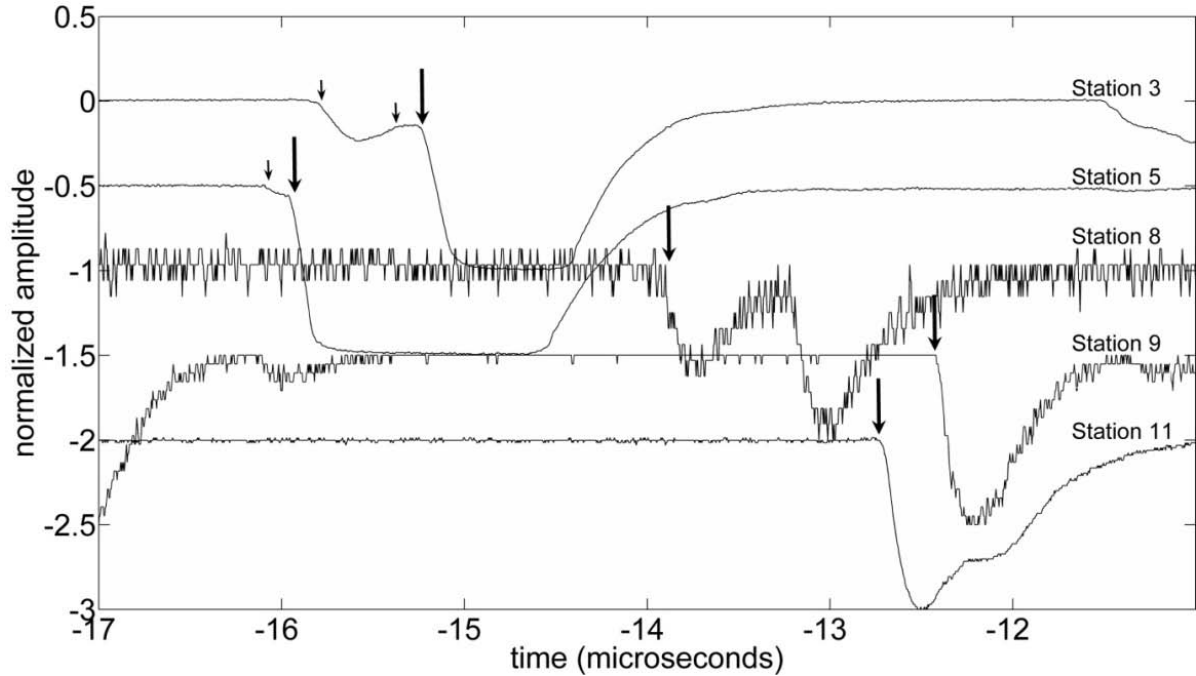


Figure 5-1. X-ray waveforms involved in the location of one event in MSE0604. The arrival times used in the solution are indicated with large arrows. The bursts responsible for the arrival times on Station 3 and Station 5 produce responses which are superimposed on responses from uncorrelated bursts (small arrows). The waveforms are shown as recorded in Launch Control and prior to any correction for fiber-optic time delays.

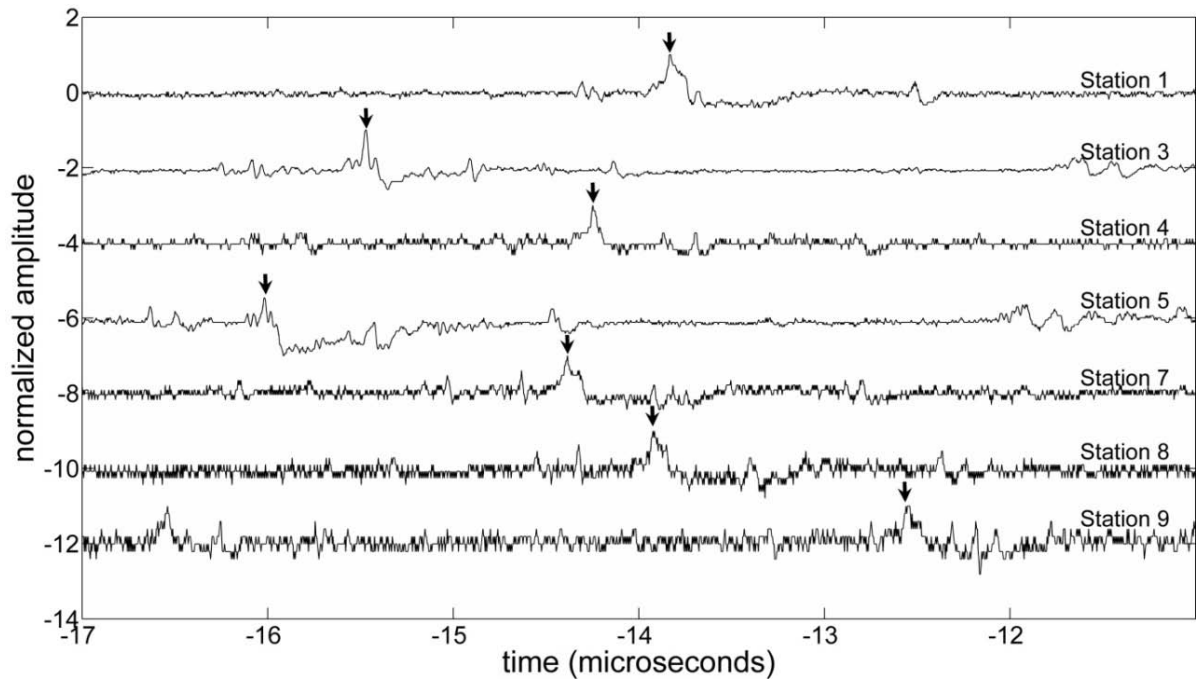


Figure 5-2. dE/dt waveforms corresponding to the X-ray pulses shown in Figure 5-1. The arrival times used for this event are indicated by the arrows.

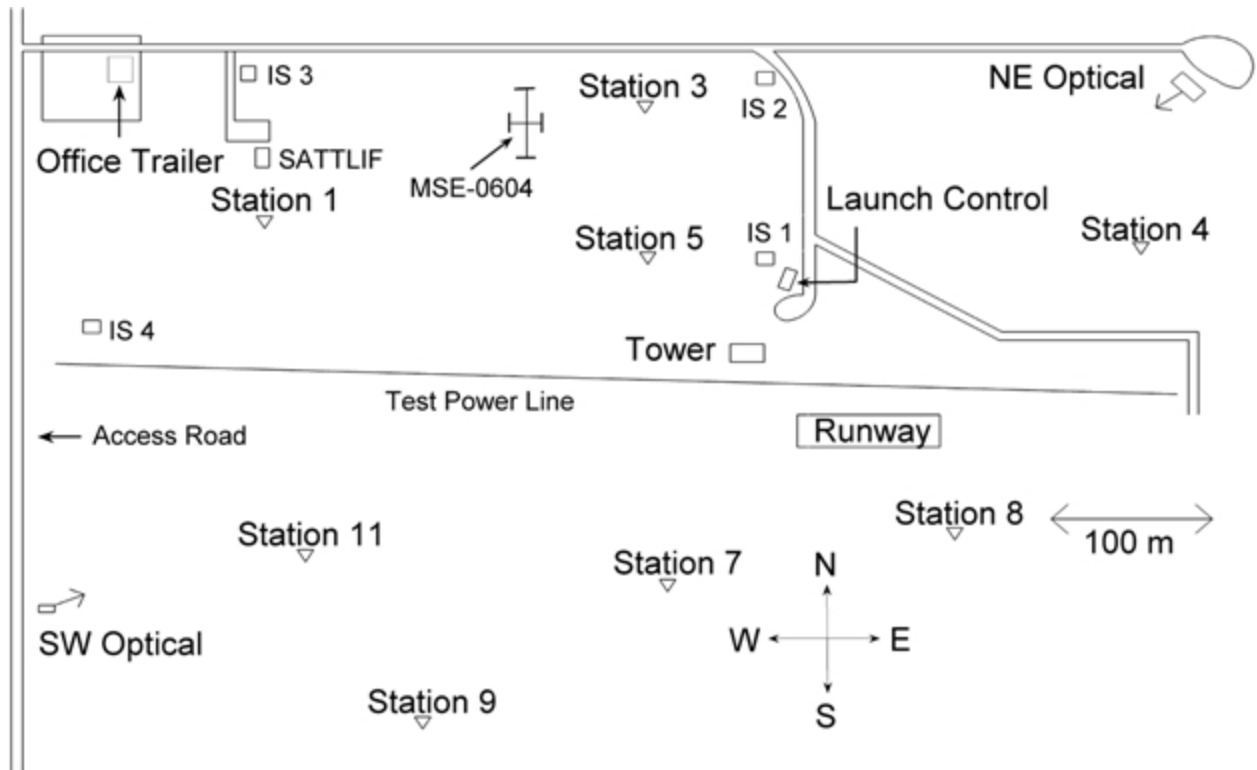


Figure 5-3. Approximate locations for the downward leaders of MSE0604 and UF0707 shown relative to the eight TOA stations (triangles). The leader of UF0707 descended over the Tower, from which triggering rocket was launched.

Table 5-1. Summary of the source pair location results for MSE0604

Event	x (m)	y (m)	z (m)	t (μ s)	Δx (m)	Δy (m)	Δz (m)	N	ΔR (m)	Δt (μ s)
dE/dt 1	241.2	-40.9	186.9	-188.830	3.2	4.4	4.0	5	48.7	0.322
X-ray 1	269.1	-60.9	152.4	-188.507	12.6	22.3	35.6	5	48.7	0.322
dE/dt2	238.4	-62.6	108.4	-70.012	1.7	3.1	6.0	7	46.8	1.303
X-ray 2	282.2	-49.9	97.8	-68.708	26.2	88.2	143.3	5	46.8	1.303
dE/dt 3	250.6	-83.4	75.1	-17.032	1.1	1.8	4.3	7	49.5	0.217
X-ray 3	288.4	-110.0	57.5	-16.815	9.9	8.6	22.4	5	49.5	0.217

Table 5-2. Summary of the source pair location results for UF0707

Event	x (m)	y (m)	z (m)	t (μ s)	Δx (m)	Δy (m)	Δz (m)	N	ΔR (m)	Δt (μ s)
dE/dt 1	386.7	-236.9	140.5	-64.934	10.8	10.6	45.4	5	34.2	0.363
X-ray 1	353.3	-239.9	147.2	-64.571	30.6	29.0	164.9	5	34.2	0.363
dE/dt2	381.8	-204.0	129.1	-17.366	3.4	3.1	16.7	5	32.9	0.113
X-ray 2	371.7	-191.1	100.6	-17.254	48.7	28.1	163.9	5	32.9	0.113
dE/dt 3	392.7	-195.0	89.7	-7.730	5.6	5.0	34.2	5	31.5	0.537
X-ray 3	380.3	-177.2	67.0	-7.193	8.3	8.6	32.1	5	31.5	0.537
dE/dt 4	389.6	-198.0	69.4	-4.141	2.9	2.7	22.4	5	39.0	0.624
X-ray 4	385.1	-169.1	43.6	-3.517	6.1	6.9	30.3	5	39.0	0.624

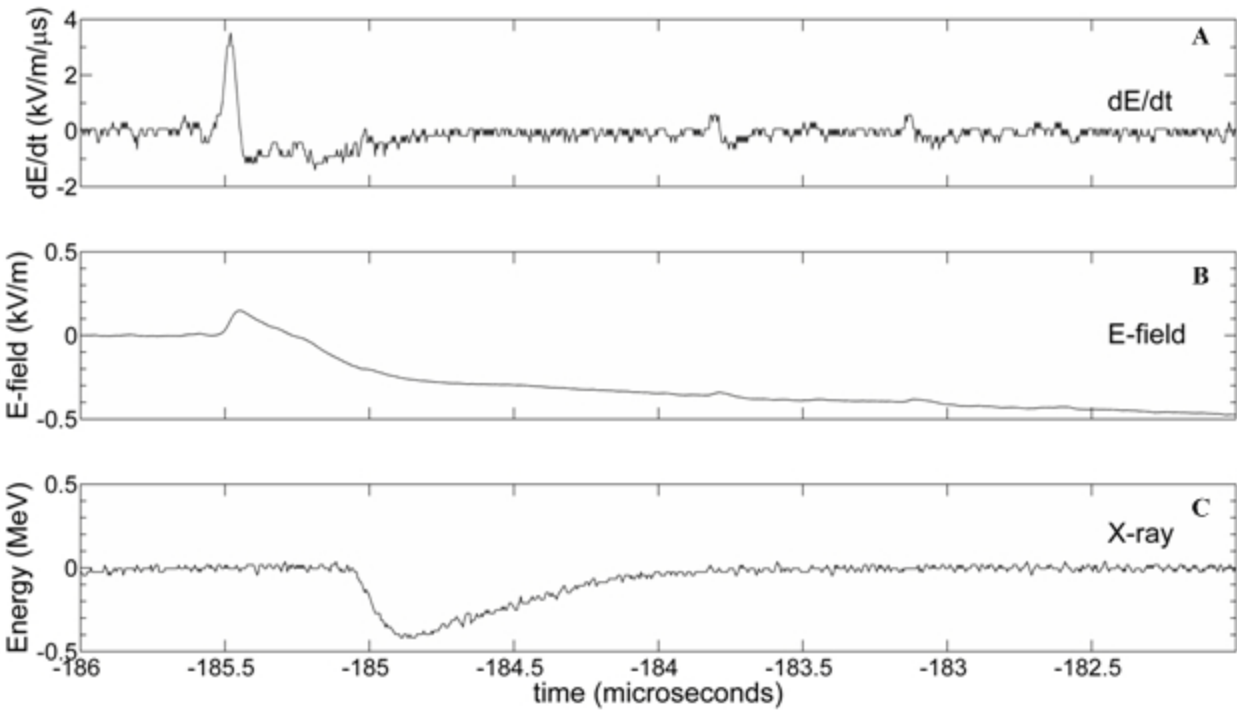


Figure 5-4. Station 1 waveforms (using atmospheric electricity sign convention) for one event during MSE0604 at a distance of ~ 250 m which illustrate the typical delay of the X-ray emission from the electric field change peak. A) dE/dt . B) X ray. C) E-field (integrated dE/dt). Comparison of the dE/dt and E-field waveforms with the X-ray waveform indicates that the X-ray emission is most likely associated with the electrostatic portion of the leader-step electric field change. The electrostatic field at ground becomes more negative as the stepped leader lowers negative charge towards ground, whereas the radiation field pulse at the start of the step, due to a current pulse, is of opposite sign to the electrostatic field change.

CHAPTER 6 RF AND X-RAY SOURCE LOCATIONS DURING THE LIGHTNING ATTACHMENT PROCESS

6.1 Introduction

As mentioned in Chapter 1, the time-of-arrival (TOA) system at the International Center for Lightning Research and Testing (ICLRT) was designed to provide higher spatial and temporal resolution than previous TOA systems. These advantages are primarily the result of the network's small size and the fact that events are identified manually as opposed to an automated routine that selects only one event per some specified time interval. In this chapter the focus is shifted from the ability to simultaneously locate two different types of sources (X-ray and dE/dt) to the ability to track low-altitude lightning processes with high resolution, which is performed with the dE/dt portion of the TOA system. Three-dimensional RF source locations are presented for three natural cloud-to-ground first strokes initiated by stepped leaders and one stroke initiated by a dart-stepped leader in a rocket-and-wire triggered flash. The stepped leader and dart-stepped leader dE/dt pulses are tracked from a few hundred meters to a few tens of meters above ground, after which pulses of different characteristics than the step pulses are observed to occur at lower altitudes. These post-leader pulses include (1) the "leader burst", a group of pulses in the dE/dt waveform radiated within about $1 \mu s$ and occurring just prior to the slow front in the corresponding return stroke electric field waveform; (2) dE/dt pulses occurring during the slow front; and (3) the fast transition or dominant dE/dt pulse that is usually associated with the rapid transition to peak in the return stroke electric field waveform. The results represent the first study of the location and characteristics of electromagnetic sources following the stepped leader and associated with the attachment and return stroke processes. As part of this characterization, the timing coincidence between X-rays and dE/dt pulses on co-located measurements is also used to examine the X-ray production of the post-leader processes.

6.2 Data and Analysis

The dE/dt records from three natural first strokes initiated by stepped leaders and one rocket-triggered lightning stroke initiated by a dart-stepped leader are presented in Figs. 6-1, 6-2, 6-6, 6-7, 6-9, 6-11, 6-13, 6-15, 6-16, and 6-17. Each of these figures uses the atmospheric electric sign convention, meaning an upward-directed electric field at ground level (equivalent to negative charge source directly overhead) corresponds to a negative field value. All records exhibited pulses associated with the stepping of a downward negatively-charged leader as well as with processes following the leader phase. The post-leader-phase processes produced pulses with different characteristics than those of the stepped-leader phase. We identify these post-leader pulses as "leader bursts", "slow-front pulses", and "fast-transition pulses", the latter two occurring during the slow-front/fast-transition sequence generally associated with the return stroke and the former with a newly-identified process apparently associated with the overall attachment process.

In the figures and tables presented, dE/dt pulses are divided and labeled into groups. Groups of pulses occurring during the leader phase are typically characterized by a dominant bipolar pulse, identified as the primary leader step (LS), along with some smaller secondary pulses which are closely related in time (typically within 3 μ s) and space (typically several meters in horizontal displacement; the vertical displacement is discussed later in more detail) to the primary leader step of the group. Groups of leader pulses are identified in the following figures and tables by capital letters, with ascending letters corresponding to later times. Groups of pulses occurring after the leader phase are classified into three general categories: (i) LB for "leader burst" pulses, (ii) SF for pulses occurring during the slow front of the electric field and field derivative waveforms, and (iii) FT for the "fast transition" pulse, the dominant dE/dt pulse of the post-leader phase. If necessary, pulses within each of the aforementioned groups are

further distinguished by numeric identifiers, with increasing numbers corresponding to pulses occurring later in time. Information regarding TOA solutions is listed in Tables 6-1 to 6-4. For each solution we give the local source coordinates (x, y, z), time of occurrence relative to trigger time (t), covariance estimates for the location uncertainties ($\Delta x \Delta y \Delta z$), the number of stations used in the solution (N), and a clarifier term to help identify the pulse within the group. The clarifiers used for leader-phase pulses denote one of three designations: (1) LS, indicating the primary leader step and typically the largest pulse of a group, as previously noted; (2) BS, indicating a secondary pulse occurring prior to the leader step; and (3) AS, indicating a secondary pulse occurring after the leader step. Finally, it is noted that the figures depicting dE/dt waveforms (see above) have been correlated to align notable features and shifted so that the peak of the fast-transition pulse occurs at time zero; hence the actual times of occurrence (t) provided in the Tables 6-1 through 6-4 do not correspond directly with these figures.

In addition to the dE/dt TOA analysis, we present the first analysis of co-located dE/dt and X-ray measurements to examine X-ray production due to low-altitude post-leader processes. The basis of this analysis is the timing coincidence between X-ray and dE/dt events as demonstrated for leader steps by *Howard et al.* [2008]. Based on the work of *Howard et al.* [2008], who found that X rays associated with the leader phase follow the leader step dE/dt peak by 0.1 to 1.3 μs , an X ray is deemed “coincident” with a dE/dt event when the X ray is detected essentially simultaneous with or within $\sim 1 \mu\text{s}$ following the dE/dt event. In the present study each pair of co-located measurements is synchronized to a common timebase and then examined for time coincidence between X-ray bursts and each of the three dE/dt post-leader group types.

6.2.1 MSE0604

Flash MSE0604, the designation indicating that it was the fourth natural flash recorded in the year 2006, occurred on 2 June 2006 at approximately 22:09 UT. First stroke dE/dt

waveforms from three stations of the network are shown in Figure 6-1. Although Figure 6-1, as well as others to be presented here, shows only the latter part of the leader phase up to the return stroke, analysis was performed on the entire waveforms ($\sim 1000 \mu\text{s}$ prior to the return stroke) to locate dE/dt pulse sources associated with various leader branches and to determine the leader speed. The records from MSE0604 were the most complex and also provided the most TOA locations of the four strokes analyzed here. Early in the waveforms of this stroke (prior to the portion shown in Figure 6-1), multiple regions of dE/dt activity, corresponding to stepped-leader branches separated by some hundreds of meters, were located by the network. The region of stepped-leader activity that ultimately connected with ground became the dominant source of dE/dt activity approximately $500 \mu\text{s}$ prior to the return stroke when it was about 350 m above ground. Over the next several hundred microseconds, this dominant region of leader activity continued extending downward as multiple branches. These branches were typically some tens of meters in length although one distinct branch did extend over a hundred meters in a generally horizontal direction.

The dE/dt waveforms in Figure 6-1 show approximately the final $70 \mu\text{s}$ prior to the first return stroke of MSE0604. TOA solutions for the pulses observed in Figure 6-1 are listed in Table 6-1. From Table 6-1, the leader-phase pulses (Groups A-K) of MSE0604 clearly exhibited a tendency to decrease in altitude (z) with increasing time. Also observed from the solutions is the fact that pulses within each group tended to be closely spaced, while groups of pulses, perhaps associated with leader stepping in different branches, were often separated by some tens of meters, including displacement in directions parallel to the ground surface. It follows from the pulse group observations that leader steps are not necessarily the result of a singular breakdown, producing a singular radiation electric field emission; rather, leader steps frequently

appear to be the result of a complex series of breakdowns which manifest itself as a “group” of pulses in the dE/dt records. Figure 6-1 illustrates the variety of waveforms that can be produced by leader steps. For instance, Group A illustrates a simple leader step signature – basically a fast, single, bipolar pulse that is initially of positive polarity and followed by a slow decay from negative polarity back to the zero level. On the other hand, Groups D, H, and I are more complex leader steps that are characterized by a dominant bipolar pulse, similar to Group A, but with an accompanying series of secondary pulses.

As the stepped leader of MSE0604 neared the ground, waveform features different from the leader steps occurred, corresponding with the transition from the stepped-leader phase to the return-stroke phase. The waveforms of Figure 6-1 are expanded in Figure 6-2 to highlight the dE/dt activity occurring during this transition. Following the final leader step (Group K), a small gradual rise, which is most notable in Figure 6-1, was observed on the two closest dE/dt waveforms (Stations 3 and 5), but not on any of the more distant stations. Approximately $2 \mu\text{s}$ after this rise began (around $-2.3 \mu\text{s}$ in Figure 6-2), a burst of four dE/dt pulses, termed here a “leader burst” (LB) to distinguish it from the characteristic leader step dE/dt pulses, was observed. This quick burst of pulses has been previously observed by *Jerauld et al.* [2007] (referred to there as a burst of pulses) in close field waveforms at the ICLRT, and it is likely related to the pulses reported by *Murray et al.* [2005] (also termed a leader burst) in distant radiation field waveforms that propagated with little distortion over tens of kilometers over salt water. The termination of the leader burst coincides with the start of the initial rising portion of the dE/dt (and E-field) waveforms, the so called “slow front” of the return stroke [e.g., *Jerauld et al.*, 2007, 2008]. Shortly after the leader burst, a pair of relatively large pulses superimposed on the slow front was observed in the dE/dt waveforms, termed here slow-front (SF) pulses, which

are similar in shape to but smaller in amplitude than the following fast-transition pulse. After the slow-front pulses, the gradual rise of the slow front continues before the occurrence of the rapid rise of the fast transition pulse.

Figure 6-3 utilizes the TOA solutions obtained by the network to produce a graphical representation of MSE0604. In Figure 6-3A, all of the sources located for this stroke are plotted to emphasize the overall geometry detected by the network, as described earlier in this section. Each source that occurred during the leader phase is represented by a circular plot symbol, with the bold circles corresponding to the dominant leader-step pulses (LS) identified in Figure 6-1 and Table 6-1. The pulses of the leader burst (LB) are represented by 'X' symbols, and the slow-front (SF) pulses are denoted by square symbols. The panels Figure 6-3B and 6-3C provide orthogonal two-dimensional views on an expanded scale to highlight the events that were observed in Figure 6-1. The symbol notation for these panels is identical to that used in the top panel; however, some lines and group identifiers are added to highlight the progression of events in the 70 μ s prior to the return stroke. The solid lines connecting the bold circles are used to denote consistent patterns of movement made by sequential leader-step (LS) pulses. Each of these connected symbols is labeled with its corresponding group identifier. The dotted line in these panels is used to highlight the sequential pattern of movement made by the pulses of the leader burst (LB). The slow-front pulses, represented by the square symbols, are also labeled but are not connected by any line.

Based on the representation in Figure 6-3, the leader pulses observed in Figure 6-1 corresponded with the stepped leader descending as four distinct branches down to an altitude between 50 and 75 m. The last dE/dt pulse of the leader phase, Group K, happened to be the final step in the leader branch that was nearest a tree line bordering the north side of the research

site at approximately $y = 20$ m. We hypothesize that the electric field from this step enhanced an upward positive leader which manifested itself as the small gradual rise observed only at the two closest stations. The leader burst, which was observed directly after this small rise, appears to have coincided with a process that quickly advanced from beneath the leader branches towards the tree line. Indeed, the pulses of the leader burst descended over 30 m in altitude and traversed a horizontal distance of about 60 m in less than a microsecond. Using the TOA locations in Table 6-1 for the leader-burst (LB) pulses, the three-dimensional speeds between sequential events are calculated to be 5.9×10^7 , 6.4×10^7 , and 4.6×10^8 m s⁻¹; and the overall speed, from the first to last pulse, is approximately 1.2×10^8 m s⁻¹. Clearly, the calculated speed between the third and fourth pulses is not physically possible. Because the distance between these two events is largely dominated by a horizontal component, which has estimated uncertainties of only a meter or so (Table 6-1), the leader burst may have involved two areas of simultaneous activity - perhaps some interaction between an upward and downward leader - rather than a process propagating from the location of LB3 to the location of LB4. Interestingly, both slow-front pulses of this stroke were located near the final pulse of the leader burst, although the vertical uncertainties of LB4, SF1, and SF2 were 10–30 m (Table 6-1). The locations determined for the slow-front pulses were within 10 m horizontally of a pine tree, the tree height being 7 m, which was struck and eventually killed by this flash. Unfortunately, records from too many stations, including all of those shown in Figure 6-2, were saturated during the fast transition so that a location for the fast transition pulse could not be obtained.

The TOA network allows an estimation of the downward velocity of the primary stepped-leader channel within several hundred meters of ground. In order to exclude laterally developing branches from the calculation, we selected a 60×60 m² plan-view area underneath the dominant

region of leader activity and included only the leader sources (no post-leader sources) that occurred in the volume above it. Figure 6-4 shows the points which were included in this calculation, with the selection area indicated by the large square outlined at ground level. All leader sources occurring above the selection area are denoted with plus symbols while the remaining leader sources are indicated with circular symbols; the post-leader events are denoted by their usual symbols (see Figure 6-3). The altitudes for these selected points were plotted versus time and then fit with a simple linear regression, with the slope corresponding with the downward leader velocity. The stepped-leader velocity for this stroke was determined to be $5.5 \times 10^5 \text{ m s}^{-1}$ with a determination coefficient between altitude and time of 0.95, as indicated in Figure 6-5A. Notice that the lowest sources of the leader did tend to be slightly below the linear fit, indicating that the velocity may have increased slightly as the leader neared ground.

Although the vertical uncertainties are larger for the leader-burst pulses (10–30 m), it is worth noting that the three-dimensional speeds between sequential leader-burst pulses have vertical components of 5.8×10^7 , 6.0×10^7 , and $6.4 \times 10^7 \text{ m s}^{-1}$, approximately two orders of magnitude higher than the events in the stepped leader.

Finally, we report on the correlated X-ray and dE/dt observations obtained for this stroke using records from the co-located NaI/PMT detectors and dE/dt antennas. Figure 6-6 displays two pairs of these waveforms, with each pair being synchronized to a common timebase. In the PMT waveforms, X rays arrive at the start of the negative going pulse. The pulse amplitude is dependent on the amount of energy deposited and the pulse shape is determined by the NaI light decay time and the RC time constant of the front-end electronics. The half-peak pulse width of a single X-ray burst is about $0.6 \mu\text{s}$; therefore, the wide pulses shown in Figure 6-6 are the result of multiple X-ray bursts. Six stations, records from two of which are shown in Figure 6-6, allowed

a comparison between dE/dt and X-ray events in the post-leader waveforms. All six detected X rays in association with the leader burst. Two of these six X-ray waveforms, including Station 5 shown in Figure 6-6, were saturated during the slow-front pulses, preventing a comparison for this event. Of the four stations remaining, three, including Station 1 shown in Figure 6-6, detected X rays in association with the slow-front pulses. None of the six X-ray measurements were saturated at the time of the fast transition pulse, allowing records from all six stations to be analyzed; three of them detected X rays in association with the fast transition. For all stations, the X-ray burst associated with either the slow-front pulses or the fast transition was smaller than the X-ray burst from the leader burst process.

Although the X-ray comparisons discussed in this chapter focus primarily on the post-leader events, it is interesting to note that Group K (around $-5 \mu s$ in Figure 7), the final leader step, produced the largest dE/dt peak of the leader phase at each TOA station, except at Station 3 where Group K was essentially matched by the peak of Group H, but the associated X-ray emission was one of the weakest detected during the leader phase of this stroke, barely detected by any of the TOA stations. The cause of this anomaly is currently unknown. It is possible that the proximity of Group K to the ground may have played some role in reducing the X-ray detection, but this view seems to be inconsistent with the copious X rays detected from the leader burst, which was closer to ground than any of the leader steps. Figure 6-3 indicates that Group K was the final step in a leader branch that was propagating away from the sensors of the TOA network, but the additional atmospheric attenuation suffered by this relatively distant step is not significant enough to explain such a dramatic reduction in the deposited energy. These observations seem to indicate that the X-ray emissions may be beamed to some degree in the direction of the leader propagation; however, *Saleh et al.* [2009] reported that their observations

of leader X-ray sources were most consistent with an isotropic source, at least in the lower hemisphere ahead of the leader tip. Since the emission's angular distribution in the upper hemisphere has yet to be determined (all the X-ray sensors are currently ground based), it is unclear what should be observed for a leader moving away from the network at an angle somewhat parallel to ground. Moreover, due to saturation of some of their sensors during low altitude events, *Saleh et al.* [2009] could not rule out the possibility that the emissions become slightly beamed as the leader approaches very near the ground. Finally, it is noted that the X-ray production from Group K could have simply been less significant than other leader steps although the X-ray production generally increases as the leader nears ground; it appears that continued study is warranted.

6.2.2 MSE0703

Flash MSE0703 occurred on 14 July 2007 at about 16:25 UT. Figure 6-7 illustrates the final 30 μ s of the closest dE/dt waveform (Station 8) for this natural-lightning first stroke. The TOA solutions for the groups of pulses identified in this figure are listed in Table 6-2. A visual representation of this stroke, similar to the one for MSE0604, is given in Figure 6-8. The symbol notation is the same as that used in Figure 6-3, but two additional plot symbols, which were not necessary before, are introduced: (1) a diamond symbol is used to denote the fast transition, and (2) a pentagram is used to denote a pulse unique to this stroke which occurred after the fast transition (labeled AFT). Overall, the leader phase of this stroke was much less active than that of MSE0604. The TOA locations did reveal some leader activity that was horizontally separated by as much as a hundred meters; however, fairly little branching was observed in the channel that dominated the leader activity and ultimately connected with ground. The sources from this channel were used to calculate the downward leader velocity, which was found to be 3.6×10^5 m s^{-1} with a determination coefficient of 0.94. These data are presented in Figure 6-5B. Similar to

MSE0604, the final sources of the leader tend to be slightly below the fit, indicating an increase in velocity.

Of primary interest in this stroke are the events that occurred around the time of the return stroke. As seen in Figure 6-7, the final leader step, Group D, was followed by a pair of distinct pulses, identified here as the leader burst (LB), which was then followed by the initiation of the slow front. It is unclear when exactly the slow front began because records from a few stations indicate that the leader burst may have included another pulse, following the two observed in Figure 6-7, although no location could be obtained for that pulse. Similar to the leader burst in MSE0604, the TOA solutions for the leader burst indicate rapid downward and horizontal movement. The three-dimensional speed calculated for this leader burst (LB) is $3.8 \times 10^7 \text{ m s}^{-1}$ with the vertical component equal to $2.9 \times 10^7 \text{ m s}^{-1}$, approximately two orders of magnitude faster than the stepped-leader downward velocity. We acknowledge that the separation of these sources is within their location uncertainties; however, the speed of this leader burst is consistent with the speeds calculated for the first three pulses of the MSE0604 leader burst.

The slow front following the leader burst consists of three large pulses occurring within a microsecond (Figure 6-7B). The first of these pulses is labeled a slow-front (SF) pulse primarily because it occurs after the start of the slow-front and prior to the dominant pulse (fast transition pulse) of the return stroke dE/dt waveform. However, the appearance of this slow-front pulse is strikingly similar to that typically observed for a fast transition pulse - a slow rising portion followed by a rapid transition to peak. A distinct feature of this slow-front pulse, compared with the other strokes presented here, is the absence of any appreciable period in which the waveform resumes its gradual rise prior to the dominant pulse. TOA solutions from Table 6-2 reveal that the slow-front pulse and the dominant pulse occurred at approximately the same location.

Following the dominant pulse, there is one final pulse (AFT), similar in appearance to the previous two, before the field-derivative decays appreciably and gives rise to a subsequent hump. The presence of a pulse following the dominant peak is not particularly common, but *Murray et al.* [2005] did document some instances in their Type B events for distant first-stroke dE/dt waveforms. *Murray et al.* [2005] reported that 49 of 131 events (or 37%) produced 136 large pulses (in addition to the dominant peak) within $\pm 1 \mu\text{s}$ of the dominant dE/dt pulse, although the pulses were nearly twice as likely to occur in the $1 \mu\text{s}$ prior to the dominant pulse as in the $1 \mu\text{s}$ following the dominant peak. The final pulse of this stroke, which occurs after the fast transition pulse, is unique to the waveforms presented here, so it is identified with a unique pulse name, AFT, in Table 6-2. The location of this final pulse is identified to be in the attachment region of this stroke and apparently lower than the slow-front and fast-transition pulses although the altitude errors for these three pulses are relatively large (SF, 16 m; FT, 20 m; and AFT, 41 m) due to their being so near the ground. Records from the video system for this flash confirm the general location of this stroke. The similarity in pulse shape, close temporal grouping, and proximity in location shared by the final three pulses of this stroke seem to indicate multiple occurrences of a common physical process.

There were five stations available to make a comparison between the dE/dt pulses and X rays occurring after the leader phase. All five detected X rays in association with the leader burst. None of them detected X rays with the slow front, and one of them detected X rays in association with the fast transition. Interestingly, two of these stations detected X rays associated with the final pulse (AFT).

6.2.3 MSE0704

Flash MSE0704, which occurred on 16 July 2007 at approximately 23:27 UT, is the third and final natural event to be presented. Two dE/dt waveforms illustrating the final $50 \mu\text{s}$ prior to

the first return stroke of this flash are shown in Figure 6-9. TOA solutions for the pulses identified in Figure 6-9 are listed in Table 6-3. A graphical representation of this stroke is given in Figure 6-10, using the same symbol notation that was defined for the previous events. The TOA locations indicated that the leader activity of this stroke was loosely divided into two regions which were roughly separated by 100–200 m. This behavior is similar to that observed during the leader phase of the other natural strokes, except that the leader region that connected with ground did not clearly dominate the dE/dt activity of this stroke. These two regions produced approximately an equal number of sources and both exhibited a tendency for branching, typically some tens of meters in length. The downward leader velocity for this stroke was calculated using the sources from the leader region that connected with ground, excluding only a few points which extended horizontally out to Group D. As seen in Figure 6-5C, the downward leader velocity was determined to be $9.0 \times 10^5 \text{ m s}^{-1}$ with a determination coefficient of 0.97.

An interesting feature of the Figure 6-9 waveforms is the varying complexity displayed by the leader pulses. Several groups throughout the leader phase exhibited the simple leader-step signature typified by Group A, while others, such as Groups B and C, were much more complex. As was the case with previously examined stepped leaders, the pulses within each group tended to be closely spaced. An exception to this trend, however, was Group C which apparently corresponded with the simultaneous activity of two separate branches, resulting in a very complex waveform signature. Indeed, the second and third pulses of Group C (C2 and C3 in Table 6-3) appear to be more closely associated with Group D than Group C based on their TOA solutions. Hence, these two pulses are labeled in Table 6-3 with the clarifier “BS” to indicate they are part of and occurred before the step (LS) in Group D. If, however, we were to associate

the second and third pulses of Group C with a separate step altogether, there is little change in the statistical analysis given later in Section 6.3.2.

From Figure 6-9 Group D can be identified as the final step of the leader phase. Although Group D was clearly associated with the connecting leader region, it apparently was not part of the connecting leader branch, which contained Groups A, B, and C. The time period between this final leader step and the start of the slow front, where we have previously observed leader bursts, did not produce any locatable events, although several stations did detect a few small pulses. Interestingly, these small pulses produced coincident X rays at more stations than the previous leader step (Group D), the slow-front pulses, or the fast transition. The production of X rays just prior to the slow front in this stroke may indicate a significant process in the attachment phase that occurs even in the absence of significant dE/dt activity. The locations provided by the TOA network for the slow-front and fast-transition dE/dt pulses are very tightly grouped except for some moderate spread (~ 20 m) in the x coordinates. It is noted that the x -coordinate uncertainties (Table 6-3) for the events of this stroke were relatively high as a result of this stroke being nearly 200 m west of the network. Regardless of these larger uncertainties, the locations determined for the fast-transition and slow-front pulses were in excellent agreement with the video record.

Examination of the dE/dt and X-ray waveforms revealed that only three stations detected X rays following the leader phase. This fact is not particularly surprising considering the location of this stroke and the relatively high attenuation rate of X rays with range ($\propto [\exp(-r/120)]/r$, as noted earlier [Saleh *et al.*, 2009]). All three stations detected X rays during the period suspected to contain a leader burst. Two of these three stations detected X rays associated with the slow-front pulses, and none of them detected X rays with the fast transition pulse. It is worth noting

that this stroke provided the only instance in the data discussed here where a station (Station 1) detected a stronger X-ray burst in association with a slow-front pulse (SF1) than it did with the leader burst (LB), or the suspected leader burst in this case.

6.2.4 UF0707

Flash UF0707, a rocket-and-wire triggered flash, was initiated on 31 July 2007 at approximately 19:36 UT. This flash consisted of an initial stage (as in all negative triggered lightning flashes, involving an upward positive leader, destruction of the triggering wire, its replacement with a plasma channel, and subsequent steady current flow between cloud and ground [e.g., *Rakov et al.*, 2003]) followed by two leader/return-stroke sequences, with each stroke terminating to the launcher mounted on the top of an 11 m tower. The focus in this section is the first of these two strokes. This stroke was initiated by a dart-stepped leader and produced a peak channel-base current of approximately 45 kA (unusually high for a rocket-triggered lightning, whose typical value is 10–15 kA [*Rakov and Uman*, 2003]). Additionally, the slow-front/fast-transition sequence, evident in both the dE/dt and channel base current records, indicate that there was a pronounced attachment phase, not dissimilar from a natural first stroke. Video and photographic records for this stroke reveal that the downward leader was a single channel that only branched in the final 6–8 m above the launcher. Further, these optical records clearly indicate the presence of upward positive leaders extending from the launcher. The rare combination of data (TOA locations, electric and electric field-derivative records, channel-base current, and close optical records) available for this stroke provides a unique opportunity to study the stepped leader and the processes of the attachment phase.

Two of the dE/dt waveforms recorded for this stroke are presented in Figure 6-11. A comparison of these waveforms with those previously presented for natural first strokes reveals that there are both similarities and differences. Like the natural-lightning waveforms, the groups

of leader pulses in Figure 6-11 display a variety of shapes. Group A, for instance, exhibited the simple leader-step signature, while Groups B and C were complex leader steps involving many secondary pulses. Indeed, the amplitude and multiplicity of the secondary pulses gave these groups a distinct appearance, different from most of the leader groups that were observed in the natural strokes. However, some groups in the natural strokes, such as Groups H and I from Flash MSE0604, did appear similar when viewed on an identical time scale. As with leader groups in the natural strokes, the secondary pulses in the leader groups of this stroke tended to originate from a similar location as the dominant pulse within the same group. The TOA locations for the pulses observed in Figure 6-11 are listed in Table 6-4. These pulses along with the rest of the pulses in the leader phase were used to produce the three-dimensional view of this stroke which is presented in Figure 6-12. The symbol notation used in this figure is the same as that previously used for the natural-lightning strokes. A number of the features observed in Figure 6-12 were confirmed via optical records. These features include the leader channel leaning southwest (decreasing x and y) away from the tower with increasing height as well as the change in channel trajectory at about 200 m altitude. This channel shape was likely established in the initial stage of the flash when the upward positive leader initiated from the wire-grounded rocket (typically at 200–300 m altitude [Rakov and Uman, 2003]) and propagated in a direction different from the original rocket trajectory. Additionally, the TOA locations do not indicate any branching of the leader phase, and the lowest sources from this stroke are over the eastern edge of the tower (left side of tower in Figure 6-12C).

The fact that a dart-stepped leader precedes the return stroke of this flash while stepped leaders precede first strokes in natural lightning is responsible for some of the most notable differences between this and the natural-lightning strokes: (1) time interval between steps, (2)

downward leader propagation speed, and (3) absence of significant branching in triggered-lightning strokes. Thus far in this chapter we have observed that pulses within each leader group tend to be very closely spaced, indicating that each group essentially corresponds to a leader step. Therefore, an estimate for the interstep interval can be obtained by simply observing the group spacing in the dE/dt waveforms. For stepped leaders (Figures 6-1, 6-7, and 6-9) a typical interval between groups is 10–20 μs , with shorter intervals clearly being observed in Figure 6-1. However, consecutive groups in Figure 6-1 rarely belonged to the same leader branch (see Figure 6-3), implying that the typical interstep interval is probably more like 15–25 μs . On the other hand, Figure 6-11 indicates that the dart-stepped leader in this stroke has an interstep interval of approximately 4–5 μs . These values are in general agreement with the typical values reported for each of these leader types [Rakov and Uman, 2003]. Since neither the TOA locations nor optical records for this stroke indicate any branching of the downward leader (at least over 8 m or so above the launcher), all of the leader points identified in Figure 6-12 were used to calculate the downward velocity. Based on our linear estimation method, the downward leader velocity was calculated to be $4.8 \times 10^6 \text{ m s}^{-1}$ with a determination coefficient of 0.99. The fit results for this stroke are shown in Figure 6-5D. This leader velocity is higher than any of the values previously reported for the stepped-leaders, as expected, and is in good agreement with values typically reported for dart-stepped leaders [Rakov and Uman, 2003].

A few microseconds after the final leader step (Group C in Figure 6-11), the dE/dt pulses identified as the leader burst (LB) occur. Howard *et al.* [2008] originally identified this group as a leader step. However, for the following reasons these pulses may be more appropriately labeled as a leader burst: (1) the pulses within this group traversed significantly more altitude than the preceding leader groups and (2) the initial pulse of the leader burst began very near the preceding

leader step, unlike previous leader steps in this stroke (see Table 6-4). Further, the X-ray records indicate that this group of pulses was one of the most significant X-ray events for this stroke and was certainly the most dominant following the leader phase, similar to leader bursts in the natural first strokes previously examined. The leader burst appears to have involved more than the three located peaks given in Table 6-4; however, some of the smaller pulses were not resolved well enough to provide locations. Following the leader burst in Figure 6-11, around $-2.3 \mu\text{s}$, there is a gradual rise in the dE/dt waveforms that continues until a sizeable and rapid transition is produced by the slow-front pulses (comprised of SF1 and SF2) which is remarkably similar in shape to the actual fast transition pulse of this stroke. Following slow-front pulses SF3 and SF4, the gradual rise resumes briefly until the onset of the fast transition (dominant pulse). Overall, the description of this stroke transitioning from the leader phase into the return stroke is very similar to that observed for the natural first strokes previously discussed, suggesting that the attachment phase for stepped and for dart-stepped leaders involves very similar processes.

The current waveform for the first stroke of UF0707 is presented in Figure 6-13 on two time scales along with the dE/dt waveform from Station 7. The current exhibited a peak of approximately 45 kA, as noted previously, and a complex slow front as opposed to the simple concave shape typically observed in the current and electric field waveforms of natural first strokes [e.g., *Weidman and Krider, 1978; Jerauld et al., 2007*]. As with previous figures, the dE/dt fast-transition peak is set to correspond to time zero. The alignment of the current waveform was based largely on the timing considerations obtained from the strike location and the known measurement delays. However, there were still a few hundred nanoseconds of ambiguity considering that the source of the current wave was likely located above the launcher at the junction point of the downward and upward connecting leader [*Jerauld et al., 2007; Willett*

et al., 1988, 1989; *Weidman et al.*, 1986; *Uman et al.*, 1973]. A reasonable and consistent time shift which accounts for this effect was introduced to the current waveform so that the start of the fast transition (end of the slow front), a noticeable feature, was aligned in both waveforms. The alignment of the end of the slow front and the beginning of the fast transition is indicated in Figure 6-13A by the middle dotted line. Interestingly, this alignment also produced matches in other features of the waveforms. The left dotted line indicates a correlation between the onset of the largest slow-front pulse (SF2) and a significant increase in channel-base current during the overall 2.1 μs slow front period. In fact, the first two dotted lines in Figure 6-13A reveal that both rapid transitions observed in the dE/dt waveform, due to the slow-front (SF1 and SF2) and fast transition pulses, each corresponded to a significant increase in base current. The final dotted line indicates an alignment between the peak of the current waveform and the beginning of a shoulder following the dE/dt peak. This alignment is interesting because the waveforms found in *Jerauld et al.* [2007] for a rocket-triggered lightning stroke indicate that a similar shoulder in the close electric and magnetic field-derivative records corresponded with a zero-crossing in the channel-base current-derivative measurement, which should correlate to a peak in the current record. In addition to these events, the start of the current slow-front, which we identify as the point where the waveform deflects from the zero-level, is identified in each panel of Figure 6-13 by a slanted arrow marker. The initial current deflection can be seen in Figure 6-13B to correspond with the start of the gradual rise in the dE/dt waveform. The duration of the current slow front, from the arrow marker to the middle dotted line, was, as noted above, about 2.1 μs , which, interestingly, is identical to the mean value for the distant electric field slow front reported by *Weidman and Krider* [1978] for 34 subsequent strokes preceded by dart-stepped leaders. Our current slow-front amplitude to total peak ratio of about 0.71 is larger than the mean

ratio of 0.40.5 for the distant electric field given by *Weidman and Krider* [1978], but it is nearly identical to the value of 0.74 for the current ratio given by *Jerauld et al.* [2007] for an unusual rocket-triggered stroke that was also preceded by a dart-stepped leader. Immediately preceding the current slow-front start shown in Figure 6-13B, a pair of bold vertical arrows denotes two pulses in the current record. Due to the relatively poor amplitude resolution of this measurement, we can only estimate from the 45 kA peak current that these pulses had peaks of at least several hundred amperes. Because these hundred-ampere pulses occurred before the sustained current of the slow front, the process responsible for these pulses appears to have involved stepping. An obvious candidate is an upward positive leader propagating in response to the descending negative leader. However, the data of *Biagi et al.* [2009] indicate that pulses observed in the channel-base current record prior to the return stroke are the result of induced effects from steps in the downward leader. It may be significant that these pulses coincided with the leader burst. No previous pulses could be attributed to an upward leader, which is expected to have a duration of tens to a couple hundred microseconds [e.g., *Yokoyama et al.*, 1990; *Wang et al.*, 2001], and the sustained current of the slow front began immediately after the second current pulse. We note that upward positive leaders were imaged with this stroke, as the video frame in Figure 6-14 shows.

At this point it is interesting to consider the implications of the current and dE/dt records with regard to the observed channel geometry. Figure 6-14 presents a single frame from the Sony (DCR-TRV900) Mini-DV camcorder located in Launch Control that imaged the first stroke of UF0707. This image reveals that the downward leader branched approximately 6–8 m above the launcher top into two primary channels, each of which connected to the launcher. The left primary channel is itself composed of two channels (exhibits a split). There are also

unconnected leader branches, directed both upward and downward. From the analysis of this stroke we know that the post-leader phase of the dE/dt records contained two rapid transitions; one was produced by the combined slow-front pulses and the other was the fast-transition pulse. Further, each of these transitions was preceded by a gradual rise in the dE/dt waveform and was also associated with a significant increase in channel-base current. These similarities, along with their proximity in location, imply that both events were the result of a common process, perhaps the connection between an upward and downward leader. Another interesting observation, although purely speculative, is that the rapid transition in the slow-front is immediately followed by another significant pulse (SF3) which may be associated with the sub-connection in the left primary channel. Although the slow-front and fast-transition pulses were among the lowest sources located for this stroke, the TOA network could not definitively identify the slow-front and fast-transition pulses as the source for the primary channel segments due to the altitude uncertainties in the TOA locations. It is worth noting, however, that the altitude uncertainties (Δz) for the sources in this stroke were uncharacteristically large because three dE/dt stations failed to record, resulting in a 5-station solution. In particular, the two stations nearest to the tower, which are critical to the altitude determination [Thomas *et al.*, 2004], were among the three non-contributing stations.

Clearly, it is important to understand the lightning physics in order to associate physical processes with waveform features, and that is one of the primary goals for this TOA network. As previously noted, the timing error can be used to determine location accuracy for specific source locations and station combinations. Because the source locations for the slow-front and fast-transition pulses in the rocket-triggered stroke, UF0707, did not descend to the top of the launcher as we might expect (Figure 6-12 and Figure 6-14), we performed Monte Carlo

simulations to examine the vertical error distributions for a source located 4 m above the launcher (approximately half the height of apparent attachment region, Figure 6-14) that was degraded by our estimated timing errors of 6–10 ns (see Section 4.3) and located by the same 5 stations as UF0707. Interestingly, our range of timing errors resulted in vertical error distributions with means of +15 to +25 m and standard deviations of 22 to 29 m. These positive mean values indicate that the altitude for a source at that position would have likely been overestimated by that range of values, and hence the final sources located from UF0707 were potentially lower than the altitudes listed in Table 6-4. Indeed, if the slow-front and fast-transition pulses of UF0707 were corrected by 15–25 m, they would be much closer to the top of the launcher, supporting the idea that the slow-front and fast-transition pulses were responsible for the primary channels imaged with this stroke (Figure 6-14). This systematic overestimation of the source height quickly disappears with increasing altitude, as the mean of the vertical error distribution falls to less than 1 m at approximately 50 m above the launcher (or about 67 m in the local coordinate system); therefore, sources located during the leader phase of this stroke are not expected to have suffered significantly from this effect. Finally, it is interesting to note that a source in the same position (4 m above the launcher) but located using all eight stations would be expected to have a vertical error distribution with a mean less than 5 m and a standard deviation less than 15 m.

The X-ray comparisons for this stroke were limited since only five dE/dt records were available. All five stations detected X rays in association with the leader burst. One station detected X rays during the slow-front pulses, and none of the stations detected X rays with the fast-transition. As a final note regarding X-ray production and lightning processes, even if the two hundred-ampere current pulses in Figure 6-13B were the result of an upward positive leader,

these occur simultaneously with dE/dt pulses (LB) that exhibited downward movement, so it is unclear if the observed X rays are due to the leader burst process (more likely, given the association of X rays with the leader bursts in the natural-lightning strokes and the fact that downward negative leader steps also produce X rays) or the upward connecting leader.

6.3 Discussion

6.3.1 Electric Field and Field-Derivative Comparison

One of the key features we have focused on in this chapter has been the transition from the leader phase to the return stroke. To this point we have used the dE/dt waveforms to discuss these processes. However, researchers have more frequently used electric field measurements to study similar processes [e.g., *Weidman and Krider, 1978*], so it is worth comparing the dE/dt and E-field records to correlate features in these two measurements. Figure 6-15 compares the measured electric field (6-15A), the time-integrated dE/dt (6-15B), and the dE/dt (6-15C) waveforms all obtained at Station 5 for MSE0704. This stroke is presented first because its E-field record most closely resembles the “classical” description for a return-stroke electric field – an initial “slow front” having duration of 2–8 μs , followed by a “fast transition” to an initial peak, this peak not always being clearly identified in very close waveforms. Additionally, Figure 16 illustrates the excellent waveshape agreement between the directly measured E-field and the integrated dE/dt obtained at the same station. For the waveforms of Figure 6-15, which were obtained at virtually the same distance, there is good agreement in the starting time and the duration of the slow front for each of the three waveforms. The slow front in both the directly measured E-field and the integrated dE/dt waveforms exhibits the characteristic concave shape that is typically observed in first-stroke currents and distant E-fields [e.g., *Weidman and Krider, 1978*; *Jerauld et al., 2007*]. The slow-front pulses, which are clearly observed in the dE/dt

waveform, correspond to only small inflections in the measured E-field and integrated dE/dt waveforms.

Figure 6-16 presents the dE/dt and integrated dE/dt waveforms from two stations for MSE0604. Unfortunately, no directly measured E-field waveforms were available for this stroke. Unlike the relatively simple structure observed in the Figure 6-15 waveforms, the waveforms of Figure 6-16 exhibit more structure and highlight the varied appearance of features at different distances and the difficulty in identifying specific processes. The Station 8 dE/dt waveform (Figure 6-16B) was obtained at a distance of 460 m from the ground-strike point, and the Station 1 dE/dt waveform (Figure 6-16D) was obtained at distance of 195 m. The fast transition of the Station 1 dE/dt waveform is saturated, so the corresponding integrated dE/dt waveform becomes distorted shortly after the transition labeled as T2. Both dE/dt waveforms in Figure 6-16 exhibit five distinct features: (1) the final leader step, Group K, (2) the leader-burst pulses, (3) the slow-front pulses, (4) the start of a rapid transition (T1) to a shoulder, and (5) the start of a rapid transition (T2) to peak. The final leader step, Group K, is identifiable in the integrated dE/dt records of both stations and appears as a simple unipolar peak. Although this leader step is much larger in the dE/dt record at Station 1 than at Station 8, it is less noticeable in the Station 1 integrated dE/dt waveform due to the large amplitude contribution of the return stroke. A similar effect is also observed in the integrated dE/dt records for both the leader-burst and slow-front pulses. Although both integrated waveforms have an overall concave shape from the start of the leader burst to the time of the first transition (T1), the inflections caused by the leader-burst and slow-front pulses are much more noticeable in the Station 8 waveform. In fact, the Station 8 integrated dE/dt waveform could be described as having a unipolar hump, due to the leader burst, followed by a slightly convex portion, due to the slow-front pulses. The two

transitions (T1 and T2) labeled in the Figure 6-16 waveforms highlight an interesting problem that occasionally arises when trying to characterize return-stroke waveforms – which of these two points should be considered as the start as the fast transition? On the other hand, some have noted for negative first return strokes, that when viewed on an expanded time scale, the slow front and fast transition in both E-field and dE/dt often appear to be one continuous process, without a clear transition [Murray *et al.*, 2005; Jerauld *et al.*, 2008]. For the case in Figure 6-16, it is evident that the point at which that transition occurs is ambiguous. Since both T1 and T2 appear to be associated with the same transition, we have identified the first transition (T1) to be the start of the fast transition. Finally, we note that the point that we selected for the start of the slow front may not necessarily be consistent with other studies because we distinguish the leader burst from slow-front processes. If one were only looking at E-field waveforms and were unaware that the leader burst was a separate process, it would likely be included as part of the slow front. Even if one is aware that there is a separate leader-burst process, it may still be difficult to identify the end of the leader burst and the start of the slow front in an E-field record.

Figure 6-17 shows (A) the integrated dE/dt and (B) dE/dt waveforms from Station 7 and (C) the directly measured E-field from Station 4 and (D) Station 9 for UF0707. The distance of each station from the launch tower is indicated in the figure. The key features in the Station 7 dE/dt waveform include the leader burst, the slow-front pulses, and the fast transition. Similar to MSE0604, the leader burst can be seen to correspond with a unipolar hump or step in the integrated dE/dt and E-field waveforms. As previously noted, two of the slow-front pulses (SF1 and SF2, Figure 6-11) generated a rapid transition that was very similar in appearance and amplitude to the fast transition. This “slow-front transition” resulted in some unusual characteristics in the electric field return-stroke waveforms. From examining the integrated

dE/dt and E-field waveforms, it cannot readily be determined exactly where the slow front begins and ends. Because the dE/dt and current waveforms for this stroke (Figure 6-13) appeared to have the same slow-front duration, the dE/dt record was used to determine the slow-front interval. When this time interval is examined in the integrated dE/dt and E-field records, it looks nothing like a “classical” slow-front. In fact, the overall fast transition to field peak appears to involve two components, one occurring during the slow-front interval and the other occurring with the fast transition. The only feature distinguishing the two components of the overall transition is a small inflection in the E-field (and integrated dE/dt), which corresponds to the slow rising interval observed between the two transitions in the dE/dt record. Although this multi-component behavior of the fast transition has not been well-documented, it has been observed in previous studies. *Murray et al.* [2005] reported that their Type B events tended to exhibit an inflection point or additional peak within the fast transition of their integrated dE/dt waveforms for distant negative first strokes. *Jerauld et al.* [2009] reported on two positive strokes that struck ground 800 m apart (but were in the same flash) which both exhibited a fast transition with two components. In both of these previous studies, similar to the data presented here, each component of the overall fast transition in the electric field corresponded to significant pulses in the dE/dt record. Finally, we note that each of the transitions (slow-front and fast) in the Station 7 dE/dt record appears to have a front-side shoulder that is about one-third to one-half the peak value. This feature appears similar to that of the fast-transition observed for MSE0604, but does not occur for the other strokes presented here. Although purely speculative, it is interesting that both of these strokes, UF0707 and MSE0604, were known to have attached to relatively tall objects, the launch tower and a tree, respectively.

6.3.2 Leader Phase

In the dE/dt waveforms throughout this chapter, the pulses were presented as groups, the reason being that pulses closely grouped in time were also found to be closely grouped in space, leading us to the conclusion that each group must correspond with a leader step. The structure of these groups was a dominant bipolar pulse, labeled as the leader step (LS), which may have smaller pulses within a few microseconds before (BS) or after (AS) it. We now examine the vertical spacing of these secondary pulses relative to the dominant pulse. Combining all leader groups listed in Tables 6-1, 6-2, 6-3 and 6-4 for both the natural and rocket-triggered flashes, we analyzed the vertical position of the secondary pulses relative to the dominant pulse as a function of whether they occurred before or after the dominant pulse in time. For the secondary pulses occurring before the leader step, BS pulses, we found that 8 out of 14 (57%) were located below the dominant pulse, with the average displacement for these 14 pulses being 0.4 m below the dominant pulse. On the other hand, 7 out of 9 (78%) secondary pulses occurring after the dominant pulse, AS pulses, were located below the dominant pulses, with an average displacement for these 9 pulses being 7.2 m below the dominant pulse. Although this is not a large sample and the average vertical displacement is smaller than or equal to the vertical resolution of our TOA network, this analysis provides the first empirical insight into the stepping process of downward negative leaders in lightning. The data indicate that most electrical activity occurring just prior to the step is very near the new step location; while after the dominant step pulse (LS), the electrical activity is below the new step. From this result we might infer that the stepping mechanism for a lightning leader is similar to that observed in the laboratory for some meters-long sparks [Gorin *et al.*, 1976; Gallimberti, 2002; Rakov and Uman, 2003]. In a negative laboratory leader, a space stem develops in the streamer zone in front of the currently-existing leader channel. The space stem gives rise to a bidirectional leader, which is positively

charged toward the existing leader and negatively charged into the gap. When the space stem connects to the main leader channel, a large step current is produced. Thereafter, an intense burst of corona streamers extends downward from the previous space stem (now part of the leader) to eventually form a new stem. Perhaps it is the corona streamers, which initially extend both upward and downward from the space stem and later extend below the new leader step, that are responsible for the secondary pulses in leader steps and for their observed vertical distributions. Because streamer tips are a currently-favored source for X-ray production [Gurevich, 1961; Dwyer, 2004; Moss *et al.*, 2006, Dwyer *et al.*, 2008], it is also worth noting that the time of occurrence for locatable X-ray emissions was found to follow the leader-step electric field change by $\sim 1\mu\text{s}$ with some evidence of weaker X-ray emission just prior to the step [Howard *et al.*, 2008], perhaps further evidence that the stepping mechanism of the lightning leader is similar to that observed in the laboratory. A possible argument against corona streamers being the source of the BS and AS pulses is that, for a similar pulse waveshape, their current would need to be an appreciable fraction of the LS current in order to produce the magnitude of BS and AS pulses observed, and it is not clear that corona streamer currents can be of the same magnitude as leader step currents.

6.3.3 Post-Leader Phase

6.3.3.1 Leader burst

A burst of pulses that occurs near or at the beginning of the slow front has been previously reported by Murray *et al.* [2005] for distant (radiation field) dE/dt waveforms from negative first strokes, as well as by Jerauld *et al.* [2007, 2008] for close negative first-stroke dE/dt waveforms. Murray *et al.* [2005] found that 75 of 131 events (or 57%) exhibited a leader burst in the interval from $-9\mu\text{s}$ to $-4\mu\text{s}$ prior to the dominant dE/dt pulse. Further, they acknowledged that many of the pulses observed between $-4\mu\text{s}$ to $-1\mu\text{s}$ of the dominant peak may have also been the result of

leader bursts. To date, there is no information or explanation for the leader burst pulses. We have shown (1) that their location is below the steps of the previous leader phase, (2) that they are associated with a rapid and significant downward movement, not typically observed with preceding leader steps (the leader burst may also cover significant horizontal distances or involve simultaneous activity by the downward leader and upward connecting leader), (3) that the leader burst produces a significant amount of X rays, and (4) that the leader burst dE/dt feature corresponds to a vertical hump or step in the electric field waveform (also supported by the waveforms of *Murray et al.* [2005] and *Jerauld et al.* [2008]).

Wang et al. [2001] studied upward positive leaders in downward negative lightning using the ALPS imaging system and a correlated E-field measurement. In one particular stroke, located approximately 2 km from their instruments, the E-field record showed a small unipolar pulse with a rise time of $0.5 \mu\text{s}$ and duration less than $2 \mu\text{s}$ occurring just prior to the slow front. This electric field pulse temporally coincided with a small optical signal observed only in the lowest channel of the ALPS system (~ 35 m above ground). Prior to this pulse, an upward leader had already extended up to a height of 88 m over a time of $53 \mu\text{s}$, giving it an average upward speed of $1.7 \times 10^6 \text{ m s}^{-1}$. The upward leader was initiated when the downward leader, having an average speed of $4 \times 10^6 \text{ m s}^{-1}$, was about 300 m above ground. *Wang et al.* [2001] could not provide an explanation for the unipolar electric field pulse; but the low altitude of the correlated optical signal and the timing and shape of the electric field pulse, consistent with the data presented here, suggest that the pulse resulted from a leader burst. If we continue this line of reasoning, the work of *Wang et al.* [2001] shows that the leader burst produces an observable light emission and occurs after the initiation of the upward positive leader.

6.3.3.2 Slow-front pulses and the fast transition

Slow front pulses have been previously reported by *Murray et al.* [2005] and *Jerauld et al.* [2007]. Modeling results provided in *Jerauld et al.* [2007] for an unusual rocket-triggered lightning indicated that the radiation field from the slow-front pulses looked similar to but smaller in amplitude than the fast-transition radiation field. Additionally, the distant radiation dE/dt pulses observed in Type B and Type C events by *Murray et al.* [2005] often appeared very similar to the dominant dE/dt pulse, indicating that the slow-front and fast-transition pulses may be produced by a similar physical mechanism. No explanations presently exist for these pulses, although we have evidence for the physical mechanism of the slow front itself [*Jerauld et al.*, 2007]. Based on the locations given for the four strokes here, we see that the slow-front pulses have a similar location as the fast transition, and even as the AFT pulse of MSE0703. Unlike the leader-burst pulses, these do not suggest a consistent pattern of motion. Based on the discussion presented by *Jerauld et al.* [2009] for a positive stroke electric field-derivative waveform, records presented in *Murray et al.* [2005], and our present data, we can reasonably conclude that the difference in slow-front and fast-transition pulses is simply terminology. We located the slow-front pulses for MSE0604 away from the main leader activity and very near the tree that was struck. The fast transition was not located for this flash, but evidence from other strokes indicates that the SF and FT pulses are located in the same general area. Because the duration of the UPL is expected to be some tens to hundreds of microseconds in duration, we do not expect the slow-front pulses to be the result of UPL propagation. Additionally, in the slow-front transition exhibited by the rocket-triggered flash UF0707, the channel-base current rose, coincident with the slow-front transition, to a value near 20 kA (Figure 6-13). That value seems unreasonably large for an unconnected upward leader, which argues that a connection had already occurred. At the time of the actual fast transition, the current rises sharply again. Two

channels are observed in the photograph of UF0707 (Figure 6-14), which may indicate that each transition corresponded to a separate channel. One of the channels had a subconnection, which may be related to the large pulse (SF3) observed immediately after the slow-front transition peak (Figure 6-11). From the E-field records, both transitions appear similar (Figure 6-17). If the fast transition corresponds to a connection, it is a logical extension that the first transition, which actually resulted in a larger current increase, was also a connection. It may be that all slow front pulses correspond to a connection. Indeed, if the electric field was not always dominated by the fast-transition, the relatively rapid electric field change caused by the slow-front dE/dt pulses may appear to be like the fast transition in the electric field on a smaller amplitude scale. We may conclude that if one integrates the slow-front dE/dt pulse or pulses, one generally obtains a smaller electric field slope than if one integrates the larger fast-transition pulse, but sometimes the difference in slope is small, and hence the identification of slow-front and fast-transition dE/dt pulses is primarily determined by their relation in time.

6.4 Summary

The leader and attachment phases of three natural first cloud-to-ground strokes and one rocket-triggered stroke, which was initiated by a dart-stepped leader, have been analyzed using the eight-station network of co-located and time-synchronized dE/dt antennas and X-ray detectors. The TOA locations of the leader-phase dE/dt pulses indicate that individual leader steps result from a series of electrical breakdowns and may be similar to leader steps in long air gap discharges observed in the laboratory. Further, the downward progression of the leader pulses within several hundred meters of ground was well fit by a linear regression, indicating velocities between 3.6×10^5 and 9.0×10^5 m s^{-1} for the natural strokes and 4.8×10^6 m s^{-1} for the rocket-triggered stroke. In addition, three post-leader processes, all of which were located beneath the steps of the leader phase, have been identified: (1) leader burst, (2) slow-front pulses,

and (3) the fast transition. All three of these processes were associated with X-ray production although the X rays were most significant with the leader burst and decreased with subsequent post-leader processes. The leader burst exhibited rapid and significant downward movement, not typically observed with the preceding leader steps (the leader burst may also cover significant horizontal distances or involve simultaneous activity by the downward and upward connecting leader), and it corresponded to a vertical hump or step that occurred just prior to the slow front in the electric field waveform. The slow-front and fast-transition pulses had similar TOA locations and appeared to be the result of a similar process, connections between upward and downward leader branches. Indeed, slow-front pulses of significant size appear to contribute to the overall fast transition in the corresponding electric field return-stroke waveform.

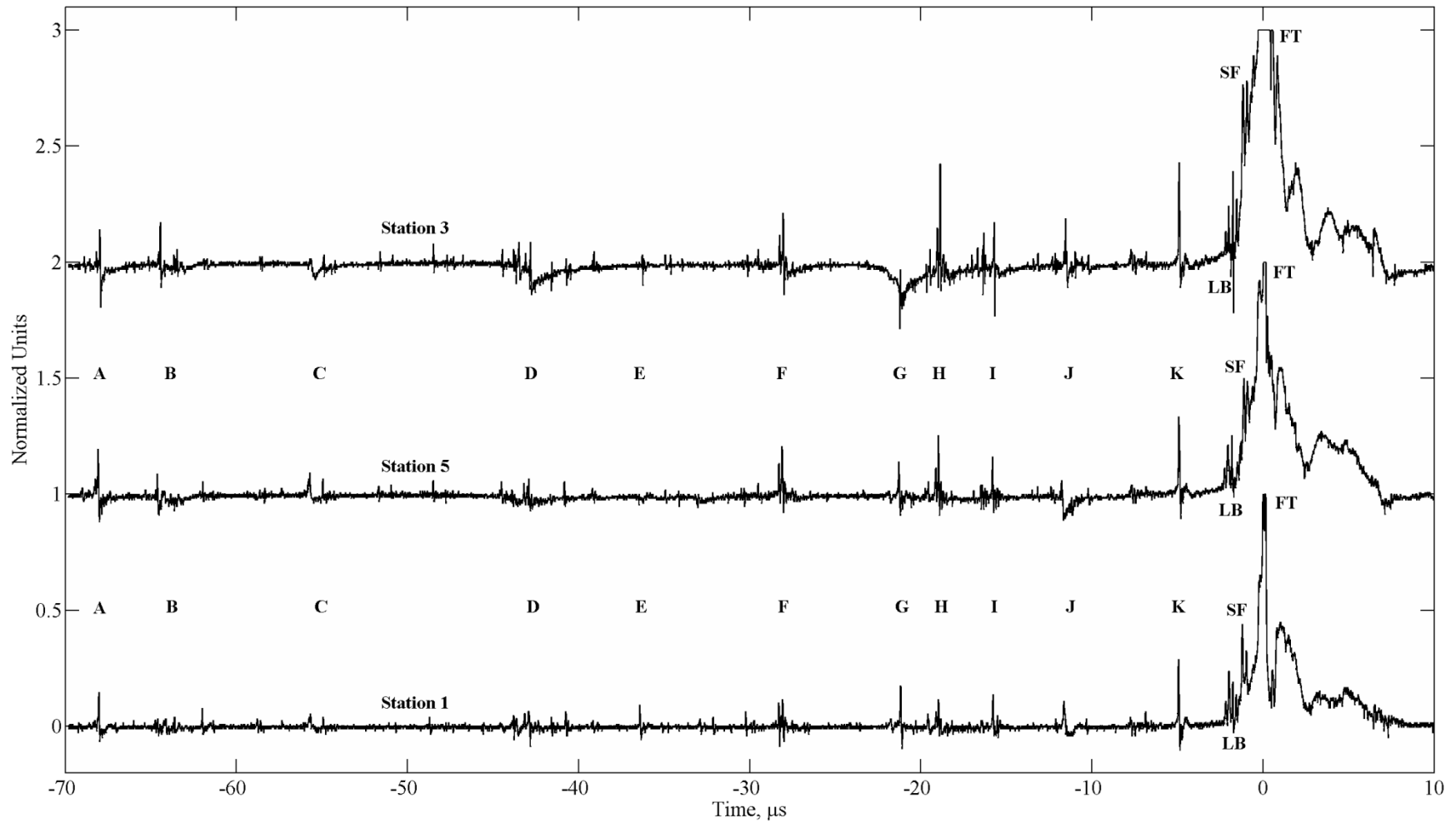


Figure 6-1. dE/dt waveforms from the three stations closest to the first stroke of MSE0604. This stroke exhibited the most active stepped leader and the most pronounced leader burst of the strokes analyzed in this chapter. The fast transition pulse could not be located due to saturation (limited by oscilloscope settings) at too many stations.

Table 6-1. Summary of TOA location results for the dE/dt pulses shown in Figure 6-1 for the first stoke of MSE0604. The results for each event include the local source coordinates (x , y , z), time of occurrence relative to trigger time (t), covariance estimates for the location uncertainties (Δx Δy Δz), and the number of stations used in the solution (N).

Pulse	Clarifier	x (m)	y (m)	z (m)	t (μ s)	Δx (m)	Δy (m)	Δz (m)	N
A1	LS	256.5	-34.8	96.1	-73.472	0.4	0.9	2.2	5
B1	BS	227.3	-57.0	114.5	-70.146	2.2	5.8	11.2	5
B2	LS	238.4	-62.6	108.4	-70.012	1.7	3.1	6.0	7
B3	AS	239.1	-63.8	98.7	-69.022	0.2	0.5	0.9	5
C1	LS	242.3	-18.3	91.9	-61.139	0.2	0.4	0.7	6
C2	AS	243.1	-18.2	81.9	-60.364	0.8	2.6	4.1	6
D1	BS	239.0	-33.1	70.7	-48.560	0.7	2.2	4.3	5
D2	BS	245.6	-28.5	83.4	-48.374	0.4	1.0	1.7	5
D3	LS	244.9	-32.4	86.4	-48.303	0.8	1.1	1.7	5
D4	AS	252.2	-34.1	71.6	-46.185	0.5	1.1	2.2	5
E1	LS	240.0	-67.1	89.3	-41.835	0.5	0.6	1.0	5
F1	BS	237.0	-10.5	77.2	-33.733	0.5	1.3	1.9	5
F2	LS	241.8	-19.6	69.3	-33.505	0.6	1.4	2.4	7
G1	LS	257.1	-33.1	73.6	-26.627	0.2	0.4	0.8	6
H1	BS	237.6	-39.4	56.2	-24.472	0.2	0.6	1.4	5
H2	LS	237.8	-42.8	53.1	-24.299	0.1	0.4	0.7	5
I1	BS	235.5	-37.8	56.1	-21.828	0.5	1.0	2.4	6
I2	LS	237.8	-37.9	52.7	-21.143	0.4	0.8	1.8	7
J1	LS	250.6	-83.4	75.1	-17.032	1.1	1.8	4.3	7
K1	BS	231.2	8.3	53.2	-12.985	0.7	3.5	5.8	5
K2	BS	234.9	-1.1	59.1	-12.290	0.8	1.9	3.3	5
K3	LS	234.7	-3.1	56.2	-10.351	0.6	1.4	2.6	7
LB1		247.1	-32.0	45.1	-7.574	0.4	0.5	1.1	5
LB2		247.2	-34.0	33.9	-7.380	0.4	0.8	2.4	6
LB3		241.4	-33.0	18.9	-7.129	0.4	1.4	7.7	6
LB4		224.7	25.6	10.3	-6.994	0.8	1.8	29.6	6
SF1		222.0	29.9	8.1	-6.637	1.0	3.2	23.4	5
SF2		221.3	28.5	26.5	-6.423	3.4	5.1	7.5	5

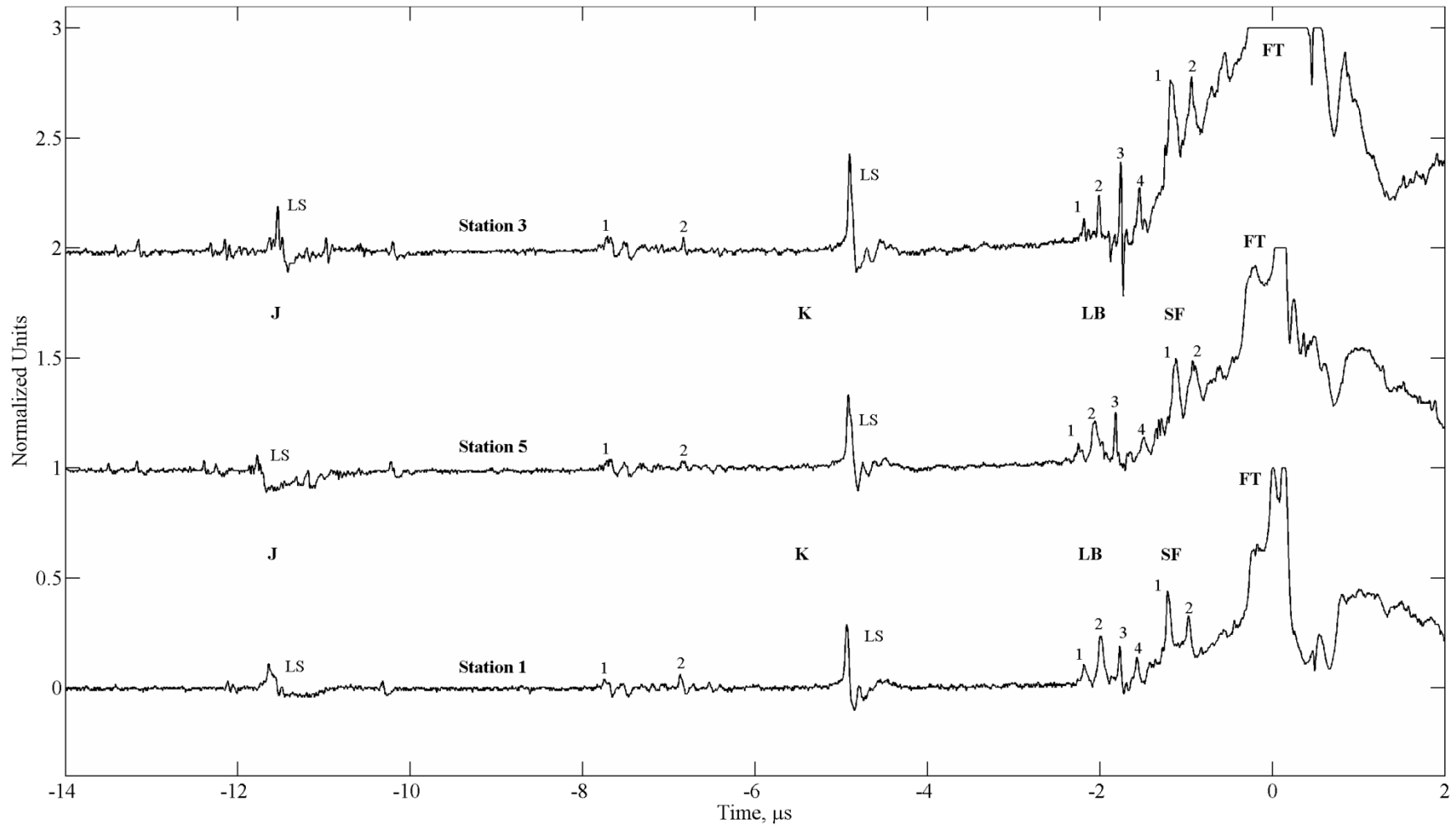


Figure 6-2. Zoomed view of the waveforms shown in Figure 6-1. This figure highlights the final leader steps and the post-leader processes.

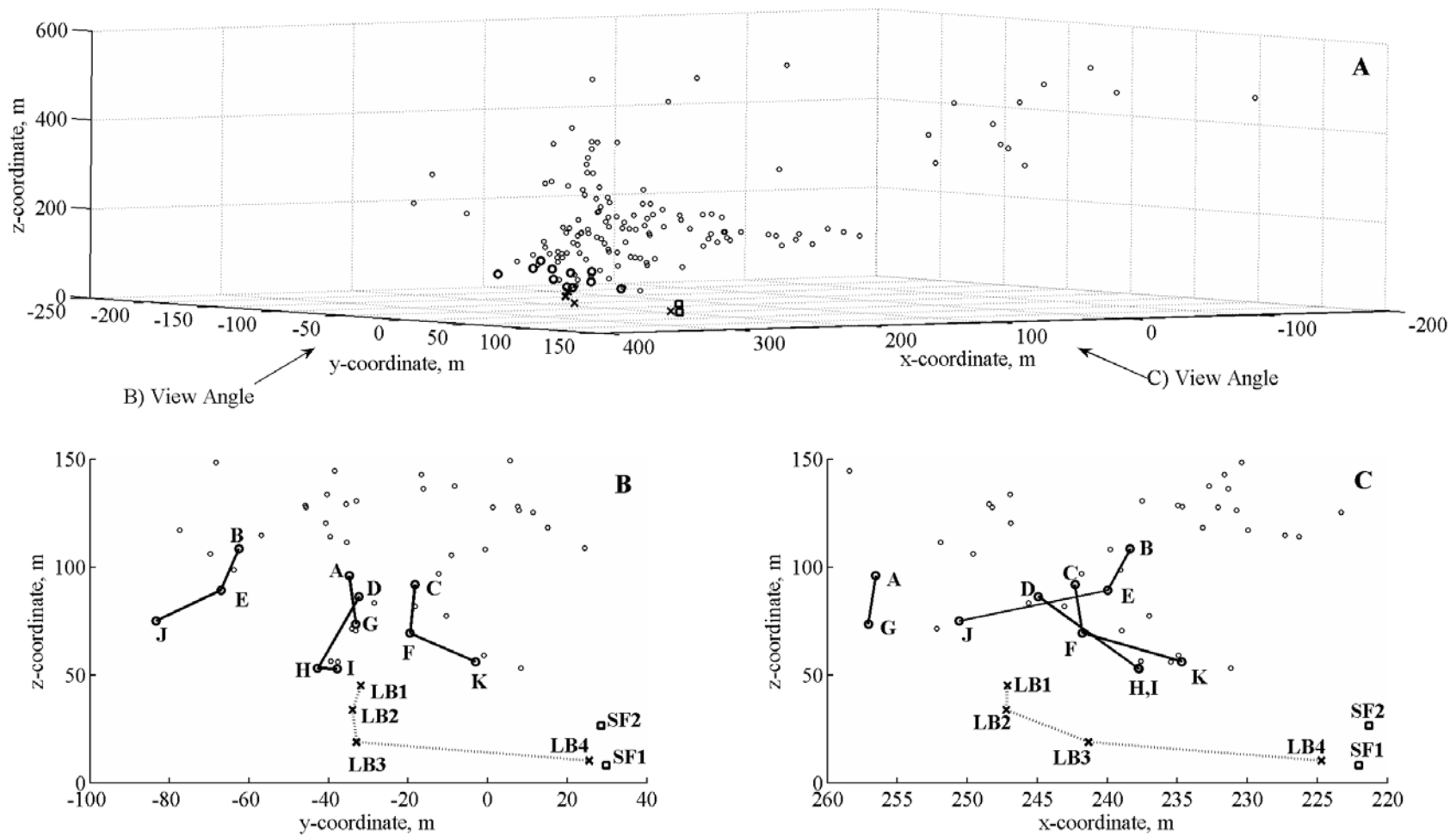


Figure 6-3. Visual representation of the first stroke in MSE0604. A) presents all the located sources in a three-dimensional space. B) and C) are orthogonal vantage points, as indicated by the arrows labeled “View Angle,” on an expanded scale to highlight the events documented in Table 6-1. Solid lines highlight patterns of movement by sequential leader groups, with the bold circles corresponding to the dominant pulses (LS) of those groups. The dotted line is used to highlight the sequential order of pulses in the leader burst (LB). Slow-front (SF) pulses are indicated with the square symbols.

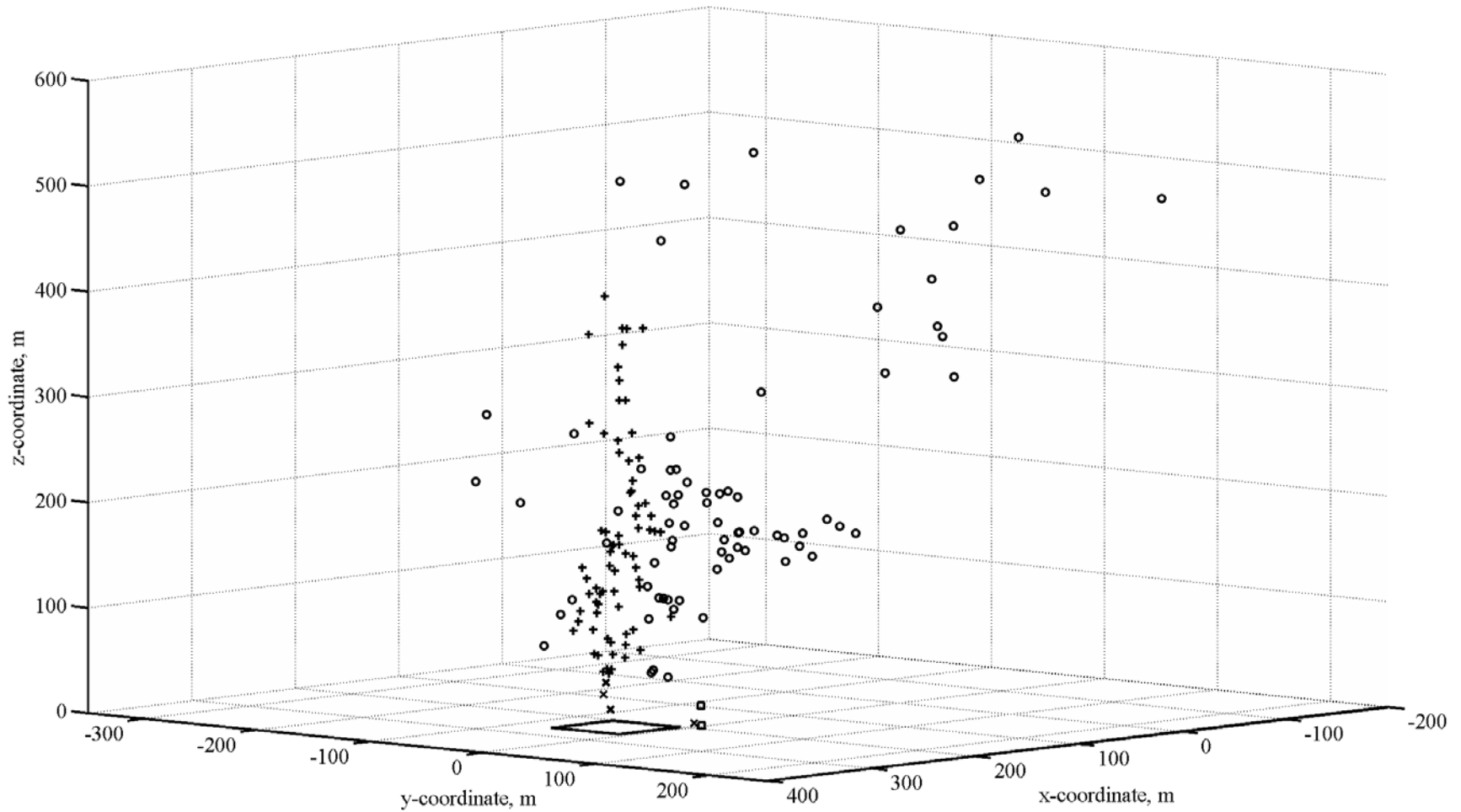


Figure 6-4. Illustration of points used in determining the downward velocity of the MSE0604 stepped leader. To limit the effects of lateral branching, only the leader sources occurring above the square outline were used. These points are indicated with the plus symbols, while circles indicate all other leader points. The post-leader events use the same symbols as Figure 6-3.

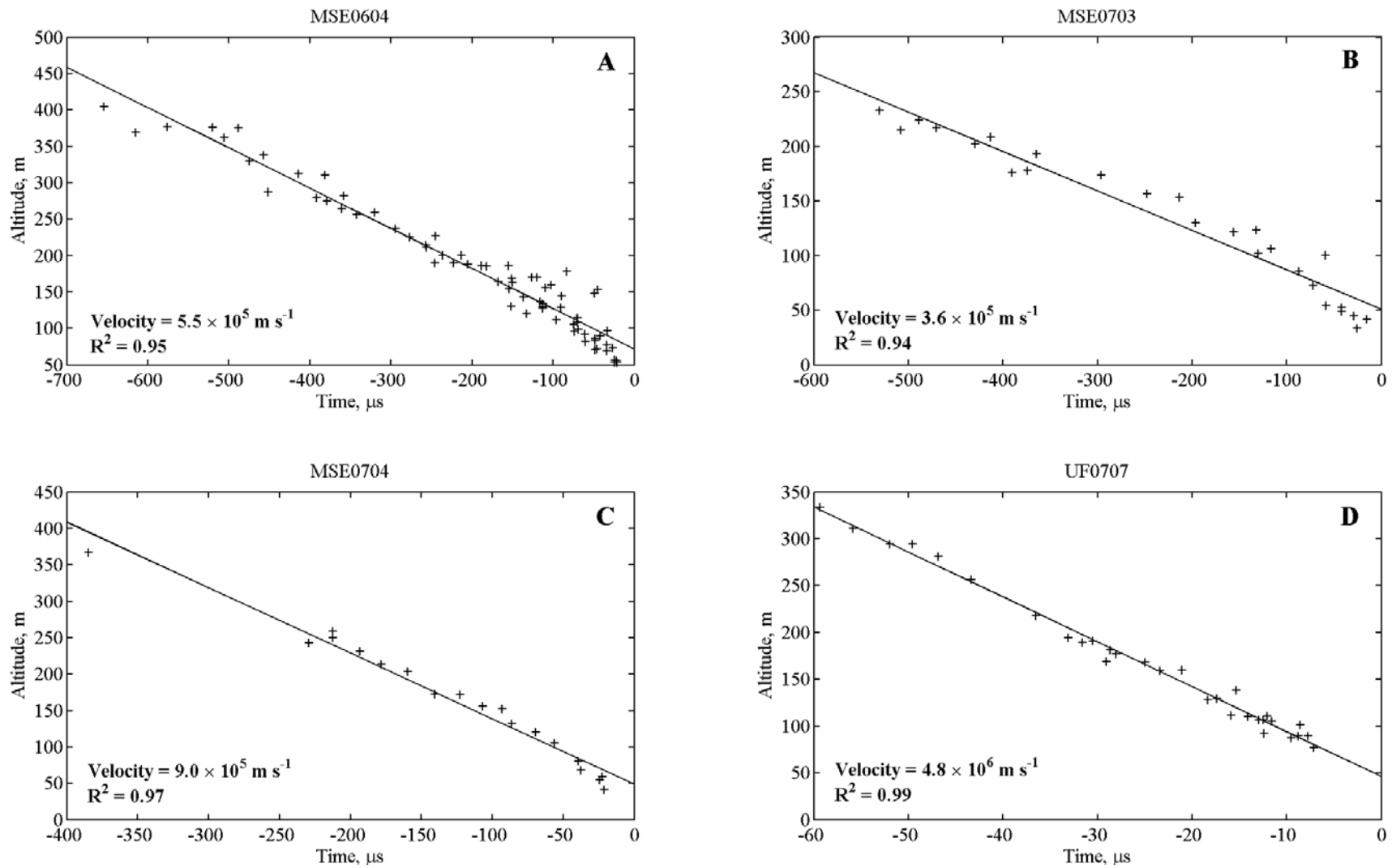


Figure 6-5. Determination of the downward leader velocity for each of the four strokes presented. A) MSE0604, B) MSE0703, C) MSE0704, and D) UF0707. Each plot indicates a strong linear dependence between leader altitude and time, with the slope corresponding to the velocity. The results for each linear fit are indicated in the appropriate figure panel.

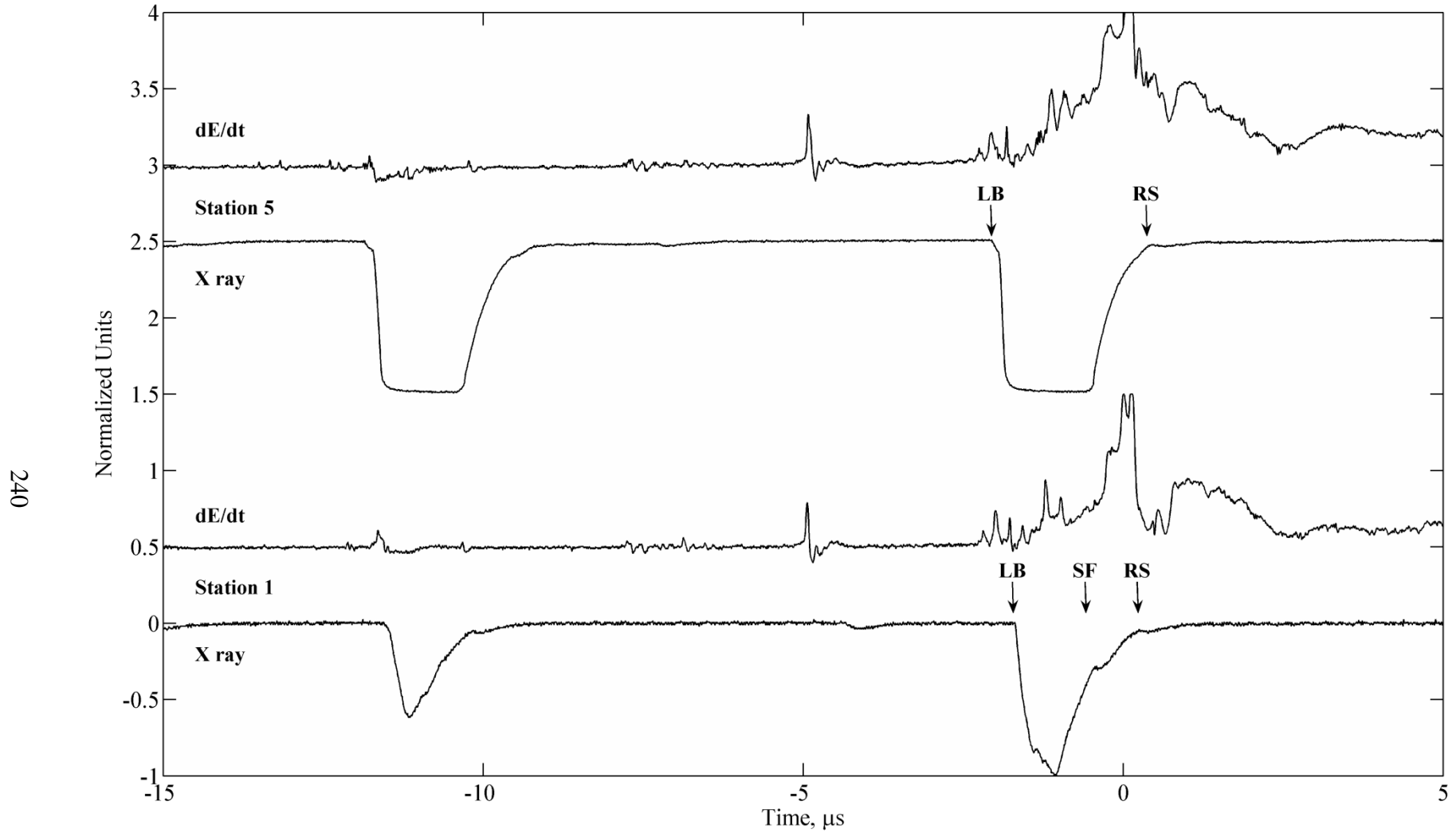


Figure 6-6. Two synchronized pairs of co-located X-ray and dE/dt measurements from MSE0604. The time coincidence between these records is used to determine the association between X rays and post-leader dE/dt events. Note that the clipping of the X-ray pulses is due to the ± 1 V range of the fiber-optic links.

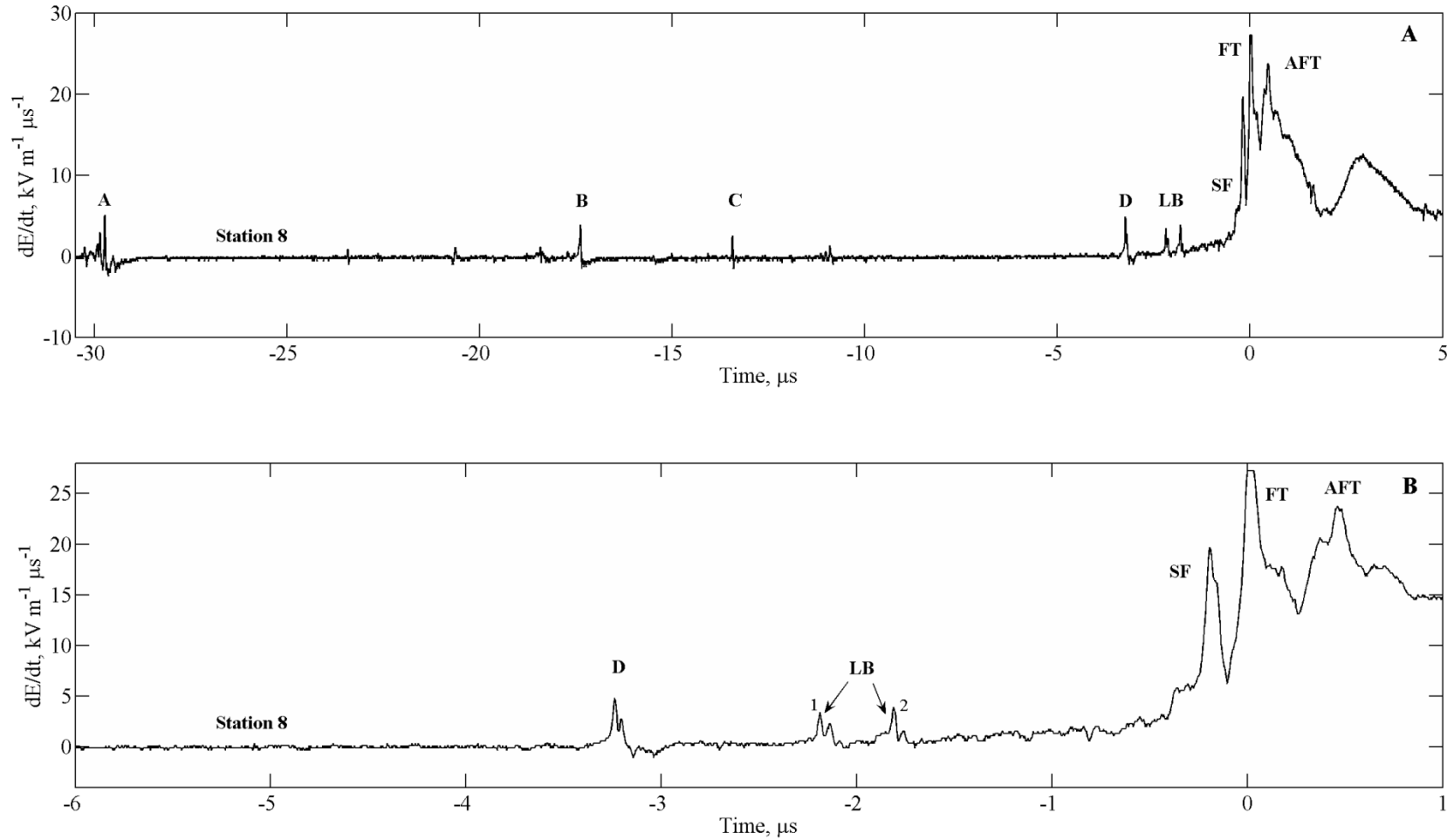


Figure 6-7. dE/dt waveform nearest the first stroke of MSE0703. A) Panel revealing a relatively inactive leader for the final $30 \mu\text{s}$ prior to the return stroke. B) A zoomed view of Panel A that highlights a complex transition and attachment phase, including a leader burst (LB) and three significant pulses associated with the return stroke. The fast transition pulse (FT) in this record is actually clipped due to saturation.

Table 6-2. Summary of TOA location results for the dE/dt pulses shown in Figure 6-7 for the first stoke of MSE0703. The results for each event include the local source coordinates (x, y, z), time of occurrence relative to trigger time (t), covariance estimates for the location uncertainties (Δx Δy Δz), and the number of stations used in the solution (N).

Pulse	Clarifier	x (m)	y (m)	z (m)	t (μ s)	Δx (m)	Δy (m)	Δz (m)	N
A1	BS	591.2	-384.2	48.9	-41.869	0.9	0.8	1.7	6
A2	LS	592.2	-388.0	52.4	-41.755	0.3	0.2	0.4	5
B1	LS	590.6	-378.6	44.4	-29.376	0.8	0.9	1.4	5
C1	LS	586.0	-377.0	33.5	-25.400	4.0	4.4	9.3	6
D1	LS	578.2	-372.0	41.7	-15.181	12.1	13.1	21.8	5
LB1		586.0	-380.7	26.9	-14.147	10.2	11.3	30.6	6
LB2		592.2	-386.3	16.4	-13.791	6.8	8.0	35.7	5
SF		592.4	-381.7	31.3	-12.164	1.6	1.6	15.7	5
FT		592.9	-381.2	34.5	-11.963	2.2	1.9	19.5	5
AFT		591.0	-383.2	12.9	-11.509	5.7	6.2	40.5	6

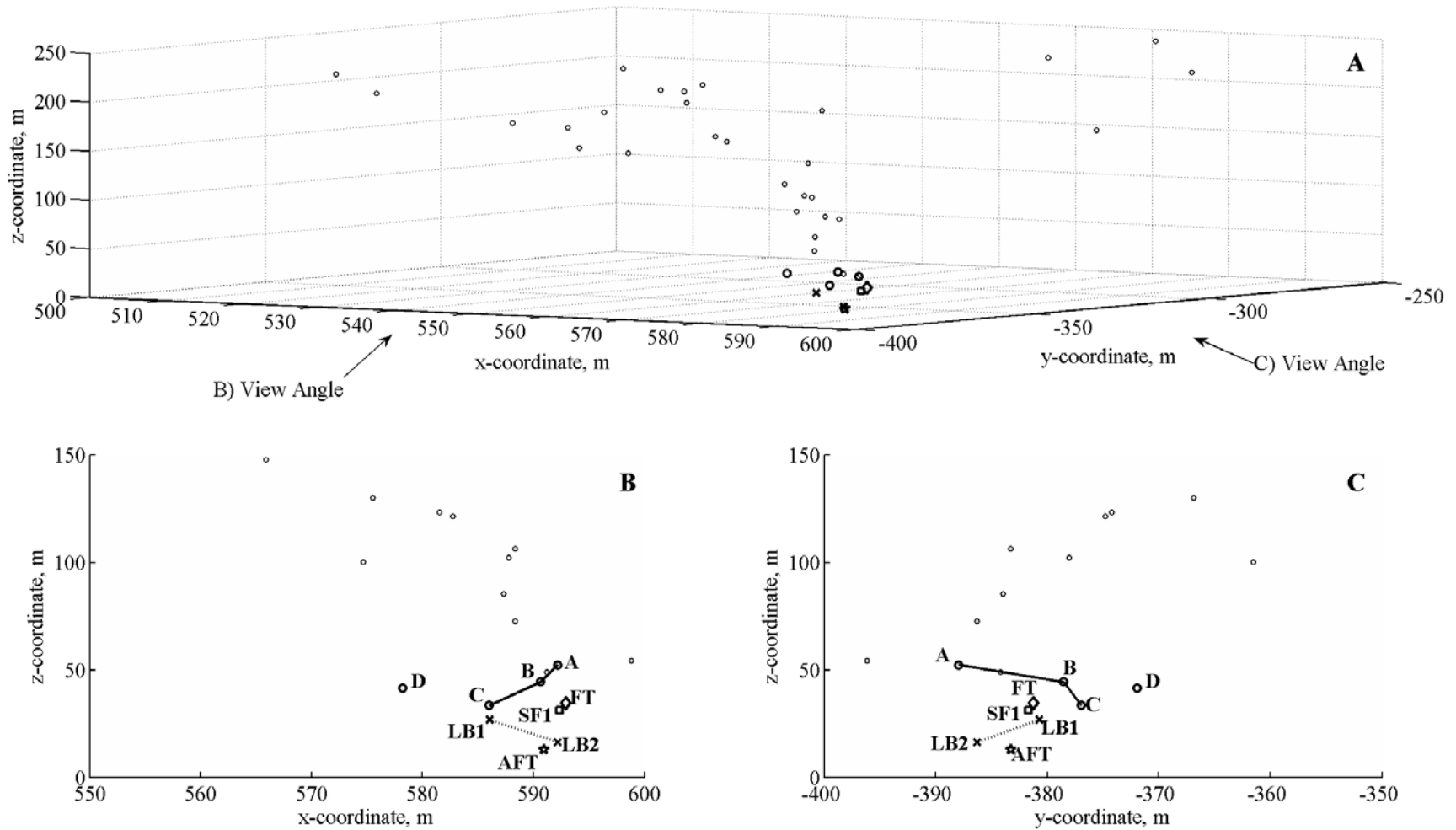


Figure 6-8. Visual representation of the first stroke in MSE0703. The symbol notation is the same as that used in Figure 6-3 except two new symbols were added: the diamond corresponding to the fast-transition and the pentagram denoting the pulse following the fast transition (AFT).

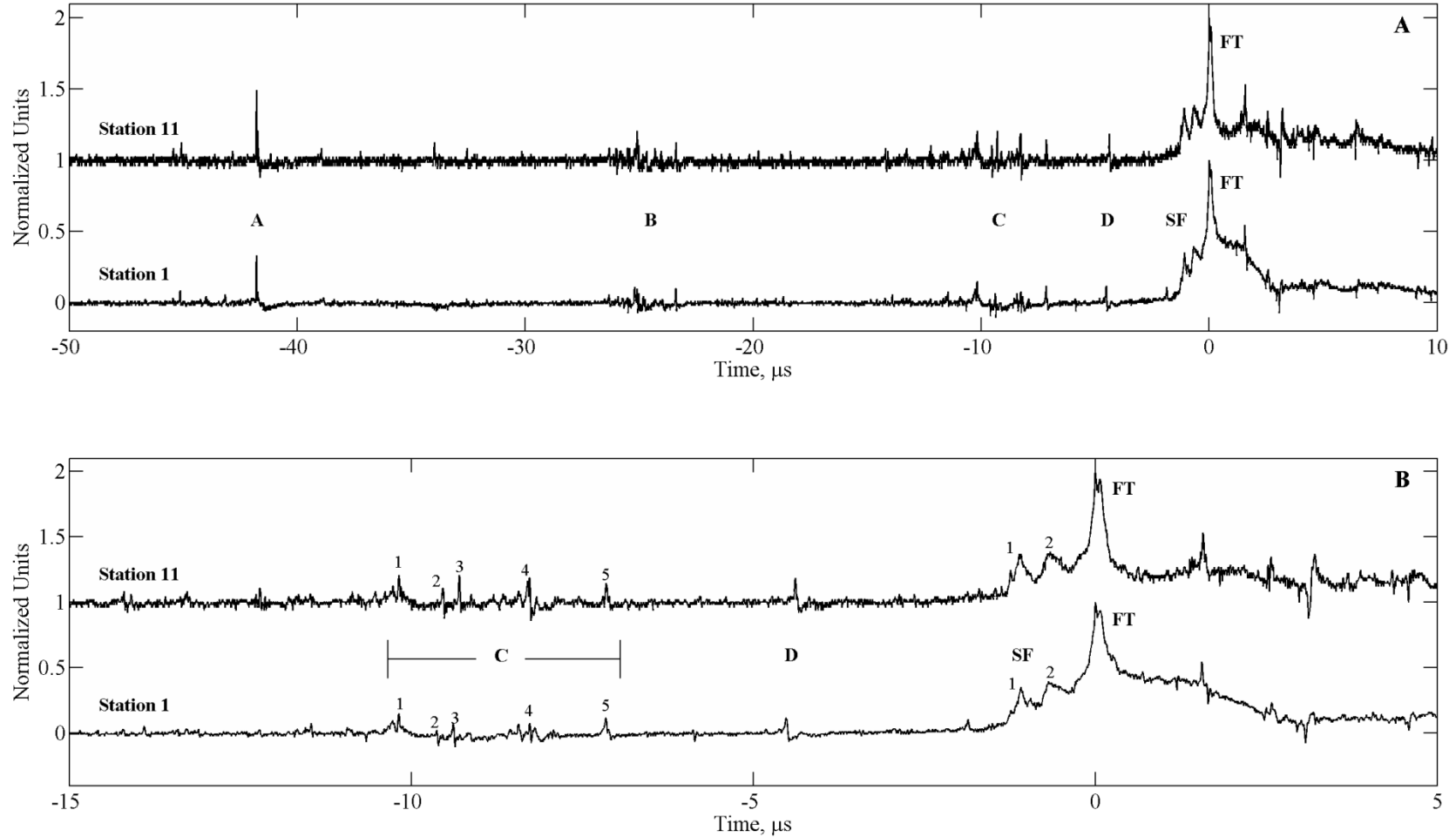


Figure 6-9. Two closest dE/dt waveforms for the first stroke of MSE-0704. A) Waveforms revealing that the leader was not particularly active but involved some complex stepping signatures. B) A zoomed view highlighting the final two leader steps and the return stroke activity.

Table 6-3. Summary of TOA location results for the dE/dt pulses shown in Figure 6-9 for the first stoke of MSE0704. The results for each event include the local source coordinates (x , y , z), time of occurrence relative to trigger time (t), covariance estimates for the location uncertainties (Δx Δy Δz), and the number of stations used in the solution (N).

Pulse	Clarifier	x (m)	y (m)	z (m)	t (μ s)	Δx (m)	Δy (m)	Δz (m)	N
A1	LS	-130.8	-120.9	104.8	-56.111	3.1	0.9	1.8	5
B1	LS	-117.0	-130.6	80.4	-39.283	13.0	3.7	7.4	5
B2	AS	-131.1	-122.0	67.6	-37.682	3.9	1.2	2.7	5
C1	LS	-107.7	-136.7	54.4	-24.381	10.9	3.3	9.5	5
C2	BS	-86.9	-102.0	97.8	-23.810	6.1	2.4	3.7	5
C3	BS	-62.9	-112.0	88.7	-23.486	9.6	3.8	6.6	5
C4	AS	-120.2	-131.2	59.1	-22.674	4.6	1.4	3.8	5
C5	AS	-118.0	-131.9	41.6	-21.373	13.1	3.8	14.2	5
D1	LS	-66.0	-91.3	94.2	-18.639	8.1	3.7	4.9	5
SF1		-123.7	-140.1	38.4	-15.326	39.0	10.3	42.2	5
SF2		-106.2	-131.2	29.8	-14.851	26.1	9.3	25.0	5
FT		-125.7	-134.6	28.9	-14.235	31.6	8.9	40.5	6

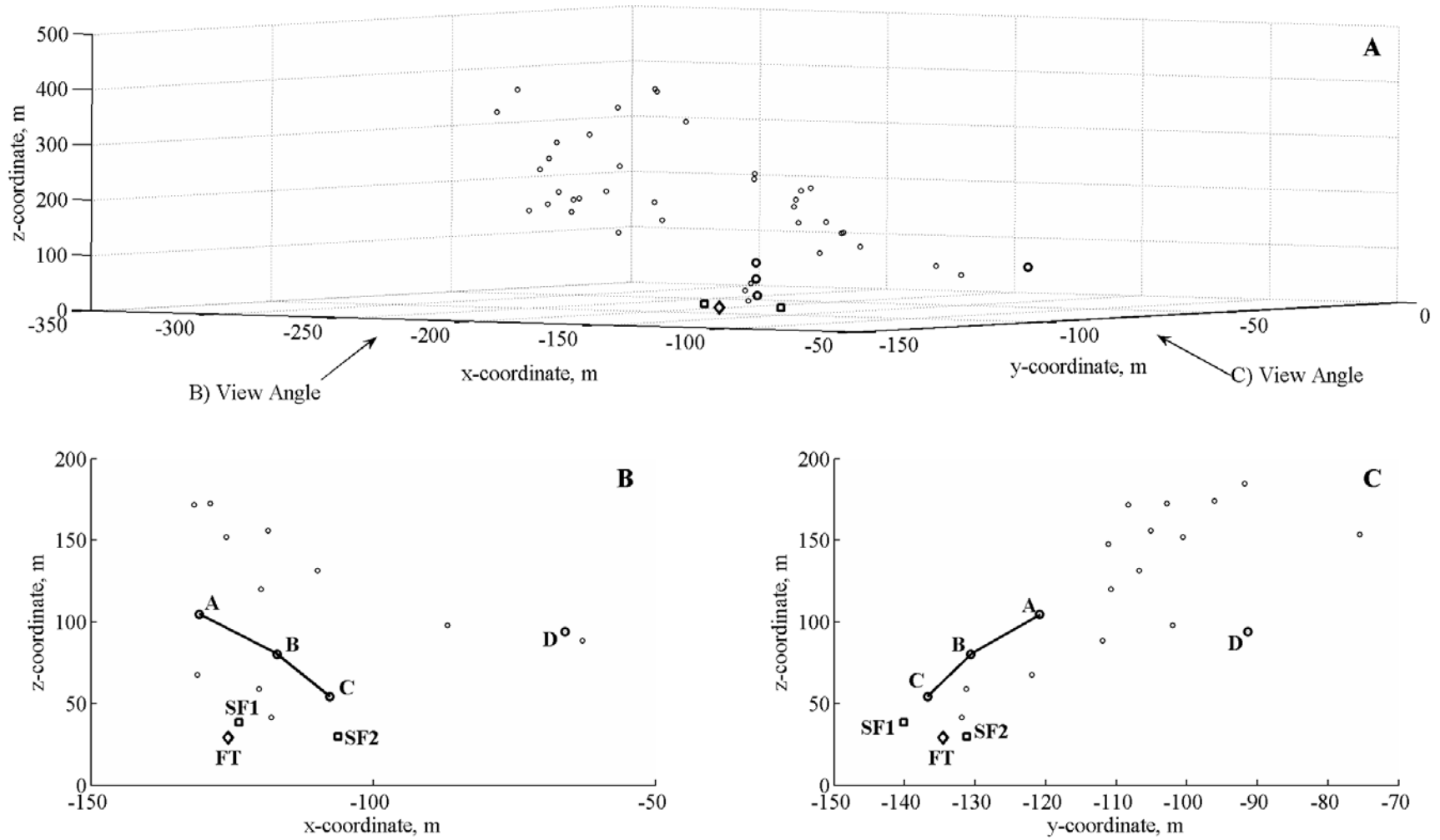


Figure 6-10. Visual representation for the first stroke of MSE0704. The symbol notation is consistent with that previously used in Figures 6-3 and 6-8.

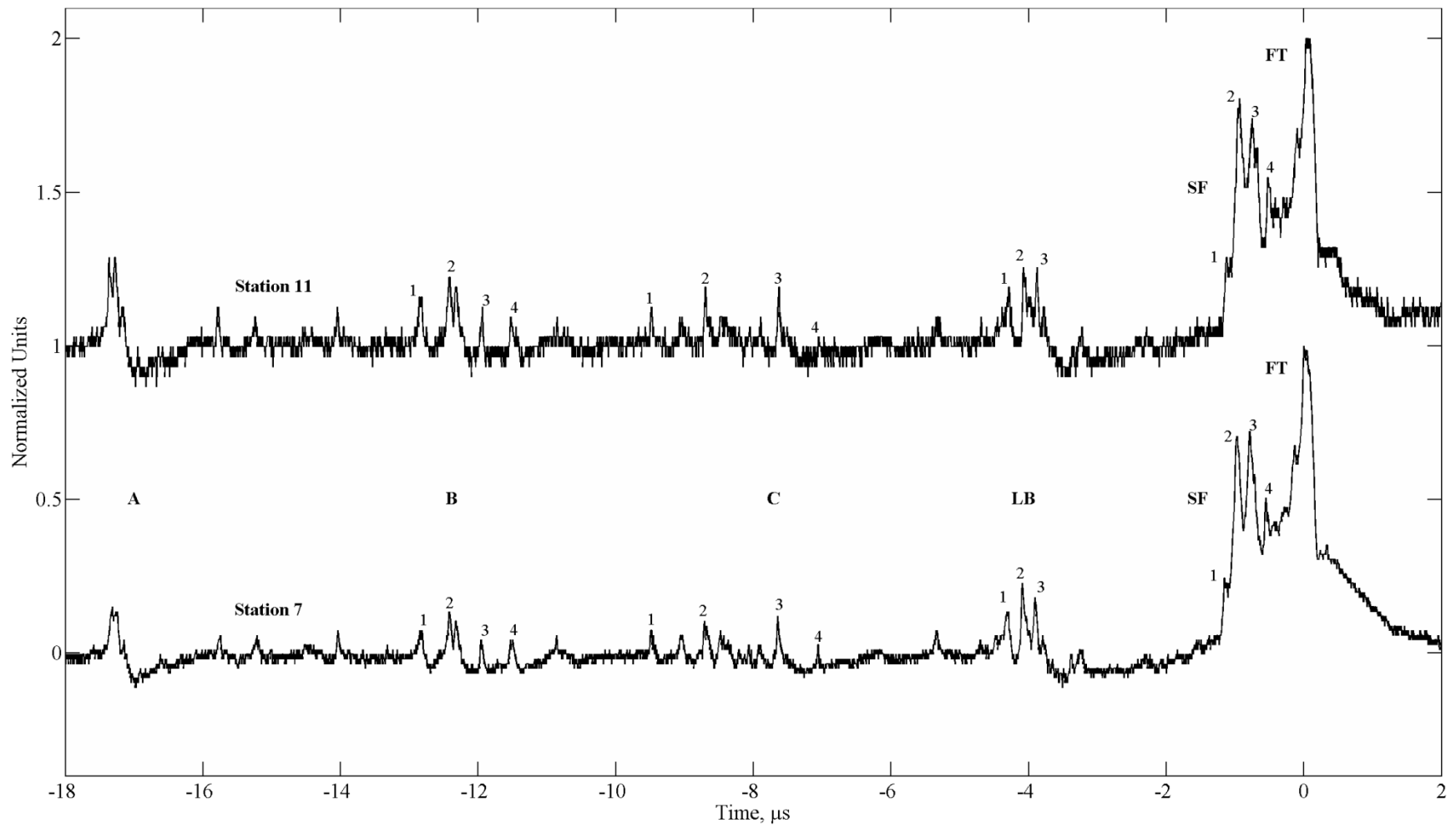


Figure 6-11. Two dE/dt waveforms for the first stroke in rocket-triggered flash UF0707. Notice the unusual transition produced by the slow-front pulses.

Table 6-4. Summary of TOA location results for the dE/dt pulses shown in Figure 6-11 for the first stroke of UF0707. The results for each event include the local source coordinates (x, y, z), time of occurrence relative to trigger time (t), covariance estimates for the location uncertainties (Δx Δy Δz), and the number of stations used in the solution (N).

Pulse	Clarifier	x (m)	y (m)	z (m)	t (μ s)	Δx (m)	Δy (m)	Δz (m)	N
A1	LS	381.8	-204.0	129.1	-17.366	3.4	3.1	16.7	5
B1	BS	384.8	-201.6	106.4	-12.933	1.8	1.7	10.1	5
B2	LS	388.0	-204.2	106.6	-12.505	2.9	2.7	15.8	5
B3	AS	386.9	-201.1	110.8	-12.056	6.2	5.7	33.0	5
B4	AS	390.1	-203.8	105.6	-11.611	7.1	6.4	37.9	5
C1	BS	387.6	-201.1	87.5	-9.554	2.1	1.9	13.1	5
C2	BS	390.2	-198.9	89.4	-8.781	0.9	0.8	5.3	5
C3	LS	392.7	-195.0	89.7	-7.730	5.6	5.0	34.2	5
C4	AS	389.2	-197.5	76.8	-7.120	5.6	5.2	39.6	5
LB1		389.2	-199.4	74.4	-4.358	1.8	1.7	13.1	5
LB2		389.6	-198.0	69.4	-4.141	2.9	2.7	22.4	5
LB3		390.4	-196.9	49.3	-3.939	3.9	3.7	40.9	5
SF1	Shoulder	387.7	-198.2	35.5	-1.171	0.5	0.5	7.4	5
SF2		388.8	-199.0	41.4	-1.002	1.9	2.0	24.5	5
SF3		392.7	-197.5	46.8	-0.818	2.1	2.1	23.5	5
SF4		390.7	-204.1	53.6	-0.572	4.5	4.5	43.3	5
FT		388.3	-203.5	55.6	-0.012	2.8	2.8	26.0	5

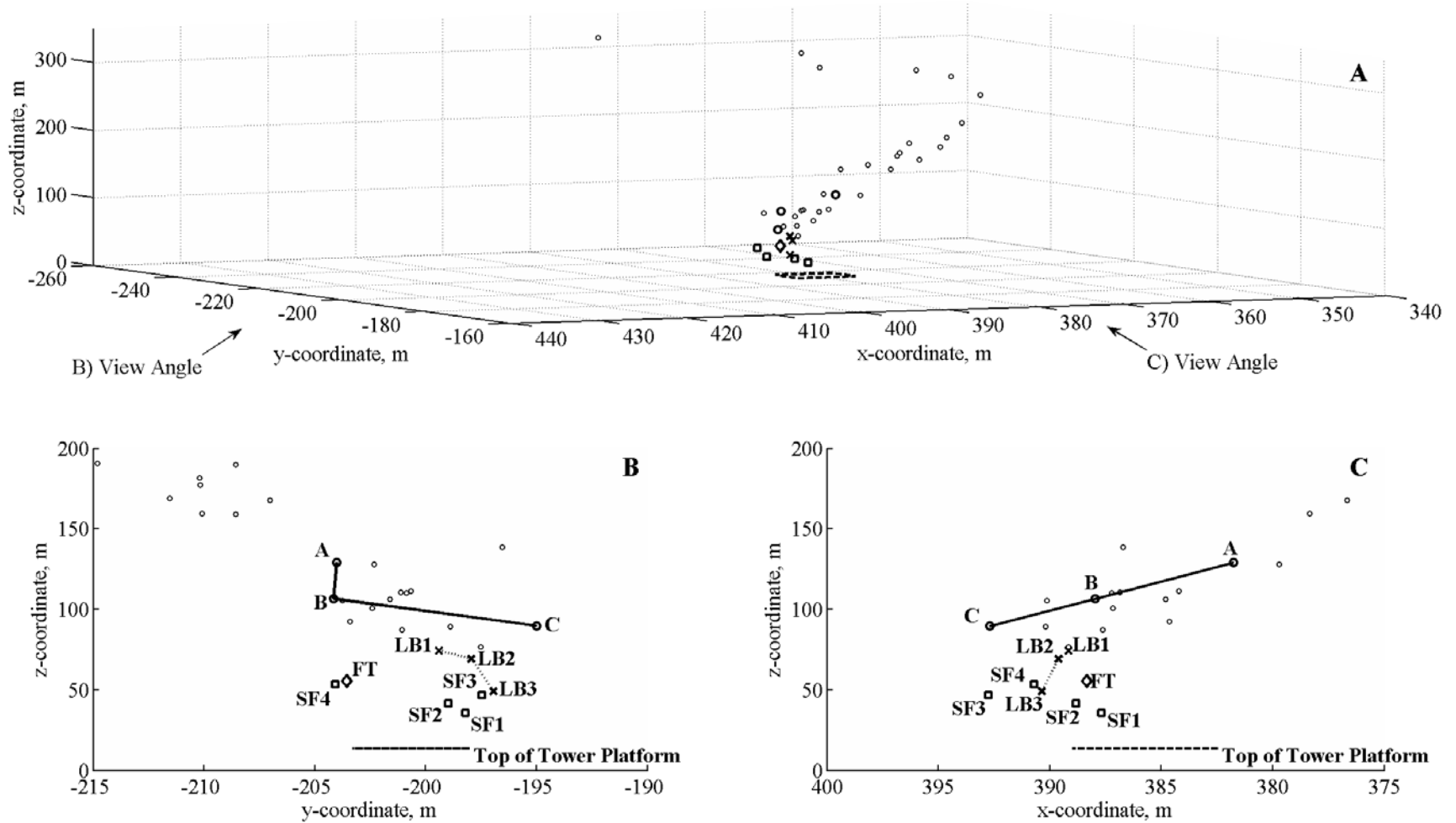
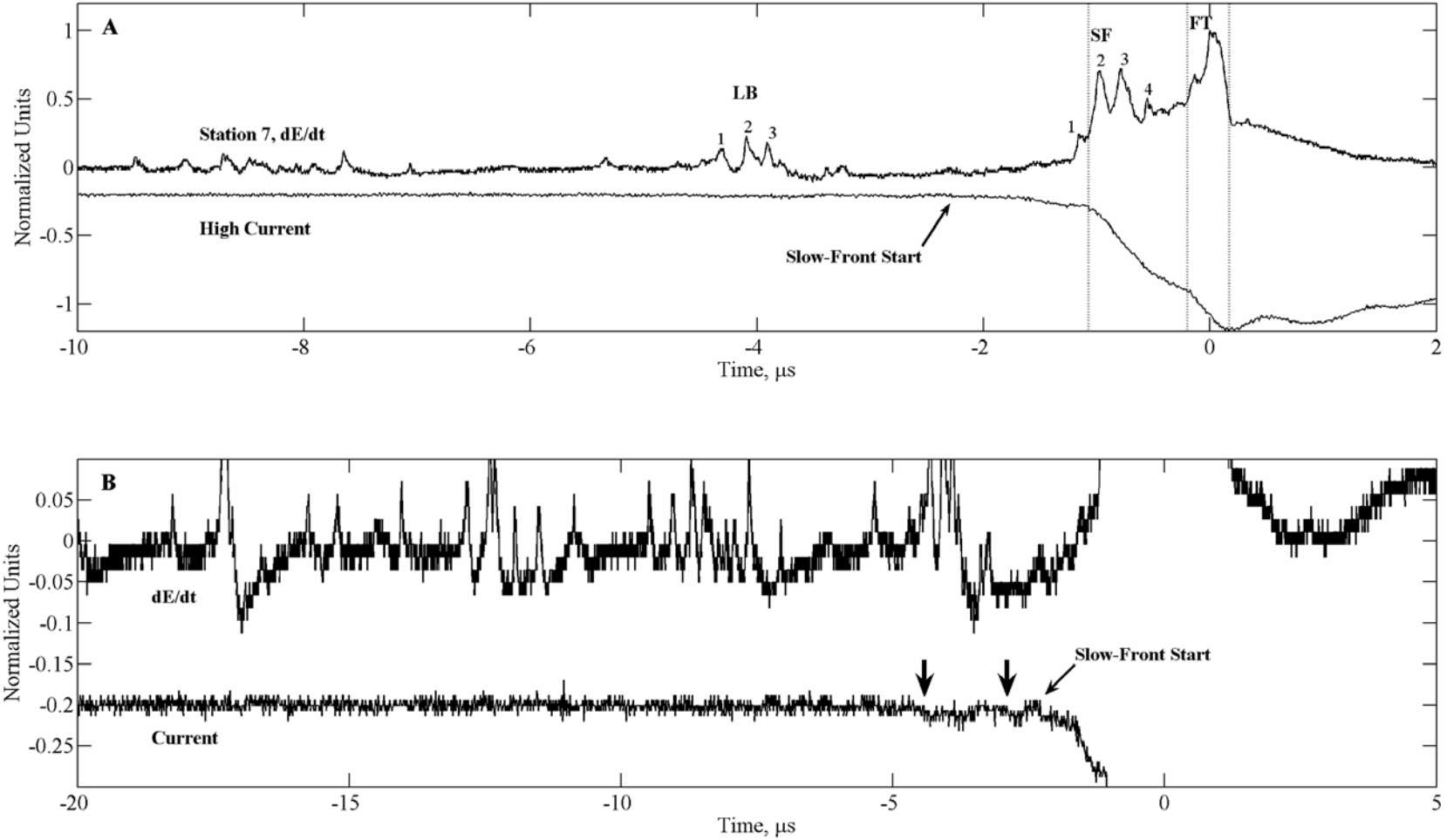


Figure 6-12. Visual representation for the first stroke in the rocket-triggered flash UF-0707. The symbol notation is consistent with that used for the natural strokes in Figures 6-3, 6-8, and 6-10. The rectangular outline below the downward leader indicates the location of the tower platform.



250

Figure 6-13. Comparison of the Station 7 dE/dt waveform and the channel-base current for rocket-triggered flash UF0707. A) The dotted lines highlight corresponding features in the two waveforms. The start of the slow front is indicated by the arrow marker. B) An alternative view of the two waveforms that highlights two hundred-ampere-level pulses in the current, which are indicated by the vertical arrows.

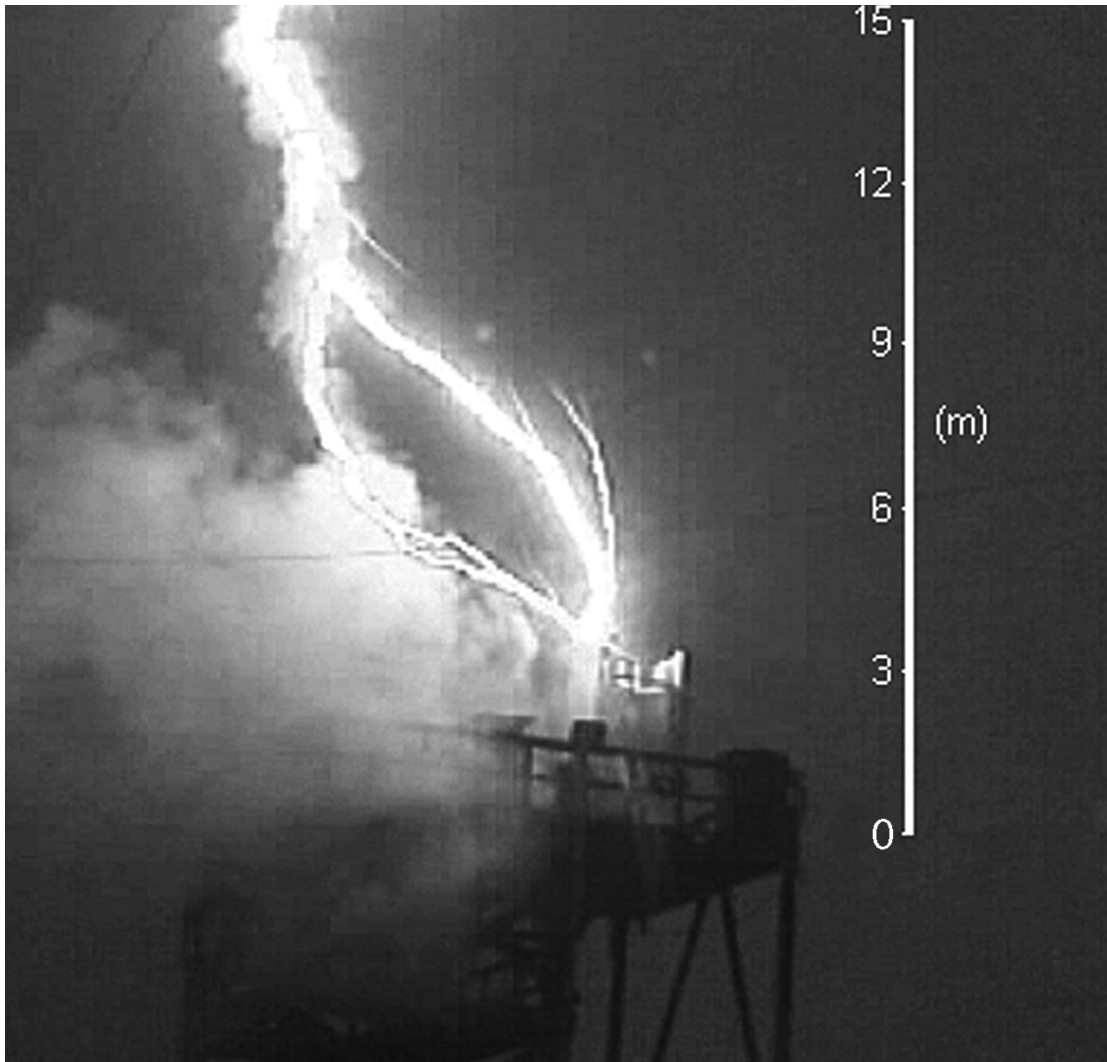
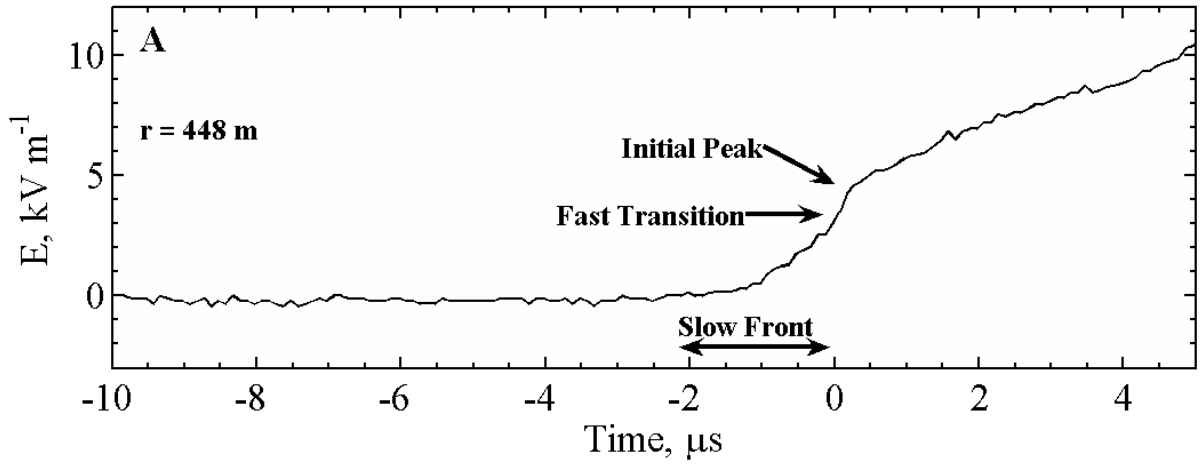
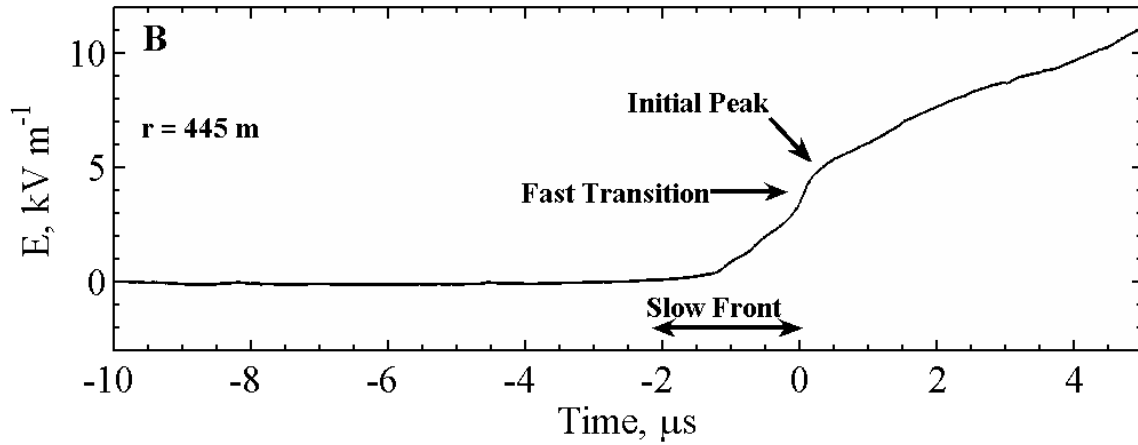


Figure 6-14. Single video frame imaging the first return stroke in flash UF0707. There are two primary connections, with a subconnection visible in the lower primary channel. The image also reveals unconnected upward and downward leader branches. The height scale on the right indicates the height of the channel above the top of the Tower platform. The height of the channel termination point is 3.3 m above the platform.

MSE0704, Station 5, E-field



MSE0704, Station 5, Integrated dE/dt



MSE0704, Station 5, dE/dt

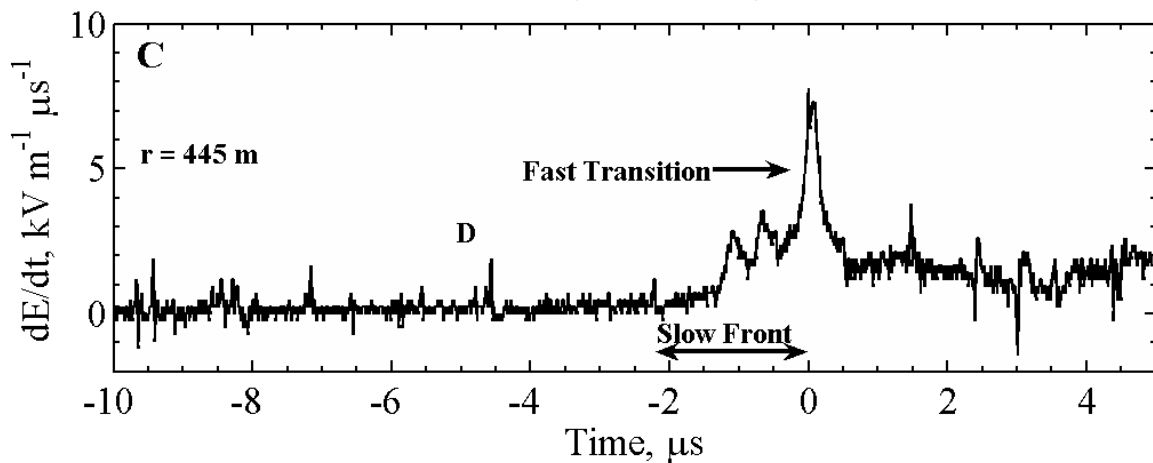


Figure 6-15. Comparison of MSE0704 return-stroke waveforms measured at Station 5. A) Measured E-field, B) time-integrated dE/dt , and C) dE/dt .

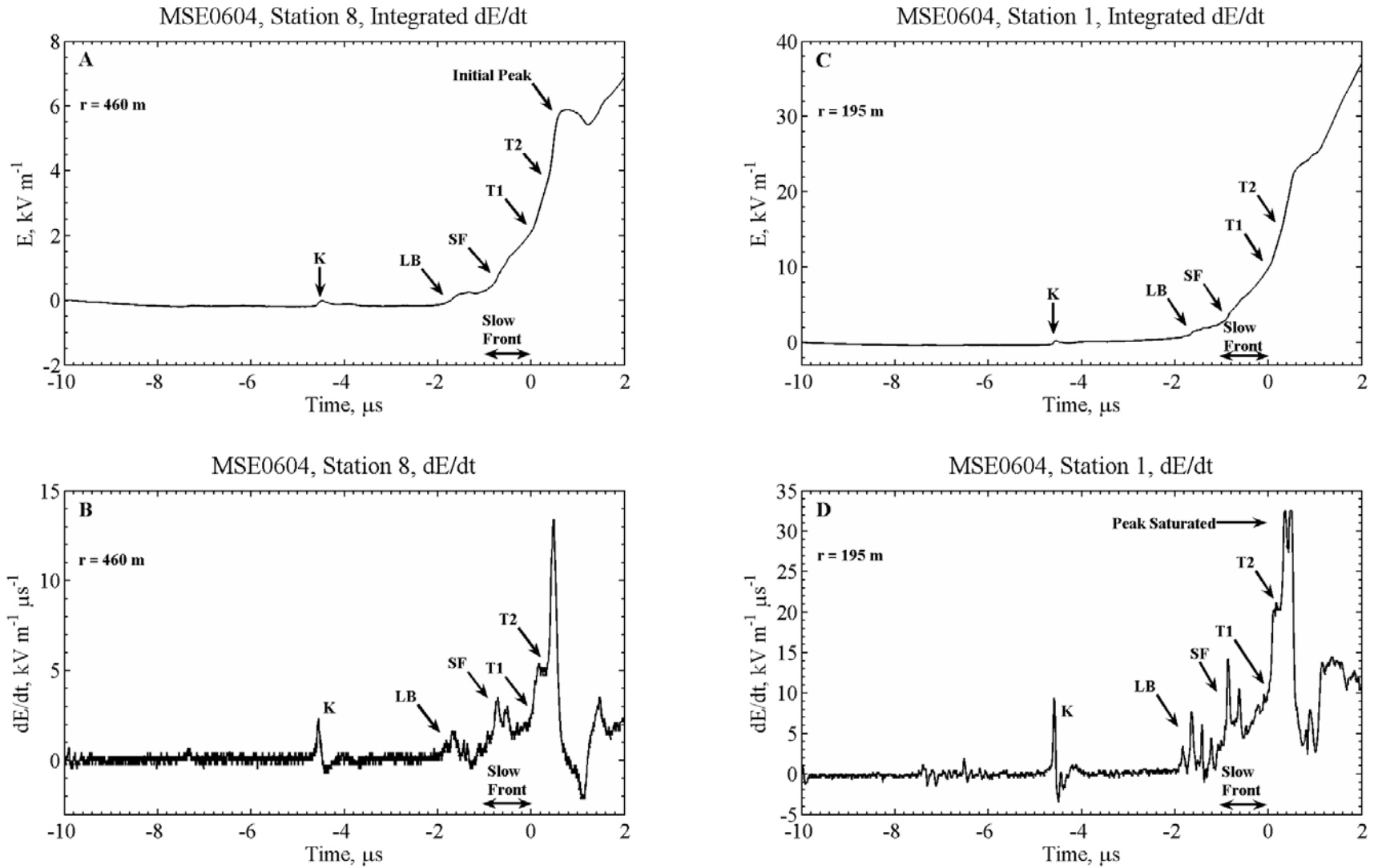


Figure 6-16. Comparison of MSE0604 return-stroke waveforms measured at Stations 1 and 8. A) Time-integrated dE/dt at Station 8, B) dE/dt at Station 8, C) time-integrated dE/dt at Station 1, and D) dE/dt at Station 1.

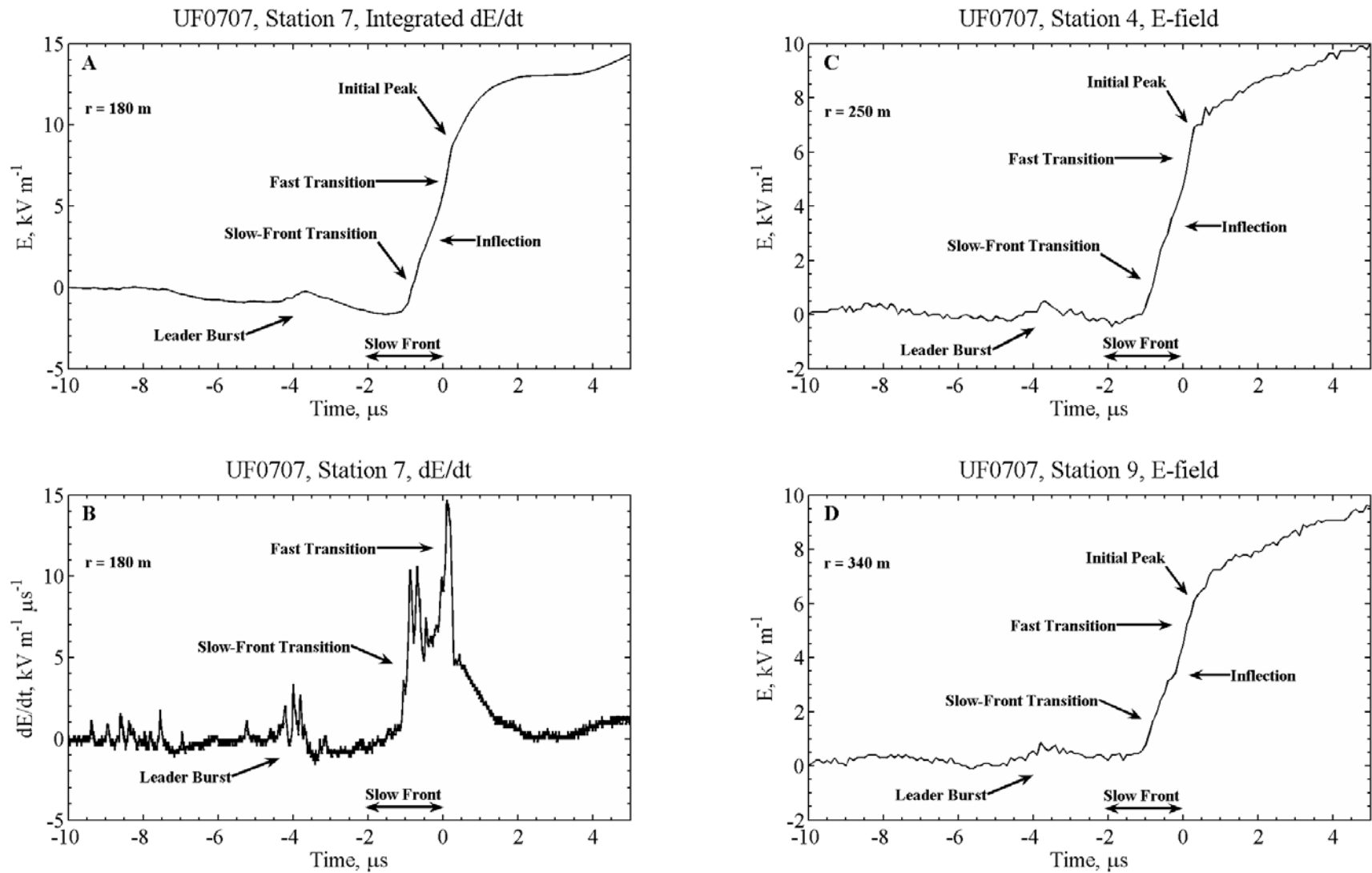


Figure 6-17. Comparison of UF0707 return-stroke waveforms measured at Stations 4, 7, and 9. A) Time-integrated dE/dt at Station 7, B) dE/dt at Station 7, C) E-field at Station 4, and D) E-field at Station 9.

CHAPTER 7

EXAMINATION OF ELECTRIC FIELD DERIVATIVE WAVEFORMS ASSOCIATED WITH STEPPED LEADERS AT CLOSE RANGES

This dissertation has focused on using the Multiple Station Experiment/Thunderstorm Energetic Radiation Array (MSE/TERA) measurements to investigate low-altitude lightning processes. Thus far, the dE/dt waveforms have been utilized primarily to determine arrival times so that sources of electrical breakdown could be located. In this chapter, the shape and amplitude of the close leader-step dE/dt waveforms obtained by the MSE/TERA network are examined in order to gain additional insights into leader-stepping process.

Surprisingly, decades of lightning research have yet to provide a significant collection of leader-step waveforms obtained at close distances, especially for natural lightning. The primary cause for this lack of data is the unpredictability of natural flash locations. Because lightning flash densities (flashes $\text{km}^{-2} \text{yr}^{-1}$) are in single digits for many regions of the world, most lightning observations are obtained at distances of tens or hundreds of kilometers. Of course, physical limitations of sensors and recording equipment have also restricted the collection of good leader-step waveforms. For instance, measurements designed to observe the overall field changes caused by leaders and return strokes will likely not have the amplitude resolution to view individual leader steps, and observations made before the digital era typically triggered on the return stroke and had very limited pretrigger capabilities, causing them to miss most of the leader phase.

Distant leader-step waveforms (both E-field and dE/dt) have provided a general characterization of leader steps and the pulses associated with them. The wideband electric field data of *Krider and Radda* [1975] indicated that the leader-step pulse duration, pulse rise time, and interstep interval all decrease as the leader nears the ground. On the other hand, the pulse amplitude typically increases as the leader nears ground, with the largest, and usually the last,

leader step having a peak amplitude value about 10% of the return-stroke pulse peak amplitude. The shape of the distant leader-step E-field pulse is characterized by a large initial peak with a smaller and slower opposite-polarity overshoot. Under conditions where pulse distortion due to propagation effects is minimal (i.e., the field propagation is over seawater), *Krider et al.* [1977] reported that the 10–90% rise times of individual step waveforms are on average 0.2–0.3 μs , and the half-peak width is typically 0.4–0.5 μs . *Weidman and Krider* [1980] reported that the 10–90% rise times of individual step E-field pulses were similar to those of the fast-transition of return-stroke E-field pulses, 40 to 200 ns with a mean of 90 ns, when propagation was over seawater. From measurements of such electric field pulses, *Krider et al.* [1977] inferred that the peak step current is at least 2–8 kA close to the ground, the maximum rate of change of step current is 6–24 $\text{kA } \mu\text{s}^{-1}$, and the minimum charge involved in the formation of a step is 1–4 mC. Similar values were also obtained by *Rakov et al.* [1998] for steps of a dart-stepped leader in rocket-triggered lightning.

In some instances, the half-peak width (T_{HPW}) of the dE/dt waveform is preferred to a direct measurement of the 10–90% rise time on a corresponding electric field pulse because the dE/dt half-peak width emphasizes the fast-rising portion of the E-field pulse, i.e., the slow front on the E-field pulse usually does not contribute significantly to the amplitude of the corresponding dE/dt pulse and, therefore, does not affect the half-peak width. *Willett and Krider* [2000] estimated the mean half-peak width of dE/dt step waveforms to be 54 ns (standard deviation 17 ns) for 114 stepped-leader pulses. *Krider et al.* [1992] reported the mean peak amplitude of dE/dt step waveforms, range normalized to 100 km, to be $13 \text{ V m}^{-1} \mu\text{s}^{-1}$ (17 values) and the mean half-peak width to be 69 ns (eight values).

The collection of close dE/dt leader-step waveforms presented in this chapter are believed by the author to be the first illustrating how step pulses vary with distance at close range. Moreover, the high bandwidth and close range should better reveal the true structure of leader-step waveforms compared to the distant leader-step measurements, which may suffer some propagation degradation, even when the field propagation is over saltwater. The waveforms presented here are a significant addition to the existing data of step pulses and should prove useful for leader-step modeling, estimating physical quantities, and determining propagation effects. The remainder of this chapter focuses on examining the structure of the leader-step dE/dt waveforms, measuring a few parameters of these waveforms, and modeling observed leader-step dE/dt pulses in order to characterize the leader step current.

7.1 Presentation of Leader-Step Waveforms

The collection of leader-step dE/dt waveforms presented in this section reveals a variety of leader pulse shapes, indicative of a complex and unique breakdown process within each step. However, this collection of waveforms also reveals that leader steps produce a characteristic dE/dt waveshape at close range, which is generally observed throughout the example waveforms presented in this chapter. This characteristic shape can be described as a bipolar pulse having a sharp initial peak with the same polarity as the return-stroke pulse, followed by an opposite-polarity overshoot which decays slowly to the background level, as can be observed in Figure 7-1.

In addition to illustrating the characteristic leader pulse shape, Figure 7-1 also illustrates the template that will be used to present the leader-step dE/dt waveforms in this section. Each figure that illustrates a leader step in this section will consist of either four or five waveforms, with all the waveforms in a single figure displayed on the same time and amplitude scales. Each leader step presented in this section was located using time-of-arrival (TOA) analysis (based on

the arrival times for the dominant peak), so the position of each measurement relative to the leader step is known. Hence, each waveform is labeled with its corresponding station number, the length of the vector \vec{R} pointing from the leader step to the dE/dt antenna, and the angle (θ) between the vector \vec{R} and the downward vertical. The spatial relationship between the leader step and the antenna in terms of \vec{R} and θ is illustrated in Figure 7-2. The waveforms in each figure are shown from top to bottom with increasing $|\vec{R}|$.

Now that the format of the presentation has been discussed, we examine the various leader step signatures. Since most of the example waveforms to be presented here were produced by the same flash, MSE0604, it seems prudent to present at least one leader step from another flash which also exhibits the characteristic pulse shape to confirm that this feature is common. A leader step from MSE0703 that exhibits the characteristic shape is shown in Figure 7-3. This characteristic shape remains prominent throughout the remaining example waveforms presented in this section; however, this shape is altered to varying degrees due to additional breakdown activity in the step and the spatial relationship between the step and the antenna.

Figures 7-4 and 7-5 both illustrate leader steps in which the shape of the pulse is affected at one or more sensors due to their position relative to the step. In Figure 7-4, the initial sharp peak of the leader pulse is essentially absent from the closest waveform observed at Station 3. The same is true for both the Station 3 and Station 5 waveforms shown in Figure 7-5, although they are the two closest stations to the step. As will be discussed in Section 7.3, the electromagnetic radiation observed at a distance from an assumed vertical, finite current-carrying element (used to approximate the leader-step channel) is dependent on the length of the element, the current distribution in the element, and the position (ground range and elevation) of the element relative to the observer. Section 7-3 also reveals that there are three components (electrostatic, induction,

and radiation) to the observed electric field (or electric field derivative) when the field observation is made at ground and the ground is a perfect conductor. Since the radiation component is the only component that fundamentally approaches zero as the current-carrying element approaches a position overhead the observation point, it stands to reason that the initial peak of leader-step dE/dt pulses is dominated by the radiation component. In the case that the leader-step dE/dt waveform is being modeled, the radiation component is proportional to the second derivative of the leader-step current.

Figures 7-6 and 7-7 are unusual leader-step waveform examples in that there is a negative dip leading into the dominant pulse peak of the closest dE/dt waveform. For all of the waveforms that exhibit this feature, the stations are extremely close to the leader step, which seems to suggest that this feature has a strong dependence on distance. This feature may be related to the electrostatic component since it has the greatest dependence on distance; however, not all waveforms at a similar range exhibit this feature. Because the electrostatic component of dE/dt waveforms is proportional to the source current, this feature may simply result from having a particular current waveshape at a significantly close distance. Notice that the different viewing angles for the closest measurements in Figures 7-6 and 7-7 result in significantly different waveform transitions associated with the dominant leader pulse, or alternately why the leader step is assumed to be vertical, it may not be.

Figures 7-8 through 7-15 provide eight additional examples of leader-step waveforms, many containing secondary pulses superimposed on and near the characteristic pulse shape. These are the same type of secondary pulses that were discussed in Chapter 6 and were divided into the before (BS) and after (AS) pulses. Note how the secondary pulses in Figures 7-13, 7-14, and 7-15 are so near the dominant peak that it almost appears that the leader-step pulse has a

slow front. However, that the leader step shown in Figure 7-1 does appear to have an actual slow front, similar to a natural first stroke.

Throughout the waveforms presented in this section, the amplitude of the opposite-polarity overshoot appears to be largely dependent on the distance from the leader step, with the overshoot typically having the largest value in the closest waveforms and barely being observed in the farthest waveforms. Hence, it is likely that the overshoot is related to the electrostatic and induction field components. Finally, we note again that the references made here in terms of different field components have been based on the assumption of a straight and vertical leader channel, which is likely not the case. In truth, the orientation of the leader channel may greatly affect the observed field. The effect of the leader channel orientation can be observed in Figure 7-13, where the Station 3 and Station 5 waveforms exhibited significantly different initial peak amplitudes despite the ranges and viewing angles to these two measurements being nearly identical.

7.2 Parameters for dE/dt Pulses of Stepped-Leaders

Due to the proximity of the leader steps to the dE/dt antennas of the MSE/TERA network, it is reasonable that the half-peak values (T_{HPW}) for the dE/dt pulses, which are generally indicative of the rise times for the corresponding electric field pulses, may be faster than any previously recorded. Although previous studies that have measured this quantity [e.g., *Willett and Krider, 2000*] have typically attempted to minimize distortion due to propagation effects by having the electromagnetic radiation propagate over salt water, there still may be some broadening of the pulse and decrease of its amplitude. Since an automated program was used to identify these step pulse peaks and calculate the half-peak width, it was not much of an extension to also measure the 10–90% rise time for the dE/dt step pulses.

As discussed in Section 2.5.1, there is some concern with the amplitude calibration of the dE/dt antennas of the MSE/TERA network. This concern arises from the fact that while integrating a dE/dt measurement always reproduces the directly measured electric field waveshape at the same station, it results in a waveform with smaller amplitude [Jerould, 2007]. The scaling factor needed to correct for this “error” usually varies from about 1.2 to 2, is different at each station, and changes from day to day. However, this scaling factor remains constant at each station for flashes that occur on the same day. It is unclear if the dE/dt, E-field, or both measurements are in error, but plotting electric field changes versus distance results in an inverse power-law dependence with distance, while plotting peak dE/dt values versus distance does not always. Despite these reservations, it is worthwhile to determine the mean peak of the dE/dt step waveforms range normalized to 100 km and compare them with previous results.

In order to obtain values for the half-peak width, rise time, and peak value, the computer program first identifies a leader step and determines its source location. As discussed in Section 7.1, leader steps that have a small viewing angle (θ) to the sensor (see Figure 7-2) have a diminished initial peak. Hence, it would seem that using leader steps which are exceedingly high above the site would produce smaller peak values and potentially contaminate these calculations. Therefore, this analysis only included leader steps that occurred within 100 μ s of the return stroke, i.e., only leader steps occurring near the ground were used. Additionally, only the three natural flashes that were discussed in Chapter 6, and permitted accurate TOA location, were used in this calculation. For measuring the peak values of the steps, only pulses that registered an initial peak of 1 kV m⁻¹ μ s⁻¹ or greater were used. Finally, pulses that exhibited any significant baseline offset or secondary pulses immediately prior to the start of the main leader pulse were excluded from the data set. For example, the Station 3 waveform in Figure 7-6 and all the

waveforms in Figure 7-13 were excluded. These criteria identified 103 waveforms produced by 21 different leader steps in the three natural flashes analyzed. Essentially, each leader step was observed at an average of 5 stations. The histogram for these peak dE/dt values normalized to 100 km, with no account taken of their angle with respect to the vertical or to the viewing angle, is shown in Figure 7-16. The mean peak of the dE/dt step pulses, range-normalized to 100 km, was found to be $7.4 \text{ V m}^{-1} \mu\text{s}^{-1}$, with a standard deviation of $3.7 \text{ V m}^{-1} \mu\text{s}^{-1}$. Recall that *Krider et al.* [1992] found a value of $13 \text{ V m}^{-1} \mu\text{s}^{-1}$ for 17 events, but we suspect that our measurements were underestimated by a factor of 1.2 to 2 because of system calibration and are also reduced due to the viewing angle.

Due to noise near the digitizer baseline, the program that determined the half-peak width and 10–90% rise time of the dE/dt pulses could only operate efficiently for pulses exceeding $1.5 \text{ kV m}^{-1} \mu\text{s}^{-1}$. This more stringent criterion restricts the previous data set of 103 waveforms to 69 waveforms produced by 20 different leader steps in three flashes. The nominal time interval of the measured data (4 ns) did not permit a precise calculation of the half-peak or 10–90% rise time, so linear interpolation was used to improve the sample resolution to 0.25 ns. After interpolation, the program selected the peak value, 0.9 peak value, 0.5 peak value, and the 0.1 peak value. The program identified all the points surrounding the peak value that were above the 0.5 peak value and then found the time difference between the first and last points. Similarly, the program identified the sample points lying between the 0.1 peak and 0.9 peak values, and found the time difference between the first and last samples. An illustration of how these values were measured is shown in Figure 7-17.

After all these values were obtained, both the half-peak widths and the 10–90% rise times were each plotted versus distance (R) to make sure there was no obvious distance dependence

over range we observed. The plot of half-peak widths and 10–90% rise times versus distance are shown in Figures 7-18 and 7-19, respectively. Clearly, neither plot shows a significant dependence with distance over this range. Finally, it is important to ensure that the half-peak width is also not dependent on the pulse peak amplitude. This can be determined by plotting the half-peak widths versus peak dE/dt normalized to 100 km. The plot in Figure 7-20 indicates that the half-peak width is not dependent on the peak amplitude. Now that there does not appear to be any bias with distance or peak amplitude, we can analyze the distributions for the half-peak and 10–90% rise times. The half-peak distribution is shown in Figure 7-21 and the 10–90% rise time distribution is shown in Figure 7-22. The means, standard deviations, and geometric means for these distributions are also shown in the figures.

7.3 Modeling of Stepped-Leader Pulses

7.3.1 Calculation of Lightning Electric and Magnetic Fields

Modeling of the electric and magnetic fields produced by lightning processes is an important analytical technique which can be used to gain insight into the physical mechanisms of lightning as well as estimate lightning parameters that were not, and perhaps cannot be, measured directly. In modeling lightning processes, a return stroke for example, it is common to model the lightning channel as a finite vertical antenna which is composed of an infinite number of infinitesimal dipoles [e.g., *Uman and McLain, 1969; Uman et al., 1975; Thottappillil et al., 1997*]. The time-dependent form of Maxwell's equations in free space can be used to calculate the electric and magnetic field contributions from each infinitesimal dipole, and the total electric and magnetic fields produced by the antenna can be determined by spatial integration of the component dipoles over the antenna. For a vertical antenna of height $H = H_T - H_B$ that carries an arbitrary continuous temporal and spatial longitudinal current distribution over a perfectly conducting ground plane, *Uman et al. [1975]* used the above technique to determine analytical

time-domain solutions for the vertical electric field and horizontal magnetic field measured on the ground ($z = 0$) at a horizontal distance r from the antenna axis. The geometry of this problem, which is most easily represented in cylindrical coordinates, is illustrated in Figure 7-23. Following some slight manipulation of the solutions presented by *Uman et al.* [1975], including a generalization for a channel that begins at any altitude, the vertical electric field and horizontal magnetic field can be equivalently expressed as

$$E_z(r, t) = \frac{1}{2\pi\epsilon_0} \left[\int_{H_B}^{H_T} \frac{2z'^2 - r^2}{R^5} \int_{R/c}^t i(z', \tau - R/c) d\tau dz' + \int_{H_B}^{H_T} \frac{2z'^2 - r^2}{cR^4} i(z', t - R/c) dz' - \int_{H_B}^{H_T} \frac{r^2}{c^2 R^3} \frac{\partial i(z', t - R/c)}{\partial t} dz' \right] \quad 7-1$$

$$B_\phi(r, t) = \frac{\mu_0}{2\pi} \left[\int_{H_B}^{H_T} \frac{r}{R^3} i(z', t - R/c) dz' + \int_{H_B}^{H_T} \frac{r}{cR^2} \frac{\partial i(z', t - R/c)}{\partial t} dz' \right] \quad 7-2$$

It is briefly noted that equivalent electric and magnetic field equations can also be obtained in terms of the line charge density ρ instead of the current i by using the continuity equation. The quantities H_B and H_T are the heights of the bottom and top of the channel, respectively. The primed coordinates indicate a source point while unprimed coordinates indicate the field (observation) point. At height z' a current $i(z', t)$ flows in a infinitesimal dipole of length dz' . Since the source is distributed vertically along the channel, $\vec{r}' = \vec{z}' = z'\hat{z}$. R is the distance between the source channel section dz' at height z' and the observation point at horizontal distance r . Hence, $\vec{R} = \vec{r} - \vec{z}' = r\hat{r} - z'\hat{z}$ and $R = R(z') = \sqrt{z'^2 + r^2}$.

The three terms of Equation 7-1 are referred to as the “electrostatic” (related to the integral of the current, or charge), “induction” (related to the current), and “radiation” (related to the current derivative) components, respectively, each with a different dependence on distance. The electrostatic component has the strongest distance dependence and is the only component that is non-zero after the current ceases to flow. The radiation component has the weakest distance

dependence and is the dominant field component for $r \gg H_T$. Similarly, the two terms in Equation 7-2 are the induction and radiation components, respectively. Since there is no term that is related to the integral of the current, the magnetic field is always zero when no current is flowing. It is interesting to note that each term in Equations 7-1 and 7-2 is in the form

$$\int_{H_B}^{H_T} f(r, z') g(i(z', t - R/c)) dz' \quad 7-3$$

where $f(r, z')$ is a geometrical factor (different for each field component) and is a function of both height and distance, while $g(i(z', t - R/c))$ is a function acting on the current.

While Equations 7-1 and 7-2 provide the means of calculating electric and magnetic fields from a given current distribution, they do not provide the current distribution itself. Since current cannot be measured directly at any elevated point in the lightning channel, the current distribution must be assumed from some reasonable model. For return strokes, which are probably the most modeled lightning process, there are several types of models. The simplest group of these models, dubbed “engineering” models by *Rakov and Uman* [1998], simply provide an equation relating the longitudinal channel current $i(z', t)$ at any height z' and any time t to the current $i(0, t)$ at the channel origin, $z' = 0$. Of course, an equivalent expression can also be obtained in terms of the line charge density $\rho_L(z', t)$ on the channel by using the continuity equation. Engineering models are generally based on observed lightning return-stroke characteristics such as channel-base current, the speed of the upward-propagating front, and the channel luminosity profile. The number of adjustable parameters in these models is usually small, perhaps one or two in addition to the current waveform.

The transmission line (TL) model [*Uman and McLain*, 1969] is a popular return-stroke model [*Willett et al.*, 1988; *Shoene et al.*, 2003b] that assumes the current waveform starts at the

bottom of the channel (typically at ground, $H_B = 0$) and propagates upward at constant velocity v with no attenuation or distortion. This is described mathematically as Equation 7-4.

$$i(z', t) = i(H_B, t - z'/v) \quad 7-4$$

A particular benefit of the TL model is that it predicts that the distant radiation fields, for times $t \leq H/v + r/c$, have the same waveshape as the current at ground, with the amplitude differing only by a scaling factor [Uman *et al.*, 1975]. Hence, the distant field, channel current, and propagation velocity of the current can each be calculated from knowledge of any two of these three parameters. Additionally, the TL model can be easily adapted to include a linear [Rakov and Dulzon, 1987] and exponential [Nucci *et al.*, 1988] current amplitude decay with height, represented by Equations 7-5 and 7-6, respectively.

$$i(z', t) = \left(1 - \frac{z' - H_B}{H}\right) \times i(0, t - z'/v) \quad 7-5$$

$$i(z', t) = e^{-(z' - H_B)/\lambda} \times i(0, t - z'/v) \quad 7-6$$

Of course, the goal here is to model leader steps instead of return strokes. Fortunately, this section has shown that the field calculations (Equations 7-1 and 7-2), the TL model (Equation 7-4), and the current decay modifications (Equations 7-5 and 7-6) are easily adapted to a finite vertical channel located at an arbitrary height. It is also important to point out, that we desire to model the electric field derivative and not the electric field itself. This can be accomplished by differentiating the calculated electric field or by differentiating the current-related term associated with each field component prior to calculating the field. There should be no problems with performing such calculations as long as the current derivative is a continuous function.

Finally, we note that the presence of a finitely conducting ground (that is, $\sigma < \infty$) results in the selective attenuation of the high frequency components of the electric and magnetic fields radiated by the lightning discharge. This attenuation is generally referred to as “propagation

effects.” Propagation effects result in the peak, rise time, and half-peak width of the lightning generated fields and field derivatives to deviate from their undistorted values, i.e., the values that would be measured over a perfectly conducting ground. A quantification of propagation effects involves a modification to the field contribution from each of the infinitesimal dipoles to account for the finite ground conductivity [e.g., *Norton, 1937; Cooray, 1987*]. In the results that follow, no attempt was made to account for propagation effects, possibly causing the discrepancies observed between the peak values of the calculated and measured fields for some of the more distant examples.

7.3.2 Modeling Results

At this point, the expressions necessary for calculating the lightning fields (Equations 7-1 and 7-2) and the engineering models necessary for describing the current distribution have been introduced, but the current waveform itself has not yet been defined. The first current waveform introduced here is obtained from the Heidler function [*Heidler, 1985*], and is expressed in Equation 7-7.

$$I(t) = \frac{I_0}{\eta} \frac{(t/\tau_1)^n}{(t/\tau_1)^n + 1} e^{-t/\tau_2} \quad 7-7$$

This function was selected because *Jerauld [2007]*, who presents a very rare attempt at leader-step modeling, used the same function to reasonably model one step from a dart-stepped leader in a rocket-triggered flash and one step from a stepped leader. For the dart-stepped leader step, *Jerauld [2007]* had electric and magnetic field derivative measurements located precisely 15 and 30 m from the strike object, and video images were used to estimate the height of the modeled leader step. For the natural leader step, the radial distance to the strike point was determined from a two-dimensional TOA location (using 4 stations), and the height of the leader step was estimated based on typical leader propagation speed and time prior to the return stroke.

Obviously, the hope here is that improved location accuracy for the natural leader steps, provided by the TOA system, will provide better modeling results. *Jerauld* [2007] selected a current propagation speed of $1.5 \times 10^8 \text{ m s}^{-1}$ and $1.7 \times 10^8 \text{ m s}^{-1}$ for the rocket-triggered step and natural step, respectively. In both cases, the current was assumed to decay exponentially with height, with a decay constant of 22 m.

Modeling results for three steps, referred to here as Step 1, Step 2, and Step 3, from the stepped-leader of MSE0604 are now presented. As *Jerauld* [2007] also noted, the complexity of natural leader step pulses often makes them difficult to model. Hence, the pulses modeled here are relatively free of secondary pulses and generally exhibit the characteristic pulse shape. The results for Step 1 show, similar to *Jerauld* [2007], the Heidler current function can reasonably reproduce the measured dE/dt waveforms. While Step 2 and Step 3 are also fit reasonably well by the Heidler current model, these steps clearly illustrate instances where the Heidler current model is physically insufficient to reproduce some aspects of the leader step waveforms. After examining Step 1, a second current model will be introduced, and the modeling results for this new current waveform are compared with the Heidler function.

Figure 7-24 illustrates the best modeling results (“best” being a subjective assessment made by the author) for Step 1 using the Heidler current waveform and current derivative shown in Figure 7-25 as input. Considering all of the assumptions and simplifications associated with this model, the fit between the measured and calculated waveforms is surprisingly good. These results were obtained using a propagation velocity of $1.2 \times 10^8 \text{ m s}^{-1}$ and an exponential decay constant of 30 m. The peak value, half-peak width, and charge transfer of the current waveform are about 4.5 kA, 605 ns, and 3.5 mC, respectively. The peak value of the dI/dt waveform was

approximately $92 \text{ kA } \mu\text{s}^{-1}$. As discussed shortly, these values are similar to those found by *Jerauld* [2007], although the half-peak width is a somewhat larger.

Figure 7-26 illustrates the modeling results for Step 2 using the Heidler current waveform and current derivative shown in Figure 7-27 as input. The current waveform used to obtain these results had a peak value, half-peak width, and charge transfer of about 2.3 kA, 300 ns, and 0.9 mC, respectively. The peak dI/dt value was approximately $66 \text{ kA } \mu\text{s}^{-1}$. The current propagation was $1.5 \times 10^8 \text{ m s}^{-1}$, and the exponential decay constant was 25 m. Note that most of the waveforms in Figure 7-26 are reasonably fit using the Heidler current model; however, the Station 3 waveform reveals an interesting feature – the measured dE/dt waveform decreases in value for the $0.5 \mu\text{s}$ prior to the main leader step. A brief examination of the Heidler current waveform reveals that the Heidler parameters cannot be adjusted to fit this feature. Hence, a different type of current function, apparently one with a slow-rising front to match the slow field variation prior to the dominant step, is necessary to replicate this feature.

Interestingly, the current derivative model that is introduced here as an alternative to the Heidler current model was first suggested by *Jerauld* [2007], except that the function was intended to model the current derivative of natural first strokes. Note that this function is still used to define the leader-step current derivative and not the leader-step current. This current derivative function, which we will refer to as the *Jerauld* model, is expressed in Equation 7-8.

$$\frac{dI(t)}{dt} = \left[\frac{\alpha_1}{1 + \left(\frac{t - T_{peak}}{\gamma}\right)^2} + \frac{\alpha_2}{1 + \left(\frac{t - T_{peak}}{0.5T_{peak}}\right)^2} \right] \times \left[\frac{1 + \beta}{1 + e^{(t - T_{peak} - 3\gamma)/\gamma}} - \beta \right] \times \left[1 - \frac{1}{1 + e^{4(t - 0.5T_{peak})/T_{peak}}} \right]$$

7-8

The right hand side of equation 7-8 is the product of three terms, having a total of 5 adjustable parameters. The first term in brackets is related to the general shape of the dI/dt

waveform, including the slow front and fast transition to peak. The quantities α_1 and α_2 affect the maximum amplitudes of the fast transition and slow front, respectively. The quantity T_{peak} sets the time of the peak of the waveform, while δ is related to the width of the fast transition derivative pulse. The second term in brackets in Equation 7-8 is related to the decay of the waveform after the peak, and is adjustable with the parameter β . Finally, the third term assures that the slow front begins at a value at or very near zero. Equation 7-8 is complex and not very intuitive, but it does provide an adequate slow front followed by a fast-transition that occurs very near the specified parameter T_{peak} . The current waveform itself can be obtained by numerically-integrating the dI/dt waveform generated by Equation 7-8. Special attention must be paid to the resulting current waveform when specifying parameters for Equation 7-8, particularly the value of β . If β is too small, the current waveform will not return to zero value after peak, and if β is too large, the current waveform will become increasingly negative. If the value of β is not precisely selected, the calculated dE/dt waveforms will ramp towards unrealistic values.

Figure 7-28 shows the modeling results for Step 2 using the Jerauld model. Figure 7-29 shows the current derivative and current used for Step 2 with the parameters $\alpha_1 = 100 \times 10^9 \text{ A s}^{-1}$, $\alpha_2 = 10 \times 10^9 \text{ A s}^{-1}$, $T_{peak} = 0.5 \times 10^{-6} \text{ s}$, $\gamma = 20 \times 10^{-9} \text{ s}$, $\beta = 1.73$. The resultant current waveform has a peak value, half-peak width, and charge transfer of 5.8 kA, 300 ns, and 2.9 mC, respectively. The peak dI/dt value was about $84 \text{ kA } \mu\text{s}^{-1}$. Since both the Heidler and Jerauld models used the same propagation velocity ($1.5 \times 10^8 \text{ m s}^{-1}$) and the same exponential spatial current decay (25 m), it is interesting to observe the difference in predicted current parameters. The half-peak width is basically identical for both models, and the peak dI/dt value for the Jerauld model is not significantly larger than using the Heidler model. However, the Jerauld model predicts a larger peak current by a factor of 2 and a larger charge transfer by a factor of 3,

and it also provides a better fit for the slow front and the negative half-cycle. Since the Heidler function appears to model the fast peak and subsequent decay of this dE/dt step relatively well, the different predictions seem to indicate that a significant amount of the step charge may be lowered during the slow front of the leader-step current.

Figure 7-30 illustrates the modeling results for Step 3 using the Heidler current waveform and current derivative shown in Figure 7-31 as input. The current waveform used to obtain these results had a peak value, half-peak width, and charge transfer of about 4 kA, 283 ns, and 1.4 mC, respectively. The peak dI/dt value was approximately $87 \text{ kA } \mu\text{s}^{-1}$. The current propagation velocity and the exponential current decay were again determined to be $1.5 \times 10^8 \text{ m s}^{-1}$ and 25 m, respectively. Similar to the Station 3 waveform in Figure 7-26, the Heidler model fails to reproduce a significant feature leading into the initial peak of the Figure 7-30 waveforms and does not model the negative half-cycle well. In this case, however, the feature appears to be a positive slow front on each of the waveforms, as opposed to a negative ramp on only the closest station. Once again, it appears that a current waveform containing a slow front may be required.

Figure 7-32 shows the modeling results for Step 3 using the Jerauld current derivative and current shown in Figure 7-33 as input. The resultant current waveform has a peak value, half-peak width, and charge transfer of 6.5 kA, 290 ns, and 3 mC, respectively. The peak dI/dt value was about $98 \text{ kA } \mu\text{s}^{-1}$. The Jerauld model used the same propagation velocity ($1.5 \times 10^8 \text{ m s}^{-1}$) and the same exponential current decay (25 m) as the Heidler model. Again, the half-peak current width predicted by each model is essential identical, and the peak dI/dt value for the Jerauld model is slightly larger than using the Heidler model. The ratios for the peak current and the charge transfer are again near 2 and 3, respectively.

It is interesting to compare the results found here with the two leader steps that *Jerauld* [2007] analyzed with the Heidler model. The best model results for the dart-stepped-leader step indicated that current had a peak value, half-peak width, and charge transfer of 5.5 kA, 300 ns, and 2 mC. The peak value for the current derivative (dI/dt) was about $110 \text{ kA } \mu\text{s}^{-1}$. The current waveform determined for the stepped-leader step had a peak value, half-peak width, and charge transfer of about 5 kA, 200 ns, and 1.2 mC. The peak value of the dI/dt value was about $115 \text{ kA } \mu\text{s}^{-1}$. Generally speaking, each of these results is consistent with the values found here. If, however, the Heidler model truly under estimates the peak value and charge transfer of the current waveform, both of these steps could have had a peak current near 10 kA. Moreover, the charge transfer of the dart-stepped-leader step, whose dE/dt waveforms were measured at very close range (15 and 30 m), may have been as high as 6 mC.

The current peak, half-peak width, and charge transfer values found here and by *Jerauld* [2007] are consistent with estimates of leader-step current waveform parameters (based on distant electric field measurements) reported by *Krider et al.* [1977] for stepped leaders. *Krider et al.* [1977] suggested that the peak step current is at least 2–8 kA and that the minimum charge transfer of a step is 1–4 mC. *Rakov et al.* [1998] gave similar estimates for dart-stepped leaders. However, the peak dI/dt value of approximately $100 \text{ kA } \mu\text{s}^{-1}$ is much larger than the 6–24 $\text{kA } \mu\text{s}^{-1}$ reported by *Krider et al.* [1977] and is similar to that observed for return strokes.

7.4 Conclusion

This chapter has provided an in-depth look into the nature of stepped-leader dE/dt pulses at close range. From an examination of the waveforms, the characteristic shape of close leader-step dE/dt pulses can be described as a bipolar pulse having a sharp initial peak with the same polarity as the return-stroke pulse, followed by an opposite-polarity overshoot which decays slowly to the background level. The waveforms also indicate that the initial peak dE/dt

amplitude is dependent on the range ($|\vec{R}|$), viewing angle to the sensor (θ), and channel orientation. Conversely, the amplitude of the opposite-polarity overshoot appears to be dominated by its dependence on distance, with the overshoot typically being largest in the closest waveforms and barely being noticeable in the farthest. The effect of the viewing angle on the initial peak amplitude can be observed in Figures 7-4, 7-5, 7-6, 7-7, 7-8, and 7-14, where the closest waveform exhibits a smaller initial peak than farther waveforms due to the small viewing angle to the closest station. Indeed, a few simple trials of leader-step modeling performed by the author (not presented here), in which all parameters (e.g., current amplitude and waveshape, wavefront velocity, current decay with height, and $|\vec{R}|$) were held constant except for θ , indicated that the initial peak amplitude decreases as θ approaches zero. The effect of the leader channel orientation can be observed in Figure 7-13, where the Station 3 and Station 5 waveforms exhibited significantly different initial peak amplitudes despite the ranges and viewing angles to these two measurements being nearly identical. Although the unknown orientation of the actual leader channel clearly affects the observed dE/dt pulses, the simple leader-step modeling performed in this chapter always assumed a straight and vertical leader channel.

The dE/dt leader steps occurring within 100 μs of the first stroke of flashes MSE0604, MSE0703, and MSE0704 were also analyzed for half-peak width, 10–90% rise time, and the peak value range-normalized to 100 km. Over the distances that we observed these values, no distance dependence was detected. The mean value of the half-peak width was found to be 33.5 ns, with a standard deviation of 5.5 ns. This value is nearly half the value previously reported by *Willett and Krider* [2000] for the half-peak width (54 ns with a standard deviation of 17 ns) under conditions in which propagation effects should have been minimal. The mean peak of the dE/dt step pulses, range-normalized to 100 km, was found to be $7.4 \text{ V m}^{-1} \mu\text{s}^{-1}$ (standard

deviation of $3.7 \text{ V m}^{-1} \mu\text{s}^{-1}$). However, we have previously discussed why these values may underestimate the actual value by as much as a factor of 1.2 to 2. Interestingly, *Krider et al.* [1992] reported the mean peak of dE/dt step pulses, range-normalized to 100 km, to be $13 \text{ V m}^{-1} \mu\text{s}^{-1}$. Finally, we determined the 10–90% rise time to be 43.6 ns (standard deviation of 24.2 ns).

Three stepped-leader pulses that were relatively free of secondary pulses were identified for leader modeling. *Jerauld* [2007] had previously shown reasonable agreement between measured lightning fields and the calculated fields using a Heidler current function as input. The same function was tested on the three steps here and shown to reasonably predict the measured fields; however, the two of these steps (Steps 2 and 3) clearly revealed that the Heidler current function neglected significant waveform activity prior to the initial pulse peak. A function introduced by *Jerauld* [2007], originally for estimating the current derivative of first return strokes, was shown to provide a better modeling of the measured fields. The current waveforms obtained from both models had half-peak widths of about 300 ns and maximum rates of current rise of about $80\text{--}90 \text{ kA } \mu\text{s}^{-1}$. The charge transfer and peak current predicted by both models ranged from about 1–3 mC and 2–6 kA, respectively. The charge transfer and peak current predicted by the *Jerauld* model were approximately a factor of 3 and 2 larger than that predicted by the Heidler model, respectively, and the *Jerauld* model fit the overall measured waveform much better. The important physical interpretation appears to be that the step-leader current involves a slow front, similar to that observed in natural first strokes.

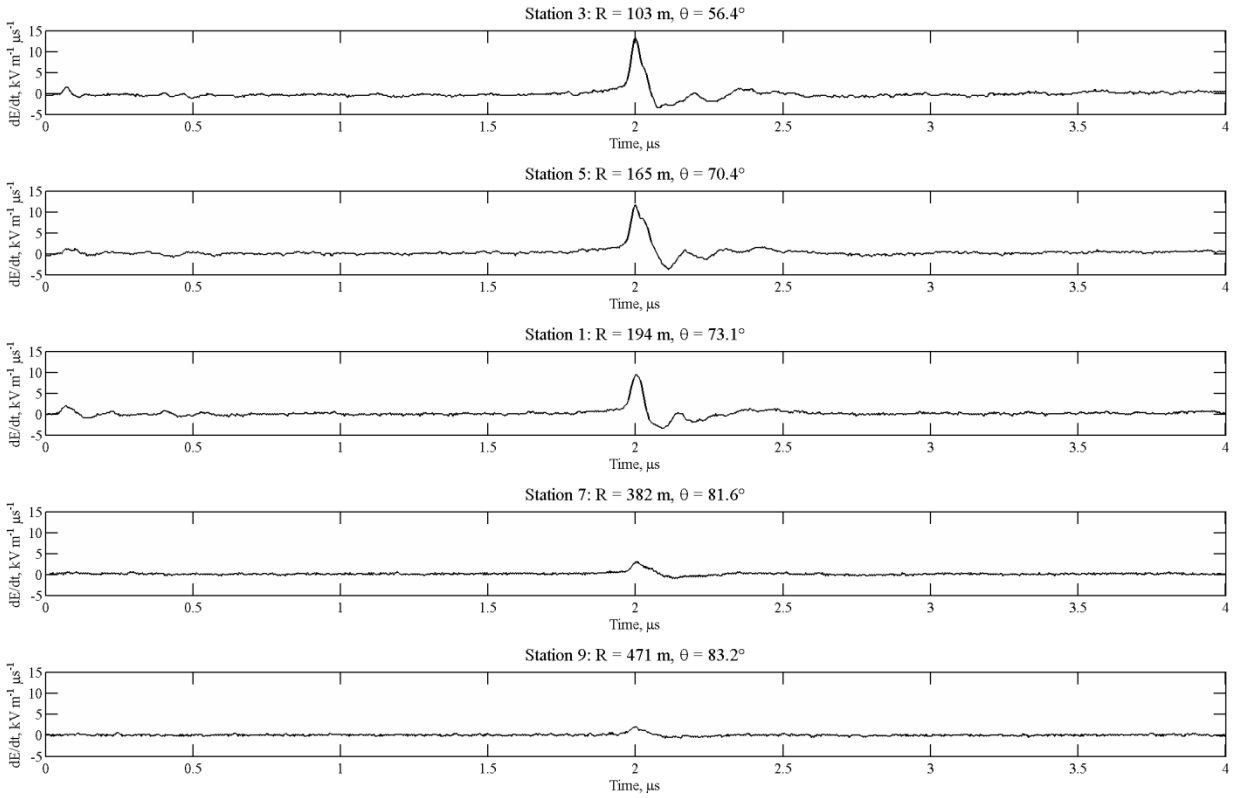


Figure 7-1. Leader step from MSE0604 exhibiting the characteristic pulse shape. The leader step occurs at $2 \mu\text{s}$ in the figure.

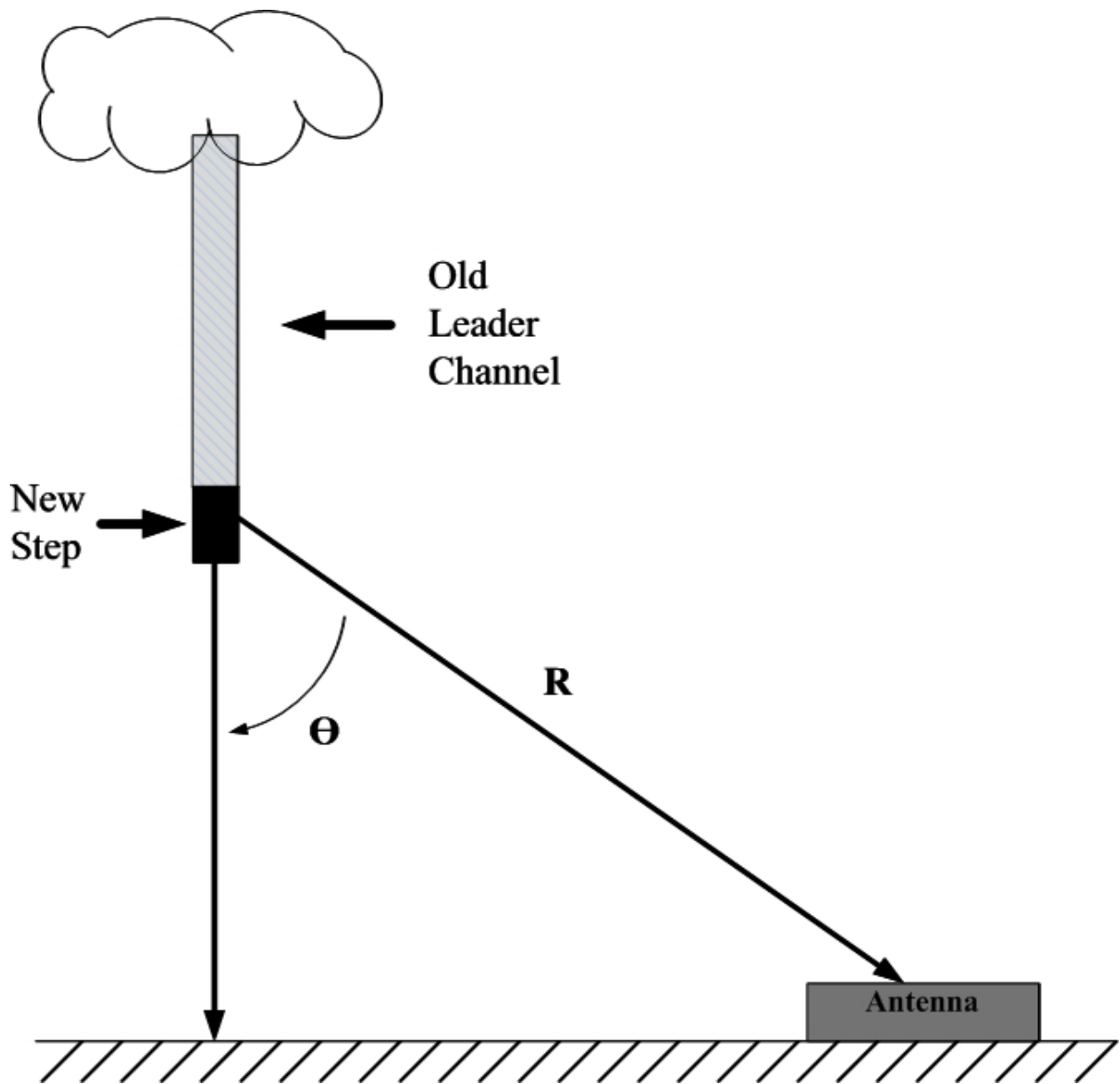


Figure 7-2. Diagram illustrating the spatial relationship between the leader step and the antenna.

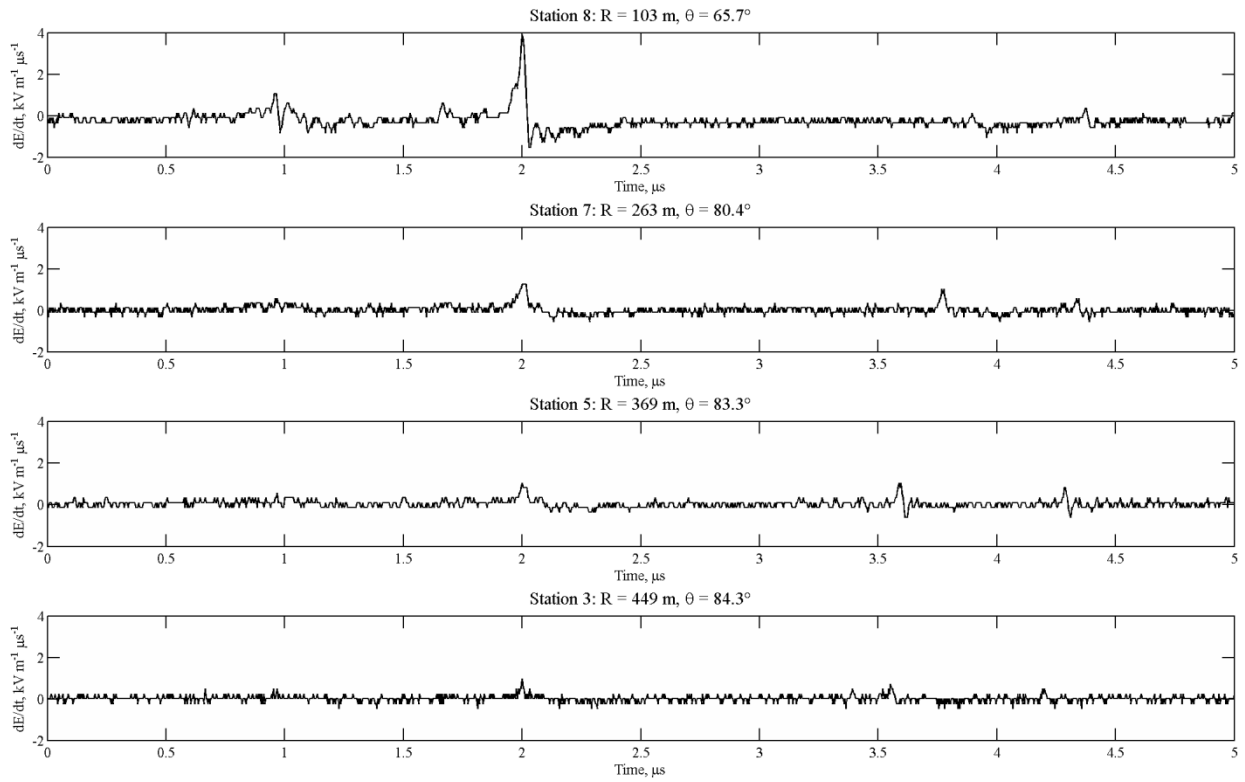


Figure 7-3. Leader step from MSE0703 exhibiting the characteristic pulse shape. The leader step occurs at $2 \mu\text{s}$ in the figure.

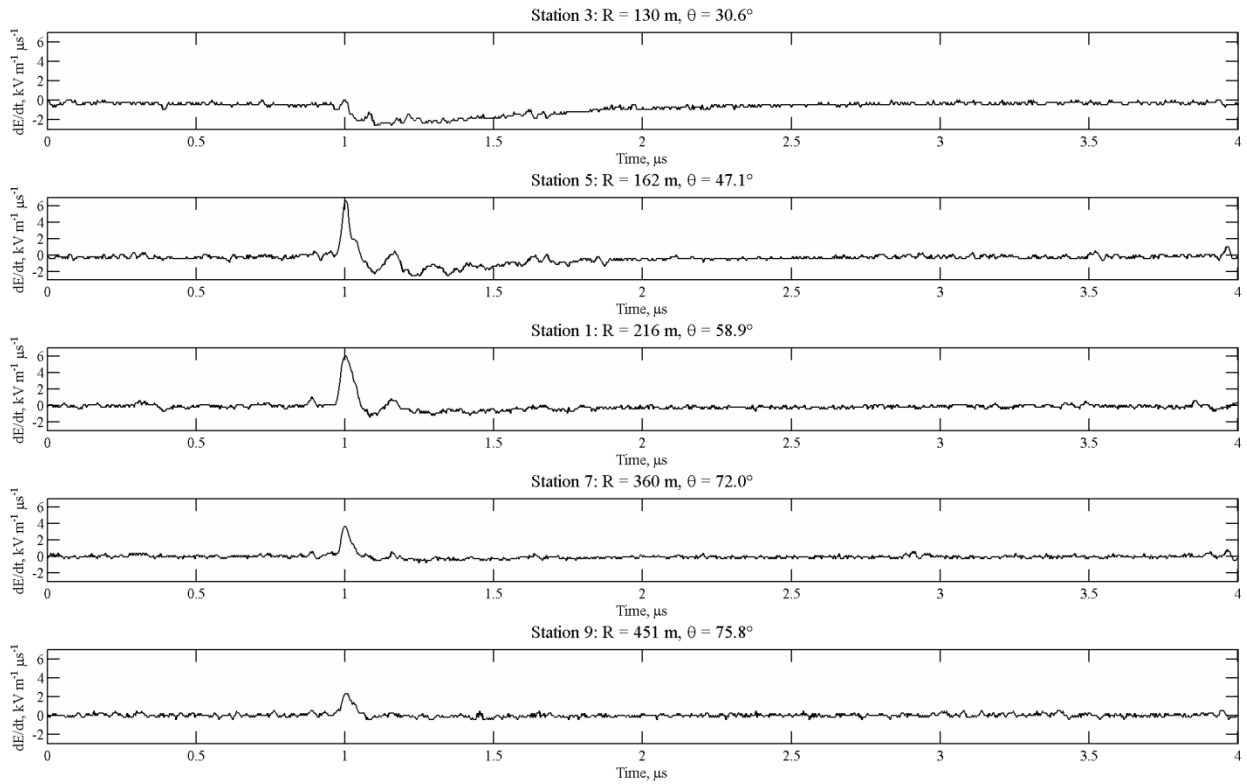


Figure 7-4. Leader step from MSE0604 where the closest station is missing the initial peak. The step occurs at $1 \mu\text{s}$ in the figure.

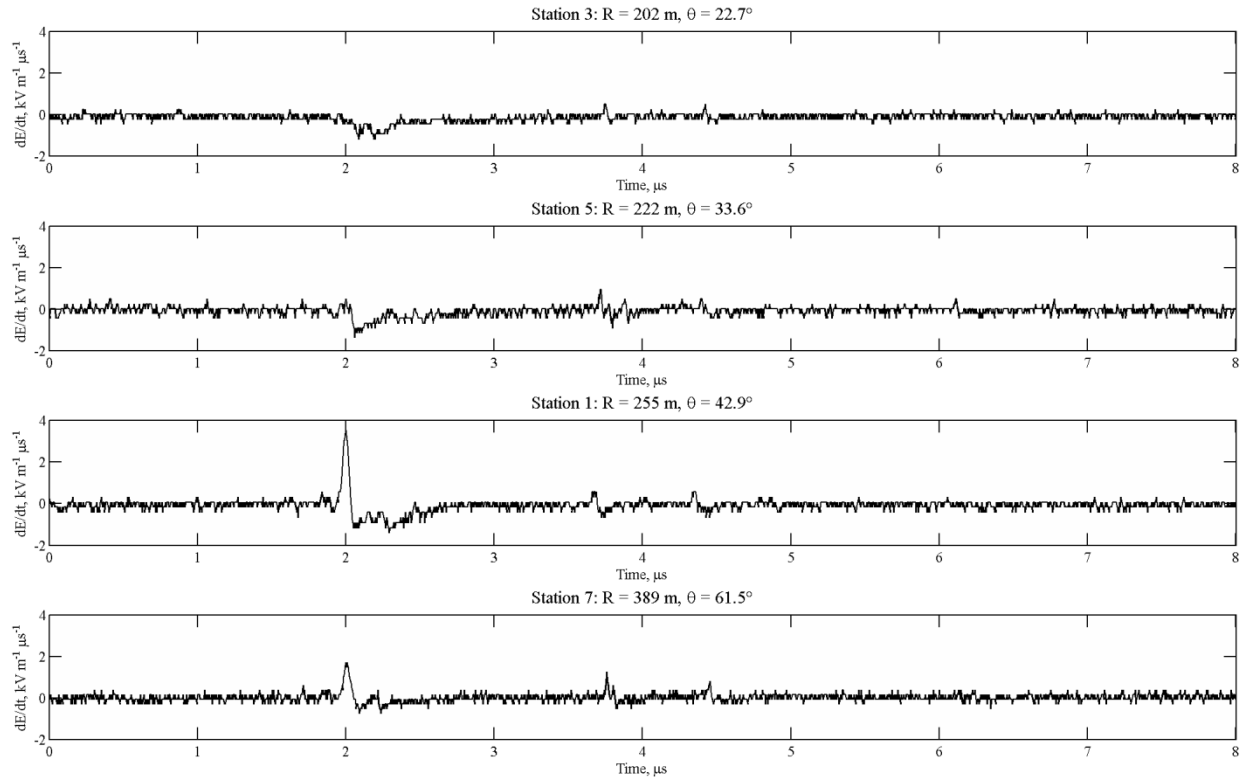


Figure 7-5. Leader step from MSE0604 where the two closest stations are missing the initial peak. The step occurs at $2 \mu\text{s}$ in the figure.

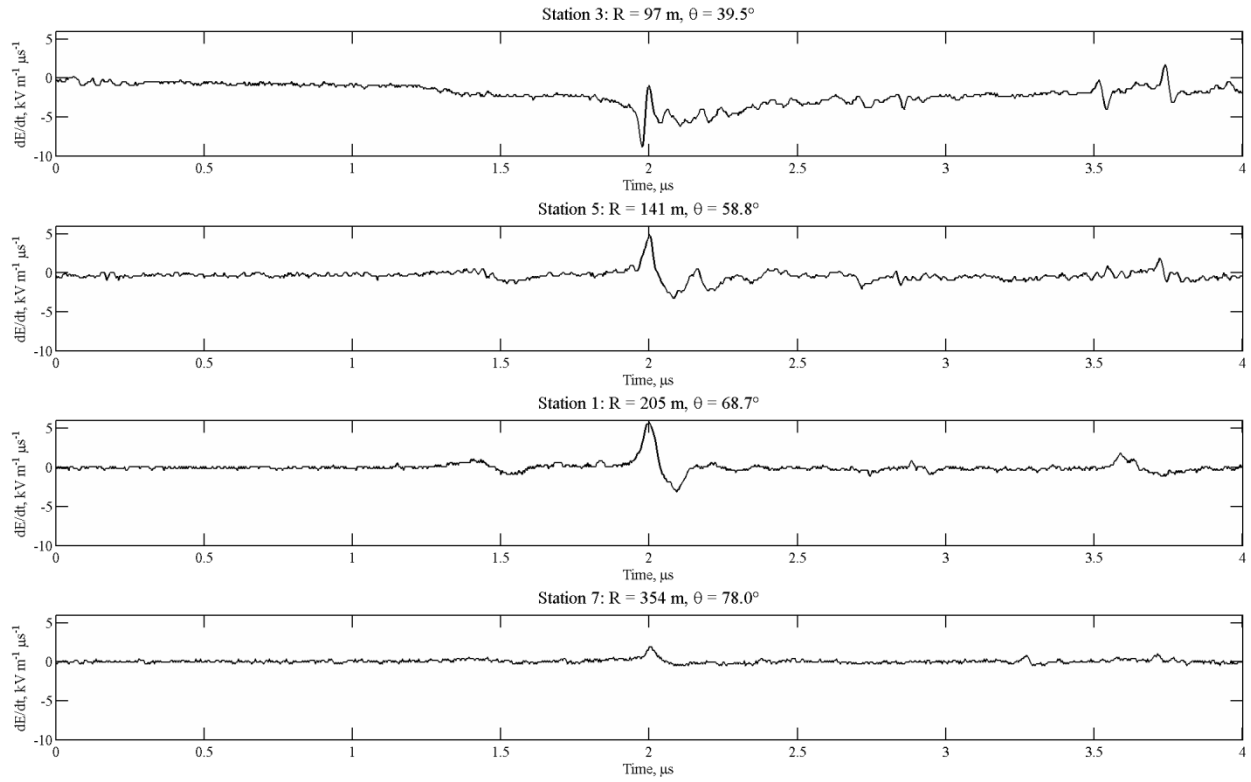


Figure 7-6. Leader step from MSE0604 which exhibits negative dip prior to the step. The step occurs at 2 μs in the figure.

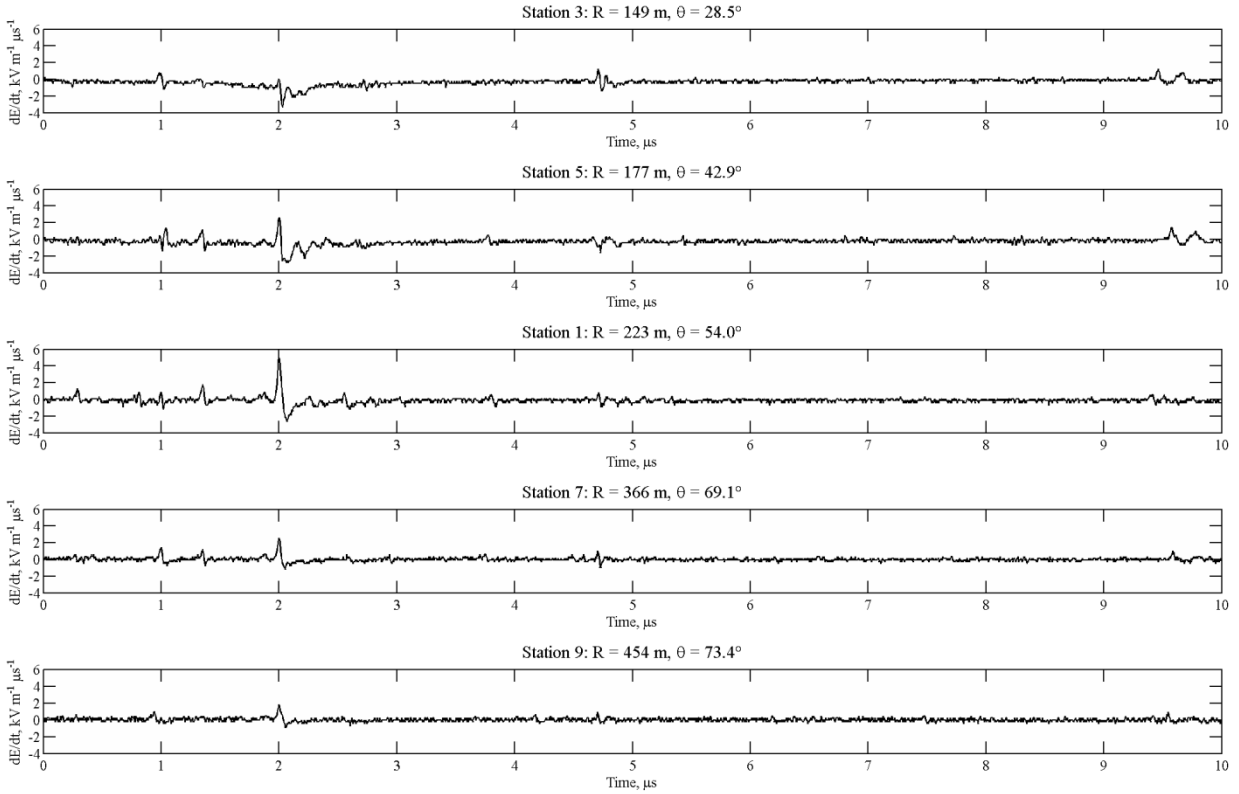


Figure 7-7. Another MSE0604 leader step with a negative dip. The step occurs at $2 \mu\text{s}$ in the figure.

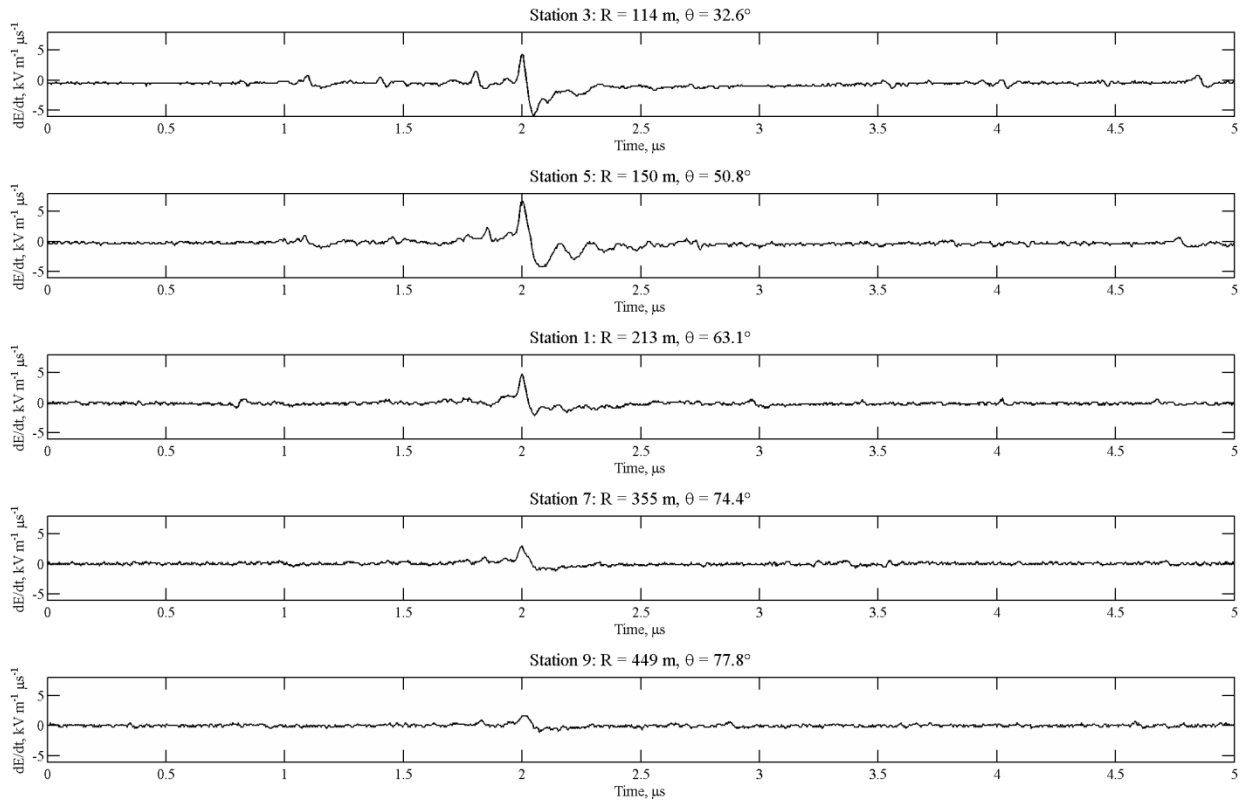


Figure 7-8. First example of a leader step with secondary pulses. The step occurs at $2 \mu\text{s}$ in the figure.

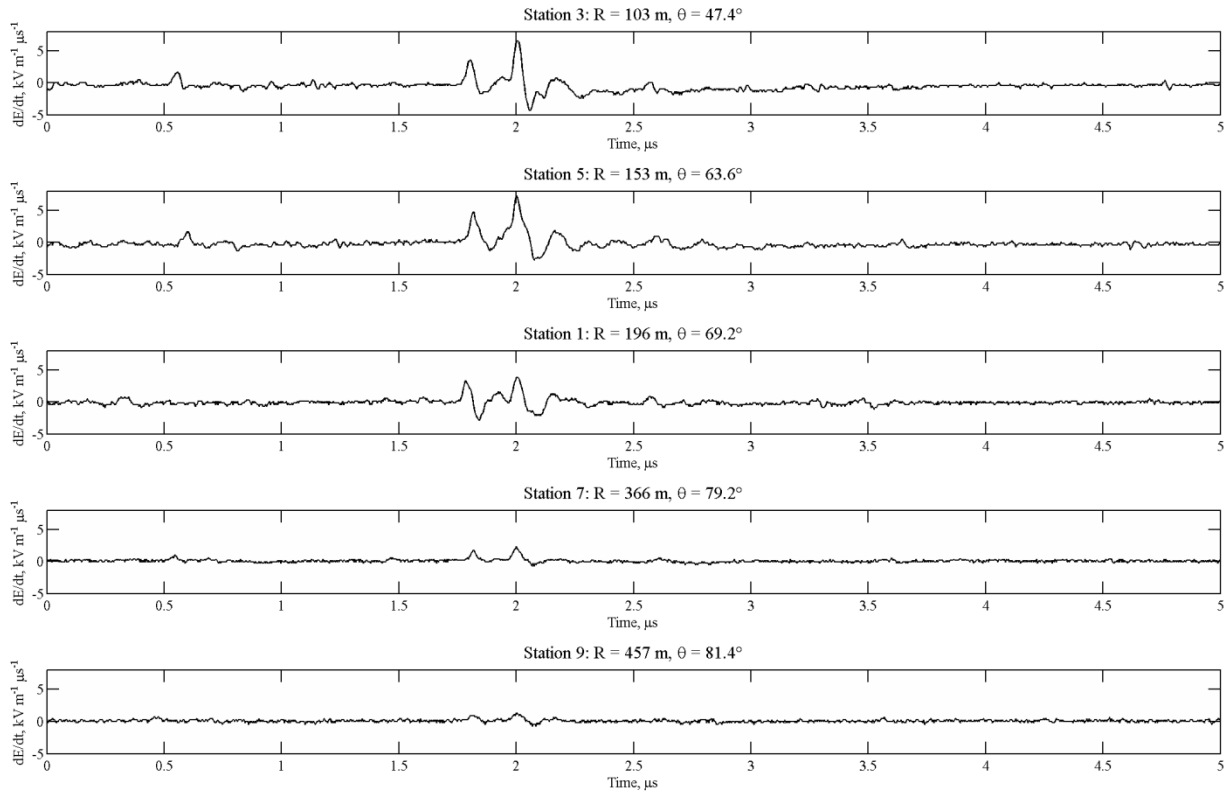


Figure 7-9. Second example of a leader step with secondary pulses. The step occurs at $2 \mu\text{s}$ in the figure.

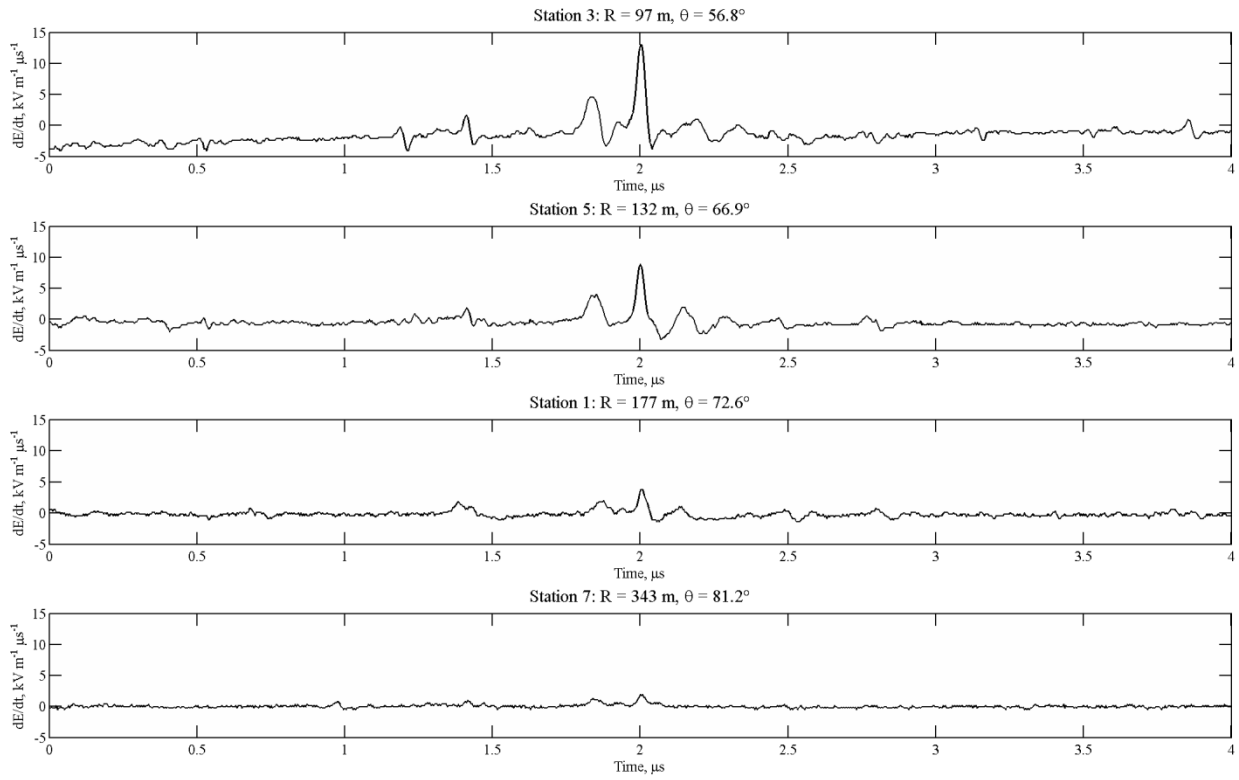


Figure 7-10. Third example of a leader step with secondary pulses. The step occurs at $2 \mu\text{s}$ in the figure.

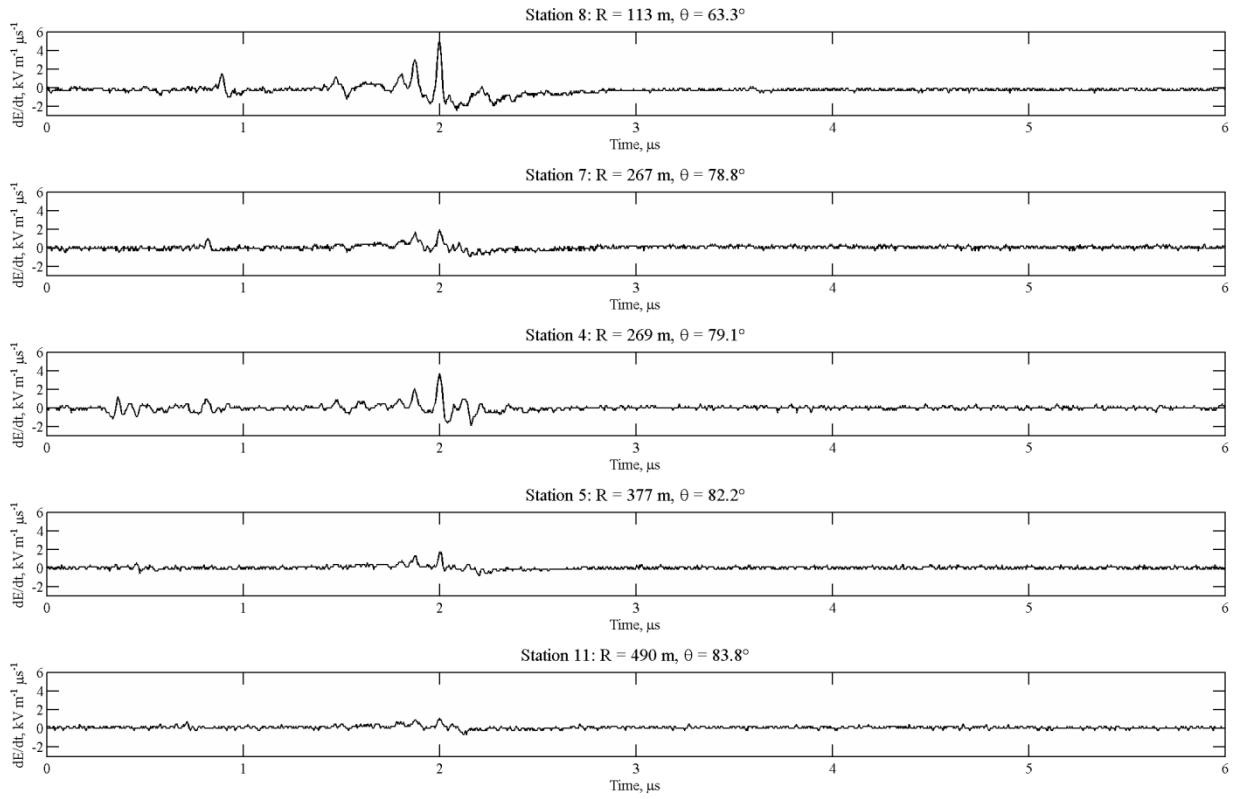


Figure 7-11. Fourth example of a leader step with secondary pulses. The step occurs at $2 \mu\text{s}$ in the figure. This leader step was obtained from flash MSE0703.

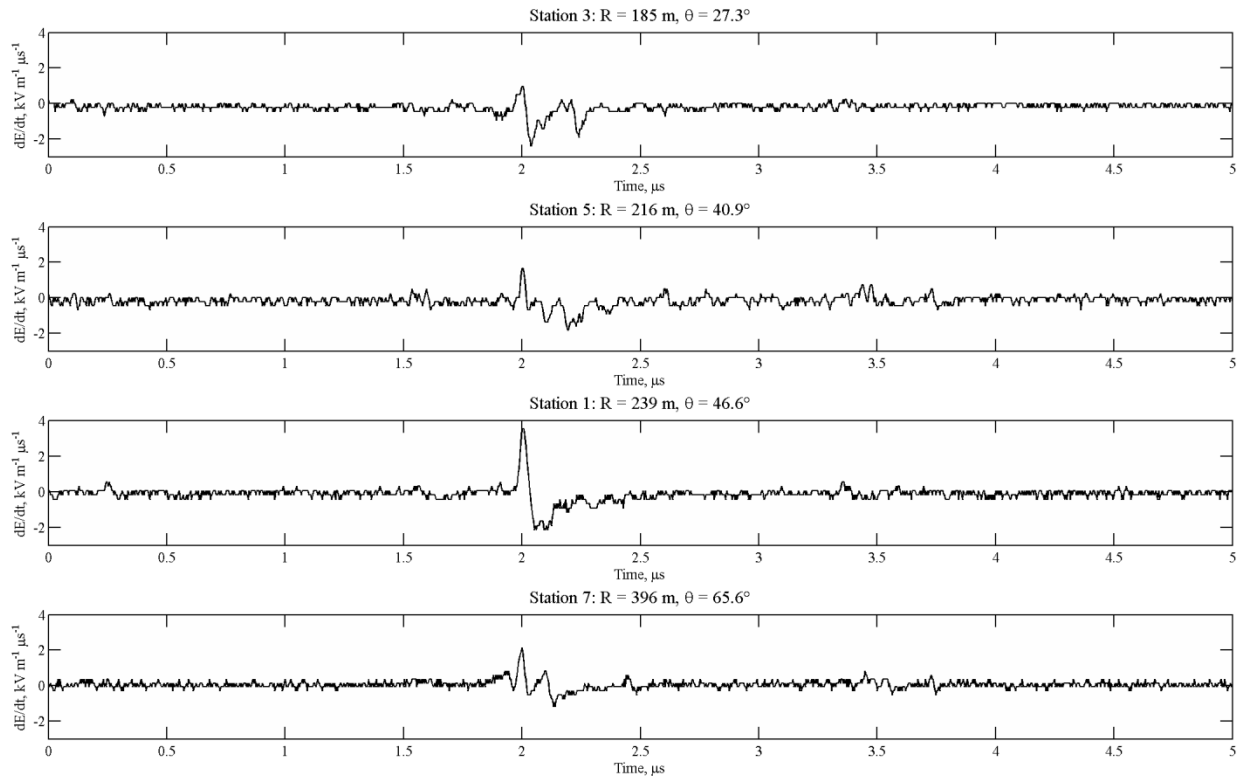


Figure 7-12. Fifth example of a leader step with secondary pulses. The step occurs at $2 \mu\text{s}$ in the figure.

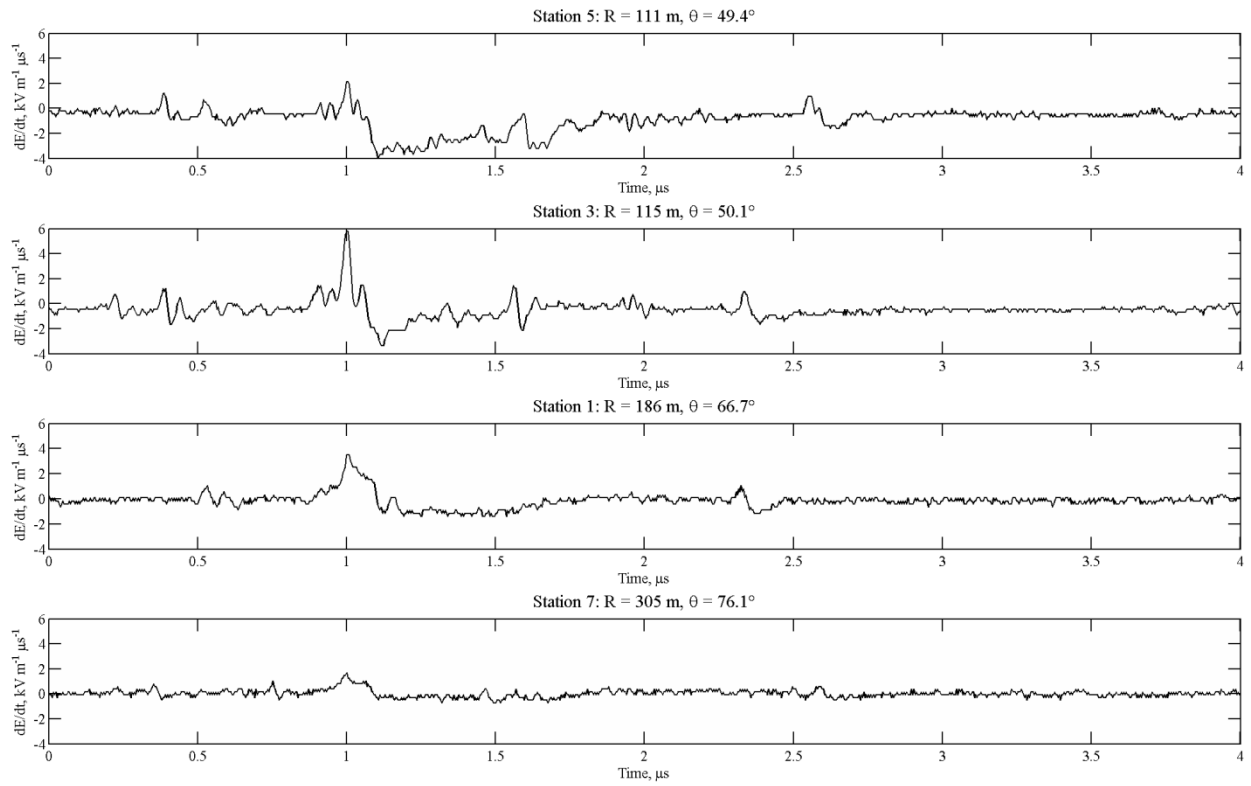


Figure 7-13. Sixth example of a leader step with secondary pulses. The step occurs at $1 \mu\text{s}$ in the figure.

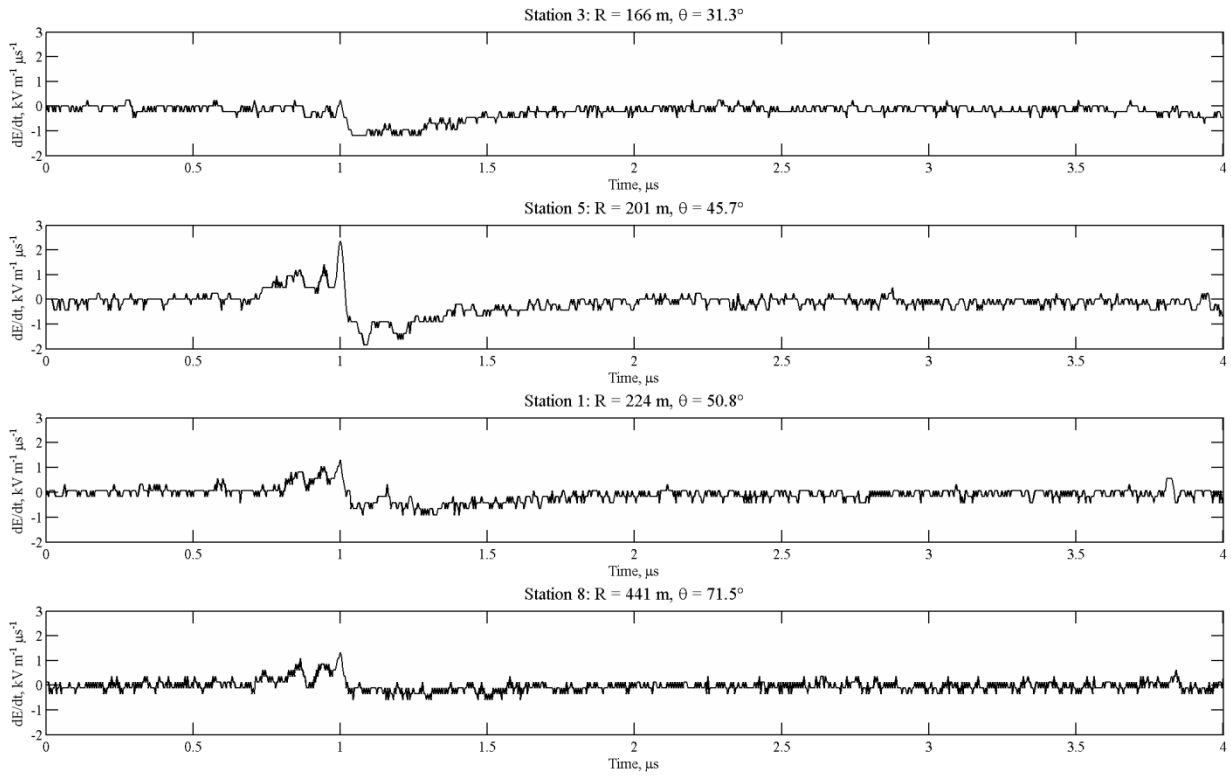


Figure 7-14. Seventh example of a leader step with secondary pulses. The step occurs at $1 \mu\text{s}$ in the figure.

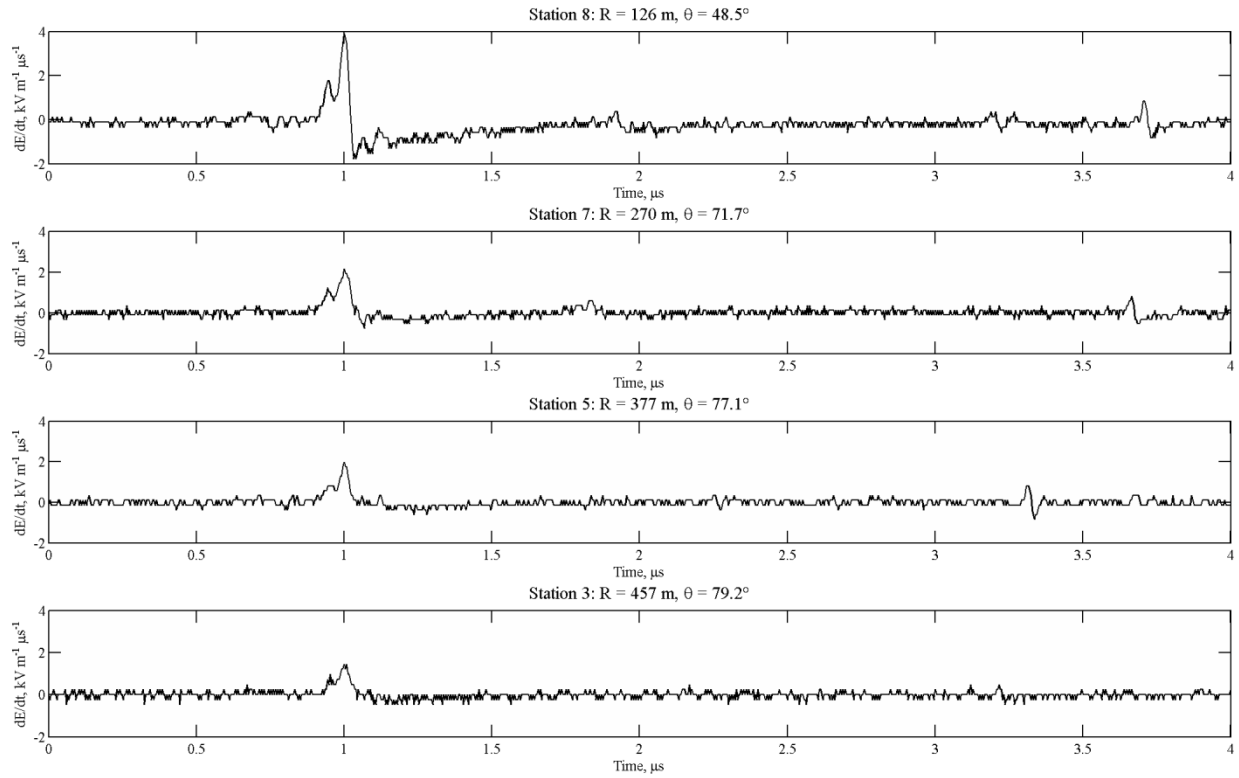


Figure 7-15. Eighth example of a leader step with secondary pulses. The step occurs at $1 \mu\text{s}$ in the figure. This leader step was obtained from flash MSE0703.

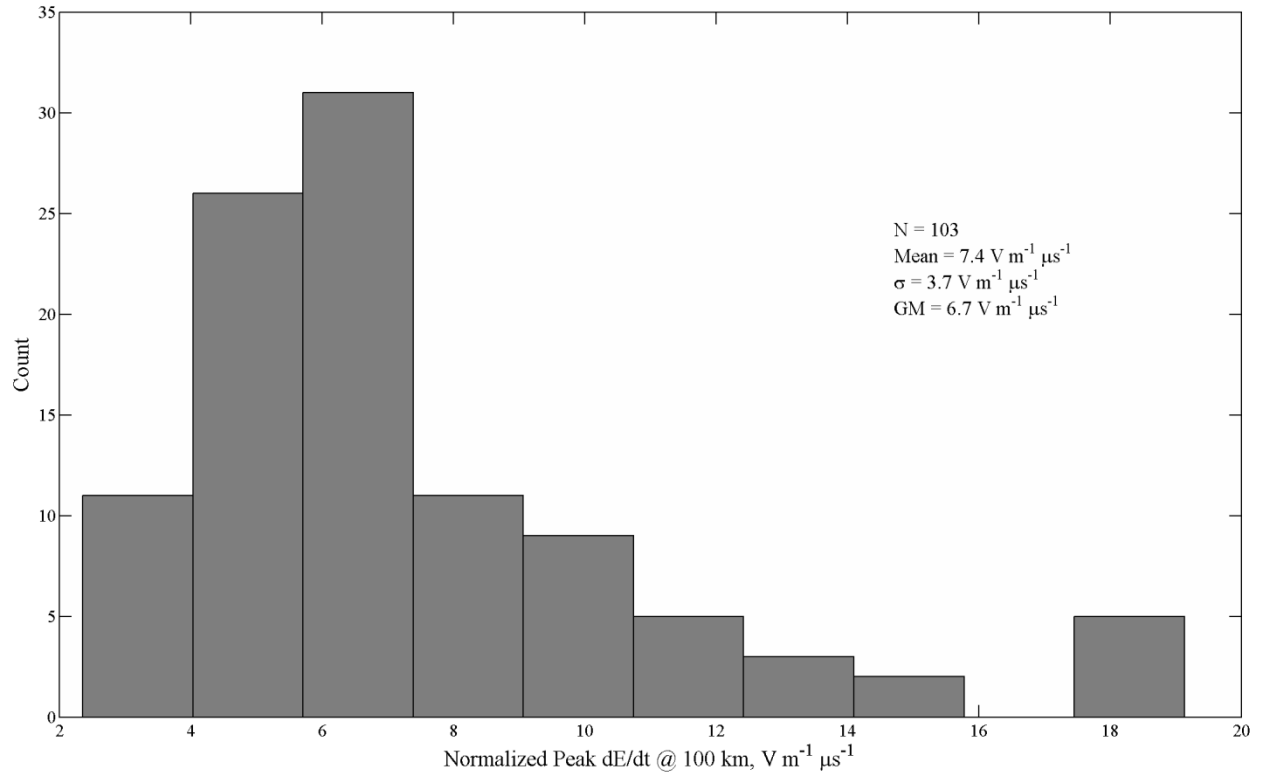


Figure 7-16. Histogram of peak dE/dt range-normalized to 100 km. The sample size (N), mean, standard deviation (σ), and geometric mean (GM) are also specified.

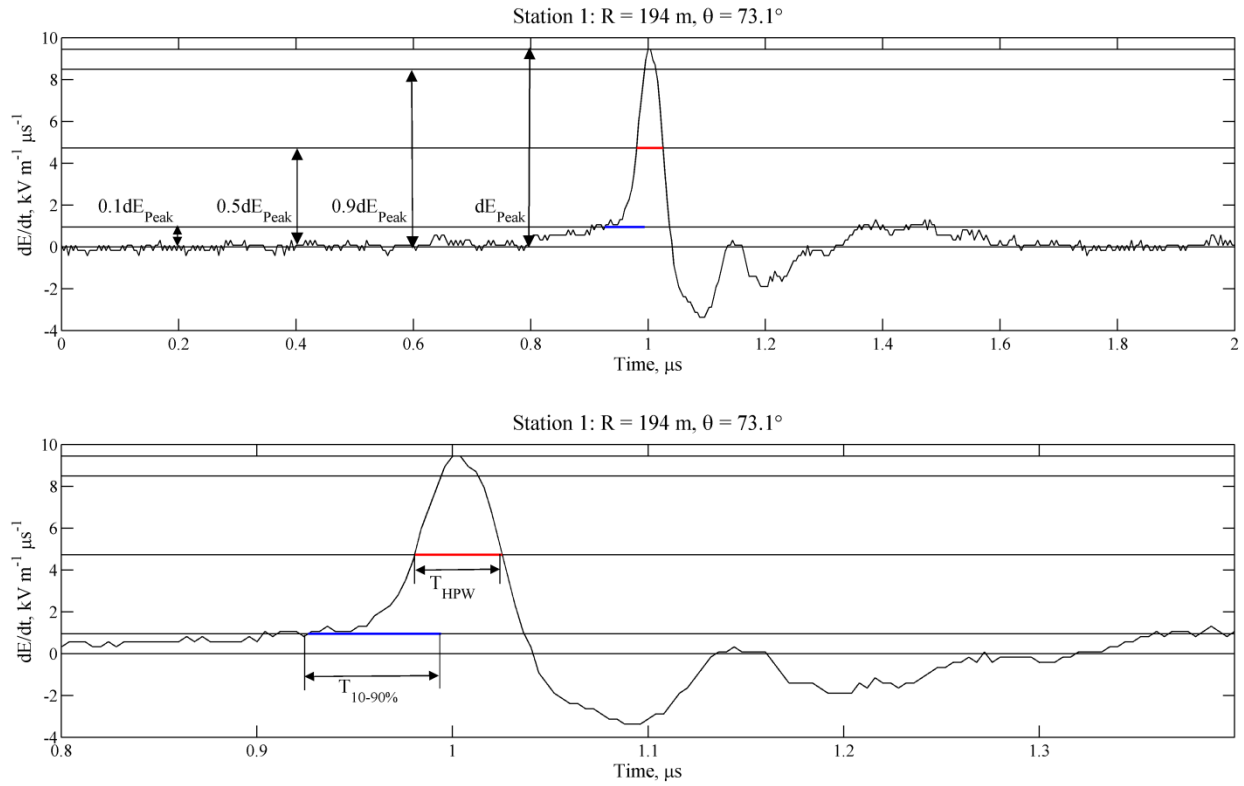


Figure 7-17. Illustration of the half-peak and 10–90% rise time parameters that are measured.

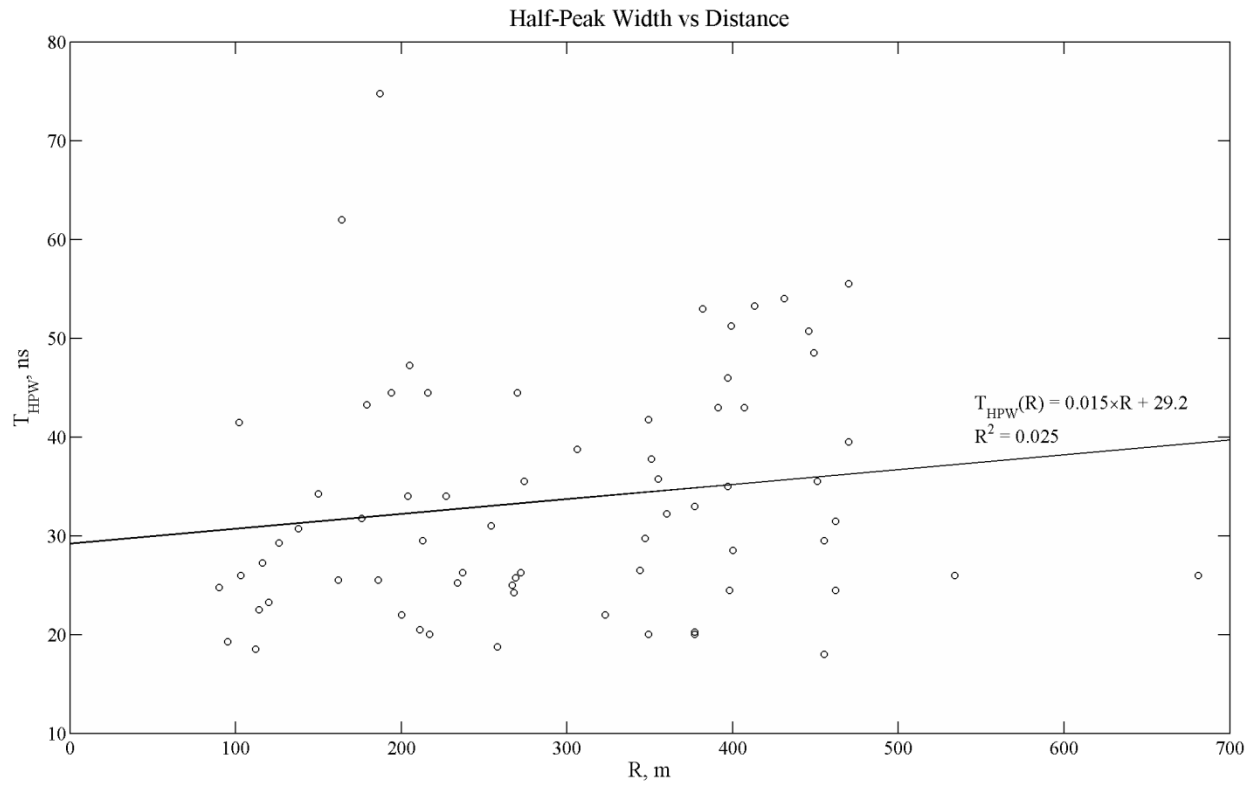


Figure 7-18. Plot of half-peak width for dE/dt leader pulses versus distance.

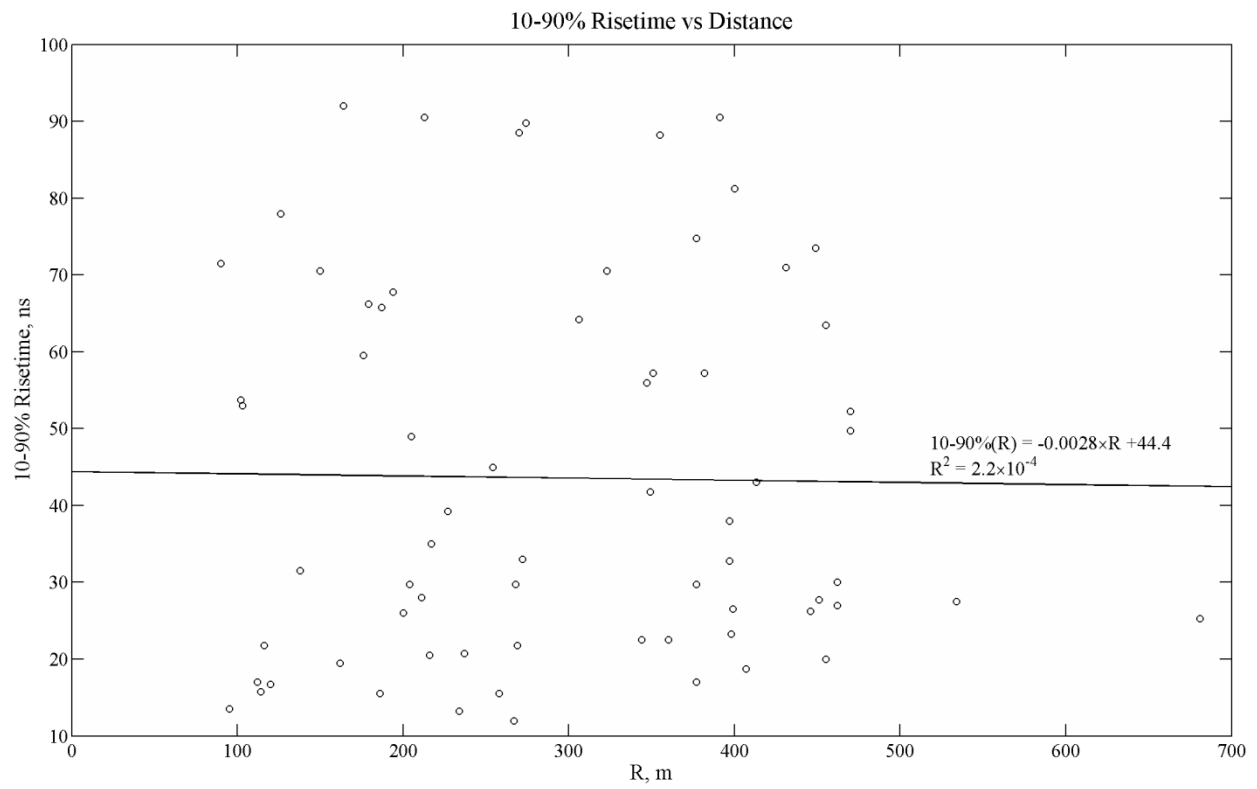


Figure 7-19. Plot of 10–90% rise time for dE/dt leader pulses versus distance.

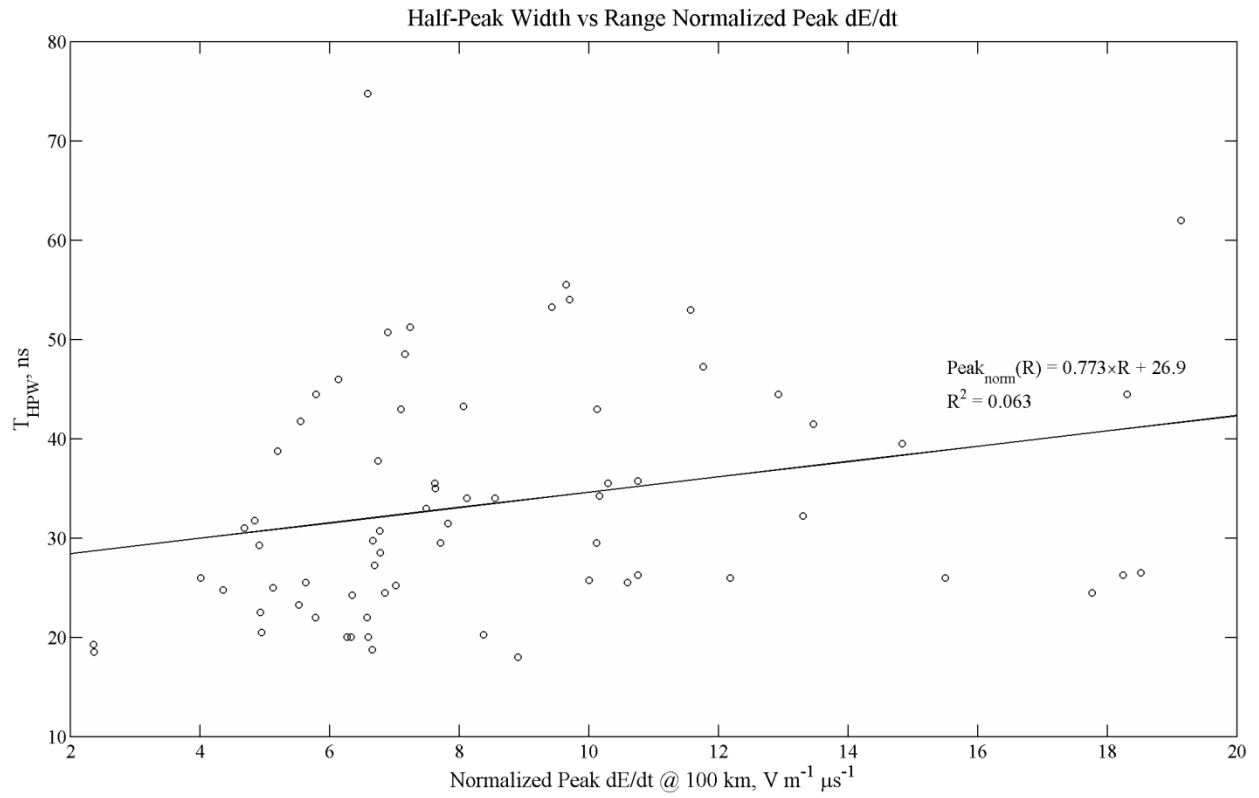


Figure 7-20. Plot of half-peak width for dE/dt leader pulses versus peak dE/dt, range-normalized to 100 km.

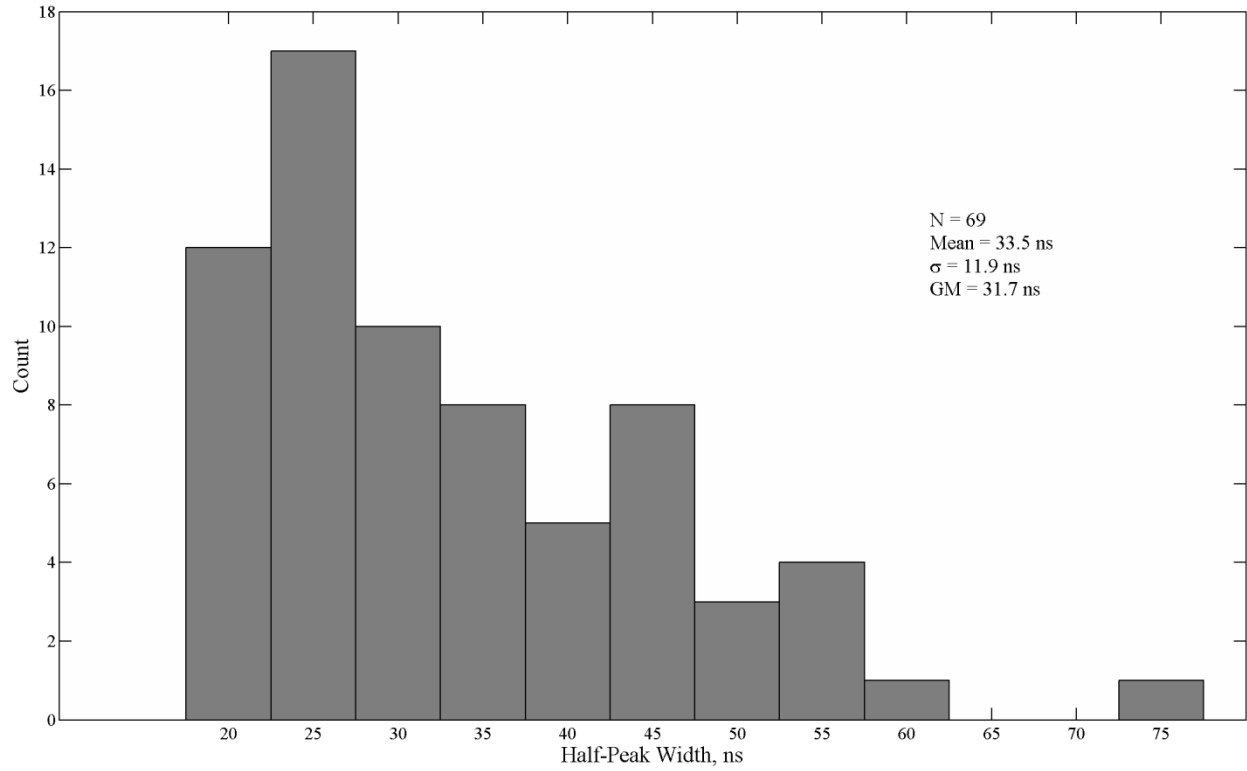


Figure 7-21. Histogram of half-peak width of dE/dt leader pulses. The sample size (N), mean, standard deviation (σ), and geometric mean (GM) are also specified.

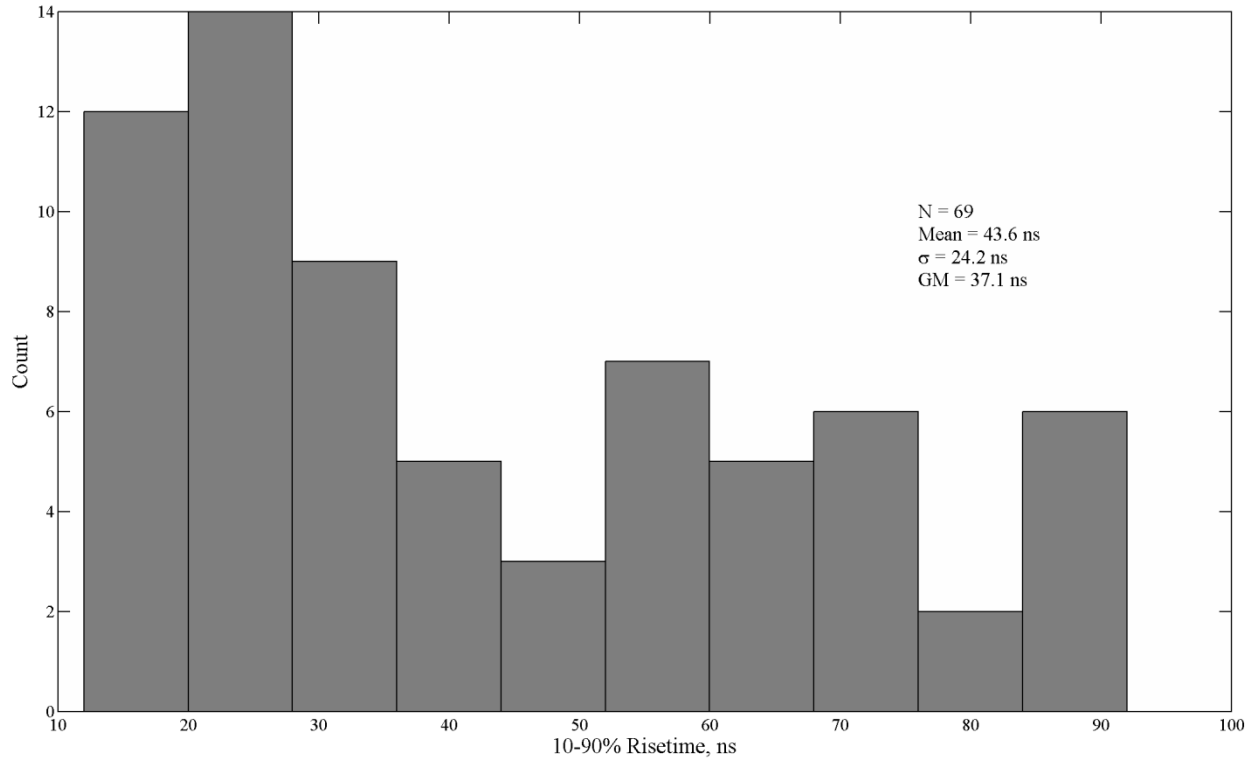


Figure 7-22. Histogram of 10–90% rise time for dE/dt leader pulses. The sample size (N), mean, standard deviation (σ), and geometric mean (GM) are also specified.

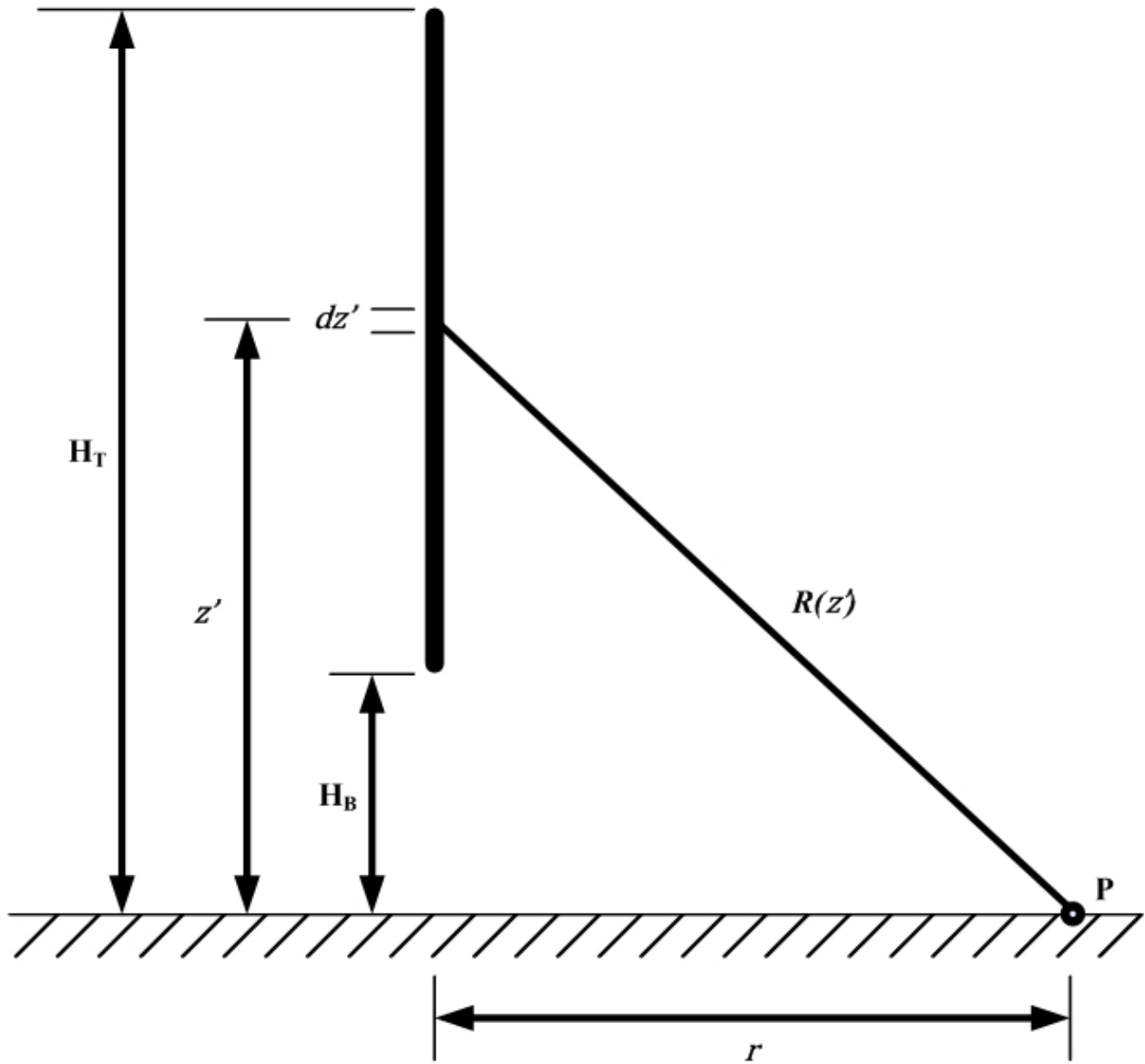


Figure 7-23. Illustration of geometry involved in calculating electric and magnetic fields on ground at horizontal distance r from a straight and vertical antenna of length $H = H_T - H_B$ over a perfectly conducting ground plane.

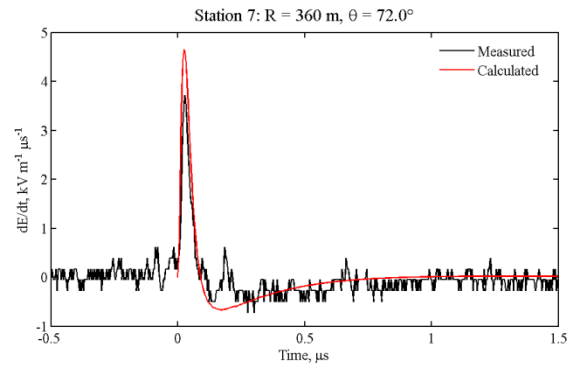
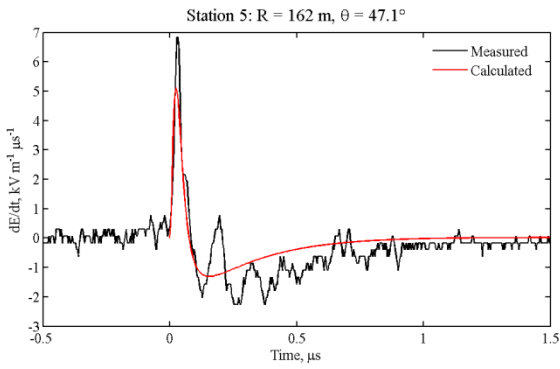
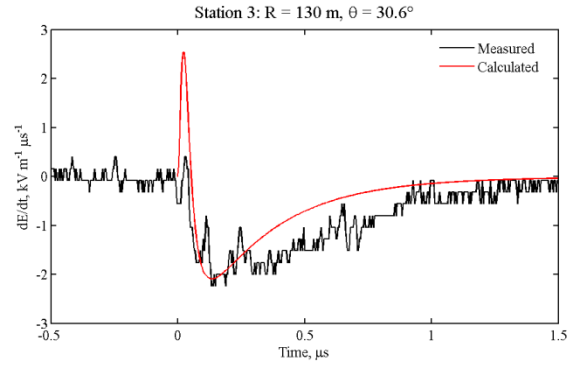
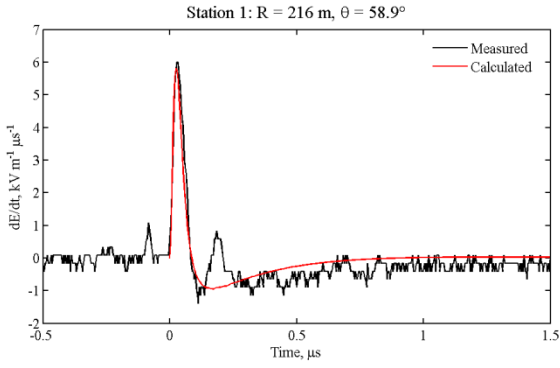


Figure 7-24. Step 1 modeling results using the Heidler model. The current front propagated with an upward speed of $1.2 \times 10^8 \text{ m s}^{-1}$, and the amplitude of the current waveform decayed exponentially with a decay constant of 30 m.

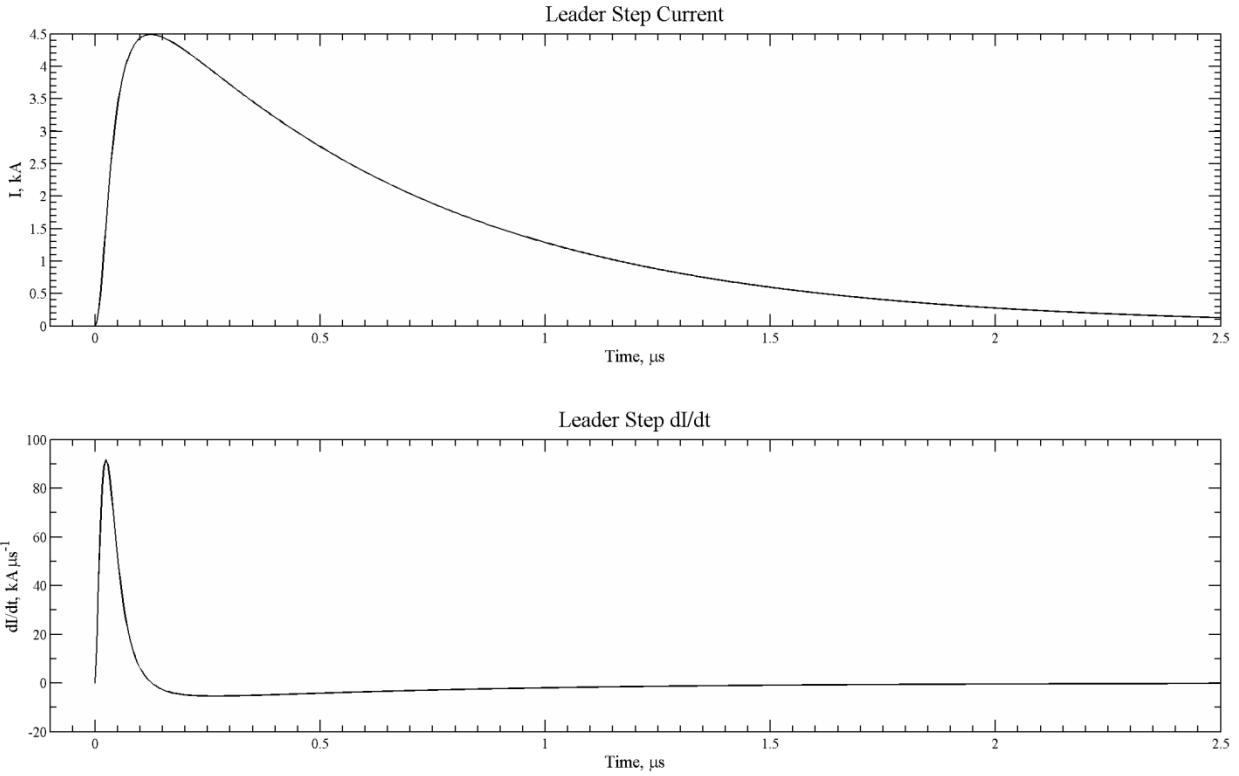


Figure 7-25. Current and current derivative waveform used in the Step 1 model results shown in Figure 7-24. The current waveform was generated using the Heidler function (Equation 7-7) with the parameters $I_0 = 4.5$ kA, $\eta = 0.750$, $n = 2$, $\tau_1 = 40$ ns, $\tau_2 = 650$ ns.

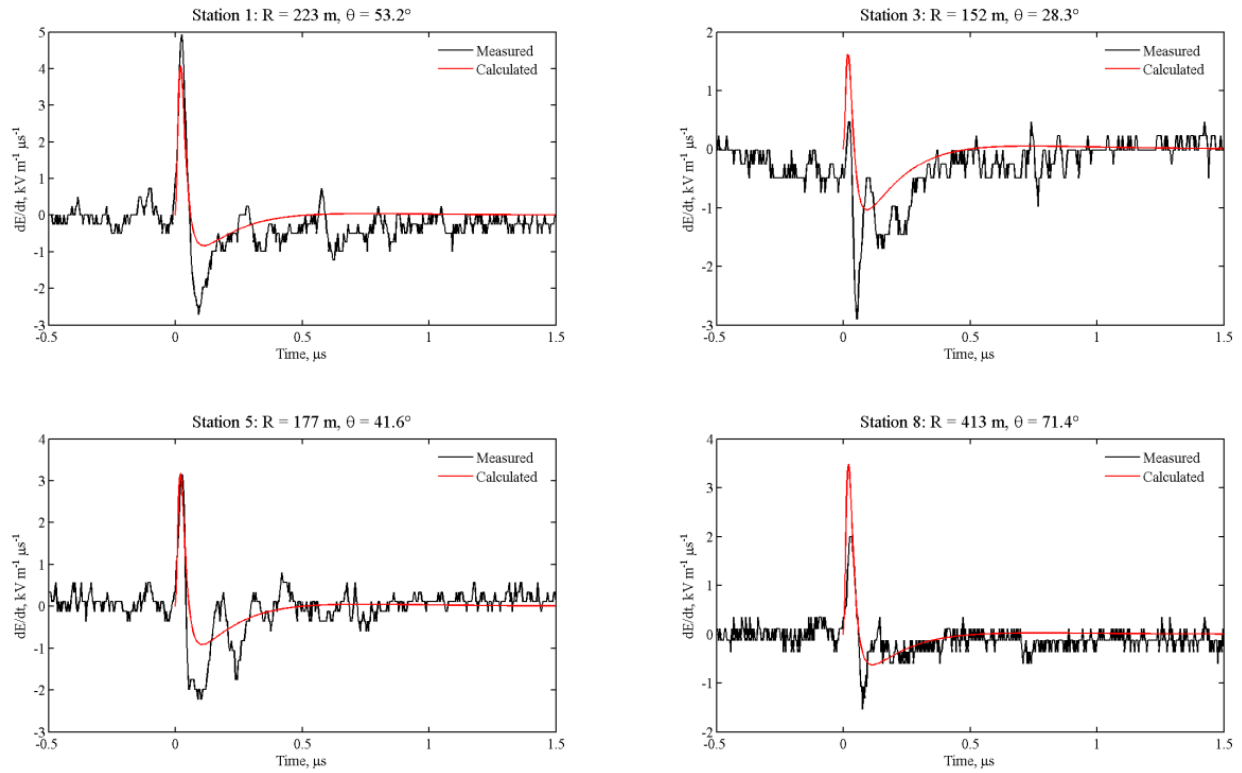


Figure 7-26. Step 2 modeling results using the Heidler model. The current front propagated with an upward speed of $1.5 \times 10^8 \text{ m s}^{-1}$, and the amplitude of the current waveform decayed exponentially with a decay constant of 25 m.

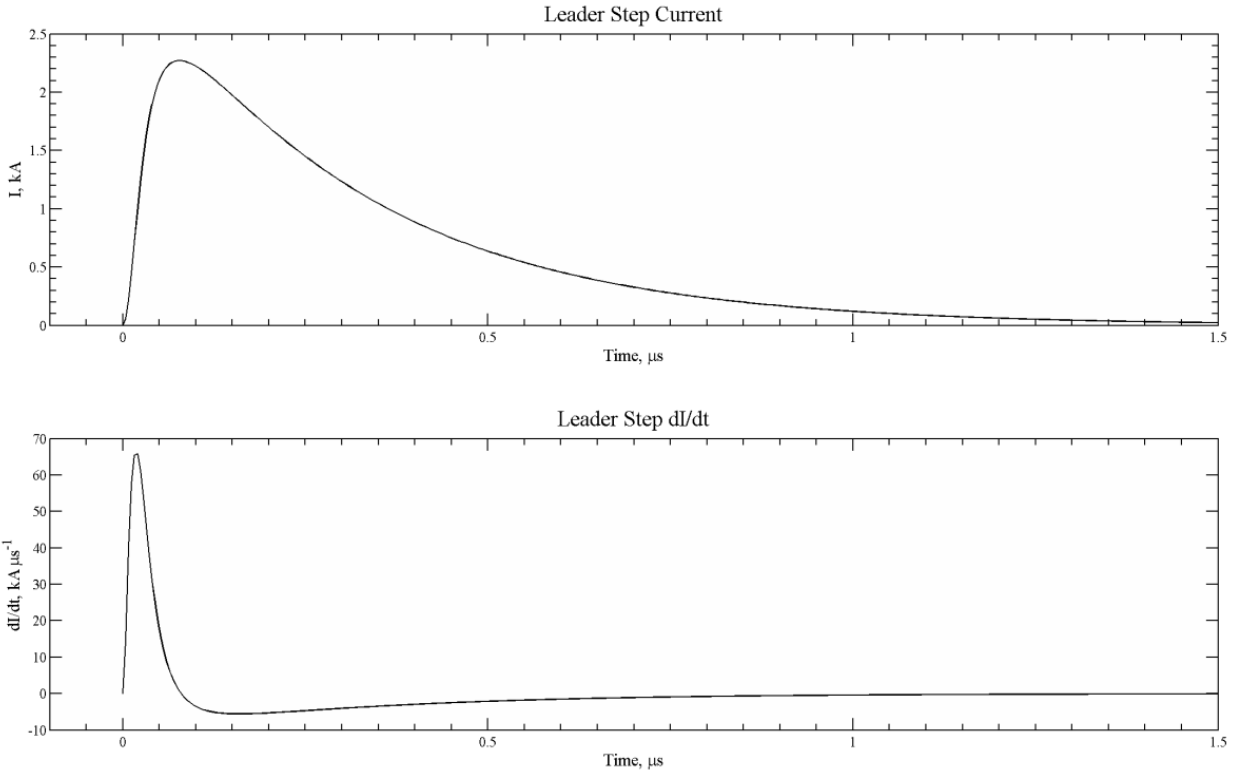


Figure 7-27. Current and current derivative waveform used in the Step 2 model results shown in Figure 7-26. The current waveform was generated using the Heidler function (Equation 7-7) with the parameters $I_0 = 2.3 \text{ kA}$, $\eta = 0.680$, $n = 2$, $\tau_1 = 30 \text{ ns}$, $\tau_2 = 300 \text{ ns}$.

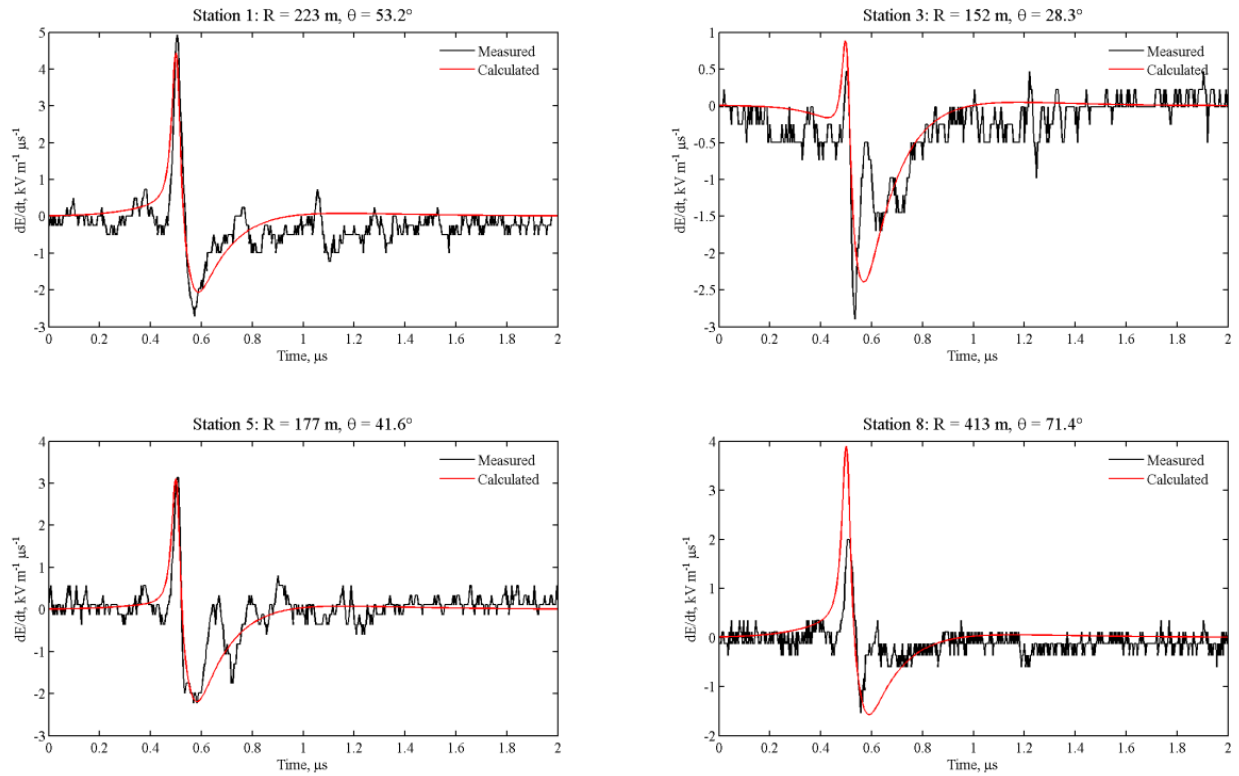


Figure 7-28. Step 2 modeling results using the Jerauld model. The current front propagated with an upward speed of $1.5 \times 10^8 \text{ m s}^{-1}$, and the amplitude of the current waveform decayed exponentially with a decay constant of 25 m.

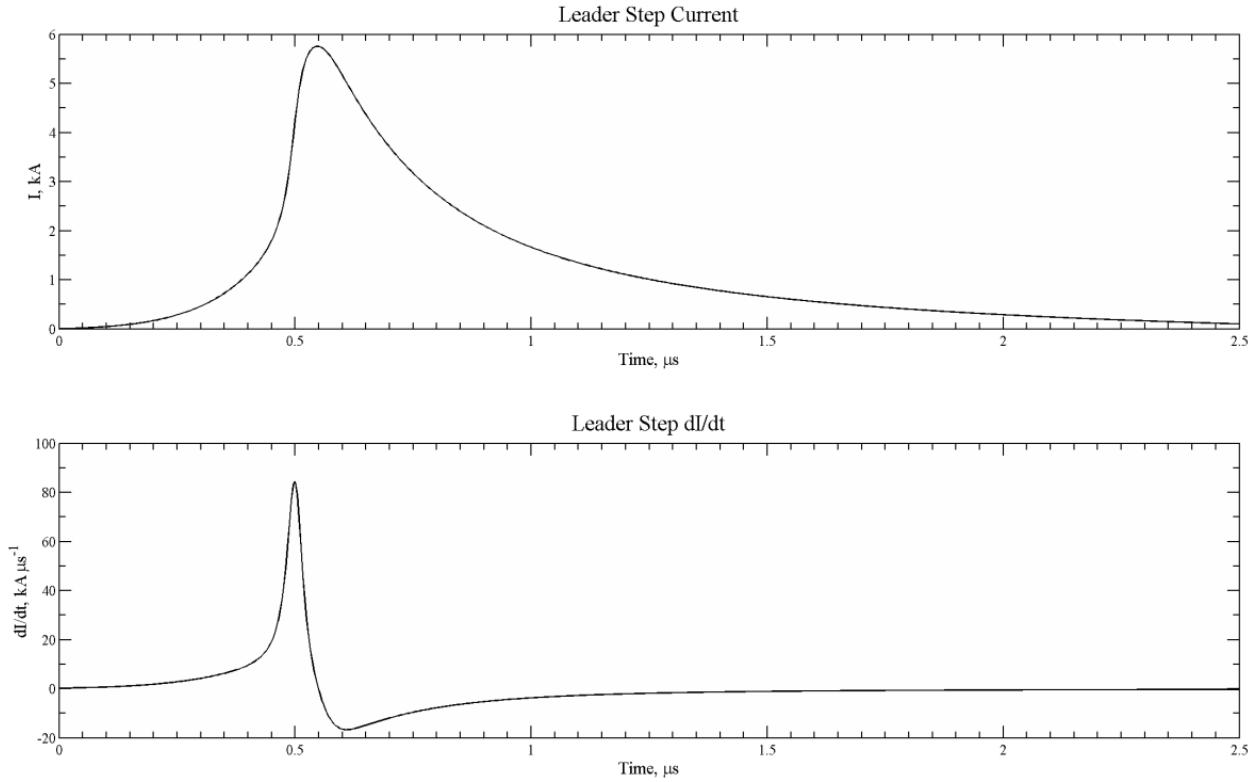


Figure 7-29. Current and current derivative waveform used in the Step 2 model results shown in Figure 7-28. The current derivative waveform was generated using the Jerauld function (Equation 7-8) with the parameters $T_{\text{peak}} = 0.5 \mu\text{s}$, $\alpha_1 = 100 \text{ kA } \mu\text{s}^{-1}$, $\alpha_2 = 10 \text{ kA } \mu\text{s}^{-1}$, $\beta = 1.73$, $\gamma = 20 \text{ ns}$.

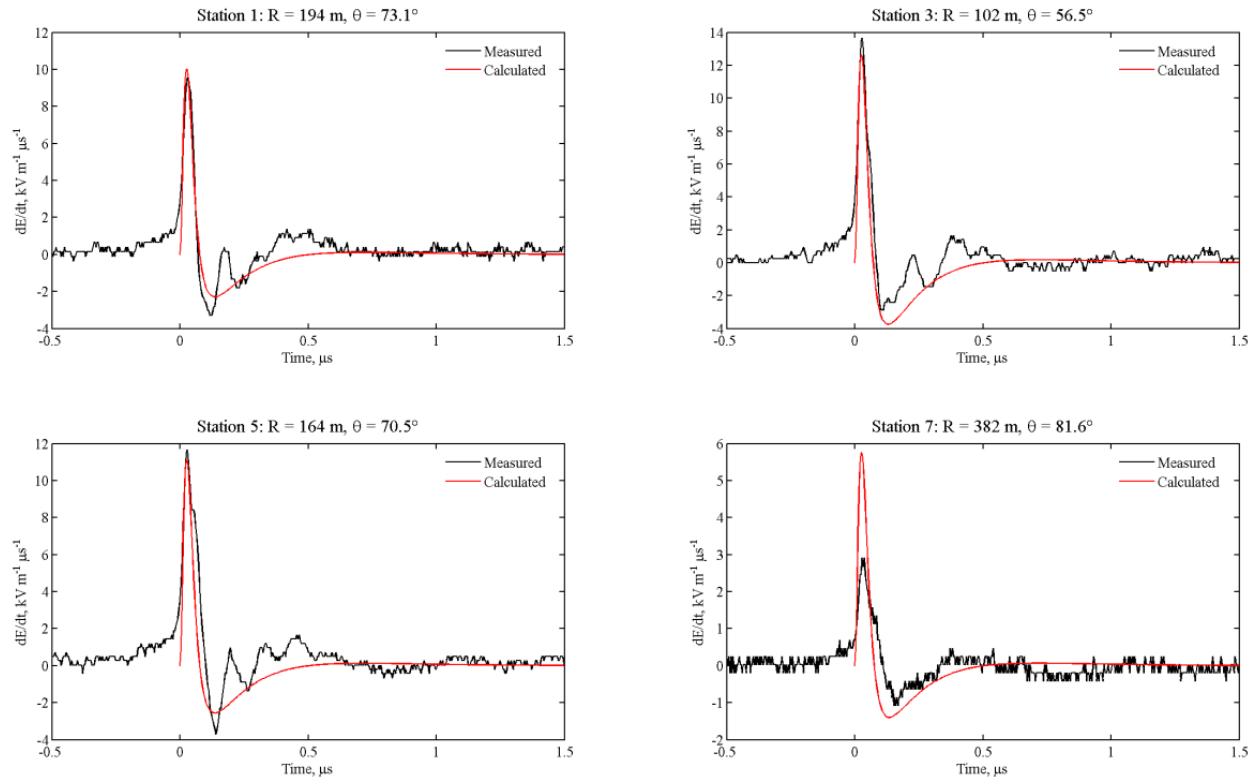


Figure 7-30. Step 3 modeling results using the Heidler model. The current front propagated with an upward speed of $1.5 \times 10^8 \text{ m s}^{-1}$, and the amplitude of the current waveform decayed exponentially with a decay constant of 25 m.

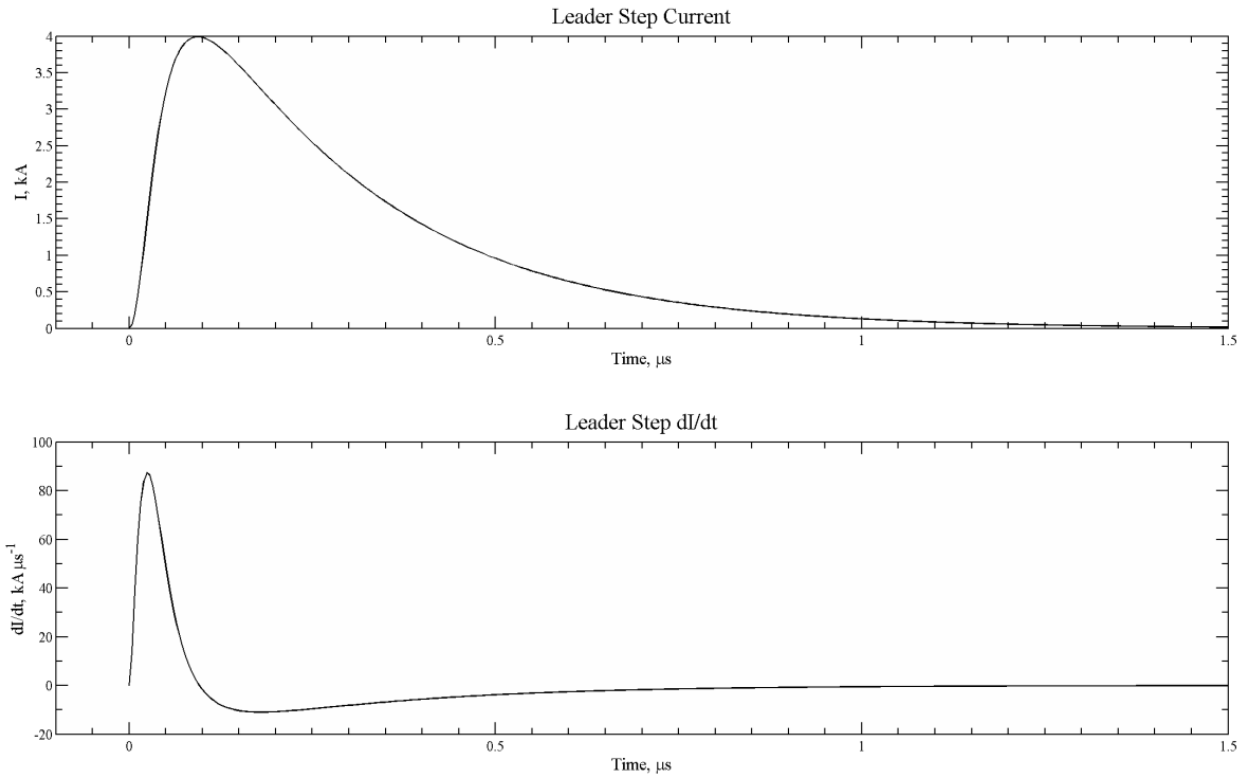


Figure 7-31. Current and current derivative waveform used in the Step 3 model results shown in Figure 7-30. The current waveform was generated using the Heidler function (Equation 7-7) with the parameters $I_0 = 4 \text{ kA}$, $\eta = 0.560$, $n = 2$, $\tau_1 = 45 \text{ ns}$, $\tau_2 = 250 \text{ ns}$.

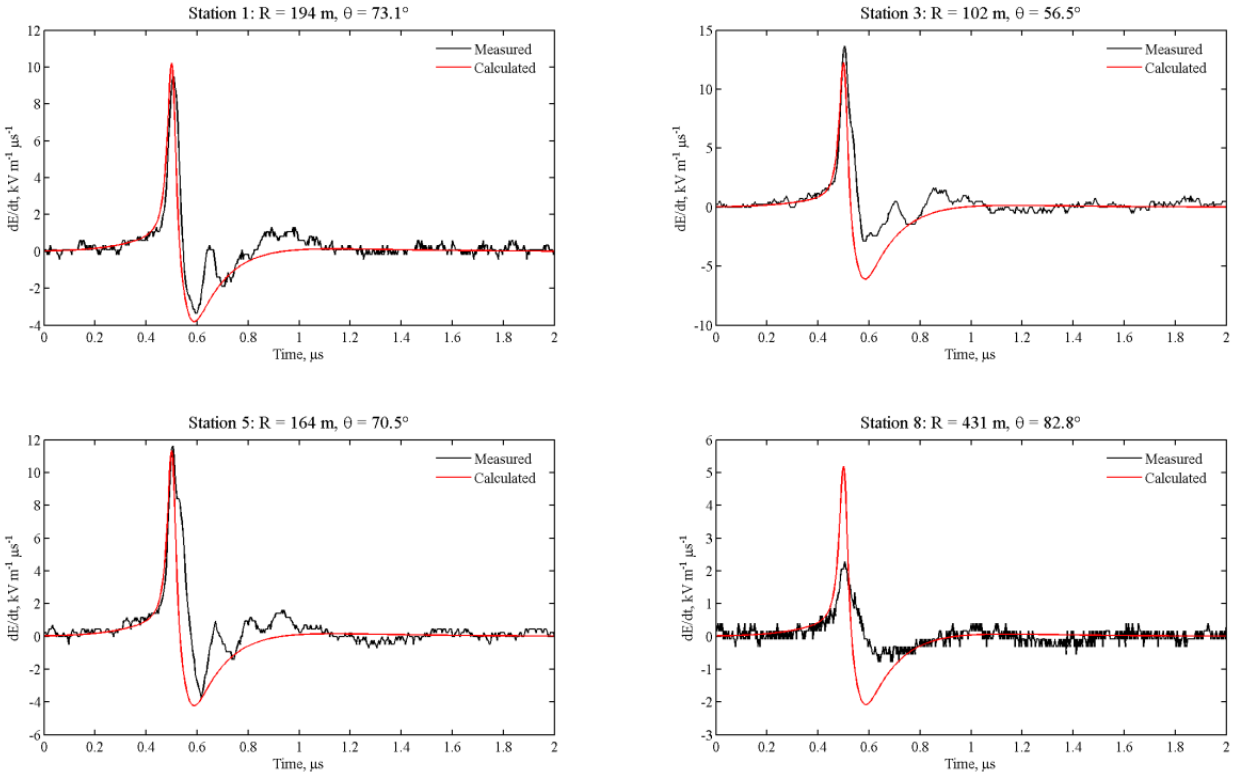


Figure 7-32. Step 3 modeling results using the Jerauld model. The current front propagated with an upward speed of $1.5 \times 10^8 \text{ m s}^{-1}$, and the amplitude of the current waveform decayed exponentially with a decay constant of 25 m.

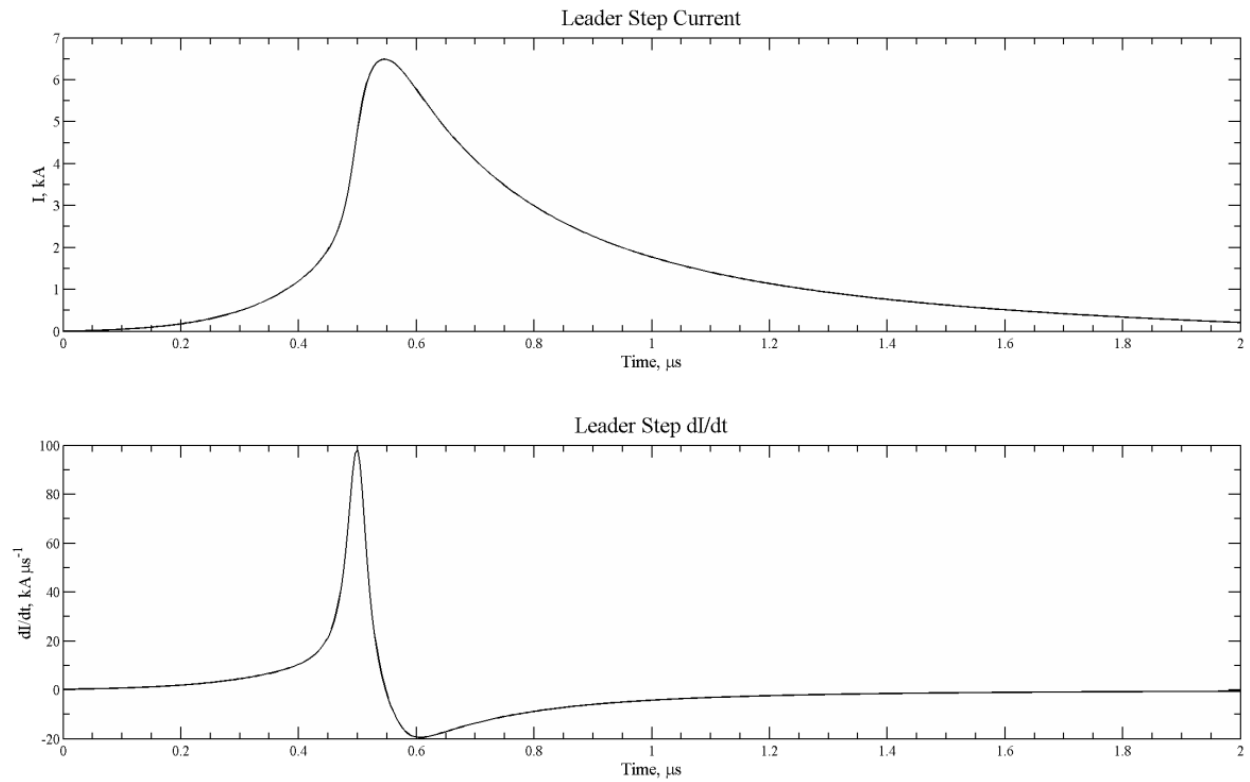


Figure 7-33. Current and current derivative waveform used in the Step 3 model results shown in Figure 7-32. The current derivative waveform was generated using the Jerauld function (Equation 7-8) with the parameters $T_{\text{peak}} = 0.5 \mu\text{s}$, $\alpha_1 = 118 \text{ kA } \mu\text{s}^{-1}$, $\alpha_2 = 10.5 \text{ kA } \mu\text{s}^{-1}$, $\beta = 1.85$, $\gamma = 20 \text{ ns}$.

CHAPTER 8 SUMMARY OF RESULTS AND RECOMMENDATIONS FOR FUTURE RESEARCH

8.1 Summary of Results

Between 2005 and 2007, the Multiple Station Experiment (MSE), a collection of electric and magnetic field and electric and magnetic field-derivative measurements, at the International Center for Lightning Research and Testing (ICLRT) underwent considerable expansion and benefited from significant upgrades in its control system and observation capabilities. Since the number of measurements and the experimental setup changed significantly each year in this period, the 2005, 2006, and 2007 configuration were each discussed and documented in Chapter 2. The two primary additions to the MSE during this time were an array of NaI scintillation detectors, known as the Thunderstorm Energetic Radiation Array (TERA), for measuring lightning produced X rays and an eight-station time-of-arrival (TOA) system for locating low-altitude lightning processes in three dimensions. The full TOA system became operational in 2006. Since the installation of the first 10 TERA boxes in 2005, the MSE has been known as the MSE/TERA network. By the end of the 2007 storm season, the MSE/TERA network consisted of 24 stations and over 60 measurements. Data from each of the measurements were transmitted via fiber-optic links to the Launch Control trailer, where the waveforms were sampled and stored on digital oscilloscopes. The system was designed to trigger either from a pair of optical sensors located at two corners of the network and viewing inward or from the rocket-triggered lightning channel-base current, so that data would only be obtained for lightning flashes within or very near the network. Battery power was conserved at each station by using computer automation to arm and disarm based on the value of the ambient electric field at ground, sensed by an electric field mill located near the Launch Control trailer and about 50 m from the launch tower.

The purpose of MSE/TERA network was to observe the electromagnetic environment produced by nearby cloud-to-ground lightning. The additions of the TERA measurements and the TOA system were particularly focused on better understanding certain areas of lightning physics, such as the leader stepping process, the X-ray production mechanism, and the attachment process. Since there is significant variation in lightning properties associated with different types of leaders, it is important to observe both first strokes initiated by stepped leaders and subsequent strokes initiated by dart or dart-stepped leaders. During the period from 2005 to 2007, data were acquired for 9 rocket-triggered flashes and 18 natural flashes that terminated within or very near the network. All of these flashes lowered negative charge to ground. Only four of these strokes (three natural and one rocket-triggered) are analyzed in detail here, due to their waveforms allowing the best TOA analysis, but all of the strokes have been documented for potential use in other studies. Indeed, some of the flashes not discussed here have already been used in other studies. Details for the data set collected by the MSE/TERA network between 2005 and 2007 are provided in Chapter 3.

The design and construction of a TOA system that provides high resolution for low-altitude lightning processes was the cornerstone of the analyses presented in this dissertation. Because of the TOA network's small size ($\sim 0.25 \text{ km}^2$), it has exceptional spatial resolution at low altitudes compared to other TOA systems and lightning mapping arrays (LMAs). The altitude errors generally remain below 10 m for sources as low as 50 m above the ground. The location errors in the plan directions are typically within 2–3 m. This TOA network also provides higher temporal resolution than other TOA systems because event selection was performed manually, versus other systems which generally use an automated routine to pick a

single peak out of a predefined time interval (typically 80 μ s). The details of the methodology and implementation of this system are discussed in Chapter 4.

One of the other unique features of the TOA network at the ICLRT was its ability to locate two different types of sources: X rays and electric field changes. All of the flashes obtained using the 2006 and 2007 configurations were examined for potentially locatable X-ray sources, i.e., correlated detection at $N \geq 5$ stations. Due to the relatively high attenuation rate of X-rays in the atmosphere, it is not surprising that these events are a rare occurrence. Indeed, only seven locatable X-ray sources were identified, all occurring in two flashes. As presented in Chapter 5, three of the sources occurred during the first stroke of natural flash MSE0604, and the other four occurred during the first stroke, initiated by a dart-stepped leader, of rocket-triggered flash UF0707. For all seven events, the X-ray source and the electric field change source of the associated leader step were co-located within 50 m. This result holds important implications for the X-ray production mechanisms proposed for leader stepping. As previously discussed, the relativistic runaway electron avalanche (RREA) model has gained great popularity, becoming the standard runaway breakdown model for atmospheric processes [Gurevich *et al.*, 1992; Gurevich and Zybin, 2001]. The RREA predicts the production of energetic electrons in electric field values lower than the breakdown field, but it generally requires a very extended field, typically a hundred meters or more. The close spatial relationship between the X-ray and electric field sources is factually damaging to this model and seems to favor the cold runaway electron model [Gurevich, 1961], which requires very large fields over much shorter distances. Moreover, Dwyer [2004] found that the observed spectrum and flux of the X-ray emissions were inconsistent with the RREA model.

Another benefit of locating both types of sources was the ability to provide the first quantitative description for the temporal relationship between these two source types. For all seven events, the time of occurrence for the X-ray source followed that of the electric field change source by 0.1 to 1.3 μs . In other words, the majority of X-ray production occurs after the leader-step process that corresponds to the peak field change value in the dE/dt waveform. This quantitative description could prove very useful for verifying future models of X-ray production. It is also noteworthy that some smaller X-ray emissions may occur prior to the source responsible for the peak dE/dt . Such observations have typically been made on sensors closest to the source, indicating that the strength of the X-ray source varies with time. This pattern of emission may also provide insight into the leader stepping mechanism, as we discuss shortly.

The dE/dt portion of the TOA network is much more effective than the X-ray measurements for tracking lightning processes, as each event typically has a distinct waveform signature and the field radiation is not attenuated much over the short distances involved with this network. In Chapter 6, this portion of the TOA network is used to obtain three-dimensional RF source locations during the leaders and attachment processes of three natural first cloud-to-ground strokes initiated by stepped leaders and one stroke initiated by a dart-stepped leader in a rocket-and-wire triggered flash. Stepped leader and dart-stepped leader dE/dt pulses were tracked from a few hundred meters to a few tens of meters above ground, after which pulses of different characteristics than the step pulses are observed to occur at lower altitudes. These post-leader pulses include (1) the "leader burst", a group of pulses in the dE/dt waveform radiated within about 1 μs and occurring just prior to the slow front in the corresponding return stroke electric field waveform; (2) dE/dt pulses occurring during the slow front; and (3) the fast

transition or dominant dE/dt pulse that is usually associated with the rapid transition to peak in the return stroke electric field waveform.

The source locations determined during the leader phase of these strokes were used to provide graphical visualizations of the lightning propagation as well as estimate the leader speed within several hundred meters of ground. The downward velocities determined for the three stepped leaders were between $3.6 \times 10^5 \text{ m s}^{-1}$ to $9.0 \times 10^5 \text{ m s}^{-1}$, while the dart-stepped leader of the rocket-triggered flash had a velocity of $4.8 \times 10^6 \text{ m s}^{-1}$. Interestingly, plots for the altitudes of leader sources in each stroke versus time were best fit by a linear approximation, indicating a constant downward velocity. The close (within several hundred meters) dE/dt waveforms obtained by MSE/TERA network also reveal that the radiation associated with the leader phase often occurs as groups of pulses. TOA analysis confirms that pulses within each group tended to be closely spaced, while groups of pulses, perhaps associated with leader stepping in different branches, were often separated by some tens of meters, including displacement in directions parallel to the ground surface. It follows that leader steps likely involve a complex series of breakdown events as opposed to a singular electrical breakdown.

The structure of each group of leader pulses could be described as a dominant bipolar pulse, referred to as the leader step (LS), which may have smaller pulses within a few microseconds before (BS) or after (AS) it. For each stroke discussed in Chapter 6, the vertical positioning of the secondary pulses relative to the dominant pulse was examined as a function of whether the pulses occurred before or after the dominant pulse in time. For the secondary pulses occurring before the leader step, BS pulses, 8 out of 14 (57%) were located below the dominant pulse, with the average displacement for these 14 pulses being 0.4 m below the dominant pulse. On the other hand, 7 out of 9 (78%) secondary pulses occurring after the dominant pulse, AS

pulses, were located below the dominant pulses, with an average displacement for these 9 pulses being 7.2 m below the dominant pulse. Although this is not a large sample and the average vertical displacement is smaller than or equal to the vertical resolution of our TOA network, this analysis provides empirical insight into the stepping process of downward negative leaders in lightning. The data indicate that most electrical activity occurring just prior to the step is very near the new step location; while after the dominant step pulse (LS), the electrical activity is below the new step. From this result we might infer that the stepping mechanism for a lightning leader is similar to that observed in the laboratory for some meters-long sparks [Gorin *et al.*, 1976; Gallimberti, 2002; Rakov and Uman, 2003]. In a negative laboratory leader, a space stem develops in the streamer zone in front of the currently-existing leader channel. The space stem gives rise to a bidirectional leader, which is positively charged toward the existing leader and negatively charged into the gap. When the space stem connects to the main leader channel, a large step current is produced. Thereafter, an intense burst of corona streamers extends downward from the previous space stem (now part of the leader) to eventually form a new stem. Perhaps it is the corona streamers, which initially extend both upward and downward from the space stem (creating the small pulses before the main LS) and later extend below the new leader step (creating the small pulses after the LS), that are responsible for the secondary pulses in leader steps and for their observed vertical distributions. Because streamer tips are a currently-favored source for X-ray production [Gurevich, 1961; Dwyer, 2004; Moss *et al.*, 2006, Dwyer *et al.*, 2008; Rahman *et al.*, 2008], it is interesting that the time of occurrence for the locatable X-ray emissions was found to follow the leader-step electric field change by $\sim 1\mu\text{s}$ with some evidence of weaker X-ray emission just prior to the step [Howard *et al.*, 2008], perhaps further evidence that the stepping mechanism of the lightning leader is similar to that observed in the

laboratory. It is noteworthy that *Biagi et al.* [2009] recently provided high-speed video records for a rocket-triggered lightning stroke involving a dart-stepped leader which appears to show a space stem in front below of the developed leader.

It was shown in Chapter 6 that the waveform characteristics change significantly after the leader phase, possibly representative of three types of processes. The first type of post-leader event manifests itself as a burst of pulses just prior to the slow front and is referred to as a leader burst. Similar pulses have previously been reported by *Murray et al.* [2005] for distant (radiation field) dE/dt waveforms from negative first strokes, as well as by *Jerauld et al.* [2007, 2008] for close negative first-stroke dE/dt waveforms. To date, there is little information and no explanation for the leader burst pulses. We have shown (1) that their location is below the steps of the previous leader phase, (2) that they are associated with a rapid and significant downward movement, not typically observed with preceding leader steps (the leader burst may also cover significant horizontal distances or involve simultaneous activity by the downward leader and upward connecting leader), (3) that the leader burst produces a significant amount of X rays, and (4) that the leader burst dE/dt feature corresponds to a vertical hump or step in the electric field waveform (also supported by the waveforms of *Murray et al.* [2005] and *Jerauld et al.* [2008], although they did not discuss the specific correlation).

In describing the waveforms of Chapter 6, two additional post-leader processes were identified: slow-front pulses and the fast transition. In the three strokes that allowed both types of events to be located, these supposedly different types of pulses had very similar source locations. The fast transition of MSE0604 could not be located due to waveform saturation at too many stations, but the two slow-front pulses were located within 10 m horizontally of a tree that was struck by the flash. In the rocket-triggered flash UF0707, there were two significant transitions

observed in the post leader portion of the dE/dt waveforms – one caused by slow-front pulses and the second by the fast transition. These two pulses produce nearly identical features in the electric field record, and both corresponded with significant increases in the channel-base current. In fact, the current rises to over 20 kA after the first of these transitions, indicating that some form of attachment had probably already occurred. Interestingly, the video records for UF0707 show that the attachment phase involved the connection of two channels. Based on this collection of evidence, it appears very likely that both slow-front pulses and the fast transition result from the same process – upward and downward leader connections in the attachment region. The size of the pulses in the dE/dt records appears to be dependent on the amount of current facilitated by the connection.

A comparison of the X-ray records with the time-synchronized dE/dt records of the post leader processes reveals that slightly more X-rays are coincident with slow-front pulses than the fast-transition pulses. X-rays were detected much more frequently with the leader burst than with either the slow-front or fast-transition pulses. Although the production of X rays from the lightning leader has been soundly established [Moore *et al.*, 2001; Dwyer *et al.*, 2003, 2004, 2005], the X-ray comparison performed here is the first confirmation that post-leader processes also produce X-rays.

Chapter 7 examined the nature of stepped-leader dE/dt pulse at close range. The presented waveforms revealed that leader-step dE/dt pulses exhibit a characteristic shape that can be described as a bipolar pulse having a sharp initial peak with the same polarity as the return-stroke pulse, followed by an opposite-polarity overshoot which decays slowly to the background level. The waveforms also indicate that the initial peak dE/dt amplitude is dependent on the range ($|\vec{R}|$), viewing angle to the sensor (θ), and channel orientation. Conversely, the amplitude of the

opposite-polarity overshoot appears to be dominated by its dependence on distance, with the overshoot typically being largest in the closest waveforms and barely being noticeable in the farthest. The presence of secondary pulses also greatly affects the appearance of each individual step. The peak amplitude, range normalized to 100 km; half-peak width; and 10–90% rise time for these close leader-step dE/dt pulses were also examined. The mean half-peak width (33.5 ns), which can be used as an indicator for the rise time of the corresponding electric field pulse, was approximately half the value previously reported by *Willett and Krider* [2000] for leader-step dE/dt pulses propagating over salt water (54 ns). Finally, a current waveform that involves a slow front was found to better predict the observed dE/dt waveforms compared to the Heidler function used to represent the leader-step current by *Jerauld* [2007]. The peak current and charge transfer were similar to values predicted by *Krider et al.* [1977] and *Rakov et al.* [1998], but the peak dI/dt was significantly larger than that predicted by *Krider et al.* [1977].

8.2 Improvements to the MSE/TERA System

Since the end of the 2007 storm season, an influx of federal funding has allowed many significant upgrades for the MSE/TERA system. One of the most significant upgrades has been with the video coverage of the site. The MSE/TERA video system, which used to record a quadrature frame on a single TIVO DVR, has been completely replaced. The past system was never very reliable due to intermitten clitches with the post-market Ethernet cards that were installed on the units. Moreover, the spatial resolution was very poor due to the use of the quadrature mode. The new system utilizes a Geovision video surveillance system which currently records 6 full screen camera views in NTSC format. The network is armed and disarmed with the rest of the network by the control computer. The video is recorded in two minute files on a computer harddrive, each file with a GPS timestamp. This technique is a

tremendous improvement over the previous video recovery procedure, which typically involved searching very long segments of video for one or two frames.

In addition to the MSE/TERA video coverage for natural events, there has also been significant improvement in the video surveillance of rocket-triggered flashes, primarily in the form of high-speed video. Rocket-triggered flashes have been imaged by as many as three high-speed cameras (1 Phantom V7.3 and 2 Photron FASTCAM SA1.1) operating at frame rates from 5,400 fps to 300 kfps. The different view angles covered by these cameras have already provided great breakthroughs in studying the initial upward positive leader and they are starting to provide great images of leader and attachment processes [e.g., *Biagi et al.*, 2009].

The TOA network has also seen its share of improvement, incorporating additional, faster sensors in the TOA network. As discovered in this work, X-ray sources have proven very difficult to locate due to the relatively large separation between the sensors (compared to the attenuation rate of X rays in the atmosphere) and the relatively slow response of the NaI detectors. The TOA network now includes an additional 8 plastic (1 m² scintillator) detectors and 2 Lanthanum Bromide (LaBr₃) detectors. The additional locations and faster response times provided by these sensors should provide more opportunities to locate X-ray sources and with higher accuracy than was performed in this work. The improved TOA network also includes 1 additional dE/dt antenna.

Finally, the MSE/TERA system has also benefited by adapting the E-field antennas to be more responsive to positive lightning. The number of E-field antennas has increased from 6 to 10, and they utilize different dynamic ranges, allowing lightning to be recorded at distances from on-site to 40 km away. The waveforms for this “positive lightning” experiment are recorded along with a crossed-loop B-field antenna, a crosslooped dB/dt antenna, and 11 NaI sensors.

8.3 Recommendations for Future Research

It is the author's opinion that the following topics all warrant additional study.

- The additional and faster X-ray sensors now in the network should provide a much larger data set from which to compare the locations of X-ray and electric field change sources, and the X-rays sources should be located with greater accuracy. Although this dissertation has provided initial results, it would be of value to analyze and compare more than seven events.
- High-speed video will likely elucidate several topics that were speculated upon in this dissertation. Waveforms for UF0707 indicated that the interstep interval for a dart-stepped leader was about 4–5 μs . The high-speed cameras currently available to the ICLRT can achieve a frame rate that would image a single step at a time. With proper time correlation between the video and dE/dt waveforms, it would be interesting to compare images of leader steps to corresponding segments of dE/dt waveforms, i.e., do leader steps imaged with a space stem involve more secondary pulses than leader steps imaged without a space stem. When a high-speed camera with a submicrosecond frame rate becomes available to the ICLRT, it will be interesting to compare the sequence of frames for a dart-stepped leader producing a multiple-branched connection in the attachment region (such as UF0707) to the dE/dt waveforms. Such a comparison could finally resolve whether slow-front pulses and the fast transition are both the result of connections in the attachment region. It would also be enlightening to image the leader burst with a camera having a submicrosecond frame rate.
- Each positive flash that is recorded by the “positive lightning” network and suspected of being within a few kilometers of the site should be analyzed for coincident X rays. To the author's knowledge, it would be the first documented case of X rays being produced by a downward positive flash.
- Although the “positive lightning” network was designed for recording positive flashes, it can also be triggered on negative flashes. If a collection of off-site negative flashes were obtained and the corresponding locations were retrieved from the NLDN network, it may be possible to determine the range at which X-rays are detected from negative downward flashes, known producers of X rays.
- It may also be worthwhile to implement two dynamic ranges for the dE/dt measurements in the TOA network. If the dynamic range is large enough to avoid saturation during the return stroke, the measurements typically do not resolve the leader steps very well.

LIST OF REFERENCES

- Babich, L. P. (2003), *High-Energy Phenomena in Electric Discharges in Dense Gases: Theory, Experiment and Natural Phenomena*, ISTC Sci. Technol. Ser., vol. 2, 358 pp., Futurepast, Arlington, Va.
- Baker, M. B., J. G. Dash (1989), Charge transfer in thunderstorms and the surface melting of ice, *J. Cryst. Growth*, 97, 770–776.
- Baker, M. B., J. G. Dash (1994), Mechanism of charge transfer between colliding ice particles in thunderstorms, *J. Geophys. Res.*, 99, 10,621–10,626.
- Bazelyan, E. M., and Y. P. Raizer (2000), *Lightning Physics and Lightning Protection*, Inst. of Phys., Bristol, UK.
- Bazelyan, E. M., B. N. Gorin, and V. I. Levitov (1978), *Physical and Engineering Foundations of Lightning Protection*, Gidrometeoizdat, Leningrad.
- Beasley, W. H., M. A. Uman, and P. L. Rustan (1982), Electric fields preceding cloud-to-ground lightning flashes, *J. Geophys. Res.*, 87, 4883–4902.
- Berger, K. (1955a), Die Messeinrichtungen für die Blitzforschung auf dem Monte San Salvatore, *Bull. Schweiz. Elektrotech. Ver.*, 46, 193–204.
- Berger, K. (1955b), Resultate der Blitzmessungen der Jahre 1947–1954 auf dem Monte San Salvatore, *Bull. Schweiz. Elektrotech. Ver.*, 46, 405–424.
- Berger, K. (1962), *Gas Discharges and the Electricity Supply Industry*, chap. Front duration and current steepness of lightning strokes to Earth, pp. 63–73, Butterworths.
- Berger, K. (1967a), Novel observations on lightning discharges: results of research on Mount San Salvatore, *J. Franklin Inst.*, 283, 478–525.
- Berger, K. (1967b), Gewitterforschung auf dem Monte San Salvatore, *Elektrotechnik (Z-A)*, 82, 249–260.
- Berger, K. (1972), Methoden und Resultate der Blitzforschung auf dem Monte San Salvatore bei Lugano in den Jahren 1963–1971, *Bull. Schweiz. Elektrotech. Ver.*, 63, 1403–1422.
- Berger, K. (1978), Blitzstrom-Parameter von Aufwärtsblitzen, *Bull. Schweiz. Elektrotech. Ver.*, 69, 353–360.
- Berger, K. (1980), Extreme Blitzströme und Blitzschutz, *Bull. Schweiz. Elektrotech. Ver.*, 71, 460–464.
- Berger, K., and E. Garbagnati (1984), Lightning current parameters. results obtained in Switzerland and Italy, uRSI Commission E, Florence, Italy, 13 pp.

- Berger, K., and E. Vogelsanger (1965), Messungen und Resultate der Blitzforschung der Jahre 1955–1963 auf dem Monte San Salvatore, *Bull. Schweiz. Elektrotech. Ver.*, 56, 2–22.
- Berger, K., and E. Vogelsanger (1966), Photographische blitzuntersuchungen de jahre 1955–1965 auf dem Monte San Salvatore. *Bull. Schweiz. Elektrotech. Ver.*, 57, 599–620.
- Berger, K., and E. Vogelsanger (1969), *Planetary Electrodynamics*, chap. New results of lightning observations, pp. 489–510, Gordon and Breach.
- Berger, K., R. B. Anderson, and H. Kroninger (1975), Parameters of lightning flashes, *Electra*, 80, 223–37.
- Bevington, P.R. (1969), *Data Reduction and Error Analysis for the Physical Sciences*, McGraw-Hill, New York, 336.
- Biagi, C. J., D. M. Jordan, M. A. Uman, J. D. Hill, W. H. Beasley, and J. Howard (2009), High-speed video observations of rocket-and-wire initiated lightning, *Geophys. Res. Lett.*, doi:10.1029/2009GL038525.
- Boccippio, D. J., S. Heckman, and S. J. Goodman (2001), A diagnostic analysis of the Kennedy Space Center LDAR network 1. Data characteristics, *J. Geophys. Res.*, 106(D5), 4769–86.
- Boyle, J. S., and R. E. Orville (1976), Return stroke velocity measurements in multistroke lightning flashes, *J. Geophys. Res.*, 81, 4461–4466.
- Brook, M., N. Kitagawa, and E. J. Workman (1962), Quantitative study of strokes and continuing currents in lightning discharges to ground, *J. Geophys. Res.*, 67, 649–659.
- Byrne, C. J., A. A. Few, and M. E. Weber (1983), Altitude, thickness and charge concentration of charge regions of four thunderstorms during TRIP 1981 based upon *in situ* balloon electric field measurements, *Geophys. Res. Lett.*, 10, 39–42.
- Carlson, B. E., N. G. Lehtinen, and U. S. Inan (2007), Constraints on terrestrial gamma ray flash production from satellite observations, *Geophys. Res. Lett.*, 34(8), L08809, doi:10.1029/2006GL029229.
- Casper, P. W., and R. B. Bent (1992), Results from the LPATS USA national lightning detection and tracking system for the 1991 lightning season, in *Proc. 21st Int. Conf. on Lightning Protection*, Berlin, Germany, 339–42.
- Chen, M., N. Takagi, T. Watanabe, D. Wang, Z. I. Kawasaki, and X. Liu (1999), Spatial and temporal properties of optical radiation produced by stepped leaders, *J. Geophys. Res.*, 104, 27,573–27,584.
- Cianos, N., G. N. Oetzel, and E. T., Pierce (1972), A technique for accurately locating lightning at close ranges, *J. Appl. Meteor.*, 11, 1120–1127.

- Clarence, N. D., and D. J. Malan (1957), Preliminary discharge processes in lightning flashes to ground, *Q. J. R. Meteor. Soc.*, 83, 161–172.
- Cooray, V. (1987), Effects of propagation on the return stroke radiation fields, *Radio Sci.*, 22, 757–768.
- Cooray, V., and S. Lundquist (1982), On the characteristics of some radiation fields from lightning and their possible origin in possible origin in ground flashes, *J. Geophys. Res.*, 87(C13), 11,203–11,214.
- Crawford, D. E. (1998), Multiple-station measurements of triggered lightning electric and magnetic fields, Ph.D. dissertation, University of Florida, Gainesville, FL.
- Crawford, D. E., V. A. Rakov, M. A. Uman, G. H. Schnetzer, K. J. Rambo, M. V. Stapleton, and R. J. Fisher (2001), The close lightning electromagnetic environment: Dart-leader electric field change versus distance, *J. Geophys. Res.*, 106, 14,909–14,917.
- Dwyer, J. R. (2003), A fundamental limit on electric fields in air, *Geophys. Res. Lett.*, 30, 2055.
- Dwyer, J. R. (2004), Implications of x-ray emission from lightning, *Geophys. Res. Lett.*, 31, L12102, doi:10.1029/2004GL019795.
- Dwyer, J. R., and D. M. Smith (2005), A comparison between Monte Carlo simulations of runaway breakdown and terrestrial gamma-ray flash observations, *Geophys. Res. Lett.*, 32, L22804, doi:10.1029/2005GL023848.
- Dwyer, J. R., et al. (2003), Energetic radiation produced during rocket-triggered lightning, *Science*, 299, 694–697.
- Dwyer, J. R., et al. (2004), Measurements of x-ray emission from rocket-triggered lightning, *Geophys. Res. Lett.*, 31, L05118, doi:10.1029/2003GL018770.
- Dwyer, J. R., et al. (2005), X-ray bursts associated with leader steps in cloud-to-ground lightning, *Geophys. Res. Lett.*, 32, L01803, doi:10.1029/2004GL021782.
- Dwyer, J. R., Z. Saleh, H. K. Rassoul, D. Concha, M. Rahman, V. Cooray, J. Jerauld, M. A. Uman, and V. A. Rakov (2008), A study of X-ray emission from laboratory sparks in air at atmospheric pressure, *J. Geophys. Res.*, 113, D23207, doi:10.1029/2008JD010315.
- Eack, K. B., W. H. Beasley, W. D. Rust, T. C. Rust, T. C. Marshall, and M. Stolzenburg (1996), X-ray pulses observed above a mesoscale convection system, *Geophys. Res. Lett.*, 23, 2915–2918.
- Eack, K. B., D. M. Suszcynsky, W. H. Beasley, R. Roussel-Dupre, and E. Symbalisky (2000), Gamma-ray emission observed in a thunderstorm anvil, *Geophys. Res. Lett.*, 27, 185–188.
- Eriksson, A. J. (1978), Lightning and tall structures, *Trans. South African IEE*, 69, 238–252.

- Fishman, G. J., et al. (1994), Discovery of intense gamma-ray flashes of atmospheric origin, *Science*, 264, 1313.
- Gallimberti, I., G. Bacchiega, A. Bondiou-Clergerie, P. Lalande (2002), Fundamental processes in long air gap discharges, *C. R. Physique*, 3, 1335–1359.
- Golde, R. H. (1947), Occurrence of upward streamers in lightning discharges, *Nature*, 160, 395–396.
- Golde, R. H. (1967), The lightning conductor, *J. Franklin Inst.*, 283, 451–477.
- Gomes, C., V. Cooray, and C. Jayaratne (1998), Comparison of preliminary breakdown pulses observed in Sweden and in Sri Lanka, *J. Atmos. Solar Terr. Phys.*, 60, 975–979.
- Gorin, B. N., V. I. Levitov, and A. V. Shkilev (1976), Some principles of leader discharge of air gaps with a strong non-uniform field, in *Gas Discharges, IEE Conf. Publ. 143*, 274–278.
- Gurevich, A. V. (1961), On the theory of runaway electrons, *Sov. Phys. JETP Engl. Transl.*, 12, 904–912.
- Gurevich, A. V., and K. P. Zybin (2001), Runaway breakdown and electric discharges in thunderstorms, *Phys. Usp.*, 44, 1119–1140.
- Gurevich, A. V., G. M. Milikh, and R. Roussel-Dupre´ (1992), Runaway electron mechanism of air breakdown and preconditioning during a thunderstorm, *Phys. Lett. A*, 165, 463–468.
- Gurevich, A. V., G. M. Milikh, and J. A. Valdivia (1997), Model of X-ray emission and fast preconditioning during a thunderstorm, *Phys. Lett. A*, 231, 402–408.
- Hagenguth, J. H. (1947), Photographic study of lightning, *Trans. Am. Inst. Electr. Eng.*, 66, 577–585.
- Hager, W. H., and D. Wang (1995), An analysis of errors in the location, current, and velocity of lightning, *J. Geophys. Res.*, 100(25), 25,721–25,729.
- Halliday, E. C., (1934), Thunderstorms and the penetrating radiation, *Proc. Cambridge Phil. Soc.*, 30, 206–215.
- Heidler, F. (1985), Traveling current source model for LEMP calculation., in *Proc. 6th Int. Symp. on Electromagnetic Compatibility*, pp. 155–162, Zurich, Switzerland.
- Hill, R. D., (1963) Investigation of electron runaway in lightning, *J. Geophys. Res.*, 68, 6261–6266.
- Holle, R. L., and R. E. Lopez (1993), Overview of real-time lightning detection systems and their meteorological uses, NOAA Technical Memorandum ERL NSSL-102, 68.

- Howard, J., M. A. Uman, J. R. Dwyer, D. Hill, C. Biagi, Z. Saleh, J. Jerauld, and H. K. Rassoul (2008), Co-location of lightning leader x-ray and electric field change sources, *Geophys. Res. Lett.*, *35*, L13817, doi:10.1029/2008GL034134.
- Hubert, P., and G. Mouget (1981), Return stroke velocity measurements in two triggered lightning flashes, *J. Geophys. Res.*, *86*, 5253–5261.
- Idone, V. P., and R. E. Orville (1982), Lightning return stroke velocities in the Thunderstorm Research International Program (TRIP), *J. Geophys. Res.*, *87*, 4903–4915.
- Idone, V. P., and R. E. Orville (1985), Correlated peak relative light intensity and peak current in triggered lightning subsequent return strokes, *J. Geophys. Res.*, *90*, 6159–6164.
- Idone, V. P., R. E. Orville, P. Hubert, L. Barret, and A. Eybert-Berard (1984), Correlated observations of three triggered lightning flashes, *J. Geophys. Res.*, *89*, 1385–1394.
- Inan, S. U., S. C. Reising, G. J. Fishman, and J. M. Horack (1996), On the association of terrestrial gamma-ray burst with lightning and implications for sprites, *Geophys. Res. Lett.*, *23*, 1017–1020.
- Jayarathne, E. R., C. P. R. Saunders, and J. Hallett (1983), Laboratory studies of the charging of soft-hail during ice crystal interactions, *Q. J. R. Meteor. Soc.*, *109*, 609–630.
- Jerauld, J. (2003), A multiple-station experiment to examine the close electromagnetic environment of natural and triggered lightning, Master's thesis, University of Florida, Gainesville, FL.
- Jerauld, J. (2007), Properties of natural cloud-to-ground lightning inferred from multiple-station measurements of close electric and magnetic fields and field derivatives, Ph.D. dissertation, University of Florida, Gainesville, FL. (Available at <http://purl.fcla.edu/fcla/etd/UFE0021279>)
- Jerauld, J., V. A. Rakov, M. A. Uman, D. E. Crawford, B. A. DeCarlo, D. M. Jordan, K. J. Rambo, and G. H. Schnetzer (2003), Multiple-station measurements of electric and magnetic fields due to natural lightning, in *Proc. Int. Conf. on Lightning and Static Elec. (ICOLSE)*, Blackpool, United Kingdom.
- Jerauld, J., M. A. Uman, V. A. Rakov, K. J. Rambo, and D. M. Jordan (2004), A triggered lightning flash containing both negative and positive strokes, *Geophys. Res. Lett.*, *31*, L08,104, doi:10.1029/2004GL019457.
- Jerauld, J., V. A. Rakov, M. A. Uman, K. J. Rambo, and D. M. Jordan (2005), An evaluation of the performance characteristics of the U.S. National Lightning Detection Network using triggered lightning in Florida, *J. Geophys. Res.*, *110*, D19106, doi:10.1029/2005JD005924.

- Jerauld, J., M. A. Uman, V. A. Rakov, K. J. Rambo, and G. H. Schnetzer (2007), Insights into the ground attachment process of natural lightning gained from an unusual triggered-lightning, *J. Geophys. Res.*, *112*, D13113, doi:10.1029/2006JD007682.
- Jerauld, J., M.A. Uman, V. A. Rakov, K. J. Rambo, D. M. Jordan, and G. H. Schnetzer (2008), Electric and magnetic fields and field derivatives from lightning stepped leaders and first return strokes measured at distances from 100 to 1000 m, *J. Geophys. Res.*, *113*, D17111, doi:10.1029/2008JD010171.
- Jerauld, J. E., M. A. Uman, V. A. Rakov, K. J. Rambo, D. M. Jordan, and G. H. Schnetzer (2009), Measured electric and magnetic fields from an unusual cloud-to-ground lightning flash containing two positive strokes followed by four negative strokes, *J. Geophys. Res.*, *114*, D19115, doi:10.1029/2008JD011660.
- Jordan, D. M., and M. A. Uman (1983), Variation in light intensity with height and time from subsequent lightning return strokes, *J. Geophys. Res.*, *88*, 6555–6562.
- Jordan, D. M., V. P. Idone, V. A. Rakov, M. A. Uman, W. H. Beasley, and H. Jurenka (1992), Observed dart leader speed in natural and triggered lightning, *J. Geophys. Res.*, *97*, 9951–9957.
- Jordan, D. M., V. P. Idone, R. E. Orville, V. A. Rakov, and M. A. Uman (1995), Luminosity characteristics of lightning M components, *J. Geophys. Res.*, *100*, 25,695–25,700.
- Jordan, D. M., V. A. Rakov, W. H. Beasley, and M. A. Uman (1997), Luminosity characteristics of dart leaders and return strokes in natural lightning, *J. Geophys. Res.*, *102*, 22,025–22,032.
- Kitagawa, N., and M. Brook (1960), A comparison of intracloud and cloud-to-cloud discharges, *J. Geophys. Res.*, *65*, 1189–1201.
- Kodali, V., V. A. Rakov, M. A. Uman, K. J. Rambo, G. H. Schnetzer, J. Schoene, and J. Jerauld (2005), Triggered-lightning properties inferred from measured currents and very close electric fields, *Atmos. Res.*, *76*, 355–376, doi:10.1016/j.atmosres.2004.11.036.
- Koshak, W. J., and H. J. Christian (1994), A nonhyperbolic solution to the problem of mapping lightning sources using VHF time-of-arrival measurements, *Eos Trans. AGU, Fall Meet. Suppl.*, *75*(44), 104.
- Koshak, W. J., and R. J. Solakiewicz (1996), On the retrieval of lightning radio sources from the time-of-arrival data, *J. Geophys. Res.*, *101*, 26,631–26,639.
- Koshak, W. J., et al. (2004), North Alabama Lightning Mapping Array (LMA): VHF source retrieval algorithm and error analyses, *J. Atmos. Oceanic Technol.*, *21*, 543–558.
- Krehbiel, P. R. (1981), An analysis of the electric field change produced by lightning, Ph.D. thesis, University of Manchester Institute of Science and Technology, Manchester, England.

- Krehbiel, P. R. (1986), *The Earth's Electrical Environment*, chap. The electrical structure of thunderstorms, pp. 90–113, National Academy Press., Washington, DC.
- Krehbiel, P. R., M. Brook, and R. McCrory (1979), An analysis of the charge structure of lightning discharges to the ground, *J. Geophys. Res.*, *84*, 2432–2456.
- Krider, E. P., G. J. Radda (1975), Radiation field wave forms produced by lightning stepped leaders, *J. Geophys. Res.*, *80*, 2653–2657.
- Krider, E. P., C. D. Weidman, and R. C. Noggle (1977), The electric field produced by lightning stepped leaders, *J. Geophys. Res.*, *82*, 951–960.
- Krider, E. P., C. Leteinturier, and J. C. Willett (1992), Submicrosecond field variations in natural lightning processes, *Res. Lett. Atmos. Electr.*, *12*, 3–9.
- Lalande, P., A. Bondiou-Clergerie, P. Laroche, A. Eybert-Berard, J. P. Berlandis, B. Bador, A. Bonamy, M. A. Uman, and V. A. Rakov (1998), Leader properties determined with triggered lightning techniques, *J. Geophys. Res.*, *103(D12)*, 14,109–14,115.
- Laroche, P., V. Idone, A. Eybert-Berard, and L. Barret (1991), Observations of bi-directional leader development in a triggered lightning flash, in *Pro. Int. Conf. on Lightning and Static Electricity*, pp. 57/1–10, Cocoa Beach, Florida.
- Lee, A. C. L. (1986), An experimental study of the remote location of lightning flashes using a VLF arrival time difference technique. *Q. J. R. Meteor. Soc.* *112*, 203–29.
- Lennon, C. L. (1975), LDAR: New lightning detection and ranging system, *Eos Trans. AGU*, *56(12)*, 991.
- Lennon, C. L., and H.A. Poehler (1982), Lightning detection and ranging, *Astronaut. Aeronaut.*, *20*, 29–31.
- Lewis, E. A., R. B. Harvey, and J. E. Rasmussen (1960), Hyperbolic direction finding with sferics of transatlantic origin, *J. Geophys. Res.*, *65*, 1879–1905.
- Lin, Y. T., M. A. Uman, J. A. Tiller, R. D. Brantley, W. H. Beasley, E. P. Krider, and C. D. Weidman (1979), Characterization of lightning return stroke electric and magnetic fields from simultaneous two-station measurements, *J. Geophys. Res.*, *84*, 6307–6314.
- Loeb, L. B. (1966), The mechanism of stepped and dart leaders in cloud-to-ground lightning strokes, *J. Geophys. Res.*, *71(20)*, 4711–4721.
- Lu, W., D. Wang, N. Takagi, V. Rakov, M. Uman, and M. Miki (2008), Characteristics of the optical pulses associated with a downward branched stepped leader, *J. Geophys. Res.*, *113*, D21206, doi:10.1029/2008JD010231.

- Lundholm, R. (1957), Induced overvoltage-surges on transmission lines and their bearing on the lightning performance at medium voltage networks, *Trans. Chalmers Univ. Technol.*, *120*, 117.
- Lyons, W. A., D. A. Moon, J. A. Schuh, N. J. Pettit, and J. R. Eastman (1989), The design and operation of a national lightning detection network using time-of-arrival technology, in *Proc. Int. Conf. on Lightning and Static Elec. (ICOLSE)*, Bath, England, pp. 2B.2.1–8.
- MacClement, W. D., and R. C. Murty (1978), VHF direction finder studies of lightning. *J. Appl. Meteorol.*, *17*, 786–795.
- Mach, D. M., and W. D. Rust (1989), Photoelectric return-stroke velocity and peak current estimates in natural and triggered lightning, *J. Geophys. Res.*, *94*, 13,237–13,247.
- Mach, D. M., and W. D. Rust (1997), Two-dimensional speed and optical risetime estimates for natural and triggered dart leaders, *J. Geophys. Res.*, *102*, 13,673–13,684.
- Maier, L., C. Lennon, T. Britt, and S. Schaefer (1995), LDAR system performance and analysis, paper presented at the 6th Conference on Aviation Weather Systems, Am. Meteorol. Soc., Boston, Mass.
- Marshall, T. C., and W. D. Rust (1991), Electric field soundings through thunderstorms, *J. Geophys. Res.*, *96*, 22,297–22,306.
- Marshall, T. C., M. P. McCarthy, and W. D. Rust (1995), Electric field magnitudes and lightning initiation in thunderstorms, *J. Geophys. Res.*, *100*(D4), 7097–7103.
- Marshall, T. C., M. Stolzenburg, C. R. Maggio, L. M. Coleman, P. R. Krehbeil, T. Hamlin, R. J. Thomas, and W. Rison (2005), Observed electric fields associated with lightning initiation, *Geophys. Res. Lett.*, *32*, L03813, doi:10.1029/2004GL021802.
- Master, M. J., M. A. Uman, W. H. Beasley, and M. Darveniza (1984), Lightning induced voltages on power lines: experiment, *IEEE Trans. PAS*, *103*, 2519–2529.
- McCarthy, M and G. K. Parks (1985), Further observations of x-rays inside thunderstorms, *Geophys. Res. Lett.*, *12*, 393–396.
- McEachron, K. B. (1939), Lightning to the empire state building, *J. Franklin Inst.*, *227*, 149–217.
- Miki, M., V. A. Rakov, K. J. Rambo, G. H. Schnetzer, and M. A. Uman (2002), Electric fields near triggered lightning channels measured with Pockels sensors, *J. Geophys. Res.*, *107*(D16), 4277, doi:10.1029/2001JD001087.
- Moore, C. B., B. Vonnegut, and D. N. Holden (1989), Anomalous electric fields associated with clouds growing over a source of negative space charge, *J. Geophys. Res.*, *94*, 13,127–13,134.

- Moore, C. B., K. B. Eack, G. D. Aulich, and W. Rison (2001), Energetic radiation associated with lightning stepped-leaders, *Geophys. Res. Lett.*, *28*, 2141–2144.
- Moss, G. D., V. P. Pasko, N. Liu, and G. Veronis (2006), Monte Carlo model for analysis of thermal runaway electrons in streamer tips in transient luminous events and streamer zones of lightning leaders, *J. Geophys. Res.*, *111*, A02307, doi:10.1029/2005JA011350.
- Murray, N. D., E. P. Krider, and J. C. Willett (2005), Multiple pulses in dE/dt and the fine-structure of E during the onset of first return strokes in cloud-to-ocean lightning, *Atmos. Res.*, *76*, 455–480.
- Murty, R. C., and W. D. MacClement (1973), VHF direction finder for lightning location, *J. Appl. Meteorol.*, *12*, 1401–1405.
- Nag, A., and V. A. Rakov (2008), Pulse trains that are characteristic of preliminary breakdown in cloud-to-ground lightning but are not followed by return stroke pulses, *J. Geophys. Res.*, *113*, D01102, doi:10.1029/2007JD008489.
- Nag, A., and V. A. Rakov (2009), Electric field pulse trains occurring prior to the first stroke in negative cloud-to-ground lightning, *IEEE Trans. Electromagn. Compat.*, *51*(1), 147–150, doi:10.1109/TEM.2008.2005488.
- Nagai, Y., S. Kawamata, and Y. Edano (1982), Observation of preceding leader and its downward traveling velocity in Utsunomiya district, *Res. Lett. Atmos. Electr.*, *2*, 53–56.
- Nemiroff, R. J., J. T. Bonnell, and J. P. Norris (1997), Temporal and spectral characteristics of terrestrial gamma flashes, *J. Geophys. Res.*, *102*, 9659–9665.
- Norton, K. A. (1937), Propagation of radio waves over the surface of Earth and in the upper atmosphere, II, *Proc. IEEE*, *25*, 1203–1236.
- Nucci, C. A., C. Mazzetti, F. Rachidi, and M. Ianoz (1988), On lightning return stroke models for LEMP calculations, in *Proc. 19th Int. Conf. Lightning Protection*, Graz, Austria.
- Oetzel, G. N., and E. T. Pierce (1969), VHF technique for locating lightning, *Radio Sci.*, *4*, 199–201.
- Olsen, R. C., D. M. Jordan, V. A. Rakov, M. A. Uman, and N. Grimes (2004), Observed one-dimensional return stroke propagation speeds in the bottom 170 m of a rocket-triggered lightning channel, *Geophys. Res. Lett.*, *31*, L16,107, doi:10.1029/2004GL020187.
- Olsen, R. C., V. A. Rakov, D. M. Jordan, J. Jerauld, M. A. Uman, and K. J. Rambo (2006), Leader/return-stroke-like processes in the initial stage of rocket-triggered lightning, *J. Geophys. Res.*, *111*, D13202, doi:10.1029/2005JD006790.
- Orville, R. E. (1968), Photograph of a close lightning flash, *Science*, *162*, 666–667.

- Orville, R. E., and V. P. Idone (1982), Lightning leader characteristics in the Thunderstorm Research International Program (TRIP), *J. Geophys. Res.*, *87*, 11,177–11,192.
- Parks, G. K., B. H. Mauk, R. Spiger, and J. Chin (1981), X-ray enhancements detected during thunderstorm and lightning activities, *Geophys. Res. Lett.*, *8*, 1176–1179.
- Peterson, D., M. Bailey, W. H. Beasley, and J. Hallett (2008), A brief review of the problem of lightning initiation and a hypothesis of initial lightning leader formation, *J. Geophys. Res.*, *113*, D17205, doi:10.1029/2007JD009036.
- Phelps, C. T. (1974), Positive streamer system intensification and its possible role in lightning initiation, *J. Atmos. Sol. Terr. Phys.*, *36*, 103–111.
- Poehler, H. A. (1977), An accuracy analysis of the LDAR system, *NASA Contract. Rep.*, CR-154631, 83.
- Poehler, H. A., and C. L. Lennon (1979), Lightning detection and ranging system (LDAR), system description and performance objectives, *NASA Tech. Mem. TM-74105*.
- Proctor, D. E. (1971), A hyperbolic system for obtaining VHF radio pictures of lightning, *J. Geophys. Res.*, *76*, 1478–1489.
- Proctor, D. E. (1981), VHF radio pictures of cloud flashes, *J. Geophys. Res.*, *86*, 4041–4071.
- Proctor, D. E. (1983), Lightning and precipitation in a small multicellular thunderstorm, *J. Geophys. Res.*, *88*, 5421–5440.
- Proctor, D. E. (1997), Lightning flashes with high origins, *J. Geophys. Res.*, *102*, 1693–1706.
- Proctor, D. E., R. Uytendogaardt, and B. M. Meredith (1988), VHF radio pictures of lightning flashes to ground, *J. Geophys. Res.*, *93*, 12,683–12,727.
- Rahman, M., V. Cooray, N. A. Ahmad, J. Nyberg, V. A. Rakov, and S. Sharma (2008), X rays from 80-cm long sparks in air, *Geophys. Res. Lett.*, *35*, L06805, doi:10.1029/2007GL032678.
- Rakov, V. A. (1990), Modern passive lightning locating systems, *Meteor. Hidrol.*, *11*, 118–23.
- Rakov, V. A. (1998), Some inferences on the propagation mechanisms of dart leaders and return strokes, *J. Geophys. Res.*, *103*, 1879–87.
- Rakov, V. A., and A. A. Dulzon (1987), Calculated electromagnetic fields of lightning return stroke, *Tekh. Elektrodinam*, *1*, 87–89.
- Rakov, V. A., and G. R. Huffines (2003), Return stroke multiplicity of negative cloud-to-ground lightning flashes, *J. Appl. Meteor.*, *42*(10), 1455–1462.
- Rakov, V. A., and M. A. Uman (1990), Waveforms of first and subsequent leaders in negative natural lightning flashes, *J. Geophys. Res.*, *95*, 16,561–16,577.

- Rakov, V. A., and M. A. Uman (1998), Review and evaluation of lightning return stroke models including some aspects of their application, *IEEE Trans. EMC*, 40(4), 403–426.
- Rakov, V. A., and M. A. Uman (2003), *Lightning: physics and effects*, Cambridge Univ. Press, Cambridge, United Kingdom.
- Rakov, V. A., M. A. Uman, G. R. Hoffman, M. W. Masters, and M. Brook (1996), Bursts of pulses in lightning electromagnetic radiation: Observations and implications for lightning test standards, *IEEE Trans. Electromagn. Compat*, 38(2), 156–164.
- Rakov, V. A., et al. (1998), New insights into lightning processes gained from triggered-lightning experiments in Florida and Alabama, *J. Geophys. Res.*, 103, 14,117–14,130.
- Rakov, V. A., D. E. Crawford, K. J. Rambo, G. H. Schnetzer, M. A. Uman, and R. Tottappillil (2001), M-component mode of charge transfer to ground in lightning discharges, *Journal of Geophysical Research*, 106, 22,817–22,831.
- Rakov, V. A., D. E. Crawford, V. Kodali, V. P. Idone, M. A. Uman, G. H. Schnetzer, and K. J. Rambo (2003), Cutoff and reestablishment of current in rocket-triggered lightning, *J. Geophys. Res.*, p. 4747, doi:10.1029/2003JD003694.
- Rakov, V. A., M. A. Uman, and K. J. Rambo (2005), A review of ten years of triggered-lightning experiments at Camp Blanding, Florida, *Atmos. Res.*, 76, 504–518, doi:10.1016/j.atmosres.2004.11.028.
- Ray, P. S., D. R. MacGorman, W. D. Rust, W. L. Taylor, and L. W. Rasmussen (1987), Lightning location relative to storm structure in a supercell storm and a multicell storm, *J. Geophys. Res.*, 99, 10,745–50.
- Reid, G. C. (1986), *The Earth's Electrical Environment*, chap. Electrical structure of the middle atmosphere, pp. 183–194, National Academy Press, Washington, DC.
- Rhodes, C., and P. R. Krehbiel (1989), Interferometric observations of a single stroke cloud-to-ground flash, *Geophys. Res. Lett.*, 16, 1169–1172.
- Roble, R. G., and I. Tzur (1986), *The Earth's Electrical Environment*, chap. The global atmospheric-electrical circuit, pp. 206–231, National Academy Press, Washington, DC.
- Rust, W. D., and D. R. MacGorman (1988), Techniques for measuring electrical parameters of thunderstorms, in *Thunderstorms, vol. 3, Instruments and Techniques for Thunderstorm Observation and Analysis*, ed. E. Kessler, pp. 91–118, Norman, Oklahoma, University of Oklahoman Press.
- Rust, W. D., and T. C. Marshall (1996), On abandoning the thunderstorm tripole-charge paradigm, *J. Geophys. Res.*, 101, 23,499–23,504.

- Saleh Z., J. Dwyer, J. Howard, M. Uman, M. Bakhtiari, D. Concha, M. Stapleton, D. Hill, C. Biagi, H. Rassoul (2009), Properties of the X-ray emission from rocket-triggered lightning as measured by the Thunderstorm Energetic Radiation Array (TERA), *J. Geophys. Res.*, *114*, D17210, doi:10.1029/2008JD011618.
- Schoene, J., M. A. Uman, V. A. Rakov, V. Kodali, K. J. Rambo, and G. H. Schnetzer (2003a), Statistical characteristics of the electric and magnetic fields and their time derivatives 15 m and 30 m from triggered lightning, *J. Geophys. Res.*, *108*, 4192, doi:10.1029/2002JD002698.
- Schoene, J., M. A. Uman, V. A. Rakov, K. J. Rambo, J. Jerauld, and G. H. Schnetzer (2003b), Test of the transmission line model and traveling current source model with triggered lightning return strokes at very close range, *J. Geophys. Res.*, *108*(D23), 4737, doi:10.1029/2003JD003683.
- Schonland, B. F. J. (1938), Progressive lightning, part 4, the discharge mechanisms, *Proc. Roy. Soc. A*, *164*, 132–150.
- Schonland, B. F. J. (1956), *Handbuch der Physik*, vol. 22, chap. The lightning discharge, pp. 576–628, Springer-Verlag, Berlin.
- Schonland, B. F. J., and J. P. T. Viljoen (1933), On a penetrating radiation from thunderclouds, *Proc. Roy. Soc., A*, *140*, 314–333.
- Schonland, B. F. J., D. J. Malan, and H. Collens (1935), Progressive lightning II, *Proc. Roy. Soc. A*, *152*, 595–625.
- Schonland, B. F. J., D. B. Hodges, and H. Collens (1938a), Progressive lightning, part 5, a comparison of photographic and electrical studies of the discharge process, *Proc. Roy. Soc. A*, *166*, 56–75.
- Schonland, B. F. J., D. J. Malan, and H. Collens (1938b), Progressive lightning, part 6, *Proc. Roy. Soc. A*, *168*, 455–469.
- Shao, X. M., Krehbiel, P. R., Thomas, R. J., and Rison, W. (1995), Radio interferometric observations of cloud-to-ground lightning phenomena in Florida, *J. Geophys. Res.* *100*, 2749–83.
- Smith, D. M., L. I. Lopez, R. P. Lin, C. P. Barrington-Leigh (2005), Terrestrial gamma-ray flashes observed up to 20 MeV, *Science*, *307*, 1085–1088.
- Starr, S., D. Sharp, F. Merceret, J. Madura, and M. Murphy (1998), LDAR, a three-dimensional lightning warning system: its development and use by the government, and transition to public availability, in *Proc. 35th Space Congress, Horizons Unlimited*, Cocoa Beach, Florida, pp. 299–305, Canaveral Council of Technical Societies.
- Susczyński, D. M., R. Roussel-Dupre, and G. Shaw (1996), Ground-based search for x-rays generated by thunderstorms and lightning, *J. Geophys. Res.*, *101*, 23,505–23,516.

- Symbalisty, E. M. D., R. A. Roussel-Dupré, and V. A. Yukhimuk (1998), Finite volume solution of the relativistic Boltzmann equation for electron avalanche studies, *IEEE Trans. Plasma Sci.*, 26(5), 1575–1580.
- Taylor, W. L. (1978), A VHF technique for space-time mapping of lightning discharge processes, *J. Geophys. Res.*, 83, 3575–83.
- Thomas, R. J., P. R. Krehbiel, W. Rison, S. J. Hunyady, W. P. Winn, T. Hamlin, and J. Harling (2004), Accuracy of the Lightning Mapping Array, *J. Geophys. Res.*, 109, D14207, doi:10.1029/2004JD004549.
- Thomson, E. M. (1985), A theoretical study of electrostatic field wave shapes from lightning leaders, *J. Geophys. Res.*, 90, 8,125–8,135.
- Thomson, E. M., P. J. Medelius, and S. Davis (1994), A system for locating the sources of wideband dE/dt from lightning, *J. Geophys. Res.*, 99, 22,793–22,802.
- Thottappillil, R., V. A. Rakov, and M. A. Uman (1997), Distribution of charge along the lightning channel: relation to remote electric and magnetic fields and to return-stroke models, *J. Geophys. Res.*, 102(D6), 6987–7006.
- Twomey, S. A., *Introduction to the Mathematics of Inversion in Remote Sensing and Indirect Measurements*, Elsevier, New York, 1977.
- Uman, M. A. (1974), The earth and its atmosphere as a leaky spherical capacitor, *Am. J. Phys.*, 42, 1033–35.
- Uman, M. A. (1987), *The Lightning Discharge*, Academic Press, Orlando.
- Uman, M. A., D. K. McLain (1969), Magnetic field of the lightning return stroke, *J. Geophys. Res.*, 74, 6899–6910.
- Uman, M. A., D. K. McLain, R. J. Fisher, and E. P. Krider (1973), Currents in Florida lightning return strokes, *J. Geophys. Res.*, 78, 3530–3537.
- Uman, M. A., D. K. McLain, and E. P. Krider (1975), The electromagnetic radiation from a finite antenna, *Am. J. Phys.*, 43, 33–38.
- Uman, M. A., V. A. Rakov, G. H. Schnetzer, K. J. Rambo, D. E. Crawford, and R. J. Fisher (2000), Time derivative of the electric field at 10, 14, and 30 m from triggered lightning strokes, *J. Geophys. Res.*, 105, 15,577–15,595.
- Uman, M. A., J. Schoene, V. A. Rakov, K. J. Rambo, and G. H. Schnetzer (2002), Correlated time derivatives of current, electric field intensity, and magnetic flux density for triggered lightning at 15 m, *J. Geophys. Res.*, 107.

- Visacro, S., A. Soares Jr., M. A. O. Schroeder, L. C. Cherchiglia, and V. J. de Sousa (2004), Statistical analysis of lightning current parameters: measurements at Morro do Cachimbo Station, *J. Geophys. Res.*, *109*, D01,105, doi:10.1029/2003JD003662.
- Wagner, C. F. (1960), Determination of the wave front of lightning stroke currents from field measurements, *IEEE Trans. Power App. Syst.*, *79*, 581–589.
- Wagner, C. F. (1963), Relation between stroke current and velocity of the return stroke. *AIEE Trans. Power Appar. Syst.*, *82*, 609–17.
- Wagner, C. F. (1967), Lightning and transmission lines, *J. Franklin Inst.*, *283*, 558–594.
- Wang, D., N. Takagi, T. Watanabe, V. A. Rakov, and M. A. Uman (1999a), Observed leader and return-stroke propagation characteristics in the bottom 400 m of the rocket triggered lightning channel, *J. Geophys. Res.*, *104*, 14,369–14,376.
- Wang, D., V. A. Rakov, M. A. Uman, N. Takagi, T. Watanabe, D. E. Crawford, K. J. Rambo, G. H. Schnetzer, R. J. Fisher, and Z. I. Kawasaki (1999b), Attachment process in rocket-triggered lightning strokes, *J. Geophys. Res.*, *104*, 2143–2150.
- Wang, D., V. A. Rakov, M. A. Uman, M. I. Fernandex, K. J. Rambo, G. H. Schnetzer, and R. J. Fisher (1999c), Characteristics of the initial stage of negative rocket-triggered lightning, *J. Geophys. Res.*, *104*(D4), 4213–4222.
- Wang, D., M. Chen, N. Takagi, and T. Watanabe (2001), Correlated sub-microsecond E-field and high-speed image of the natural lightning attachment process, in *Proc. Int. Conf. Lightning and Static Elec. (ICOLSE)*, Society of Automotive Engineers (SAE), Seattle, Washington.
- Weidman, C. D., and E. P. Krider (1978), The fine structure of lightning return stroke wave forms, *J. Geophys. Res.*, *83*(C12), 6239–6247.
- Weidman, C. D., and E. P. Krider (1979), The radiation field waveforms produced by intracloud lightning discharge processes, *J. Geophys. Res.*, *84*, 3159–3164.
- Weidman, C. D., and E. P. Krider (1980), Submicrosecond risetimes in lightning radiation fields, In *Lightning Technology*, 29–38, NASA Conf. Publ. 2128, FAA-RD-80-30.
- Weidman, C. D., J. Hamelin, C. Leteinturier, and L. Nicot (1986), Correlated current-derivative (dI/dt) and electric field-derivative (dE/dt) emitted by triggered lightning, paper presented at International Aerospace and Ground Conference of Lightning and Static Electricity (ICOLSE), U.S. Air Force, Dayton, Ohio.
- Willett, J. C., E. P. Krider (2000), Rise times of impulsive high-current processes in cloud-to-ground lightning, *IEEE Trans. Ant. Propag.*, *48*, 1442–1451.

- Willett, J. C., V. P. Idone, R. E. Orville, C. Leteinturier, A. Eybert-Berard, L. Barret, and E. P. Krider (1988), An experimental test of the "transmission-line model" of electromagnetic radiation from triggered lightning return strokes, *J. Geophys. Res.*, 93(D4), 3867–3878.
- Willett, J. C., J. C. Bailey, V. P. Idone, A. Eybert-Berard, and L. Barret, (1989), Submicrosecond intercomparison of radiation fields and currents in triggered lightning return strokes based on the transmission-line model, *J. Geophys. Res.*, 94, 13,275–13,286.
- Williams, D. P., and M. Brook (1963), Magnetic measurement of thunderstorm currents, 1: continuing currents in lightning, *J. Geophys. Res.*, 68, 3243–3247.
- Wilson, C. T. R. (1920), Investigations on lightning discharges and on the electric field of thunderstorms, *Phil. Trans. Roy. Soc. A*, 221, 73–115.
- Wilson, C. T. R. (1925), The acceleration of beta-particles in strong electric fields such as those of thunderclouds, *Proc. Cambridge Philos. Soc.*, 22, 534–538.
- Yokoyama, S., K. Miyake, T. Suzuki, and S. Kanao (1990), Winter lightning on Japan Sea Coast – development of measuring system on progressing feature of lightning discharge, *IEEE Trans. Pow. Del.*, 5, 1418–1425

BIOGRAPHICAL SKETCH

Joseph Sean Howard was born in 1981 in Pensacola, Florida and is the second of three children. In 1990, he moved with his family to Lake City, FL, where he eventually graduated as salutatorian from Columbia High School in 1999. In 2001, he obtained his Associate of Arts degree from Lake City Community College (LCCC), graduating as valedictorian, before transferring to the University of Florida (UF). In May 2004, Mr. Howard graduated summa cum laude with a Bachelor of Science in electrical engineering from UF. He also received the most prestigious award (Electrical E Award) granted by the Department of Electrical and Computer Engineering for graduating with a grade point average above 3.90. Benefitting from a 3/2 program, he was able to receive a Master of Science in electrical engineering in December 2005. Mr. Howard became involved with the lighting research laboratory in 2004, and he participated in lightning experiments at the International Center for Lightning Research and Testing (ICLRT) between 2004 and 2007. He also served as the Student Team Leader at the ICLRT from 2006 to 2007. He has authored and co-authored 6 papers in reviewed journals, 5 papers in conference proceedings, and 3 technical reports.